2015

Molecular dynamics simulation of the grain boundary deformation behaviours in Al

Kuiyu Cheng
University of Wollongong

UNIVERSITY OF WOLLONGONG

Department of School of Mechanical, Materials and Mechatronics Engineering

Faculty of Engineering

Molecular Dynamics Simulation of the Grain Boundary Deformation Behaviours in Al

Kuiyu Cheng

This thesis is presented as part of the requirements for the award of the Degree of

DOCTOR OF PHILOSOPHY

From

University of Wollongong

February 2015

DECLARATION

I, Kuiyu Cheng, declare that this thesis, submitted in fulfilment of the requirements for the award of Doctor of Philosophy, in the School of Mechanical, Materials and Mechatronics Engineering, University of Wollongong, Australia, is wholly my own work unless otherwise referenced or acknowledged, and has not been submitted for qualifications at any other university or academic institution.

Kuiyu Cheng

February 2015

ACKNOWLEDGEMENTS

I wish to express deep gratitude to my supervisors Prof. Kiet Tieu, and A/Prof. Cheng Lu for their support, patience, and guidance throughout all these years.

I also wish to take the opportunity to thank the staff and students within the School of Materials, Mechanical, and Mechatronics Engineering for all the help and assistance given.

I will always be grateful to the University of Wollongong for providing the HDR and UPA scholarships.

I really appreciate my parents in law Ms. Lihui Huang and Chaohui Guo and my parents Ms. Dexin Lv and Mr. Houxian Cheng for their unwavering support. Their continuous encouragement helped me to grow through this PhD thesis.

Finally, I give my heartfelt thanks to my wife Ms. Qi Guo for her love, encouragement, patience, and sharing during my doctoral work for without her, it would have been impossible for me to finish this thesis.

Thank you all,

Kuiyu Cheng.

LIST OF PUBLICATIONS DURING THE PHD COURSE

Published and accepted

- L. Zhang, C. Lu, K. Tieu, L.Q. Pei, X. Zhao, **K.Y. Cheng**, "*Molecular dynamics study on the grain boundary dislocation source in nanocrystalline copper under tensile loading*" **Materials Research Express** (Accepted).
- L.Q. Pei, C. Lu, X. Zhao, L. Zhang, **K.Y. Cheng**, G. Michal, K. Tieu, "*Brittle versus ductile behaviour of nanotwinned copper: A molecular dynamics study*" **Acta Materialia** 89 (2015) 1-13.
- **K.Y. Cheng**, C. Lu, K. Tieu, "*Response of the Al Σ5 <001>{310} symmetric tilt grain boundary to the shear deformation simulated by molecular dynamics*" **Science of Advanced Materials** (1947-2935), 6 (7), (2014) 1322.
- **K.Y. Cheng**, K. Tieu, C. Lu, X. Zheng, H.T. Zhu, "*Molecular dynamics simulation of the grain boundary sliding behaviour for Al Σ5 (210)*" **Computational Materials Science** 81 (2014) 52–57.
- **K.Y. Cheng**, C. Lu, K. Tieu, "*Microstructural evolution and mechanical property of AA5050 alloy deformed by accumulative roll bonding*" **Metallurgical and Materials Transactions B** 45 (2014) 399-403.
- **K.Y. Cheng**, C. Lu, K. Tieu, "*Abnormal ductility increase of commercial purity Al during accumulative roll-bonding*" **Metallurgical and Materials Transactions B** 45 (2014) 404-408.
- **K.Y. Cheng**, K. Tieu, C. Lu, H.T. Zhu, L.Q. Pei, "*Effect of pre-heating on the microstructural evolution and super-plasticity of Al deformed by accumulative roll bonding*" **Steel Research International** 84 (2014) 1209-1215.
- X. Zheng, H.T. Zhu, K. Tieu, **K.Y. Cheng**, "*Molecular dynamics simulation of confined n-alkanes ordered structure and crystalline bridges*" **International Journal of Surface Science and Engineering**, 8 (2014) 201.
- L.Q. Pei, C. Lu, K. Tieu, H.T. Zhu, X. Zhao, **K.Y. Cheng**, L. Zhang, *"Influence factors for brittle-to-ductile transition in twinned copper"*. **TMS Annual Meeting** *(2014).*

- L. Zhang, C. Lu, K. Tieu, X. Zhao, L.Q. Pei, **K.Y. Cheng**, "*Atomistic Simulation on the Structure and Mechanical Response of Σ3, Σ5 Tilt Grain Boundaries under Tension*" **TMS Annual Meeting** (2014) pp. 815-823
- L. Zhang, C. Lu, G. Michal, Tieu, X. Zhao, L.Q. Pei, **K.Y. Cheng**, "*Molecular dynamics study on the atomic mechanisms of coupling motion of [0 0 1] symmetric tilt grain boundaries in copper bicrystal*" **Materials Research Express** 1 (2014) 015019.
- L.Q. Pei, C. Lu, K. Tieu, H.T. Zhu, X. Zhao, **K.Y. Cheng**, L. Zhang, "*A Molecular Dynamics Simulation of Fracture in Nanocrystalline Copper*" **Journal of Nano Research** 23 (2013) 50-56.
- **K.Y. Cheng**, C. Lu, L.C. Zhang, K. Tieu, Y. Sun, "*Deformation Mechanism in Nanoindentation of* $Ti_{63.375}Fe_{34.125}Sn_{2.5}$ *Alloy*" **TMS Annual Meeting** (2012) 971-977.
- X. Zheng, H.T. Zhu, K. Tieu, **K.Y. Cheng**, Molecular dynamics simulation of confined n-alkanes: ordered structure and vibrational friction force, **AMPT2012**, 23-26 September (2012) Wollongong (NSW, Australia).
- Y. Sun, C. Lu, A.K. Tieu, Y. Zhao, H. Zhu, **K.Y. Cheng**, C. Kong, "*Fracture behaviours of TiN and TiN/Ti multilayer coatings on Ti substrate during nanoindentation*" **TMS Annual Meeting** (2012) pp. 963-970.

Submitted

- **K.Y. Cheng**, C. Lu, K. Tieu, L.Q Pei, C. Lu, X. Zhao, L. Zhang, G. Michal, "*Coupled grain boundary motion in aluminium: the effect of structural multiplicity*" **Scientific Report** (Submitted)

ABSTRACT

Grain boundary (GB), a special solid-solid interface in materials, exists in all polycrystalline materials, thereby being closely related to physical, chemical and mechanical properties (conductivity, catalysis, segregation, corrosion, ductility and strength etc) of the polycrystalline materials, especially in ultra fine and nano crystalline materials. In the present study, the molecular dynamics method has been used to simulate the grain boundary deformation behaviours, which include grain boundary sliding (GBS) behaviour, grain boundary coupling behaviour and the interaction between grain boundaries and dislocations. The following results have been obtained.

First, grain boundary sliding behaviour was strongly sensitive to the temperature. At low temperature, the GBS was very sensitive to the imposed ways of external applied forces. However, at high temperature, the two grains smoothly slid away from each other in the way of viscous grain boundary sliding under the shear deformation. Regardless of the type of driving force and misorientation, the bicrystal system tended to resist the applied force by GB rotation. Moreover, the grain boundary rotated among some of the Σ5 asymmetrical and symmetrical tilt GB boundaries under shear deformation and led to the normal stress σ_{xx} in the bicrystal system. Under particular circumstances, reaction of the grain boundary dislocations during shear deformation could release uncommon edge lattice dislocations from the grain boundary. The uncommon edge lattice dislocations with <110>/2 Burgers vectors have the [001] line direction and glide on the {110} planes.

Secondly, the structural multiplicity of the symmetric tilt Σ5(310) boundary in aluminium and its influence on the GB behaviour were simulated at a temperature range of 300K - 600K using molecular dynamic simulations. Two starting atomic configurations were adopted in the simulations which resulted in three different GB structures at different temperatures. Under the applied shear deformation each GB structure exhibited its unique GB behaviour. A dual GB behaviour, namely the transformation of one GB behaviour to another during deformation, was observed for the second starting configuration at a temperature of 500K. The atomistic mechanism responsible for the behaviour of each GB was analysed in detail in this paper.

Next, it was found that it was easier for the $a\sqrt{2}/2$ full screw dislocation to cut through the lower misorientation grain boundaries than the higher misorientation grain boundaries. The incident dislocation could transmit from one grain across the asymmetrical grain boundary into the neighboring grain for low misorientation tilt asymmetrical grain boundaries. As a result, the traveling distance of partial dislocations was proportional to the imposed shear strain. The depinning of the trailing partial dislocation required relatively large shear strain. The incoming slip plane and outgoing slip plane were not necessarily the same and the grain boundaries harmonized the deformation as a whole.

At last, the Σ13 (320) symmetrical tilt grain boundary presented strong tension-compression asymmetric ability: the asymmetry of stress-strain curves with respect to the load directions; the yield strain was increased as the grain size decreased for compression, while for tension the corresponding yield strain was increased as the grain size increased. The Young's modulus decreased as the grain size decreased (or the grain boundary volume fraction increased). Both tensile and compressive yield strength were decreased as the grain size decreased. This obeyed the inverse Hall-Petch relationship in the current range of grain size. Regardless of the grain size, the severe yielding was caused by the nucleation of partial dislocations at the grain boundaries for compression, while for tension the severe yielding was caused by the nucleation of partial dislocations inside the grains rather than at the grain boundaries. As regard to the deformation mechanisms, the softening was caused by the grain boundary yielding and the nucleation and propagation of dislocations, while the hardening was caused by dislocation interactions and grain boundary blocking.

TABLE OF CONTENTS

LIST OF FIGURES

LIST OF TABLES

1 INTRODUCTION

Grain boundary (GB), a special solid-solid interface in materials, exists in all polycrystalline materials, thereby being closely related to physical, chemical and mechanical properties (conductivity, catalysis, segregation, corrosion, ductility and strength etc) of the polycrystalline materials. Therefore, materials scientists have engaged for many decades in linking synthesis and improvement of crystalline materials to grain boundary involved mechanisms. These mechanisms include grain-boundary sliding, grain-boundary dislocation emission and annihilation, grain coalescence or grain boundary migration, dislocation pile-ups at grain boundaries and etc [1-4]. For instance, one of the dominant features in superplasticity is the role played by grain boundary sliding (GBS) which can contribute more than 50% of the total strain during superplastic deformation [1-4]. Even for quick plastic forming which operates at faster strain rates and lower temperatures than superplastic forming (SPF), the GBS can still account for certain plastic deformation [2, 5, 6]. As temperature goes up, the GBS will account for more plastic deformation in both above processing methods. Moreover, the effect of grain boundary on material properties becomes more significant especially with smaller grain sizes [7-16]. It is readily understandable that the fraction of atoms ascribed to the grain boundary or the grain boundary fraction, in other words, is increased as the grain size decreased. It can be seen that in a schematic depiction of a nanocrystalline material (Figure 1.1) [17], as the grain size is decreased to nano-scale, the fraction of white grain boundary atoms without crystalline symmetry is obviously increased and has a comparable quantity with the black crystalline atoms. This is consistent with the results from Palumbo et al. as shown in Figure 1.2, where the change of the volume fraction of intergrain regions and triple-junctions is plotted as a function of grain size [18]. By assuming that the grains have the shape of spheres or cubes, Meyers et al. proposed a simple estimation of the volume fraction of interfaces in the nanocrystalline material as 3D/d (where D is the average interface thickness and d is the average grain diameter) [10]. Thus, the volume fraction of interfaces or grain boundaries can be as much as 3% ~ 50%, as the grain size is decreased to 100 ~ 5 nm grains. It is the high

density of interfaces with a substantial fraction of atoms that gives the nanocrystalline materials increased strength/hardness [19-49], improved toughness [50-71], reduced elastic modulus and ductility [10, 15, 62, 72-96], enhanced diffusivity [97-102], higher specific heat, enhanced thermal expansion coefficient (CTE), and superior soft magnetic properties [103-120], or even some abnormal behaviours such as strain softening, annealing hardening [30, 121-130] and inverse Hall-Petch relation [21, 47, 131-156] in comparison with conventional polycrystalline materials. Therefore, the importance of the research on grain boundary involved mechanisms stands to reason in mechanical processing and materials science. In light of the incentive for widespread research in grain boundary, several grain boundary that involved plastic deformation mechanisms in metal materials are investigated in detail by molecular dynamics (MD) method in the present thesis work.

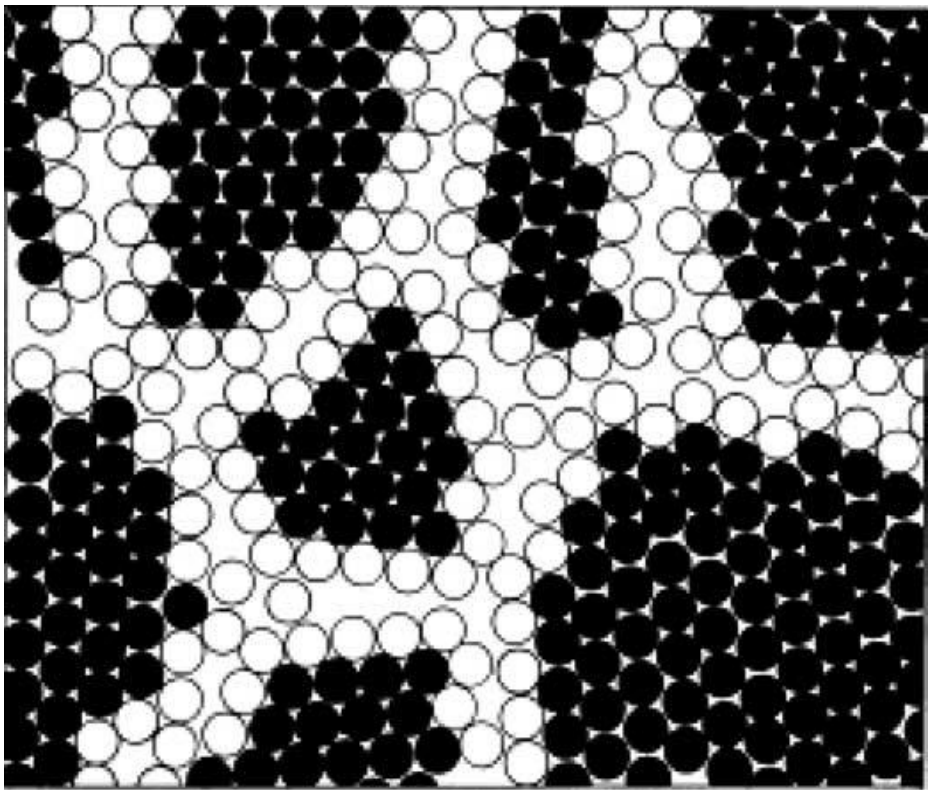

Figure 1.1 The two-dimensional schematic depiction of crystalline grain atoms (black balls) and non-crystalline grain boundary atoms (white balls) in a nanocrystalline material [17].

The general plastic deformation mechanisms include, but not limited to, pile-up breakdown, shear band formation, core and mantle model, grain boundary sliding,

grain boundary migration, grain boundary rotation, grain boundary dislocation creation and annihilation and mechanical twinning [10, 15, 74, 93, 157-169]. It can be seen that most of these mechanisms are closely related to the existence of grain boundaries. In particular, all the grain boundary behaviours can be understood by the interaction between grain boundaries and other lattice defects (dislocations, faults, vacancy, solutes and cracks etc). With the availability of the advanced tools for processing and characterization and modern computation techniques, these mechanisms have been gradually developed and illustrated. In this chapter, some general grain boundary that involved deformation mechanisms based on experimental observation is first simply reviewed. Secondly, some models of computer simulations are reviewed. Especially, the advantage and application of MD method on grain boundary research are mainly discussed. In the next place, some essential concepts and definitions concerning grain boundary theory are introduced. Then, the last part presents the framework of this thesis.

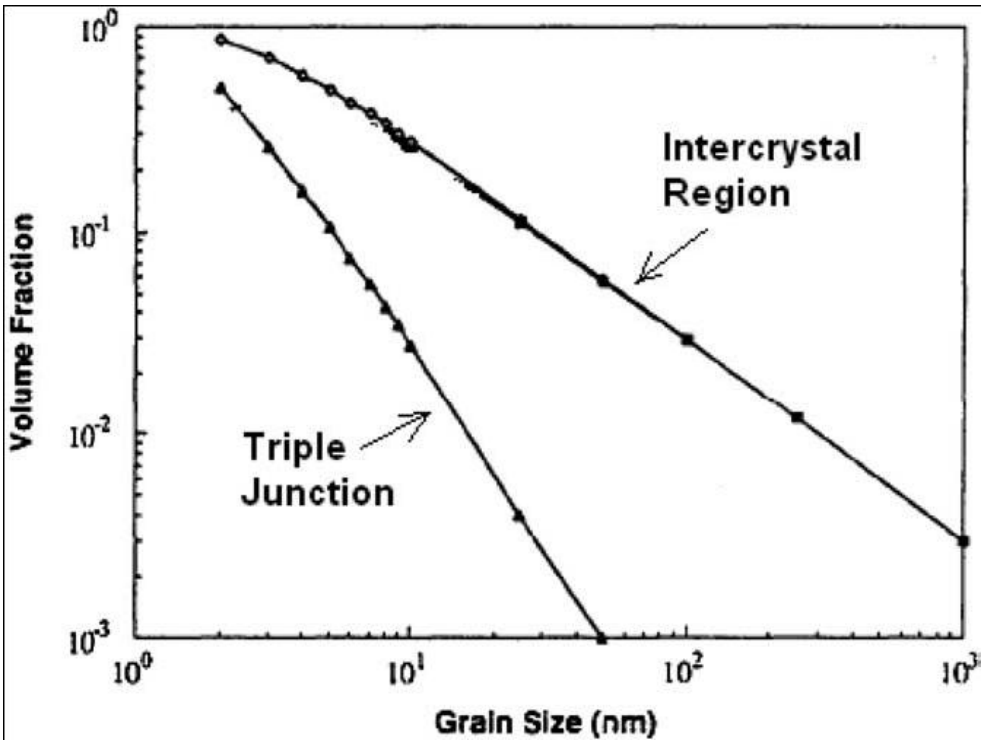

Figure 1.2 The effect of grain size on calculated volume fractions of intercrystal regions and triple junctions, assuming a grain-boundary thickness of 1 nm [18].

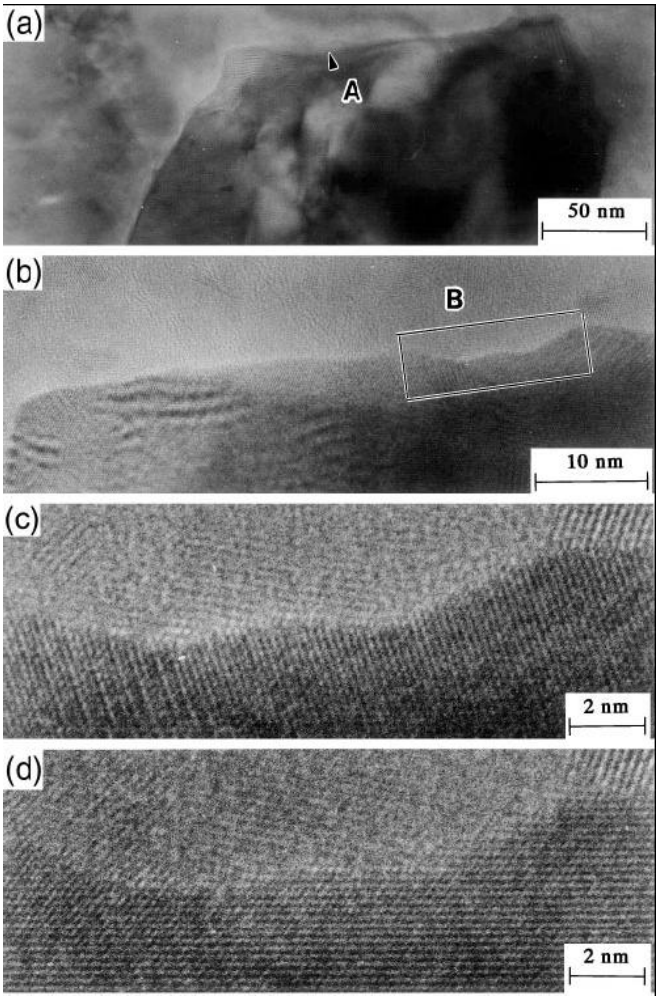

Figure 1.3 a) Electron micrograph of grain boundaries in Cu, b) enlargement of region A shown in a), (c) and (d) enlargement of region B shown in (b); note one-dimensional {111} fringes in lower grain appearing continuous up to grain boundary [170].

1.1 General Grain Boundary Models Based on Experiment Observation

1.1.1 Experimental observation of the grain boundary

Thanks to the advanced observation and characterization tools such as high resolution transmission electron microscope (HRTEM) and in-situ observation techniques etc, the details and what actually takes place in the vicinity of grain boundary are able to be presented in front of the world. Figure 1.3 shows the TEM and HRTEM micrographs of practical grain boundaries in Cu. It can be seen that the grain boundary is very narrow and, as is apparent from the right-hand portion of

Figure 1.3c) and 1.3d), the width is less than ~0.5 nm, equivalent to about two atomic spacings [170]. These images confirm that there is no region exhibiting a "gas-like" amorphous structure at the grain boundary [7].

The grain boundaries shown in Figure 1.3 are complex and really practical in materials, while there are also many simple grain boundaries in the nature world. Figure 1.4 shows the simplest grain boundaries, tilt and twist grain boundaries [171]. These actually exist in the practical materials and are extensively applied in computational methods to reveal the mechanical behaviour of materials.

1.1.2 Grain boundary mediated deformation

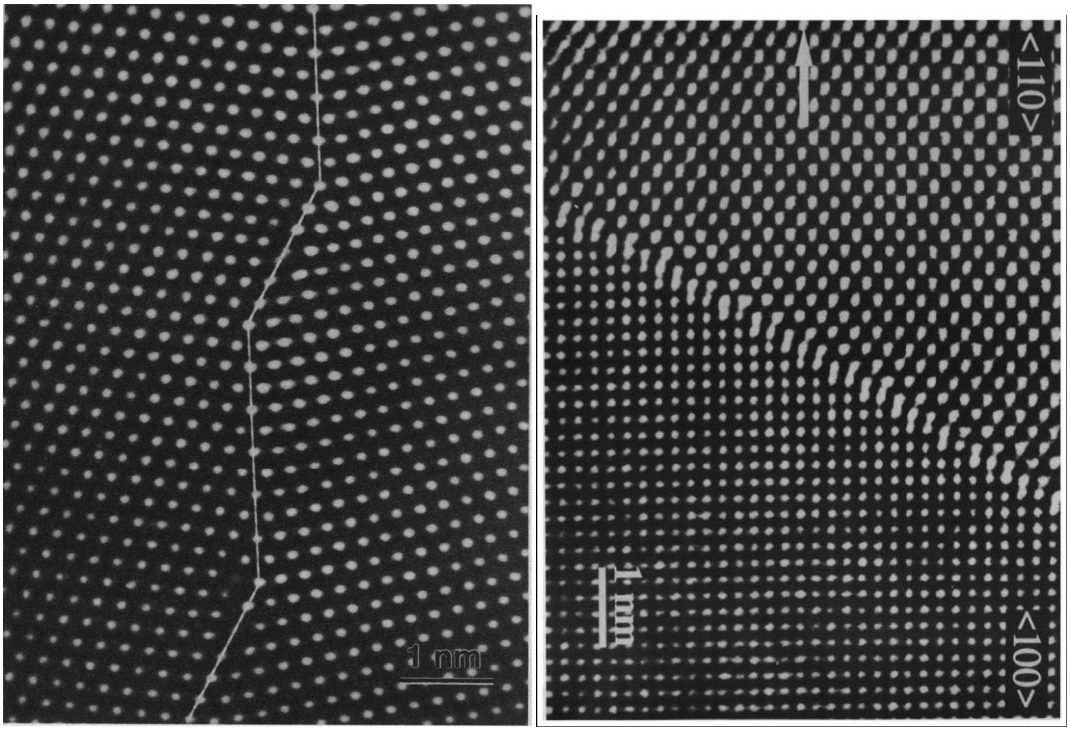

Figure 1.4 a) White column HREM image of θ=52.9o <110> tilt grain boundary in Au (This grain boundary is vicinal to (113)(113) and shows almost perfect (113)(113) grain boundary structures along short, symmetrical facets, while the misfit is concentrated at asymmetrical facets close to (111)(001)) and b) HREM image of Au grain boundary with tilt and twist components (The misorientation axis lies in the planeof the film and is indicated by an arrow) [171].

It has been proposed that GB-mediated plasticity (e.g., GB sliding and/or grain rotation) substitutes for conventional dislocation nucleation and motion as the

dominant deformation mechanism when grain sizes are reduced to below a certain value [172-174]. However, there was no direct experimental evidence of a transition in deformation mechanisms, i.e., from a dislocation-mediated deformation to a GB-mediated deformation [175-179], before Shan et al.' novel work [180].

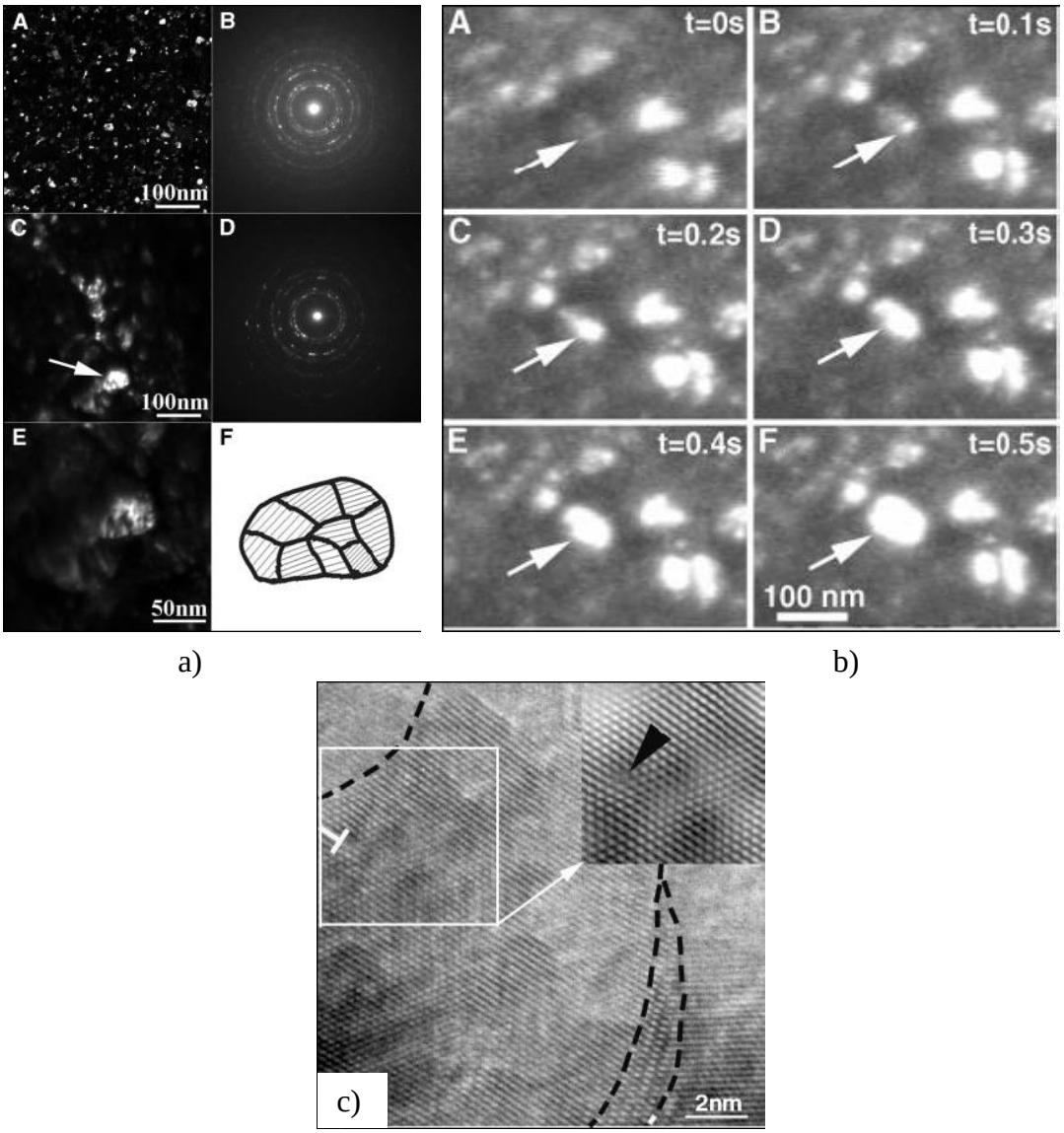

Figure 1.5 a) TEM micrographs showing the evolution of the Ni microstructure during in situ straining; b) DFTEM observation of the rapid genesis of an agglomerate (e.g., white arrow) depicted by individual still frames extracted from a dynamic video sequence and c) A typical HRTEM image of a thin area formed by deformation. A dislocation (white T) is trapped inside a grain close to the GB (delineated by black dashed line). The inverse Fourier-filtered image (inset) from inside the white box shows the dislocation (black arrowhead) with more clarity [180].

As shown in Figure 1.5, Shan et al. directly showed that grain boundary-mediated processes have become a prominent deformation mode by in situ dynamic transmission electron microscope observations of nanocrystalline nickel films with an average grain size of about 10nm. Additionally, in the vicinity of grain boundary trapped lattice dislocations were also observed in individual grains following deformation. It should be noted that this grain boundary mediated deformation was mainly governed by diffusion-assisted grain boundary processes. Later this deformation behaviour was also experimentally found in different materials [181-185]. Ivanisenko et al. reported a change in primary deformation mechanism that was induced by stress-induced grain growth in nanocrystalline palladium. Here for grain size below 40nm grain boundary mediated processes (shear banding, grain boundary sliding and grain rotation) controlled the deformation, with dislocation slip, twinning, and grain boundary diffusion that provided the accommodation [181]. In an overview study, Ovid'ko summarized the general grain boundary mediated deformation mechanisms – rotational deformation, grain boundary diffusional creep, triple junction diffusional creep, grain boundary sliding and emission or sink of lattice dislocations on grain boundary [186]. The specific explanations of each deformation mechanism are given within the corresponding Figures 1.6~1.10. The details, if interested, can be found in the reviewed paper [186].

It can be seen that, in the grain boundary mediated deformation behaviours, the grain boundary sliding (GBS) is a very important deformation mode. It is also accompanied with other grain boundary mediated deformation behaviours in polycrystalline materials. Moreover, not only does it seriously affect the deformation behaviour in nanocrystalline materials, but also governs the conventional polycrystalline materials at elevated temperatures with direct consequences on processes such as creep failure and superplastic formability. Therefore, GBS and relevant experimental studies have been extensively performed using bicrystals, tricrystals and polycrystalline samples to characterise or quantify GBS in metals and alloys [81, 187-195]. In particular, the bicrystal and tricrystal experimental results can be conducted with specific pertinence to various concerning issues regarding grain boundary. These results can present relatively more direct and clear observation at the grain boundary area [195-201]. By investigating the <101>

direction tilt zinc bicrystals with different misorientations, Watanabe et al. showed that grain boundary sliding strongly depended on the misorientation and was difficult in exact- or slightly off-coincidence boundaries. This was based on the movement of crystal lattice dislocations along the grain boundary by a combination of climb and glide [196].

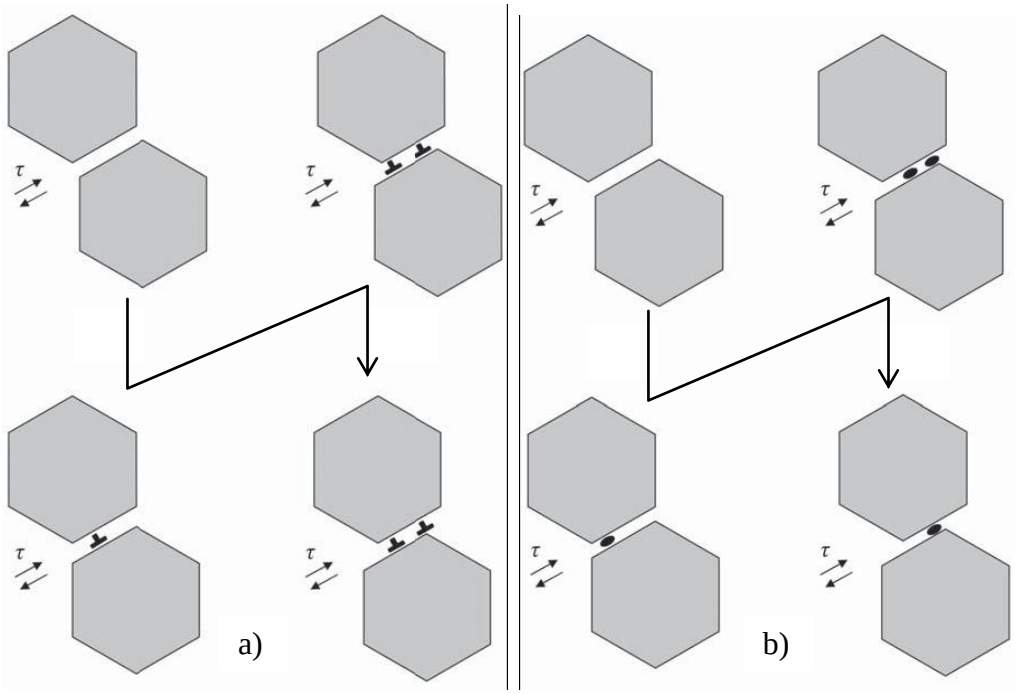

Figure 1. 6a) Grain boundary sliding occurs through a) movement of grain boundary dislocations and b) local shear events (ellipses) in grain boundaries (The black arrows indicate the deformation process). In terms of the dislocation theory, a local shear event is effectively treated as either nucleation of an isolated dislocation loop or formation of a kink pair at pre-existent line dislocation in the grain boundary phase [186].

In a series of Sheikh-Ali el al' studies, the model of grain boundary sliding operating under the conditions of plastic incompatibility was constructed. This was based on the possibility of separating the contributions of extrinsic grain boundary dislocations of different origins to the overall grain boundary shear [197-199]. Sheikh-Ali el al also gave the quantitative estimates of contributions of extrinsic grain boundary dislocations to grain boundary sliding and intragranular strain in the vicinity of the boundary [197-199]. In Maruyama et al.'s results [200], grain boundary sliding and migration were impeded by very small amount of aluminium addition (less than 0.1 mass%). This reduced the creep rate by one order of magnitude in zinc bicrystals and

polycrystals; moreover, the grain boundary was also significantly strengthened by the aluminium addition. Besides, Miura et al. compared the bicrystal response of a Cu–9at%Al alloy with a tricrystal that included a boundary node and confirmed that a boundary node can suppress grain boundary sliding [201]. Even the specific grain boundary structure unit can influence the GBS behaviour. Matsunaga et al. compared

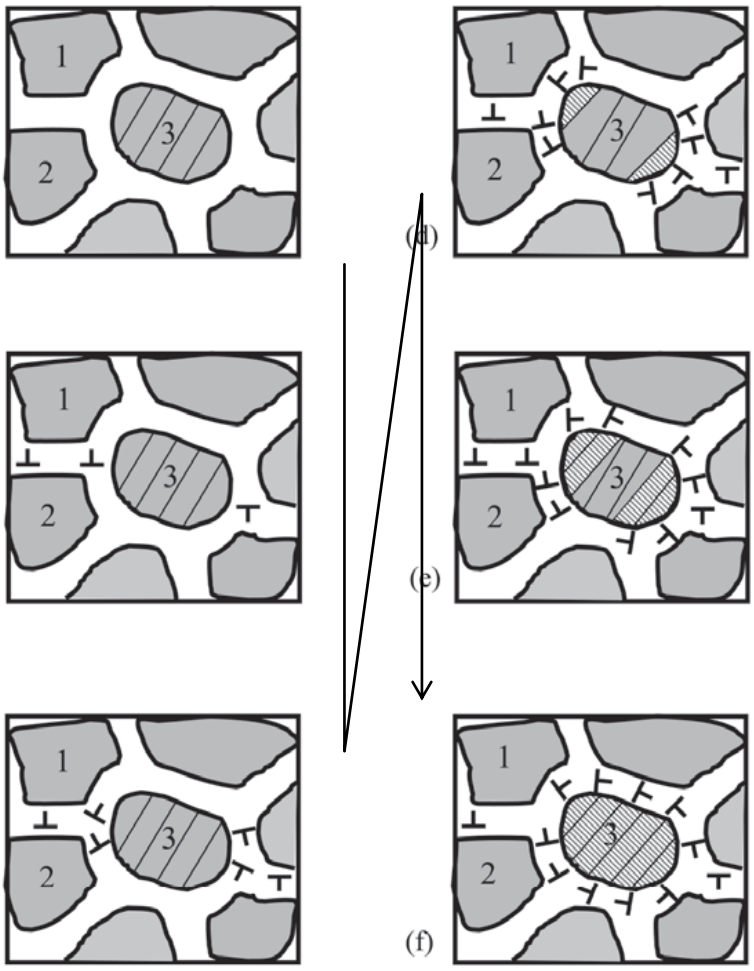

Figure 1.7 Grain boundary sliding transforms into crystal lattice rotation in the neighbouring grain in deformed nanomaterial (The black arrows indicate the deformation process). The relative shear of two nanoscale grains 1 and 2 along their common boundary is conducted by gliding grain boundary dislocations, whereas the crystal lattice rotation in the neighbouring nanoscale grain 3 is conducted by climbing grain boundary dislocations [186].

two types of Σ7 grain boundaries in Al_2O_3 bicrystals to investigate a relationship between the core structures and the sliding behaviour. They found that the *Σ*7/{2 -3 1 0} boundary containing larger open spaces at the core exhibited a much higher

sliding rate than the Σ7/{4 -5 1 0} with smaller open spaces at the core. This was due to the significant grain boundary diffusion arising from the open core structure of Σ7/{2 -3 1 0}[202, 203].

To sum up, the GBS behaviour is very complicated with concurrent accommodation processes, which may involve grain boundary migration (GBM), coupled motion, maintenance of the grain compatibility during GBS, grain rotation, diffusion, or dislocation motion. Any variants like vacancy, solutes or ledges can affect the GBS behaviour. Therefore, more detail in the vicinity of the grain boundary should be unveiled. As is highly demanded, the computer simulation method becomes a much powerful tool in such a small area and has resolved many relevant intractable issues. Next, the advantage of application of computer simulation in grain boundary research is reviewed.

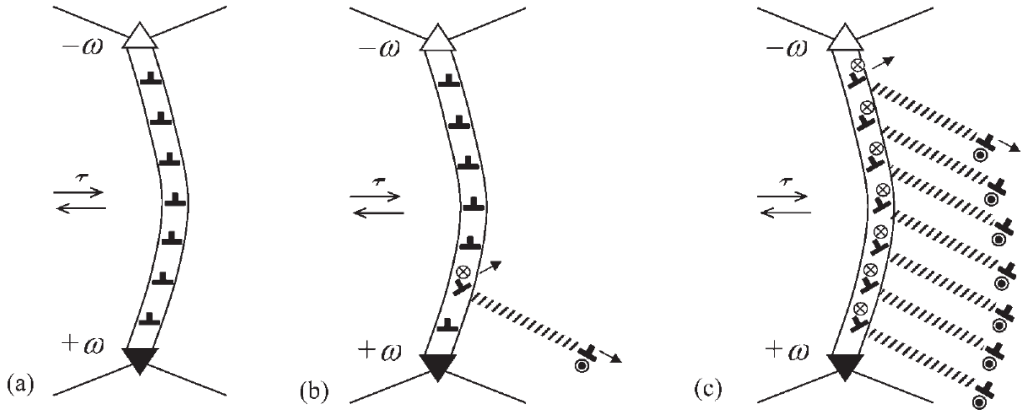

Figure 1.8 Emission of partial dislocations from high-angle grain boundary: a) High-angle grain boundary contains ‘intrinsic’ grain boundary dislocation and bows under the shear stress action; b) Partial dislocation is emitted from grain boundary due to transformation (splitting) of a grain boundary dislocation; c) Twin deformation occurs through emission of groups of partial dislocations from grain boundaries and their further movement in grain interiors (Twin occupies area swept by moving partial dislocations) .

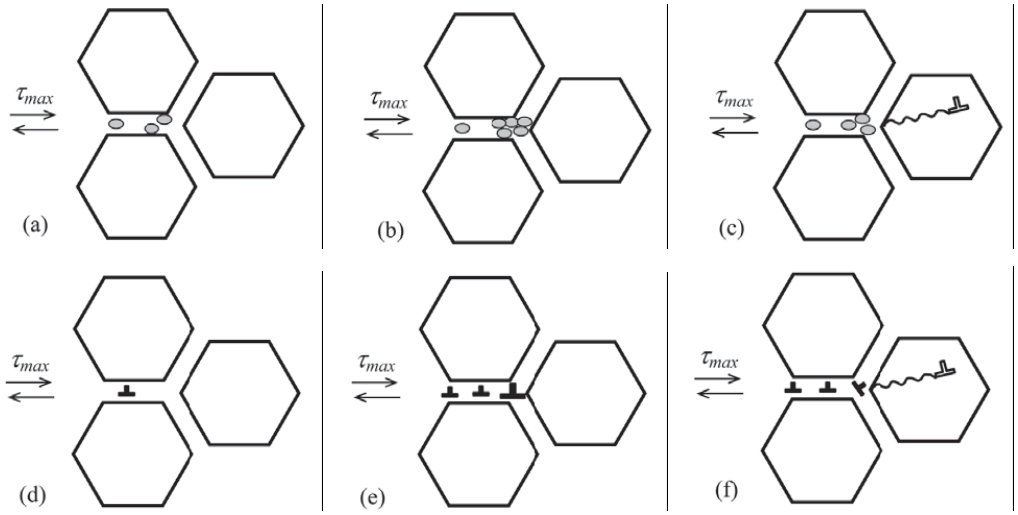

Figure 1. 9 Emission of partial dislocation from triple junction of grain boundaries: a) grain boundary sliding is realized through local shear events (events of nucleation of dislocation loops in grain boundary) driven by the shear stress action. Local shear events intensively occur in a grain boundary whose plane is oriented along the maximum shear stress action. The boundary plane changes its orientation at the adjacent triple junction which thereby serves as obstacle for grain boundary sliding through local shear events; b) the unfinished plastic shear or, in other terms, the Burgers vector is stored at the triple junction due to local shear events; c) when the stored Burgers vector magnitude reaches some critical value, a lattice dislocation of either perfect or partial type is emitted from the triple junction into a grain interior; d) grain boundary sliding is realized through movement of grain boundary dislocations which are stopped at triple junction; e) the sum Burgers vector of grain boundary dislocations is stored at the triple junction; f) when the stored Burgers vector magnitude reaches some critical value, a lattice dislocation of either perfect or partial type is emitted from the triple junction into a grain interior [186].

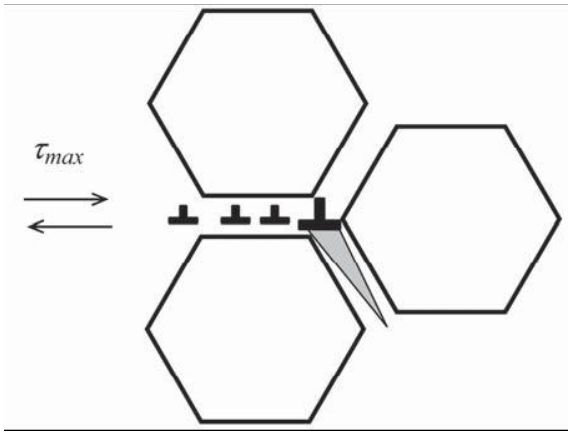

Figure 1. 10 Nanocrack generation occurs at dislocated triple junction [186].

1.2 Computer Simulation of Grain Boundary Deformation Behaviour

The numerical methods have gradually become a must in materials science, as closed form solutions for polycrystalline plastic flow on any size scale are beyond the classical analytical solution methods. The most common numerical methods, especially in the interest of grain boundary research, are finite element methods (FEM), molecular dynamics (MD) methods and ab initio electronic structure methods (ab initio). They have their own respective advantages and disadvantages in GB research. The newest relevant work can be found in [204-207] for FEM, [16, 208-212] for MD and [213-216] for ab initio methods. Before the selection of the numerical method for the present thesis, it is worthwhile to compare the strengths and weaknesses of these methods.

1.2.1 The strengths and weaknesses of respective numerical methods

Generally speaking, for any numerical methods, the length scale, time scale and computational cost are mostly concerned and closely related to their applications in different aspects of materials science.

First, the ab initio methods have the advantage that they can be made to converge to the exact solution. This happens when all approximations are sufficiently small in magnitude and when the finite set of basic functions tends toward the limit of a complete set. In addition to being accurate and having strong physical underpinnings, another advantage of the ab initio methods is that it can treat both pure elements and multi-component systems with a comparable amount of computational effort. This greatly facilitates the exploration of chemical effects on materials properties [212-216]. Moreover, sometimes the smallest calculation can give the best result for some properties. However, their computational cost is the most dominant shortage of ab initio methods. They often take enormous amount of computer time, memory, and disk space due to the numerical complexity. The general method scales nominally as N^4 (N is the number of basic functions) and with other correlated calculations may scales as N^5 for Møller–Plesset perturbation theory (MP2), N^6 for MP4 and N^7 for coupled cluster. This means a calculation twice as big takes 16, 32, 64 and 128 times as long to complete for respective corresponding calculations. Correspondingly, the length scale of the ab initio methods is largely limited. With today's computers, the

largest systems that can be relaxed statically contain only a few hundred atoms and can run for times in the order of tens of picoseconds [212]. Nowadays, the problem of computational expense is usually alleviated through simplification schemes [217].

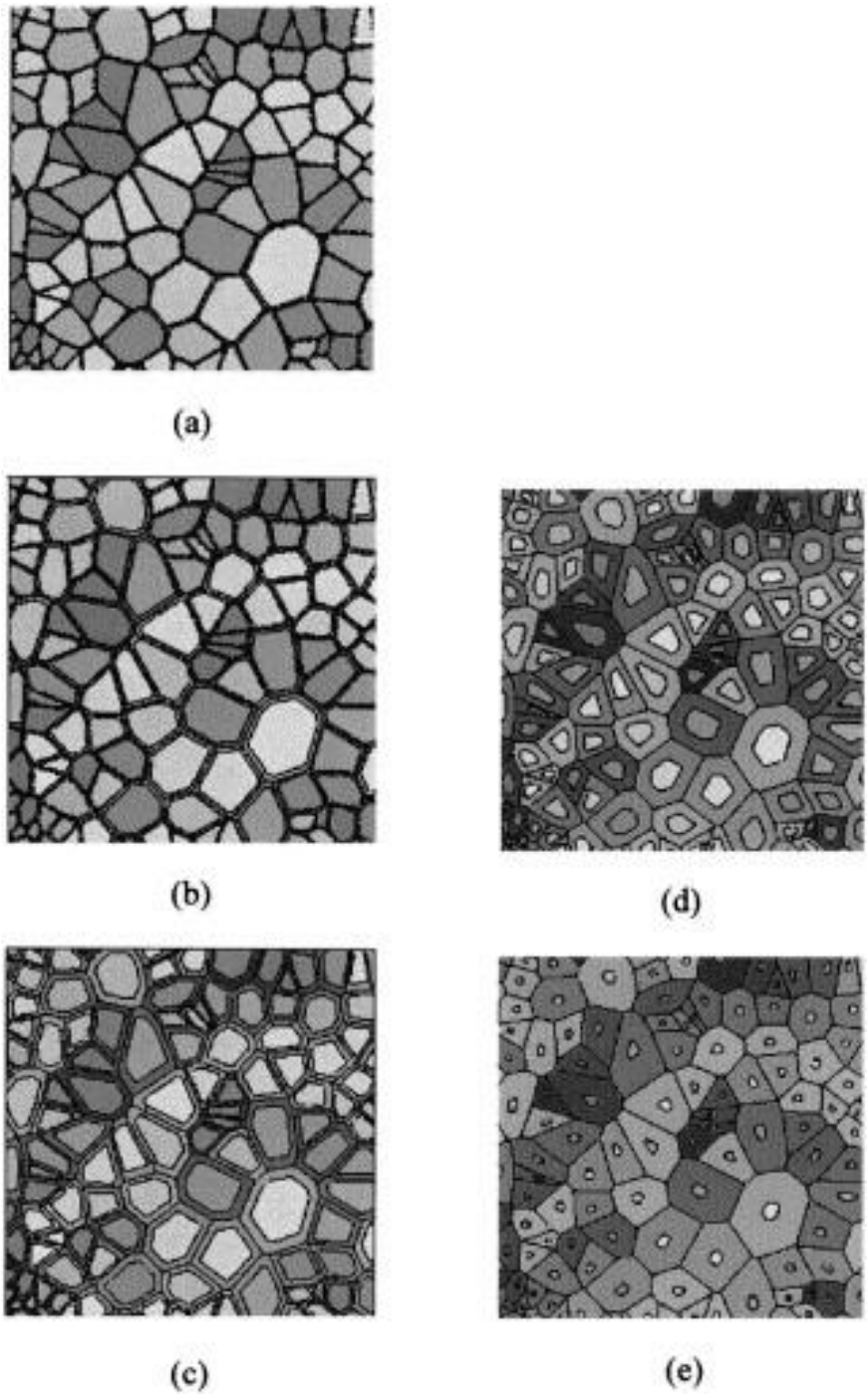

Figure 1.11 Simulated polycrystalline aggregate used in computations: (a) D = 100 μm, t = 3.33 μm; (b) D = 10 μm, t = 0.665 μm; (c) D = 1 μm, t = 0.133 μm; (d) D = 0.1 μm, t = 0.0265 μm and (e) D = 0.026 μm, t = 0.0103 μm (D is grain size and t the thickness of the work hardened grain-boundary layer. Here $t = (k_1 k_2 D)^{1/2} = k_{MA} D^{1/2} = 0.133D0.7$) [218].

Secondly, for the finite element method, the advantage is that it is a continuum modelling method and therefore has no intrinsic length scale. The absence of an intrinsic length scale in the FEM is very valuable computationally. This is because it allows the simulations of systems having dimensions with several orders of magnitude apart that uses approximately the same amount of computational work. Likewise, the primary issue of the FEM arises from its continuum characteristics at nano-scale or 'grain boundary interest scale'. For example, the crystal plasticity (CP) implemented in FEM is based on the dislocation motion, while the dimensions of the individual grains that is reduced to the nano-scale may be small enough that traditional dislocation structures do not exist or do not behave in the classical manner [10]. Therefore, at the nano-scale as shown in Figure 1.11, length scale effects must be introduced through the material models into the finite element calculation to treat the grain boundary and grain interior separately [218-222]. For phenomena that only exist at the length scales under investigation, it is a major challenge for FEM [10] to obtain the material constants and verify the accuracy of the model independently from the systems that are being investigated.

Compared with the previous two numerical methods, the MD directly incorporates the atomic length scales of the crystal into the computation, as it directly models the atoms. Therefore, the limitation of intrinsic length scale with molecular dynamics is also one of its strengths. Recent advances in computing power have enabled simulation of nanocrystalline materials with grain sizes up to 50 nm. Besides, this has been instrumental in just clarifying the details of the transition from a dislocation-based to grain boundary-based deformation regime [150]. These include the nucleation and annihilation of dislocations at grain boundaries [223-226], the formation of nano-twins [223, 227, 228], the formation of shear bands [229] and grain boundary migration and sliding [212]. Furthermore, with the largest computers available today, the largest sample that may be simulated is as large as 1 μm^3, which makes direct comparisons to macroscopic experiments impossible for nanocrystalline materials [10].

Another limitation of the MD method arises from the time scales. The solution of a MD simulation is advanced in time using an explicit time integration method which imposes a stability limit on the time step size. Therefore, the time step size is a few

percent of the period of atomic vibration in practice. Correspondingly, the simulation times (~10^{-12} to 10^{-9} s) are lower by many magnitudes than actual times at conventional strain rates (a few seconds to a few minutes). Thus all current MD simulations take place at extremely high strain rates (~10^{8}) that are generally unpractical experimentally.

Even so, the advantage of MD is just correspondent to its disadvantage: the MD method can only be applied in limited material size and with short time steps. It is, however, a useful tool to investigate material structures and corresponding mechanical properties at the 'grain boundary interest scale'. This is due to the difficulty in experimentally investigating the local response of atomic-level resolution of phenomena. Although clearly imperfect, the MD methods for the time being are still capable of providing important insights into the behaviour of GBs or interfaces in materials. Besides, the most important and significant results having been obtained by MD and are, indeed, leading our knowledge [10]. Therefore, the MD method is selected to investigate the potential mechanisms of grain boundary mediated deformation in the present work.

1.2.2 General grain boundary description

To better understand the grain boundary behaviour and the relevant MD simulations, basic concepts of grain boundary are necessary to be introduced before the main body of this thesis. All the following in this section is referenced to [230-232].

Tilt and twist grain boundaries: The simplest boundary is that of a tilt boundary where the rotation axis is parallel to the boundary plane. As shown in Figure 1.12a), this boundary can be constructed by cutting a single, contiguous crystallite or grain into two sides, rotating each sides inversely with the same angle $\theta/2$ around the Z-axis and removing the overlapped atoms. Then a symmetrical tilt grain boundary parallel to the rotation axis is finished with misorientation of θ. Note that the coherent twin boundary is a special one of the symmetrical tilt grain boundaries. If each side rotates with different angles, it is called the asymmetrical tilt grain boundary. An alternative is a twist boundary where the mis-orientation occurs around an axis that is perpendicular to the boundary plane (Figure 1.12b). This type of boundary incorporates two sets of screw dislocations. If the Burgers vectors of the

dislocations are orthogonal then the dislocations do not strongly interact and form a square network. In other cases the dislocations may interact to form a more complex hexagonal structure.

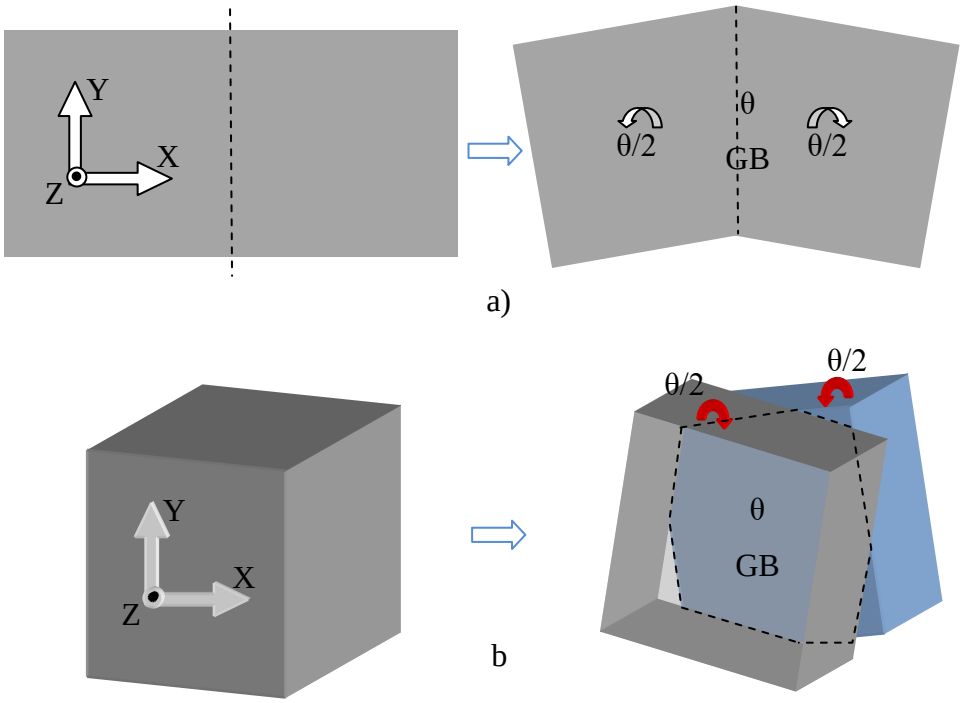

Figure 1.12 Formation of a) the tilt grain boundary and b) twist grain boundary.

Coincident site lattice: for certain angles some lattice points of lattice 1 coincide exactly with some lattice points of lattice 2 or repeated units are formed from points where the two misoriented lattices happen to coincide. Then, the coincidence site lattice (CSL), the new structure formed above, develops. In coincident site lattice (CSL) theory, the degree of fit (Σ) between the structures of the two grains is described by the reciprocal of the ratio of coincidence sites to the total number of sites. It is the unit cell volume of the CSL in units of the unit cell volume of the elementary cells of the crystals. Thus a grain boundary with high Σ might be expected to have a higher energy than one with low Σ. Low-angle boundaries, where the distortion is entirely accommodated by dislocations, are Σ1. Some other low Σ boundaries have special properties especially when the boundary plane is one that contains a high density of coincident sites. Examples include coherent twin boundaries (Σ3) and high-mobility boundaries in FCC materials (Σ7). Deviations

from the ideal CSL orientation may be accommodated by local atomic relaxation or the inclusion of dislocations into the boundary.

Displacement shift complete lattice: The set of all possible displacement vectors which preserve the CSL defines a new kind of lattice, the so-called Displacement shift complete (DSC) lattice. Displacing one grain of a grain boundary with a CSL by a vector of the corresponding DSC lattice thus preserves the structure of the boundary. This is because it preserves the symmetries of the CSL. Most importantly, translation vectors of the DSC lattice are possible Burgers vectors b_{GB} for grain boundary dislocations. As for lattice dislocations, only the smallest possible values will be encountered for energetic reasons. There are also some general rules for DSC lattice: the larger the elementary cell of the CSL, the smaller the elementary cell of the DSC-lattice; the DSC lattice indeed can be seen as the reciprocal lattice (in space) of the CSL; the volumes of CSL, crystal lattice and DSC lattice relate as $\Sigma : 1 : \Sigma^{-1}$ for cubic crystals.

The above-mentioned concepts with respect to grain boundaries are mostly related to the present thesis, as all the MD studies are performed with the symmetrical or asymmetrical tilt grain boundaries.

1.2.3 Grain boundary configuration

Compared to the practical grain boundary structures as reviewed in Section 1.1.1, the computer modelling of grain boundaries by MD method is intensively simplified, especially for the bicrystal or tricrystal models. In some cases of the nanocrystalline modelling with large systems [21, 93, 172, 233], as a sample in Figure 1.13, the grain boundary configurations are relatively comparable to the complexity of those in practical nanocrystalline materials [94]. These nanocystalline models are usually constructed by the Voronoi method which seeds the research domain with randomly distributed points serving as the centres of each grain during atoms filling. Therefore, the characteristic of the Voronoi method is that grains are of nearly uniform size, equiaxed and convex with no reentrant corners [10]. In spite of these limitations, the grain boundary configurations constructed by MD method in nanocrystalline systems are mostly close to those in practical nanocrystalline materials. They indeed reflect

the consistent mechanical responses, such as the inverse Hall-Petch relation [21, 93, 172].

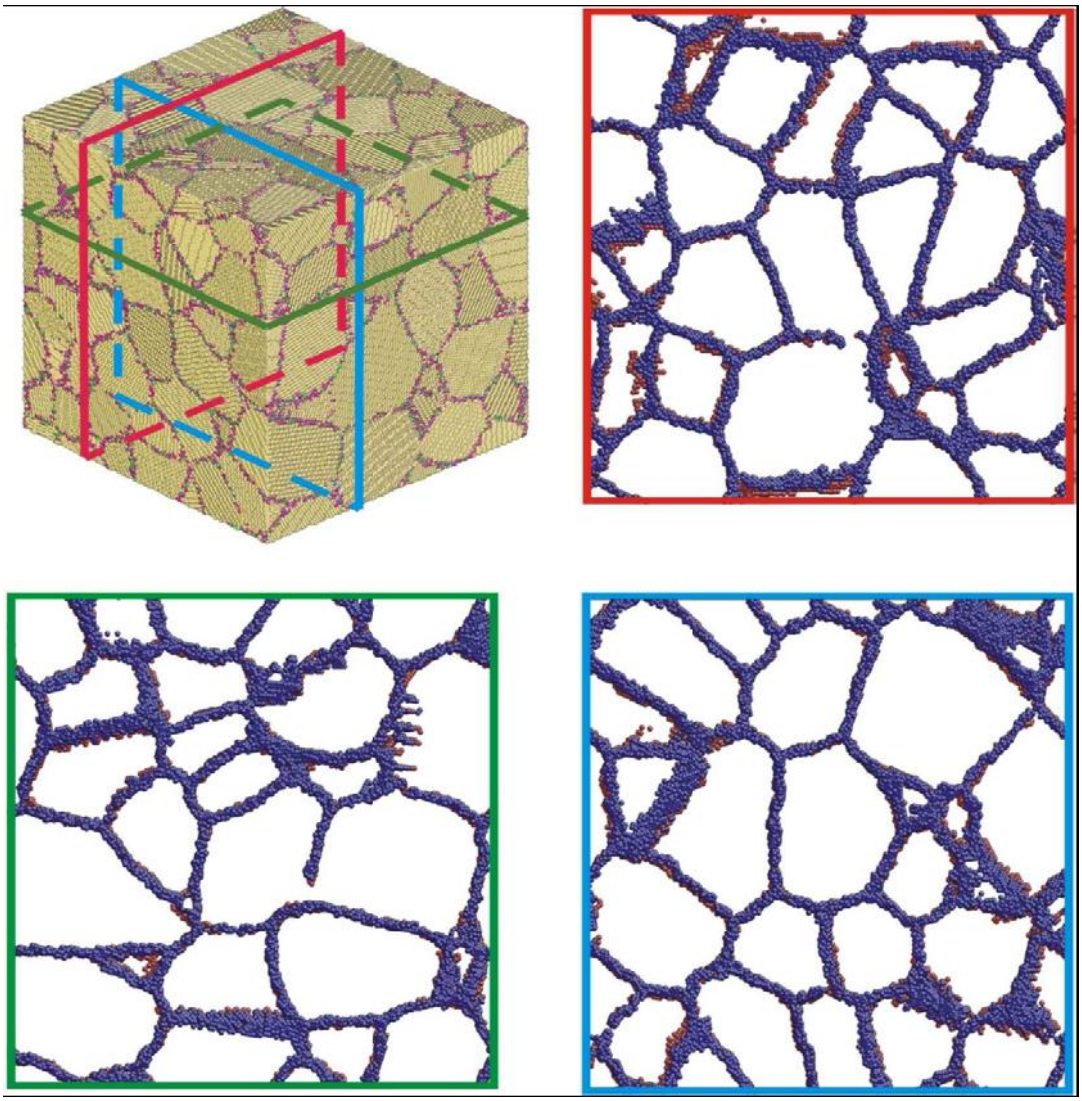

Figure 1.13 Illustration of the grain boundary migration in nanocrystalline palladium. Three mutually perpendicular cross-sections of the sample are shown with different colors: red (normal x), green (normal y), and blue (normal z). Blue-colored atoms belong to the cross-section of the undeformed sample; red atoms belong to the same cross–section, but made in the sample after 3% of tensile strain. Only non–12–fold coordinated atoms were made visible [233].

Actually, most MD modelling of grain boundaries has been concentrated on the symmetrical boundaries, i.e. boundaries which possess mirror symmetry of crystallographic planes and directions across the boundary plane [212, 234-240]. These symmetrical grain boundaries are relatively readily constructed by tilting two

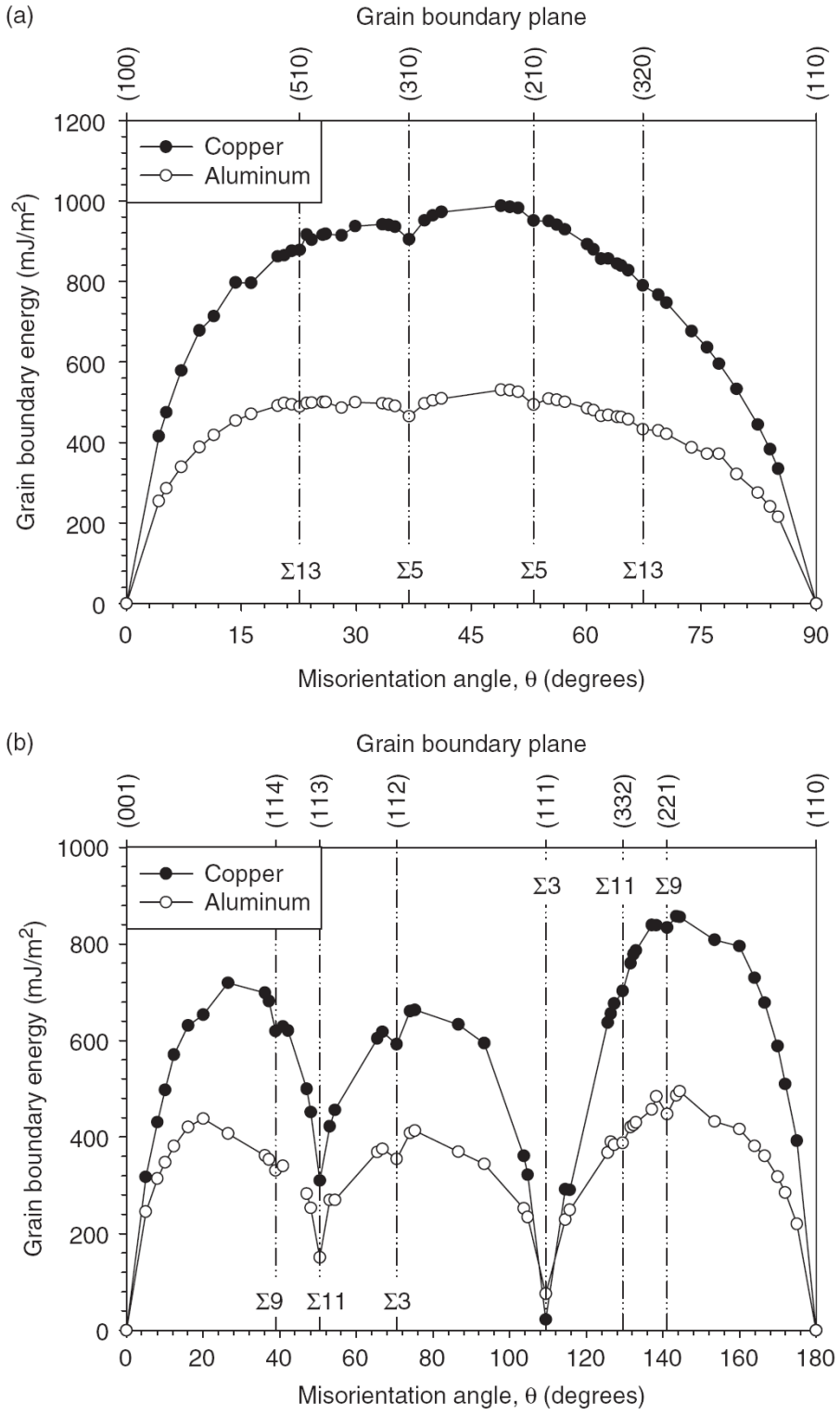

Figure 1.14 Structures and energies of symmetric tilt grain boundaries with the (a) [100] and (b) [110] tilt axes [240].

sides of a grain reversely with a same angle and along the same axis. Although these boundaries are the simplest ones, atomistic simulations about them can reveal certain

interesting properties of grain boundaries. Such properties include their structures, structural descriptions, relation between the grain boundary energy and misorientations, dissociation reactions and others. Figure 1.14 shows the grain boundary energy as a function of misorientation angle θ for the FCC <100> and <110> tilt symmetrical tilt grain boundaries [240]. These boundaries are the most common ones simulated by MD methods. There is much significance of the relation between the grain boundary energy and misorientations in explaining variety of the grain boundary deformation behaviours to be discussed later. It can be seen that the grain boundary energy varies strongly with the misorientation angle for the <110> tilt axis. The cusps on the curves should indicate the favourable grain boundary structures. There is a definitive relationship between grain boundary energy and the symmetrical grain boundary structures, which can be characterized by structural units.

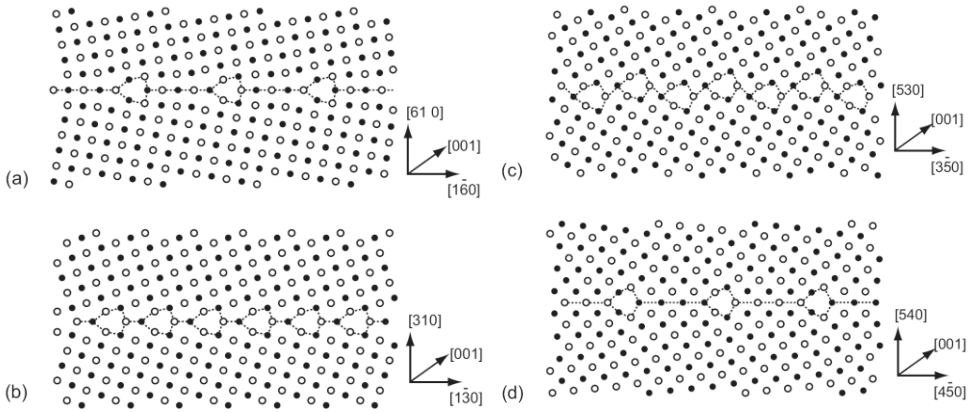

Figure 1.15 Atomic structures of selected <100> symmetrical tilt grain boundaries in Cu studied in this work of [235]: (a) Σ37 (610) (θ=18.9^o); (b) Σ5 (310) (θ=36.9^o); (c) Σ17 (530) (θ=61.9^o);(d) Σ41 (540) (θ=77.3^o). The filled and open circles represent atomic positions in alternating (002) planes.

Besides, grain boundaries with certain misorientation angles correspond to favoured structural units [241]. The typical grain boundary structures of the FCC <100> and <110> symmetrical tilt grain boundaries with corresponding structure units are presented in Figure 1.15 [235]and Figure 1.16 [239]. It can be seen that the <100> symmetrical tilt grain boundary structures are considerably oversimplified compared with those of the <110> symmetrical tilt grain boundaries. Also, all the grain boundaries can be described by the same structure unit, making the corresponding MD simulations apt to analyze. For the <110> symmetrical tilt grain boundaries,

however, the grain boundary structures show certain complexity with a series of structure units and sometimes facets, which appear commonly in asymmetrical boundaries [242], may form on some of the <110> symmetrical tilt grain boundaries.

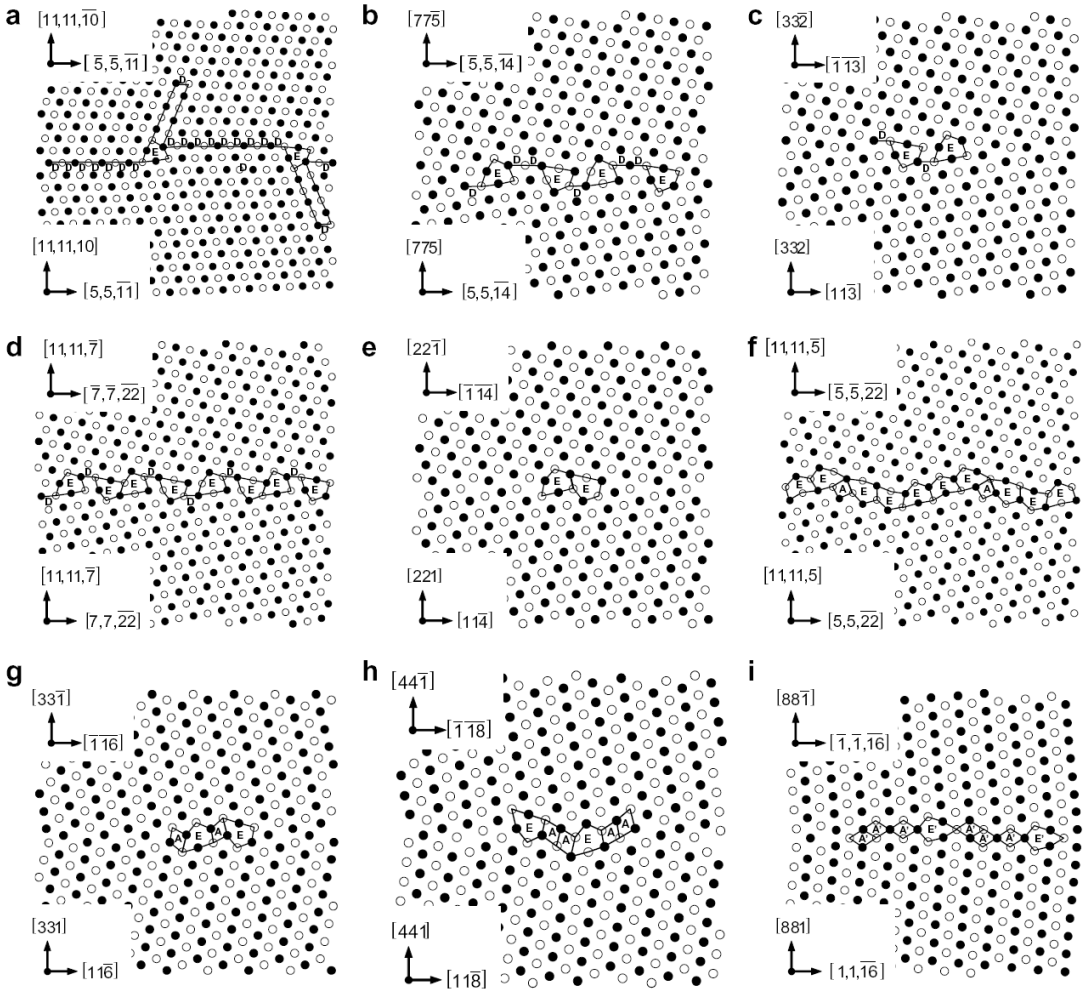

Figure 1.16 Nine <110> GB structures with the E structural unit in Cu: (a) Σ171 (11,11,10) θ=114.5o, (b) Σ123 (775) θ=126.4o, (c) Σ11 (332) θ=129.5o, (d) Σ291 (11, 11, 7) θ= 131.5o, (e) Σ9 (221) θ= 141.1o, (f) Σ267 (11,11,5) θ=144.4o, (g) Σ19 (331) θ=153.5o, (h) Σ33 (441) θ=160.0o, and (i) Σ129 (881) θ=169.9o. The structures are viewed along the [1-10] tilt axis; atoms on consecutive (2-20) planes are shown as black and white. The GB normal and period vectors for the lower and upper crystal are shown in the left-hand corner boxes [239].

The structure unit conception is relatively useful in some specific situation to explain the mechanical response of symmetrical tilt grain boundaries. This part will be discussed latter. It should be noted that the validity of the structure unit model for all materials has never been fully proven yet, though it has been used to describe the

grain boundary structures in a range of different materials. Rittner et al. pointed out in their study that while the structure unit description is applicable to the Al boundaries, it cannot be used to describe the Ni structures. This is because the grain boundary dislocation cores in the Al boundaries are more localized than they are in Ni [237]. Therefore, the structure unit method in symmetrical tilt grain boundaries has been drawing the attention of researchers. Moreover, symmetrical tilt grain boundaries at other tilt axes have also been investigated.

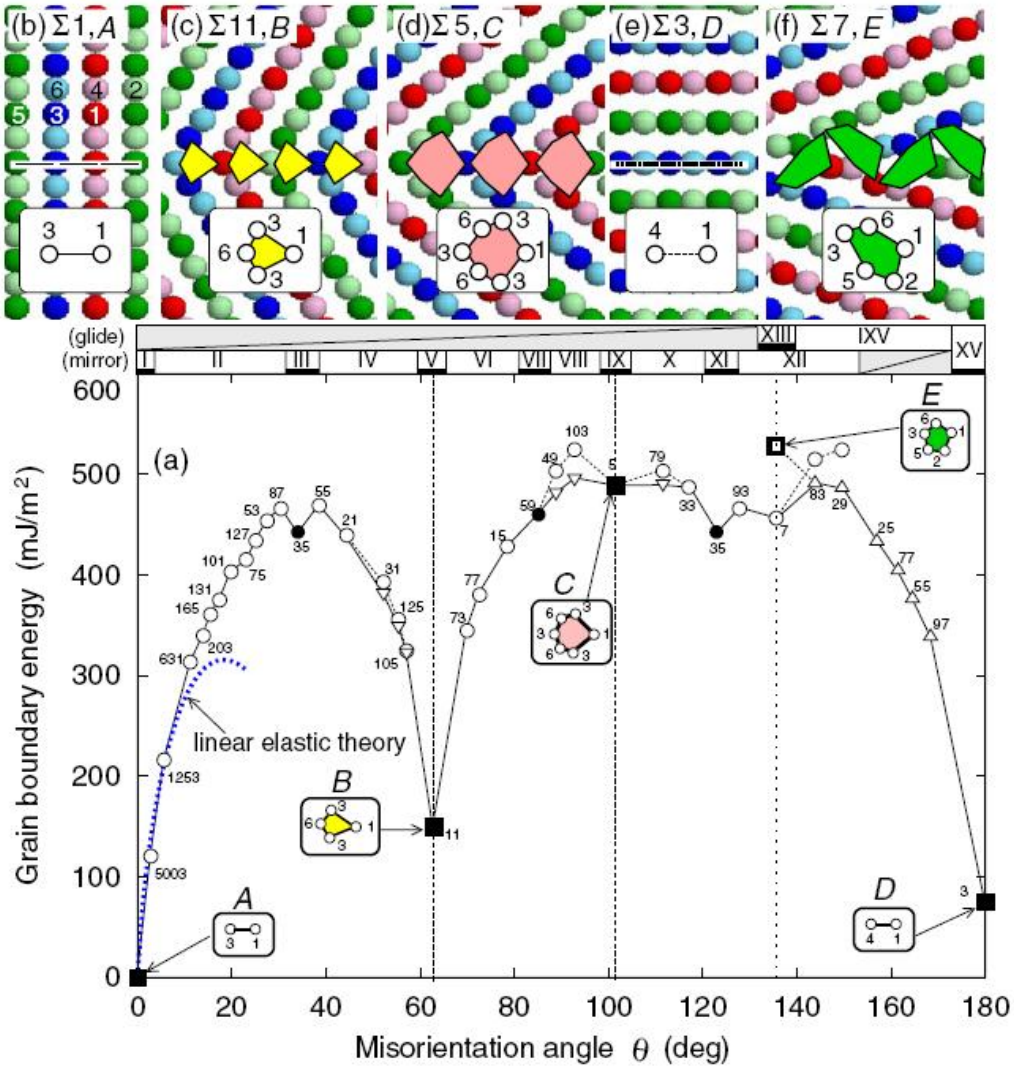

Figure 1.17 a) Relationship between grain-boundary energy and misorientation angle in <112> tilt grain boundaries. ■, ●, ○, △, and ▽ represent favored (GI, V, XI, XIII, and XV), short period (GIII, VII, and XI), long period (mirror: GII, IV, VI, VIII, X, and XII), long period (glide: IXV), and other boundaries, respectively. [b–f] Five varieties of structural units found in <112> tilt grain boundaries [243].

In Shimokawa et al.' recent study (Figure 1.17), the relationship between grain boundary energy and misorientation angle θ in Al <112> tilt grain boundaries was investigated and all the grain boundary structures can be described by the combination of five fundamental structural units A, B, C, D, and E [243].

Besides, regardless of the tilt axes, all the low angle symmetrical tilt grain boundaries can be taken as arrays of edge dislocations with Burgers vector *b*. Using the linear elastic theory Read and Shockley have calculated the energy of such arrays, situated in an infinite medium of shear modulus μ and Poisson's ratio ν, with the expression as follows:

$$\gamma_{GB} = E_0\theta(A_0 - \ln\theta),$$

where

$$E_0 = \mu b/4\pi(1-\nu) \text{ and } A_0 = 1 + \ln(b/2\ \pi r_0)$$

and r_0 is the core energy of a single boundary dislocation [244]. Note the blue dot line in Figure 1.17. This was calculated by this linear elastic dislocation theory and matched well with the MD results at the low angle range.

As mentioned before, the MD modelling on symmetrical grain boundaries is extensive and has gradually become relatively mature. However, most grain boundaries in practical polycrystalline materials are asymmetrical. Asymmetrical boundaries have also been studied by MD method [212, 240, 242] but not as extensively as the symmetrical ones. These boundaries are often curved and they sample a range of different asymmetrical planes. So far, the current understanding of atomic structure, energies γ and mechanical properties of asymmetrical grain boundaries remains rather limited [212]. Nevertheless, looking at the active side, the MD calculation has reflected certain basic features of some simple asymmetrical grain boundaries. In most MD studies, the asymmetrical boundaries are generally constructed by introducing an inclination angle α to the corresponding symmetrical tilt grain boundaries [212, 240, 242, 245-248]. In Tschopp et al.'s study, the structure and energy of the asymmetric tilt grain boundaries in Cu and Al were investigated with the Σ5and Σ13 systems rotated about the <100> misorientation axis,

and the Σ9 and Σ11 systems rotated about the <110> misorientation axis [240]. They argued that asymmetric tilt boundaries with low index normals do not necessarily have lower energies than boundaries with similar inclination angles Figure 1.18 and the asymmetric boundaries could be faceted into the symmetric tilt boundaries Figure 1.19. It can be seen that the structure unit description is also useful in the asymmetric tilt boundaries. Importantly, it is worth noting the faceting phenomenon. This is because this phenomenon is very general in the asymmetric tilt boundaries and plays

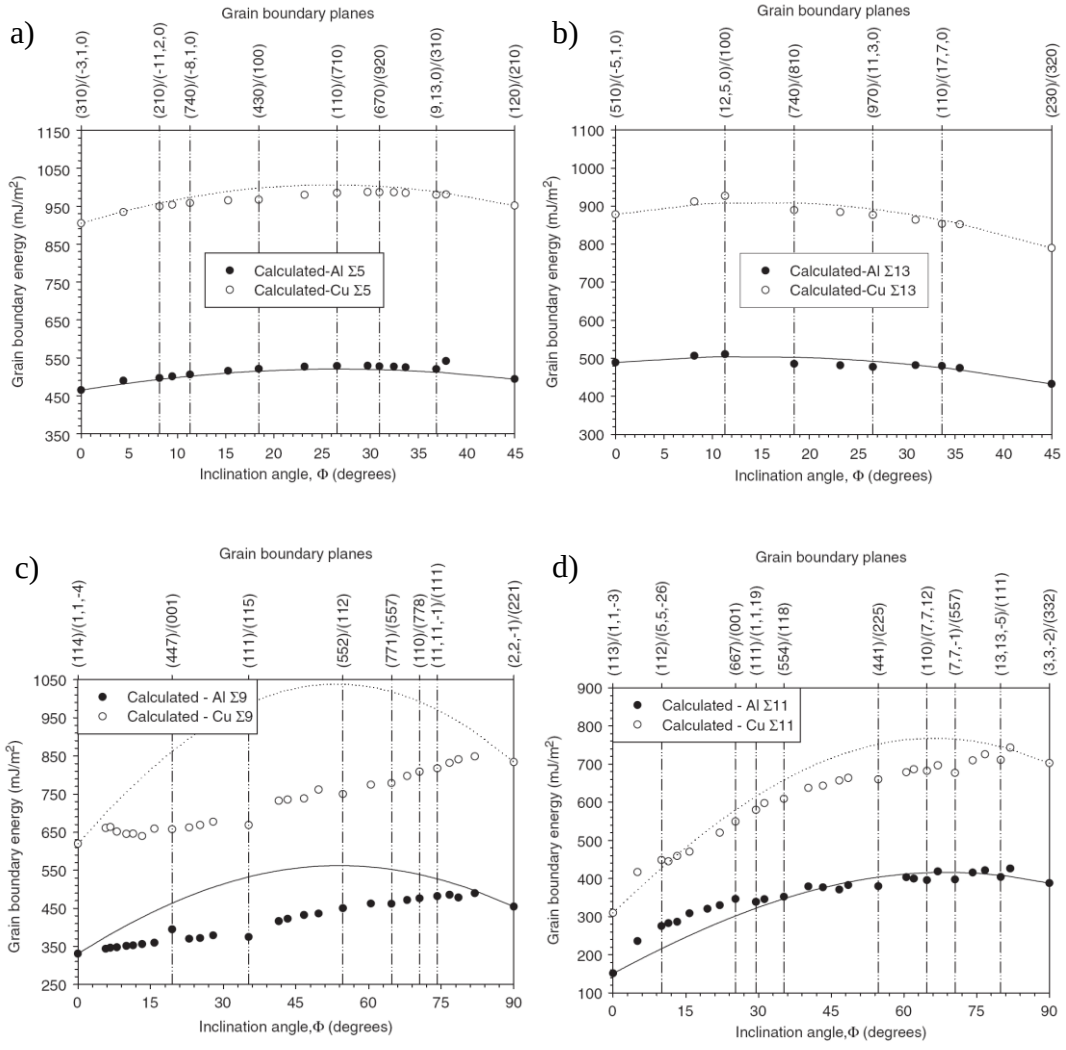

Figure 1.18 Grain boundary energy of a) Σ5, b) Σ13 asymmetric tilt grain boundaries with the <100> tilt axis and c) Σ9, d) Σ11 asymmetric tilt grain boundaries with the <110> tilt axis as a function of inclination angle. The trend lines represent the ideal decomposition of the asymmetric boundary into the two symmetric tilt grain boundaries for Cu (solid line) and Al (dotted). The upper x-axis shows the grain boundary planes for a few select boundaries [240].

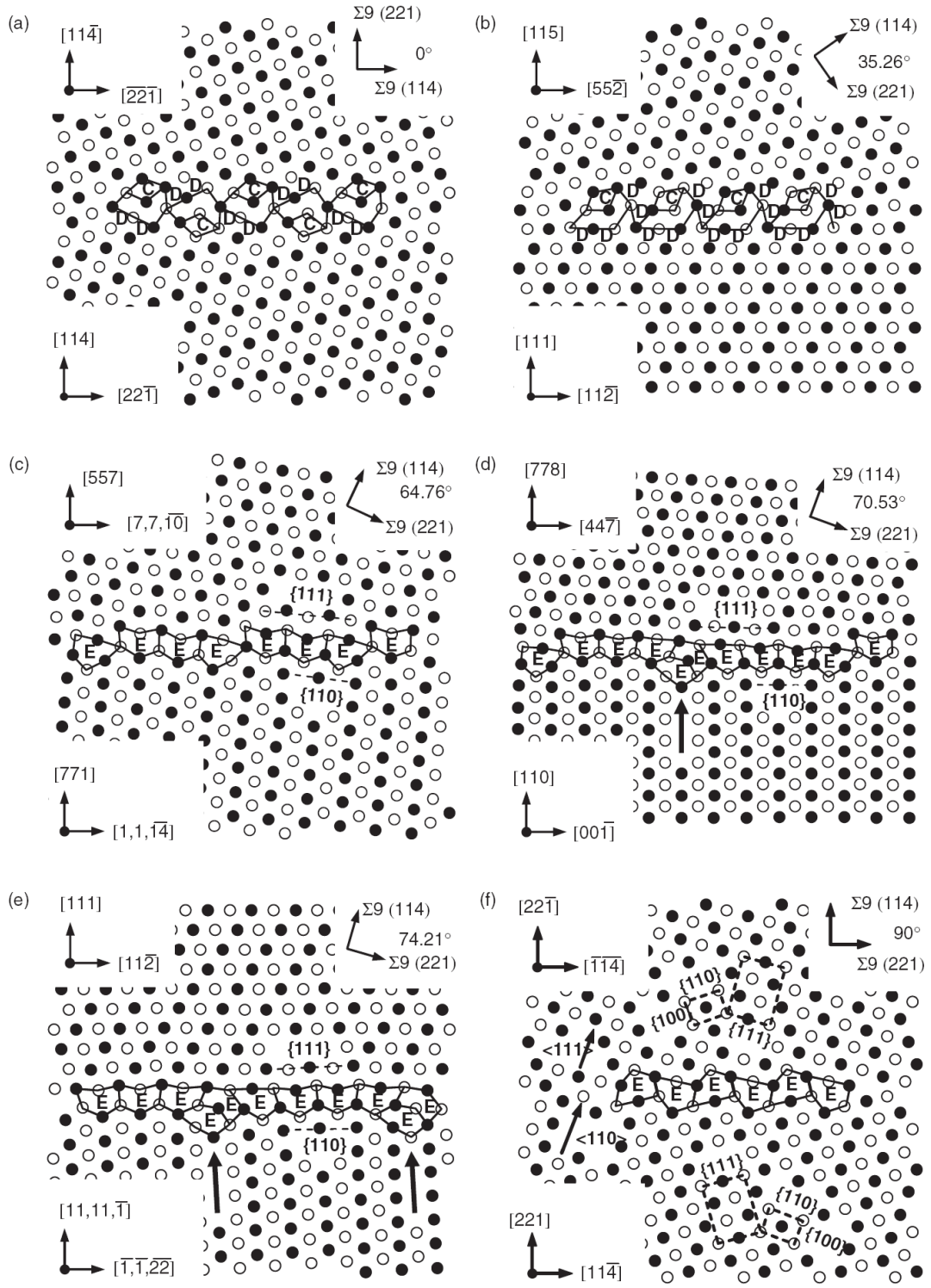

Figure 1.19 Six low-index Σ9 GB structures in Cu with various inclination angles. The low-index planes bounding the grain boundary structure are labelled.

a significant role in grain boundary deformation behaviour. Brown et al. found that the Σ11 [110] asymmetrical grain boundaries tended to break into nanometer-scale

facets. Besides, the facet planes often correspond to a nearby symmetrical boundary with a low energy. Alternatively, these boundaries may dissociate into a low angle GB formed by Shockley partial dislocations and a high-angle non-Σ11 boundary [242]. They also proposed that the asymmetrical grain boundaries locally deviating away from the macroscopically imposed coincident site lattice (CSL) misorientation, and incorporating facets of a non-Σ11 boundary may reduce the total grain boundary energy [242]. With respect to the facet stability, Hamilton et al. found that the equilibrium facet size of Σ3 (110) in Al grew with the increasing cross-sectional area of the boundary. This suggested that finite-size facets were unstable unless the boundary plane was confined between surfaces, triple junctions or other defects [249]. Later, Wu et al. suggested that the Σ3 (110) faceting behaviour reported in Hamilton et al.'s work presents only one possible case, while in other cases, the finite-size facets were found to be very stable. However, neither of them grew during the simulations or grew extremely slowly due to a high-energy barrier of facet migration arising from large grain boundary stresses [250].

These results are considerably meaningful at leading to possible mechanisms of the size effect on grain boundary structures and the coarsening process in confined systems such as nanograined materials, thin films and nano-wires/-pillars [212].

1.2.4 General grain boundary sliding behaviour

In recent years atomistic simulation method has been widely applied to investigate the grain boundary sliding behaviour at the atomistic scale. It is found that the grain boundary sliding behaviour can be influenced by various factors such as grain boundary energy, specific structure, impurities and defects etc.

Chandra and Dang addressed the dependence of grain boundary sliding behaviour on a variety of applied stresses for symmetric tilting grain boundaries. They found that the magnitude of the energy barriers is much higher in pure grain boundary sliding than when migration accompanies sliding. They also found that the grain boundary sliding displacement is proportional to applied force, GB energy, and time [251]. Namilae et al.'s simulations of grain boundary sliding also show a clear dependence of magnitude of sliding on grain boundary energy. Besides, more sliding was found

at boundaries with higher grain boundary energies for a constant external shear field at a series of [110] symmetric tilting grain boundaries at 448 K [252].

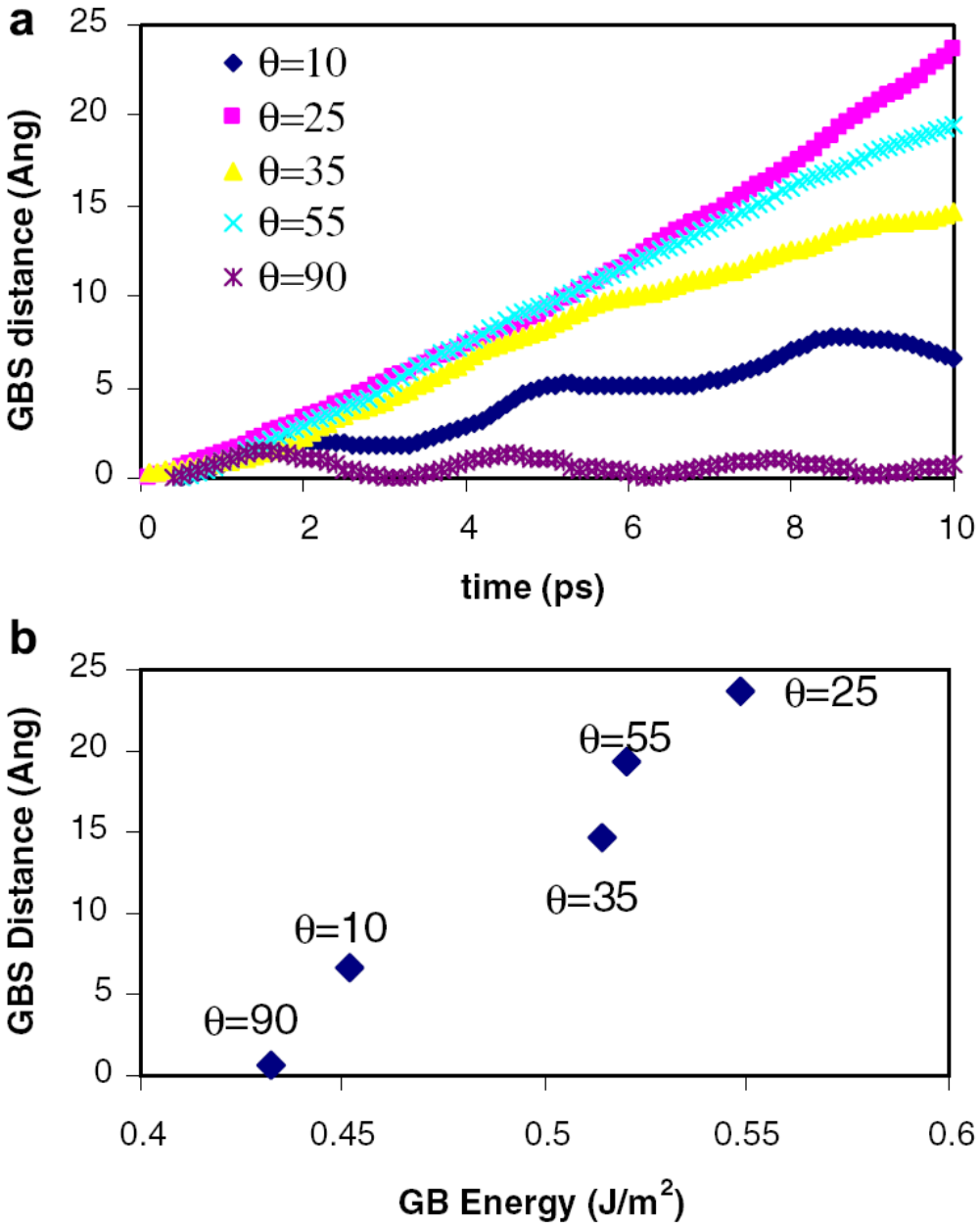

Figure 1.20 The effect of misorientation angle on GBS: (a) sliding distance as a function of time and (b) sliding distance as a function of grain boundary energy [253].

However, Sansoz et al. found that the grain boundary energy alone cannot be used as a relevant parameter to predict the sliding of nanoscale high-angle boundaries when no thermally activated mechanisms are involved. The specific grain boundary structure also plays a significant role [254]. They suggested several points: 1) the

onset of sliding by atomic shuffling are correlated to the E structural unit present in the period of Σ tilt grain boundaries; 2) grain boundary sliding strength in the athermal limit shows slight variations between the different interface configurations, but has no apparent correlation with the grain boundary structure; 3) the metal potential has a stronger impact on crystal slip than on the intrinsic interface behaviour. , Grain boundary sliding along a high-symmetry Σ11 [110] (113) tilt GB in Al was investigated in a series of studies [255-257]. It is found in these studies that a perfect grain boundary with the ground-state structure exhibited an extremely high sliding resistance and the extrinsic defects. Such defects include small steps and partial dislocations, reduced the critical stress of sliding by orders of magnitude.

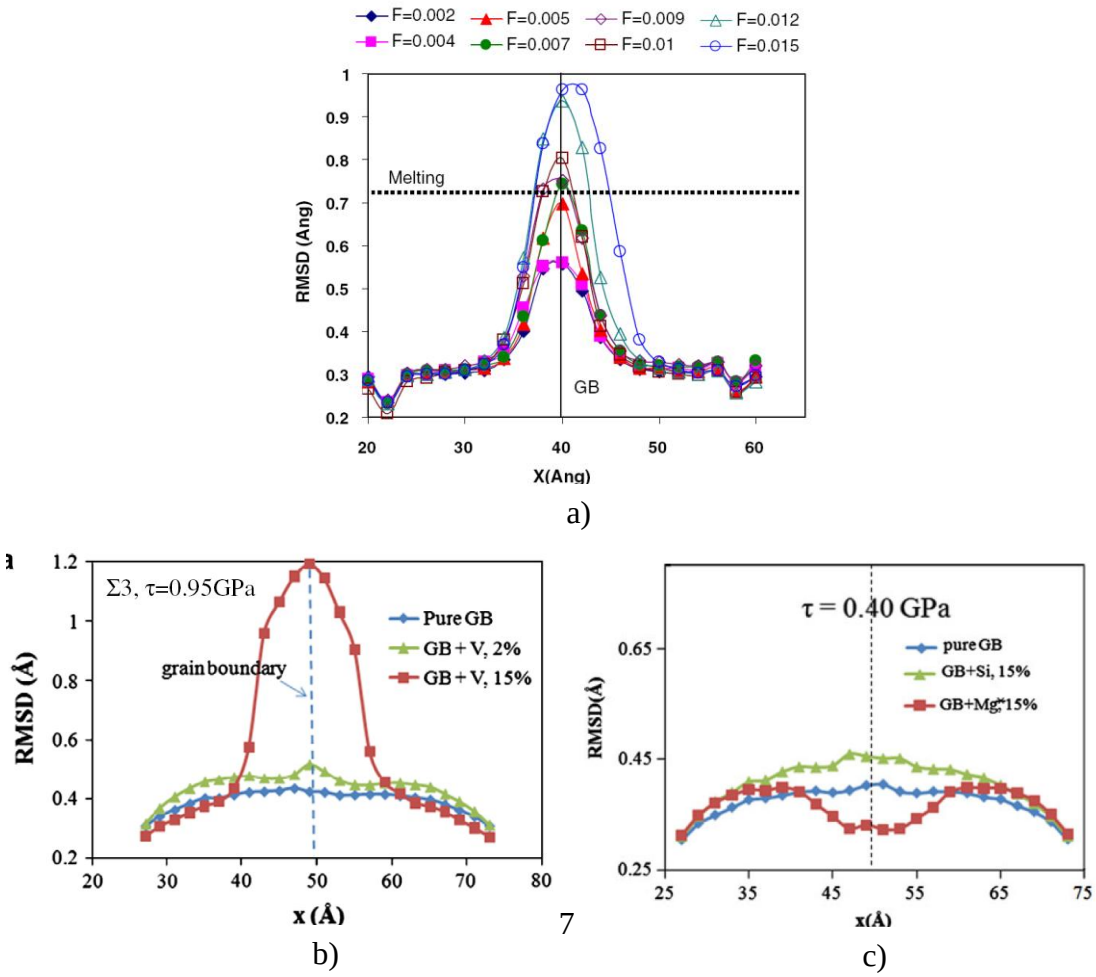

Figure 1.21 Average atomic root-mean-square thermal displacement (RMSD) as a function of their x positions: a) effect of the applied forces (eV/A˚), b) effect of the vacancy and c) effect of the different solutes [158, 253, 258].

Very recently, Qi and Du et al. have investigated the GBS behaviour, also including the effects of vacancy and solution, over a large range of shear forces and grain boundary misorientation angles for Al at 750 K [158, 253, 258]. They have proposed that a threshold stress for sliding exists [253]. Besides, the addition of vacancies can decrease the threshold stress for grain boundary sliding of the low energy grain boundaries by increasing the grain boundary diffusivity, but it has no effect on high energy grain boundaries [158]. They also found that solution atoms can enhance GBS in high-energy GBs by weakening Al bonds and by increasing atomic mobility. Alternatively, they can inhibit GBS by forming atomic clusters and decreasing diffusivity [258].

Figure 1.20 clearly shows that there was no direct correlation between sliding distance and grain boundary angle, but the grain boundary sliding distance monotonically increased with grain boundary energy. Figure 1.21 shows the effects of applied forces [253], vacancies [158] and different solute atoms [258] on the average atomic root-mean-square thermal displacement (RMSD) which reflects the mobility of atoms.

Besides, during grain boundary sliding, disconnections such as ledges and dislocation extensions could inject partials into the grains. This could contribute to the accommodation of the stresses at grain boundaries [256].

1.2.5 Grain boundary shear-coupled migration

The grain boundary motion coupled to shear deformation was firstly reported for small angle tilt boundaries [259, 260] and later was also considerably observed for high-angle grain boundaries [261-270]. Moreover, the MD studies on this coupling behaviour are particularly productive [169, 211, 212, 234-236, 245-247, 271-275], since it plays an active role in the mechanical behaviour of nanograined materials and in the structural changes that take place in them under stress at low temperatures [169]. Grain boundary motion coupled to shear deformation is believed to be the main cause of the grain coarsening observed to take place at low temperatures in nanograined polycrystals under stress: grain growth under nanoindentations, near loaded crack tips or during further plastic deformation processing or fatigue of nanomaterials [169, 270, 276-283].

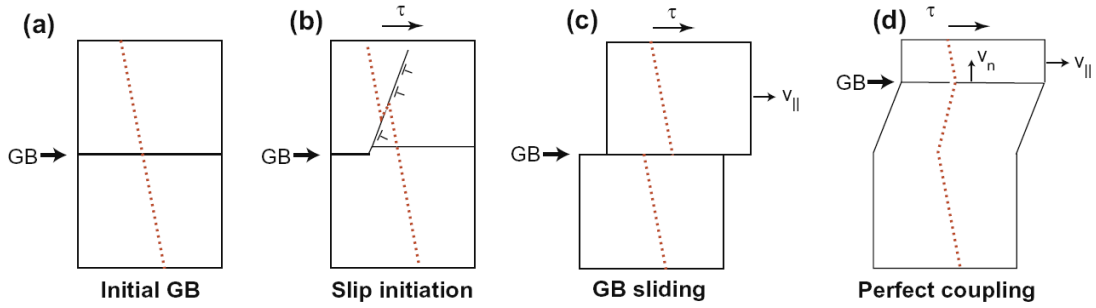

Figure 1.22 Possible mechanical responses of a plane grain boundary to applied shear stresses τ: a) initial bicrystal with a dotted line showing a set of inert markers, b) the grain boundary initiates slip by emitting a dislocation c) rigid grain boundary sliding with a grain translation velocity $v_{//}$; note the discontinuity of the marker line and d) grain boundary motion coupled to shear deformation (v_n is the normal GB velocity) [212].

The basic idea of the coupling effect is that the grain boundary motion is coupled to grain translations and can be visually illustrated in Figure 1.22 d) compared to other possible mechanical responses of a plane grain boundary to applied shear stresses Figure 21 b) and c) [130]: either a shear stress applied to a grain boundary induces its normal motion (Figure 1.22 d), or the grain boundary motion (induced by an applied shear stress or by any other driving force) produces shear deformation of the volume swept by the motion. This coupling effect can be characterized by a factor β equal to the ratio of the tangential grain translation to the associated normal grain boundary displacement. The ideal coupling factor β is thought to be a purely geometric parameter. It is only dependent on the grain boundary bicrystallography and independent of temperature, driving forces and materials [169, 212, 234-236, 271, 273, 275]. The significance and understanding of coupling behaviour can be abstracted from its outstanding characteristics.

Stick-slip phenomenon: the typical shear stress behaviour and grain boundary displacement during the coupled grain boundary motion are illustrated in Figure 1.23. It can be seen that, due to elastic deformation of the material, the stress increases basically linearly until a critical value is reached. At that point, the boundary makes a rapid move to a new position by a nearly constant distance away from the previous one. Then the stress drops to a value depending on the simulation block size in the normal direction. This value can be either positive or negative [234]. Again, the shear stress increases linearly until the next peak and the process repeats. Thus, the

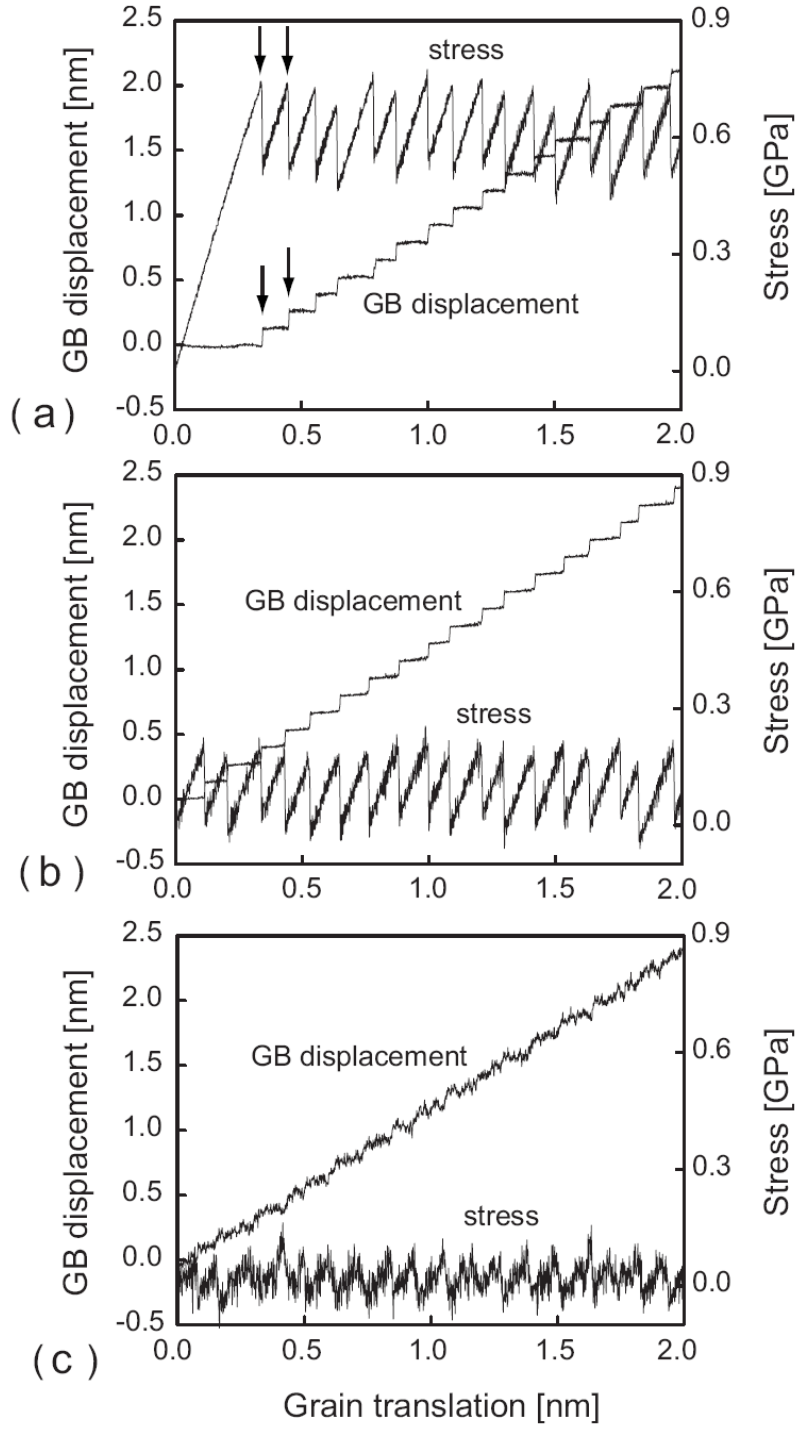

Figure 1.23 Grain boundary displacement and shear stress at a) 100K, b) 500K and c) 900K. The imposed grain translation velocity v=1m/s and the arrows indicate the correlation between the peaks of stress and the increments of the grain boundary motion [275].

shear stress displays a very clear stick-slip (or called stop-go) behaviour. As expected, the scatter in the stress peak heights and positions increases with temperature.

Besides, the average height of the stress peak decreases with the increasing temperature or decreasing $v_{//}$.

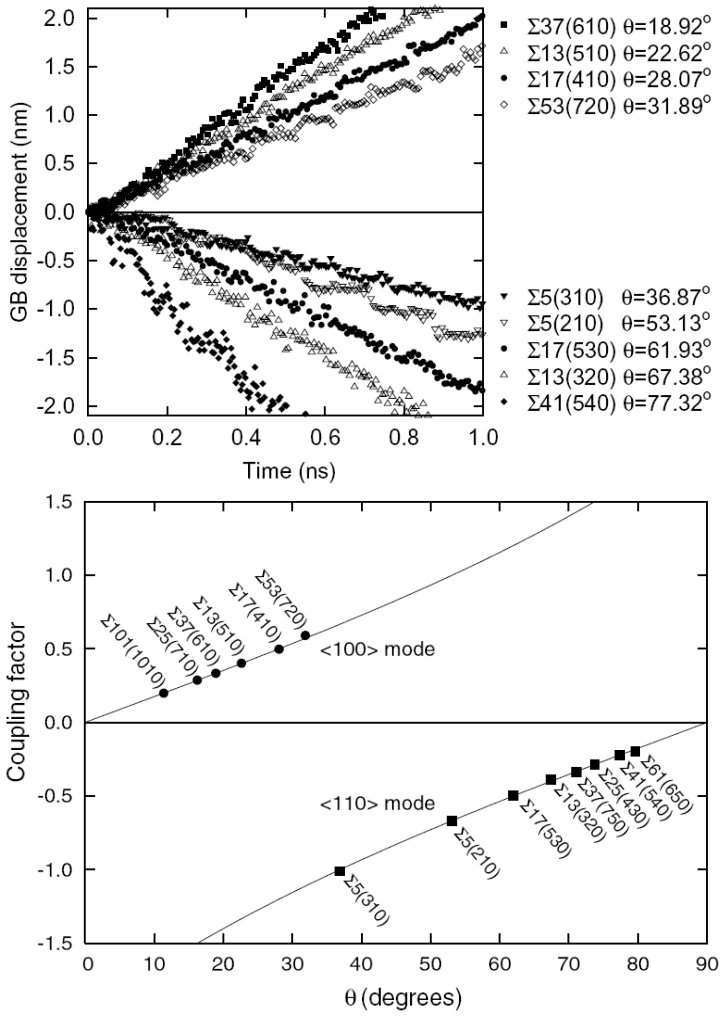

Figure 1.24 a) grain boundary displacement versus time during MD simulations at 800 K under a shear parallel to the grain boundary plane and normal to the tilt axis <100> and b) the coupling factor β obtained by MD simulations at 800 K as a function of the tilt angle θ. The shear rate is 1 m/s and the lines represent two branches of b predicted by the geometric model of coupling [234].

Moreover, it should be noted that the regime at high temperatures and slow velocities is sometimes characterized by a linear stress-velocity relation as shown in Figure 22 c). During this dynamic transition from the stick-slip regime to driven Brownian motion, the GB remains perfectly coupled and follows a geometrical value of β [212].

Multiplicity of coupling modes: due to the crystal symmetry, multiple coupling modes can be implemented in a given grain boundary, each characterized by a

different β value, atomic mechanism and critical stress [234, 235, 271]. For example, the Frank-Bilby vector (the net dislocation content of the GB) has been successfully applied to determine the coupling factor β for FCC <100> tilt grain boundaries [235, 271]. As the Frank-Bilby equation yields a multiplicity of geometrically possible coupling factors (a multiplicity of β values for the bicrystal to select from the structural point of view and a multiplicity of geometrically possible grain boundary dislocation sets), after two ideal values – 2tan (θ/2) for <100> mode or -2tan (π/4-θ/2) for <110> mode where the θ is misorientation of two grains – were finally determined. As shown in Figure 1.24, the active mode is dependent on the orientation of the applied shear stress, the geometric parameters of the boundary and its magnitude relative to the critical resolved shear stresses of different coupling modes [234]. The critical stresses of the coupling modes vary with temperature, and their crossovers can produce mode switches [212, 234]. It is worth noting that the multiplicity of coupling modes could endow high-angle GBs with much flexibility responding to applied stresses or other driving forces. This flexibility is important for many processes involving GB motion, in particular for accommodating the incompatibility in the movements of adjacent GBs or parts of a curved one. The most profound concern is that, by switching between one mode with $\beta_1 > 0$ and another with $\beta_2 < 0$, while the adjacent grains slide away from each other the boundary might appear to be stationary. Moreover, the coupled motion behaviour was found not only in symmetrical tilting GBs, but also in asymmetrical tilting GBs [240, 254, 271, 284]. These tilting grain boundaries exist substantively in many materials, such as thin polycrystalline metal films (<111> tilting GB) [285, 286] and directional solidified superalloys (<100> or <110> tilting GB) [287, 288]. Therefore, it is of much significance to obtain the understanding of the dual behaviour of grain boundaries. It is also important to find which factors might lead to the coupling mode switch, as it may offer certain unexpected macroscopic plasticity to these materials.

Misorientation dependent at high temperature: the mechanical response at different temperatures is extremely important for materials engineering. It is found by the MD simulations that the grain boundaries with high angle misorientations lose their ability in coupling to stresses at high temperatures and in responding to applied

stresses by rigid sliding without any normal motion [234]. As clearly shown in Figure 1.25, the transition from coupling to sliding usually occurs continuously over

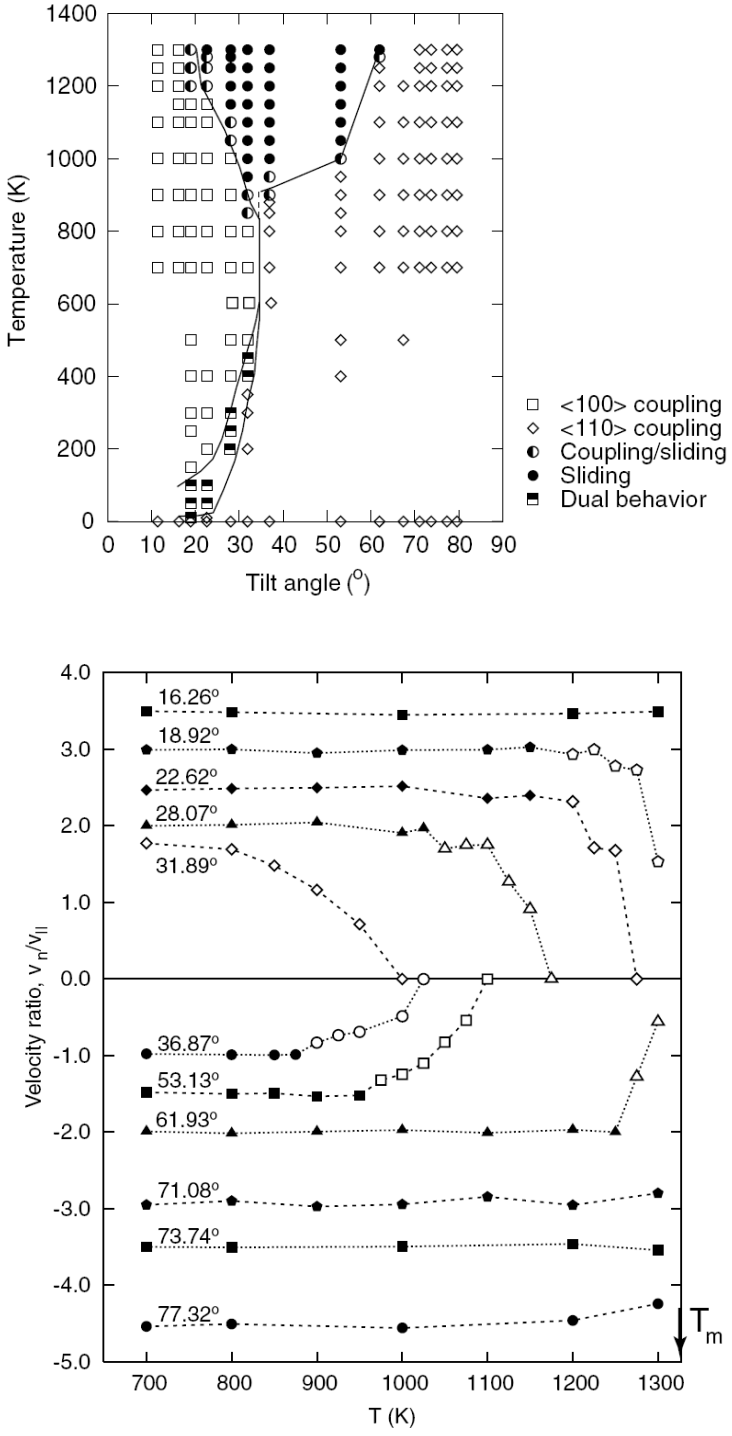

Figure 1.25 a) Diagram of mechanical responses to shear of [001] symmetrical tilt GBs in Cu and b) temperature dependence of the velocity ratio $v_n/v_{//}$ obtained by MD simulations with the shear rate $v_{//}$ = 1 m/s. Open symbols indicate temperatures at which GB sliding events were observed. T_m is the bulk melting temperature [234].

a temperature range until coupling completely disappears for grain boundaries with larger misorientationsFor grain boundaries with smaller misorientations, however, the coupling persists regardless of the temperatures. Two possible mechanisms are proposed for this transition. In one, the grain boundary structure becomes highly disordered, which precludes the deformation and rotation of the structural units. In other cases, the GB structure remains well ordered and is able to support coupled motion, but the temperature activates sliding mechanisms with lower critical stresses, making sliding the dominant response to the applied stress [212, 234, 271].

Diffusion unnecessary: another outstanding characteristic of coupling is that the atomic diffusion is not necessary for the grain boundary coupled motion which can be only implemented by deformation and rotation of structural units forming the boundary. The unit transformations may take place by a nucleation and growth mechanism in which the transformed grain boundary area is bounded by a growing disconnection loop. In the case of <100> coupling mode for <100> tilt grain boundaries, finite temperatures are necessary to activate the in-plane and out-of-plane atomic displacements [234].

There are also other studies that investigate what may affect the grain boundary coupled motion. It was found that the grain boundary coupled motion of symmetrical tilt boundaries can be perturbed by the presence of nano-cracks or nano-precipitates lying on the boundary plane [169]. Some simulations have shown that coupled motion can be blocked by constraints imposed by triple junction lines and other defects [289]. Besides, some grain boundaries such as twist grain boundaries are prohibited from coupled motion by symmetry [234].

1.2.6 Interaction between grain boundary and dislocations

The prediction of increased partial dislocation spacing, of dislocation generation and annihilation at grain boundaries and slip transferring across grain boundaries are of special significance. This is because they play a significant role in the mechanical properties of materials. However, many aspects with respect to the interaction between interfaces and dislocations are still not well understood. In the recent twenty years, the atomic-level simulation of materials has provided many fundamental insights into this area [93, 212, 233, 243, 248, 285, 290-306].

Nucleation or generation of the dislocations at grain boundaries: Atomistic simulations of dislocation nucleation mechanisms for asymmetric Σ3 grain boundaries in Cu show that grain boundary plane plays an important role in mechanical behaviour [248]. The stress required for dislocation nucleation is highest at the coherent twin boundary and lowest at intermediate inclination angles. Additionally, dislocation nucleation is preceded by dislocation dissociation from the grain boundary. Tschopp et al. have also investigated how grain boundary structure influences dislocation nucleation under uniaxial tension and compression for a specific class of symmetric tilt grain boundaries that contain the E structural unit [303]. It was found that the stress required for dislocation nucleation increased with the decreasing spacing of the E structural units for uniaxial tension. For uniaxial compression, however, there was no same trend and the nucleation stresses were averagely three times greater than those in tension. Importantly, the resolved stress normal to the slip planes was found to play an important role in the nucleation of dislocations. For uniaxial tension, partial dislocations were nucleated on the {111} slip plane with the maximum resolved shear stress. For uniaxial compression, both full and partial dislocations were nucleated not only on the {111} but also on {100} slip planes with the maximum resolved shear stress. The dislocations on the {100} slip plane observed only in compression indicated that the activation of this slip system may be impacted by the resolved stress normal to the slip plane. In another study from Shimokawa, recently, structural unit dependence of dislocation emissions was simulated under tensile and compressive loading on Al bicrystals with <112> tilt grain boundaries. These can be represented by a combination of five favoured grain boundary structural units [243]. If the Burgers vectors of grain-boundary dislocations and lattice dislocations of practicable slip systems in the neighbouring grains are close to each other, lattice dislocation emissions from grain boundaries accompanied by a transition of grain-boundary structure with long periodicity into the neighbouring favoured boundary can occur under appropriate loading directions with respect to the Burgers vectors of grain-boundary dislocations. Consequently, it was found that there are grain boundaries with strong asymmetric ability to generate dislocations related to their structural units under tensile or compressive loadings.

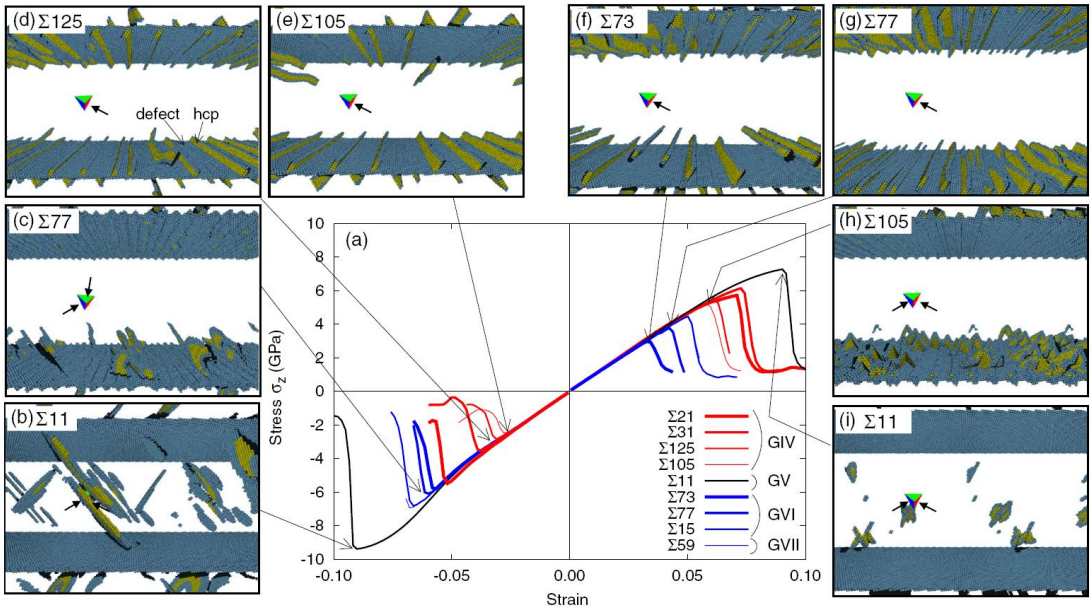

Figure 1.26 a) Stress-strain curves for Al bicrystal models in the vicinity of the Σ11 boundary under tensile and compressive deformation at a strain rate of 1_109 1/ s and at 10 K. [b) and i)] For the Σ11 boundary, which is a favoured boundary, dislocations are nucleated not from the grain boundary but from the intragranular region under tensile and compressive loadings. Yellow and dark blue colored atoms correspond to atoms in the local hcp structure and defect structure, respectively. Atoms in the FCC structure are not shown in these pictures. The regular tetrahedrons represent the Thompson tetrahedron to identify the slip systems and the arrows represent the activated slip systems [243].

Figure 1.26 shows the structural unit dependence of dislocation emissions from serial of <112> tilt grain boundaries for Al under tensile and compressive loading. Besides, the MD studies also show that the crack nucleation is preceded by the emission of several dislocations [293]. Additionally, the dislocation nucleation at twin boundaries can govern the softening and maximum strength in nano-twinned metals [93]. These are more directly related to mechanical behaviour of materials.

Cutting through homogeneous grain boundaries: By investigating the interaction between screw dislocations and coherent twin boundaries for Al, Cu and Ni, Jin et al. found that a screw dislocation approaching the coherent twin boundary from one side may propagate into the adjacent twin grain by cutting through the boundary. Alternatively, it may dissociate within the boundary plane, depending on both the applied strain and the material dependent energy barrier for the nucleation of Shockley partial dislocations [292]. Later, purely stress-driven interactions between

60^o non-screw lattice dislocation and coherent twin boundaries are simulated by the same authors [291]. It was found that the 60^o non-screw lattice dislocation can dissociate into different partial dislocations gliding into the twin as well as along the twin boundary. Also, a sessile dislocation lock was found to be possibly generated at the CTB if the transited slip is incomplete. The energy barriers for the formation of Shockley partial dislocations still played the dominant role. A range of FCC metals were modelled with a total of 10 embedded-atom method (EAM) potentials by Chassagne et al. [304]. The aim was to determine the influence of material and interatomic potential on the interaction between an a/2<110>{111} screw dislocation and a Σ3{111}<110> coherent twin boundary. They showed that the absorption of the dislocation into the coherent twin boundary or transmission into the twinned region and reaction stress strongly depend on the potential used and are controlled by the material parameter $\gamma_S/\mu b_P$, rather than the sign of the ratio $(\gamma_{US}-\gamma_S)/(\gamma_{UT}-\gamma_S)$ [292] (where γ_S is the stacking fault energy, μ the shear modulus, b_P the Shockley partial Burgers vector, γ_{US} the unstable stacking fault and γ_{UT} the unstable twinning energies). Moreover, there exists a critical reaction stress independent of the potential. Below this value the dislocation is absorbed in the CTB and above it the dislocation is transmitted into the twinned region. Dewald et al. investigated the interaction of screw-dislocations with a series of symmetric <110> tilt coincident grain boundaries (Σ3, Σ9 and Σ11) in Al. They found that it is very difficult for the lattice dislocations to cut through the low energy high-symmetry Σ3 and Σ11 boundaries. This was true even if the head dislocation was fully absorbed and a pile-up formed in one grain [290]. However, for the Σ9 boundary with a relatively complex atomic structure, the incoming screw dislocations were absorbed on one side and nucleated newly on the other side and then cut through the boundary. Moreover, this process depends very sensitively on the orientation of the applied stress and on the precise location where the dislocations enters the boundary. By simulating the interactions of lattice dislocations with symmetrical and asymmetrical tilt grain boundaries in Ni, Bachurin et al. also found three important parameters determining the ability of the dislocation to penetrate the boundary [285]. Those parameters are the exact site where the dislocation meets the grain boundary, the misorientation angle of the grain boundary and the sign of the Burgers vector of the incoming dislocation. Interestingly, the inclination angle does not make a significant difference on the transmission scenario

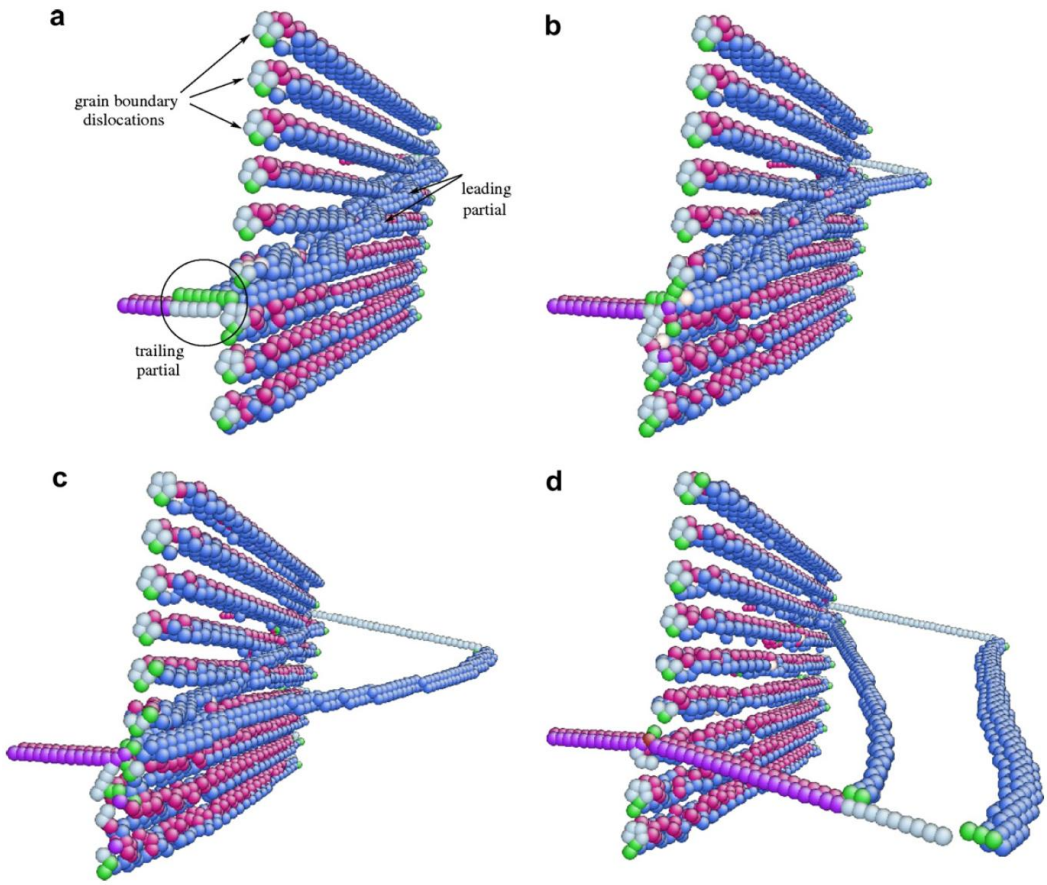

Figure 1.27 Snapshots showing different steps of the interaction between a positive dislocation and a symmetrical Σ57 tilt grain boundary. Atoms are colored according to their coordination number. Only atoms with non-FCC coordination are shown. (a) At 0.64% strain the leading partial dislocation enters the grain boundary, whereas the trailing partial (indicated by the circle) is blocked before entering the grain boundary; (b) nucleation of the leading partial dislocation at 1.04% strain at the (back) free surface; (c) propagation of the leading partial dislocation into grain 2 at 1.12% strain; (d) propagation of the trailing partial dislocation into grain 2 at approximately 1.20% strain [285].

of full dislocations. Besides, only limited partial dislocation nucleation was found at the investigated high-angle grain boundary. Figure 1.27 shows the four characteristic stages of the interaction between the incoming lattice dislocation and the grain boundary. Atomistic simulations of the interactions between dislocations and grain boundaries were also studied for Bcc metals. Similar results were obtained for the interactions between the 1/2<111> edge dislocation and three symmetric tilt grain boundaries in tungsten [294]. For example, the dislocation may be both absorbed and transmitted and the outcome depends sensitively on the grain boundary structure and

the exact site of the interaction. Furthermore, the interaction is often related to the nucleation of grain boundary dislocations. Additionally, the motion of grain boundary dislocations associated with grain boundary migration is always found to accompany the transmission process.

There have also been extensive MD simulations on the interaction of dislocations with heterophase interfaces, such as FCC-FCC systems Cu-Ni [295, 297, 305, 306], Cu-Ag [297], Cu-Al [296] and FCC-Bcc systems Cu-Nb [298, 299, 301, 302]. Since they are beyond the scope of this thesis, the detail of these results is not presented here.

1.3 Scope of this thesis

To sum up, computer modelling is currently a method of the study of materials and their properties as important as experiments. Experiments have been performed for several thousand years, while computer modelling started about fifty years ago [10]. In order to predict more accurate results, therefore, further work and efforts should be conducted on computational physics and development of the computational potential. As discussed before, there have been extensive studies with respect to the application of MD method in grain boundary research for the recent fifty years. However, the following reviewed aspects are still disputed or ambiguous:

a) although the asymmetric grain boundaries are most common in crystalline materials, there are much less studies on them than on the symmetric ones;

b) the grain boundary sliding always takes place with concurrent accommodation processes, which may involve grain boundary migration, maintain the grain compatibility during grain boundary sliding, grain rotation, diffusion or dislocation motion [27-28], which makes it very complicated;

c) the effect of grain structural multiplicity on grain boundary coupled motion has rarely been studied;

d) many aspects with respect to the interaction between interfaces and dislocations are still not well understood;

e) the dependence of mechanical properties of the polycrystalline materials on the grain boundaries has been mostly attended and disputed.

Therefore, in the present thesis, the molecular dynamics method has been used to simulate the grain boundary deformation behaviours. First, the grain boundary sliding behaviour was investigated for a serial of Σ5 symmetrical and asymmetrical tilting grain boundaries under different conditions. Secondly, the structural multiplicity of the symmetric tilt Σ5(310) boundary and its influence on grain boundary behaviour were investigated. Next, the interaction between a straight 1/2[110] screw dislocation with several [110] asymmetrical tilt grain boundaries were simulated with different applied shear stress. At last, the Σ13 (320) symmetrical tilt grain boundary was used to simulate the size effect and tension-compression asymmetry.

2 SIMULATION METHOD AND DETAILS

In this chapter, the molecular dynamics (MD) method is outlined first. The specific MD codes used in this thesis and the relevant assistant software are then introduced.

2.1 Molecular Dynamics Methods

The MD method simulates physical movements of atoms and molecules and then obtains the desired properties. Figure 2.1 is a highly simplified description of the molecular dynamics simulation algorithm [307]. First, the MD simulation usually starts with giving the atoms initial positions, and in some particular cases, the initial velocities or other attributes of the atoms are also required. Second, a proper force field should be given to define the forces between the atoms, potential energy and the accelerations obtained from the new forces. Then, the trajectories of atoms or molecules can be determined by alternatively calculating forces and numerically solving the Newton's equations of motion for a system of interacting particles with specific constraints or environments. This process proceeds and repeats until the final results are obtained. To better understand the mechanisms of MD method, some basic concepts and knowledge are necessary to be introduced.

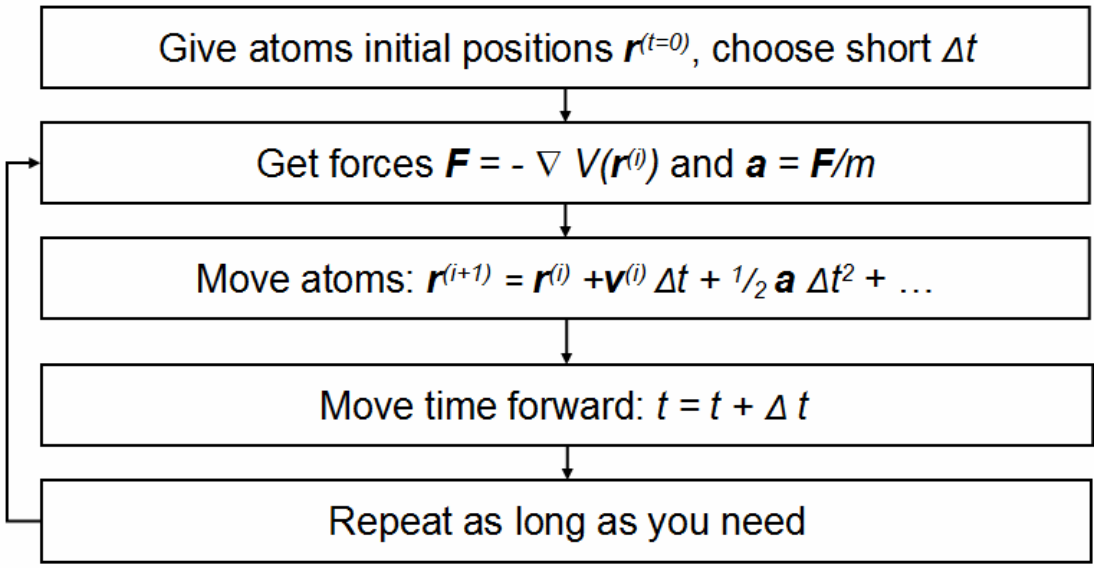

Figure 2. 1 A highly simplified description of the molecular dynamics simulation algorithm [307].

2.1.1 Force fields or potential functions

The definition of a potential function or a description of the terms, by which the atoms or molecules in the simulation will interact, is required for a molecular dynamics simulation. There are many types of potentials in the fields of physics, chemistry and materials sciences, such as empirical and semi-empirical potentials, pair potentials versus many-body potentials, polarisable potentials and so on. Here, two popular potentials with a widespread application in materials science are listed.

Lennard-Jones potential: The Lennard-Jones potential, which is also known as the L-J potential and 6-12 potential, is a mathematically simple model that approximates the interaction between a pair of neutral atoms or molecules. In 1924, John Lennard-Jones first proposed a form of this potential [308]. The most common expressions of the L-J potential are

$$V_{LJ} = 4\varepsilon\left[\left(\frac{\sigma}{r}\right)^{12} - \left(\frac{\sigma}{r}\right)^{6}\right] = \varepsilon\left[\left(\frac{r_m}{r}\right)^{12} - 2\left(\frac{r_m}{r}\right)^{6}\right]$$

where ε is the depth of the potential well, σ is the finite distance at which the inter-particle potential is zero, r is the distance between the particles, and r_m is the distance at which the potential reaches its minimum. It can be seen that the potential function has the value $-\varepsilon$ at r_m and the distances are related as $r_m = 2^{1/6}\sigma$. These parameters can be fitted for accurate quantum chemistry calculations or reproduction of the experimental data. Despite the existence of more accurate potentials , the L-J potential is extensively applied in computer simulations due to its computational simplicity.

Embedded atom method (EAM): the embedded atom model, embedded-atom method or EAM, is an approximation describing the energy between two atoms. It is widely applied in the computational materials science, especially for the metal materials. The energy is a function of a sum of functions of the separation between an atom and its neighbours. In the original model proposed by Murray Daw and Mike Baskes [309, 310], the latter functions represent the electron density. EAM is related to the second moment approximation to tight binding theory, also known as the Finnis-Sinclair model. In a simulation, the total energy Ei of an atom *i*, is given by

$$E_i = F_\alpha \left[\sum_{i \neq j} \rho_\beta \left(r_{ij} \right) \right] + \frac{1}{2} \sum_{i \neq j} \varphi_{\alpha\beta} \left(r_{ij} \right)$$

where F_α is an embedding function that represents the energy required to place atom i of type α into the electron cloud, ρ_β is the contribution to the electron charge density from atom j of type β at the location of atom i, r_{ij} is the distance between atoms i and j and $\varphi_{\alpha\beta}$ is a pair-wise potential function. The Embedded-atom method is not only particularly appropriate for metallic systems, but also widely used in computational chemistry and computational physics.

A potential can be very complicated. For example, in chemistry and biology it is usually referred to as a force field and may be defined at many levels of physical accuracy.

2.1.2 Integration Algorithms

The potential energy is a function that describes the atomic positions (3N) of all the atoms in a system and the nature of this function can be very complicated. Therefore, there is no analytical solution to the equations of motion. The equations of motion must be solved numerically. So far, numerous numerical algorithms have been developed for integrating the equations of motion. However, there are common criteria of these algorithms. They should be computationally efficient, conserve energy and momentum, and permit a long time step for integration. Several important algorisms are simply explained here.

First, all the integration algorithms assume the positions, velocities and accelerations can be approximated by a Taylor series expansion:

$$r(t + \delta t) = r(t) + v(t)\delta t + \frac{1}{2} a(t)\delta t^2 + \cdots$$

$$v(t + \delta t) = v(t) + a(t)\delta t + \frac{1}{2} b(t)\delta t^2 + \cdots$$

$$a(t + \delta t) = a(t) + b(t)\delta t + \frac{1}{2} c(t)\delta t^2 + \cdots$$

Where *r* is the position, *v* is the velocity (the first derivative with respect to time), *a* is the acceleration (the second derivative with respect to time), etc.

For the Verlet algorithm:

$$r(t+\delta t) = r(t) + v(t)\delta t + \frac{1}{2}a(t)\delta t^2$$

$$r(t-\delta t) = r(t) - v(t)\delta t + \frac{1}{2}a(t)\delta t^2$$

Summing these two equations, one obtains

$$r(t+\delta t) = 2r(t) - r(t-\delta t) + a(t)\delta t^2$$

The Verlet algorithm, which uses no explicit velocities, calculates new positions at time $t+\delta t$ by using positions and accelerations at time *t* and the positions from time $t-\delta t$. Although of moderate precision, the Verlet algorithm is straightforward and its storage requirements are modest.

For the Leap-frog algorithm:

$$r(t+\delta t) = r(t) + v\left(t+\frac{1}{2}\delta t\right)\delta t$$

$$v\left(t+\frac{1}{2}\delta t\right) = v\left(t-\frac{1}{2}\delta t\right) + a(t)\delta t$$

It first calculates the velocities at time $t+1/2\delta t$ and then calculates the positions, *r*, at time $t+\delta t$ using the calculated velocities. In this way, the velocities leap over the positions which then leap over the velocities. The velocities are explicitly calculated in the Leap-frog algorithm, while they are not calculated at the same time as the positions. Moreover, the velocities at time *t* can be approximated by the following relationship:

$$v(t) = \frac{1}{2}\left[v\left(t-\frac{1}{2}\delta t\right) + v\left(t+\frac{1}{2}\delta t\right)\right]$$

For the Velocity Verlet algorithm:

$$r(t+\delta t) = r(t) + v(t)\delta t + \frac{1}{2}a(t)\delta t^2$$

$$v(t+\delta t) = v(t) + \frac{1}{2}[a(t) + a(t+\delta t)]\delta t$$

The Velocity Verlet algorithm, which has no compromise on precision, calculates the positions, velocities and accelerations at time *t*.

For the Beeman's algorithm:

$$r(t+\delta t) = r(t) + v(t)\delta t + \frac{2}{3}a(t)\delta t^2 - \frac{1}{6}a(t-\delta t)\delta t^2$$

$$v(t+\delta t) = v(t) + v(t)\delta t + \frac{1}{3}a(t)\delta t + \frac{5}{6}a(t)\delta t - \frac{1}{6}a(t-\delta t)\delta t$$

The Beeman's algorithm gives a more accurate expression for the velocities and better energy conservation compared to the Verlet algorithm. However, the more complex expressions make the calculation more expensive.

In practice, much more complicated versions of the algorithm are applied in almost all MD codes, including two steps (predictor and corrector) in solving the equations of motion and many additional steps such as temperature and pressure control, analysis and output.

2.1.3 Ensembles

An ensemble is a collection of all possible systems which have different microscopic states but an identical macroscopic or thermodynamic state. There are different ensembles with different characteristics with four of the most common ensembles listed here.

Microcanonical ensemble (NVE) : The thermodynamic state characterized by a fixed number of atoms, N, a fixed volume, V, and a fixed energy, E. This corresponds to an isolated system.

Canonical Ensemble (NVT): This is a collection of all systems whose thermodynamic state is characterized by a fixed number of atoms, N, a fixed volume, V, and a fixed temperature, T.

Isobaric-Isothermal Ensemble (NPT): This ensemble is characterized by a fixed number of atoms, N, a fixed pressure, P, and a fixed temperature, T.

Grand canonical Ensemble (mVT): The thermodynamic state for this ensemble is characterized by a fixed chemical potential, m, a fixed volume, V, and a fixed temperature, T.

The specific settings and algorithms vary with different MD codes and should be carefully selected with respect to different interests of research. The detail of MD simulation method can be found online and in many MD books such as The Art Of Molecular Dynamics Simulation by Rapaport [311] and will not be further discussed in this thesis. The specific MD simulation method used in this thesis will be presented in the following parts.

2.2 Simulation codes and conditions

The MD simulations in this thesis were conducted by Lammps software [312] with embedded-atom method (EAM) potentials. LAMMPS, an acronym for Large-scale Atomic/Molecular Massively Parallel Simulator, is a classical molecular dynamics code and is distributed by Sandia National Laboratories, a US Department of Energy laboratory. It is an open source code under the terms of the GPL and has potentials for many materials, such as soft materials (biomolecules, polymers) and solid-state materials (metals, semiconductors) and coarse-grained or mesoscopic systems. It can be used to model atoms or, more generically, as a parallel particle simulator at the atomic, meso, or continuum scale. LAMMPS can run on single processors or in parallel using message-passing techniques and a spatial-decomposition of the simulation domain. The code is designed to be easily modified or extended with new functionality.

The EAM potentials of Al and Cu developed by Mendelev et al. were used here [313]. These potentials have been demonstrated to be in good agreement with the

first-principles and measured liquid diffraction data and can well predict the liquid structure.

All the MD simulations in this thesis were performed in the isothermal-isobaric (NPT) ensemble (Nose – Hoover thermostat) with 0 pressures in each direction. The MD integration time step was 1fs.

The common neighbour analysis (CNA) technique [314] and the centro-symmetry parameter [315] were used to characterize whether the atom is part of a perfect lattice, a local defect (e.g. a dislocation or stacking fault), or at a surface or interface. The CNA parameter, which gives a classification of all the atoms by their local crystallinity, is a scalar quantity and will be a number from 0 to 5. The CNA value of 1 means the corresponding atoms belong to the FCC structure, 2 for the HCP structure, 3 for the BCC structure, 4 for the icosohedral structure and 5 for the unknown structure. The CNA value will be 0 for atoms not in the specified computation group. Therefore, the partial and full dislocations, stacking faults, interfaces and point defects can be identified. However, the CNA parameter is readily affected by the thermal fluctuations when simulated at relatively high temperature. Therefore, in particular cases, the centro-symmetry parameter, which is also a useful measure of the local lattice disorder around an atom in solid-state systems, was used to avoid the effect of thermal fluctuation as much as possible. The centro-symmetry parameter is also a scalar quantity but a rational number >= 0. For FCC materials, the centro-symmetry parameters of the atoms from the bulk, dislocation cores, stacking faults and free suface are 0, ~1.0, ~5.0 and ~23.0 respectively. Therefore, the effect of thermal fluctuation can be severely reduced by appropriately adjusting the range of the centro-symmetry parameters. The visualization tool VMD [316] and AtomEye [317] were applied in this thesis to produce illustrations of the simulated systems. The commercial software Matlab was used to pre- and post-process the simulated results.

The above settings are common for all the simulations and the specific diversification of the simulation according to each case will be further described in respective chapters.

3 GRAIN BOUNDARY SLIDING BEHAVIOUR

3.1 Introduction

One of the dominant microstructural features in superplasticity is the role played by grain boundary sliding (GBS) which can contribute more than 50% of the total strain during superplastic deformation [1, 2]. Even for quick plastic forming which operates at faster strain rates and lower temperature than SPF, the GBS can still account for certain plastic deformation [2]. Understanding the mechanism for GBS and the microstructural features that may affect GBS is highly demanded in materials processing industry. Therefore, GBS behaviour has been extensively studied by theory, simulation or experimental work [318-322].

GBS was shown to be dependent on the orientation of the grain boundary, temperature and dislocation structures of ordered and random boundaries [323]. In Fukutomi et al.'s results, it shows that no GB sliding is expected until the applied stress reaches an "internal stress" for aluminium at 773 K [324]. In recent years, atomistic simulation method has been widely applied to investigate the GBS behaviour at the atomistic scale and many meaningful results have been obtained [158, 251-253, 256, 258, 325]. More sliding was found at boundaries with higher grain boundary energies for a constant external shear field at a series of [110] symmetric tilting grain boundaries at 448 K [252]. Chandra and Dang also addressed the dependence of GBS behaviour on various applied stresses for symmetric tilting grain boundaries (STGB) [251]. Moreover, the effects of dislocations, vacancies, impurities and disordered atomic layers at the boundary on GBS can also be obtained by atomic simulations [256, 325].Very recently, Qi and Du et al. have investigated the GBS behaviour, also including the effects of vacancy and solution, over a large range of shear forces and grain boundary misorientation angles for aluminum at 750 K [158, 253, 258]. They have proposed that a threshold stress for sliding exists [253]. Additionally, the addition of vacancies can decrease the threshold stress for grain boundary sliding of the low energy grain boundaries by increasing the grain boundary diffusivity, but it has no effect on high energy grain boundaries [158]. They have also found that solution atoms can enhance GBS in high-energy GBs by

weakening Al bonds and by increasing atomic mobility or inhibit GBS by forming atomic clusters and decreasing diffusivity [258].

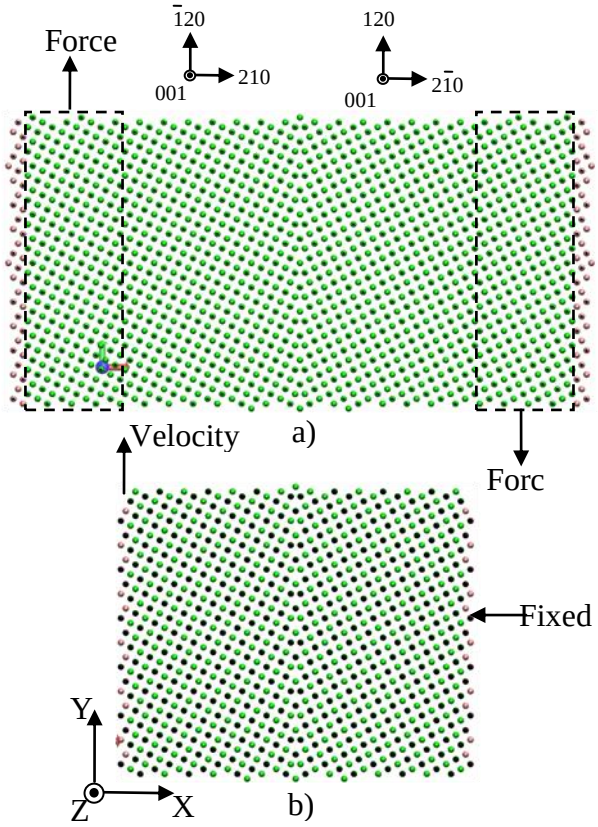

Figure 3.1 Geometry of the bicrystal model with the symmetrical Σ5 (210) tilt grain boundary: a) GBS driven by constant force and b) GBS driven by constant shear rate. The crystallographic orientations of the bicrystal are also indicated. The green and green with black shadow balls represent rows of atoms with positions in alternating (002) planes. The purple balls indicate the fixed boundaries.

However, the GBS always takes place with concurrent accommodation processes. Such processes may involve grain boundary migration (GBM), maintain the grain compatibility during GBS, grain rotation, diffusion or dislocation motion [211, 212], making GBS very complicated. The GBS mechanisms of various grain boundaries at different condition are still unclear.

In this chapter, the response of GBS to a constant shear rate or shear force was investigated for the Al Σ5 (210) and Al Σ5 (310) symmetrical tilting grain boundaries and several asymmetrical tilting grain boundaries at 500~750K. It is found that under

a constant shear force the GBS only simply experienced certain GBM and slid away from each other when a threshold stress was reached. Moreover, this threshold stress was dependent on the temperature. However, under a constant shear rate, the GBS was strongly related to the temperatures. At 500K, the GBS experienced a relatively complicated process involving GBM, coupled motion, and grain rotation. However, at 750K it only involved certain GBM and coupled motion.

3.2 Effect of External Driving Force on the GBS Behaviour for STGB

First, we term the model of GBS driven by constant force as constant force model and model of GBS driven by constant shear rate as constant rate model. The three dimensional bicrystal models were constructed with the Al [001] symmetrical tilting Σ5 (210) GB and the geometry is illustrated in Figure 3.1. For all the models, during the relaxation calculations, all the atoms in the simulation model were set free. The equilibrium simulation model and grain boundary structure was prepared using a combination of molecular statics and MD simulations. A molecular statics calculation using an energy minimization procedure with a standard conjugate-gradient algorithm was carried out to determine the minimum energy configuration of the simulated model. After the minimum energy structure was attained, the simulation model was relaxed using MD in the isobaric-isothermal (NPT) ensemble at a pressure of 0 bar in all directions and a corresponding temperature (300K, 400K, 500K, 600K, 700K and 750K) for 10 ps. Once the equilibrium state of the simulation model and the stable structure of GB were reached, an external shear force or shear velocity was applied on the model. During the dynamic deformation, periodic boundary condition was applied in the Z-direction which is parallel to the tilt axis and the GB plane, while in the Y-direction the free boundary condition was applied and fixed boundary condition was used in the x direction.

For the constant force model (Figure 3.1a), the simulation system had a dimension of $108.546 \times 54.273 \times 40.4527 Å^3$ in $X \times Y \times Z$ and contained 14170 atoms. Four layers of atoms at each side of the border in the x direction were conditionally fixed to be only able to move in the Y-Z plane. Adjacent to each side of the border atoms, a group of atoms containing 2600 atoms in each grain were used to impose an external force at each time step as shown

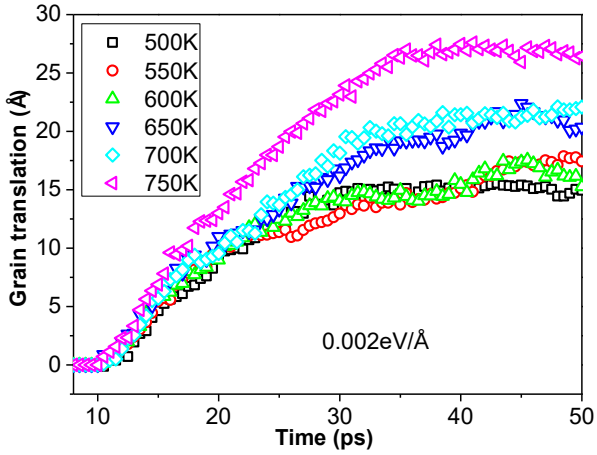

a)

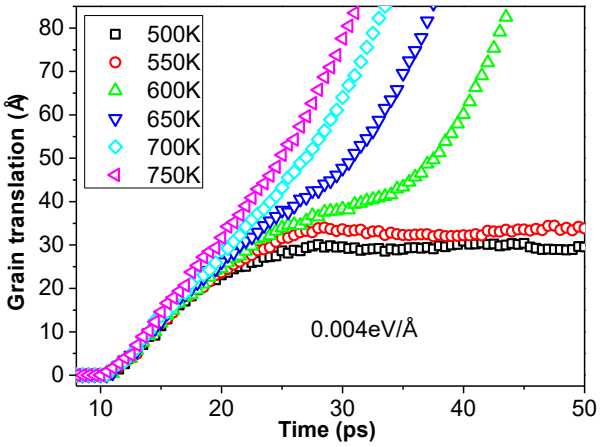

b)

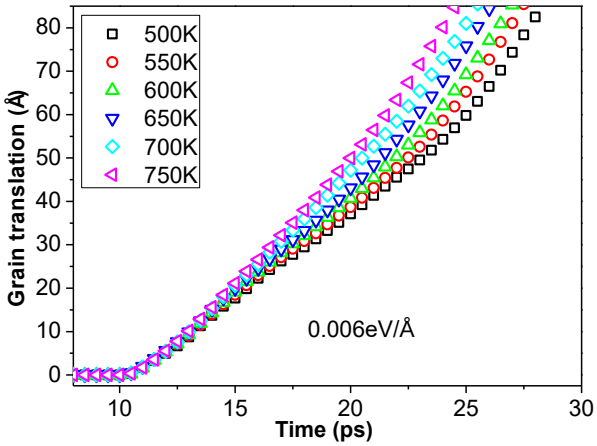

c)

Figure 3.2 Grain translation as a function of time under different applied force for the symmetrical Σ5 (210) tilt grain boundary: a) 0.002eV/Å, b) 0.004eV/Å and c) 0.006eV/Å.

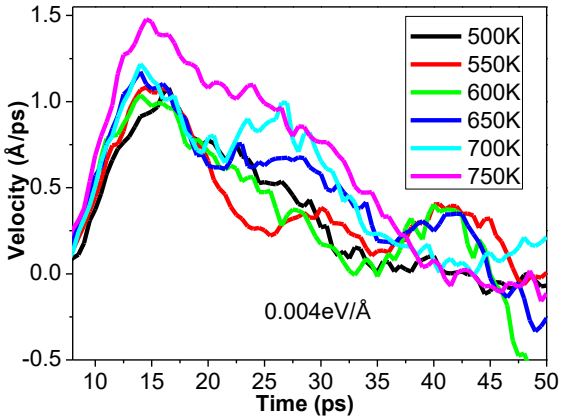

a)

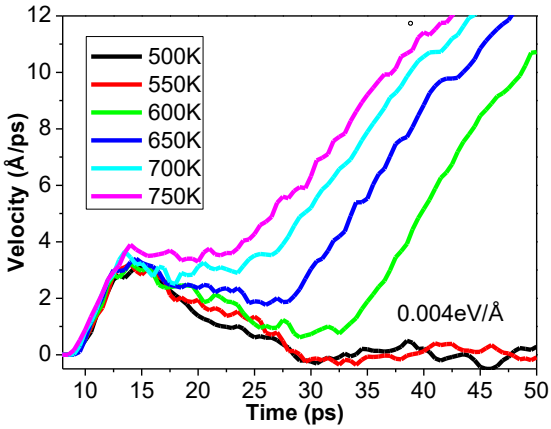

b)

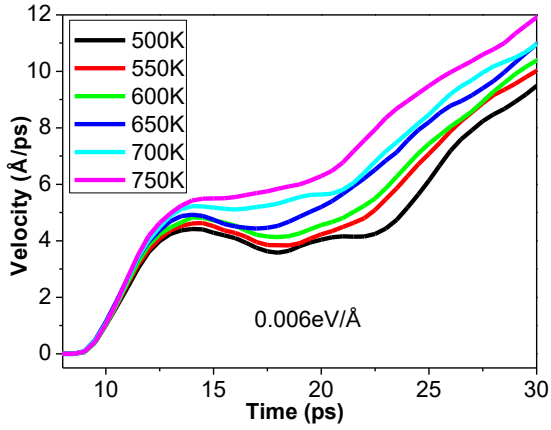

c)

Figure 3.3 Grain boundary sliding velocity as a function of time under different applied force for the symmetrical Σ5 (210) tilt grain boundary: a) 0.002eV/Å, b) 0.004eV/Å and c) 0.006eV/Å.

in Figure 3.1a) to realize the GBS process. The applied force was in the range of 0.002~0.006eV/Å on each atom. Correspondingly, the shear stresses imposed on the initial grain boundary were 2.68×10^{-2} GPa, 5.36×10^{-2} GPa and 8.03×10^{-2} GPa respectively. The relative sliding distance between two grains was defined as the distance between the centres of mass of the border atoms in the X-direction in the present study, as the GB position changed during the MD simulation.

For the constant rate model (Figure 3.1b), the simulation system had a dimension of $65.1276\times54.273\times40.4527\text{Å}^3$ in $X\times Y\times Z$ and contained 8630 atoms. The boundary conditions in Y- and Z-directions were the same as that of the constant force model. In the X-direction, the border atoms composed of three-layer atoms at each side were completely fixed in all directions. During the MD simulation, the GBS process was achieved by moving the fixed atoms of the left grain with the same constant velocity v, while the fixed atoms in the right grain remained fixed. The velocity v was determined by different times of the length in the y direction of the simulation block, which were equivalent to 5.4273m/s, 27.1365m/s and 54.273m/s in the present study. The simulation temperatures of 300K, 400K, 500K, 600K, 700K and 750K were selected for the present study to cover the range of interest and were controlled by the isothermal-isobaric (NPT) ensemble (Nose–Hoover thermostat) with 0 pressures in each direction. The MD integration time step was 1fs. Before the driving force was applied, the bicrystal system was thermally relaxed at the corresponding simulation temperature for 10ps for the constant force model and 50ps for the constant rate model.

3.2.1 Grain boundary sliding of the Σ5 (210) GB driven by constant force

Figure 3.2 shows the effect of applied force and temperature on the GBS behaviour. It can be seen that GBS occurred more or less for all the conditions, as the force chosen in the present study is relatively larger compared to Qi et al.'s study. In that study, no sliding was observed when the applied force was low enough (below 0.002eV/Å in their study) [253]. For 0.002eV/Å, the two grains slid away from each other for certain distance which was increased with the increasing temperature, and then they stopped sliding by oscillating around the balanced position.

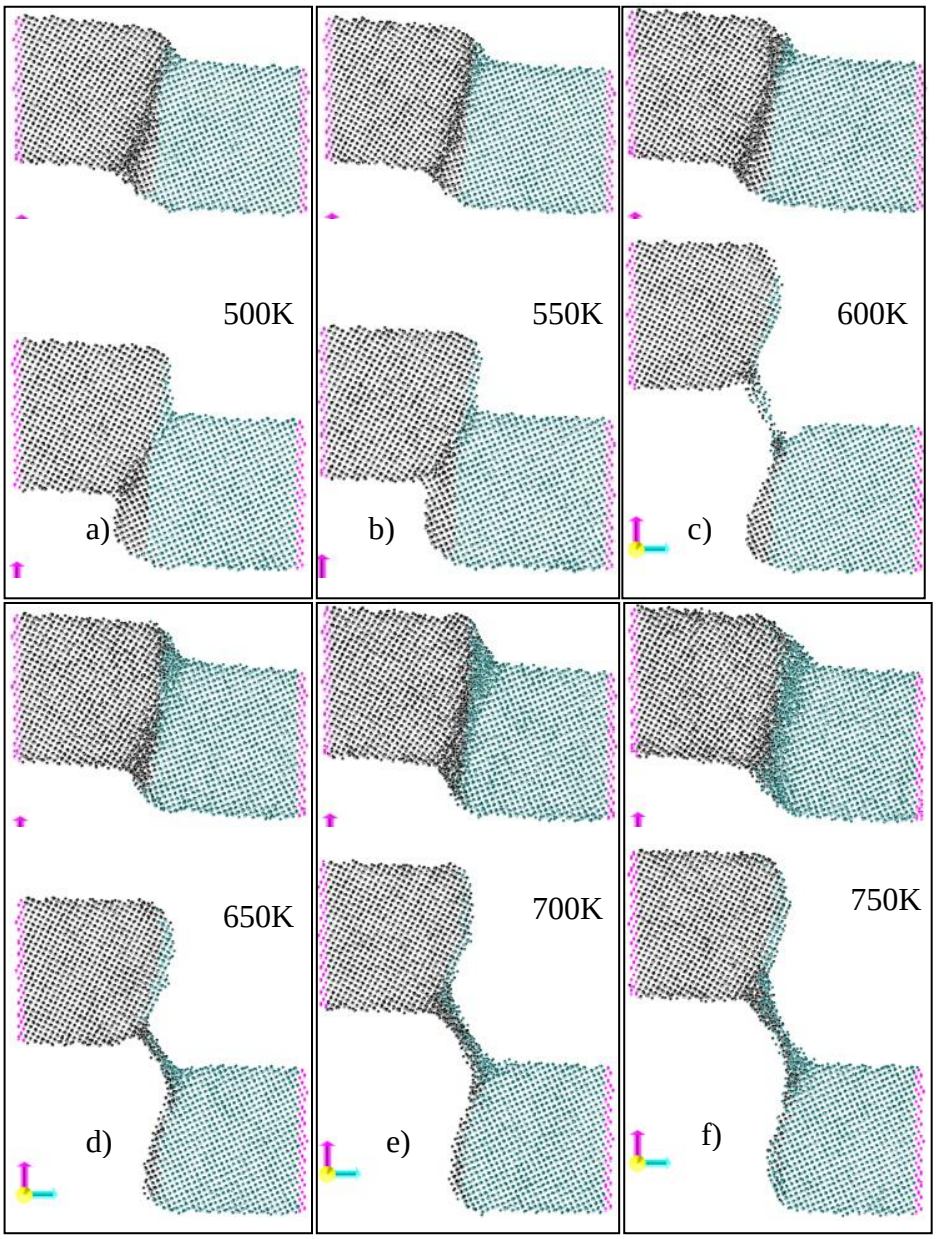

Figure 3.4 Snapshots at the beginning and the near end of the simulation at different temperatures under the applied force of 0.004eV/Å for the symmetrical Σ5 (210) tilt grain boundary: a) 500K, b) 550K, c) 600K, d) 650K, e) 700K and e) 750K.

For 0.004eV/Å, the GBS behaviour below 550K was similar to that for 0.002eV/Å, whereas the final sliding distances were larger than those at the same temperatures for 0.002eV/Å. Above 600K, two grains slid away completely from each other, and the sooner the higher temperature. As the force went up to 0.006eV/Å, two grains slid away completely from each other at all temperatures. Since the slope of the grain translation versus time curve is simply the average velocity of GBS, the GBS velocity versus time is shown in Figure 3.3 to reveal the common features of the

GBS driven by constant force. It can be clearly seen that the whole process of the GBS driven by constant force shows clear three successive features: the velocity of GBS increased, slowed down or even decreased, and increased again (in case of that two grains slid away completely from each other). The decreased (slowed down) part of GBS velocity indicates that some resistance occurred during GBS process and the applied force was required to overcome the resistance for further GBS. To reveal what took place in this stage, snapshots at the beginning and the near end of the simulation at different temperatures under the applied force of 0.004eV/Å are shown in Figure 3.4.

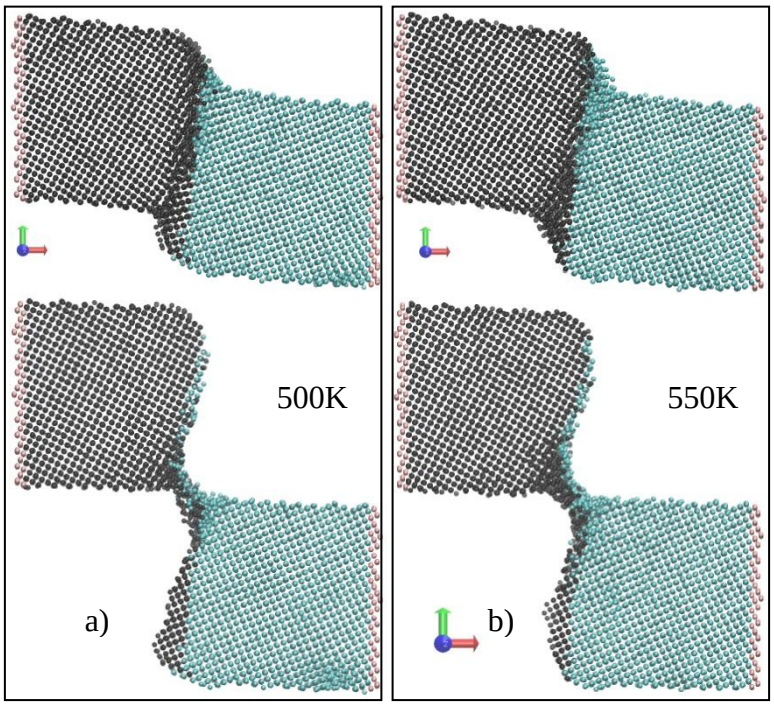

Figure 3.5 Snapshots at the beginning and the near end of the simulation at different temperatures under the applied force of 0.006eV/Å for the symmetrical Σ5 (210) tilt grain boundary: a) 500K and b) 550K.

It shows that during GBS the GB first rotated from the initial (210) plane to the (100) plane (in the reference of left grain) due to the unbalanced GB migration and then the GBS process continued on this plane until the end of simulation. As no periodic condition was applied in Y-direction in the present study, the unbalanced GB migration took place due to the surface strain which tends to form the low energy plane surface. Because of this GB rotation, the new GBS plane formed an angle of 26.57^{o} with the applied force. Therefore, not only did the resolved stress on GBS

plane become smaller, but also a resolved normal stress was created to exert on the GBS plane. This normal stress had an effect on dividing the GB which can be neutralized by local atoms accommodation or initiating defects or even cracks. Correspondingly, the applied force should be large enough to form the required resolved normal stress and the further GBS may continue. Because of this resistance, the increase of GBS velocity slowed down and in some cases the GBS velocity even decreased in the middle of GBS.

With GBS proceeding, the GB area gradually reduced as well as the resistance and the GBS velocity increased again. It is also readily understood that this resistance would be smaller at high temperature due to lower atom bonding force which is favourable for atom diffusivity and accommodation. Moreover, as the temperature increased, the GB layer became thicker and the GBS showed viscous sliding characteristics as shown in Figure 3.4. It should be mentioned that no crack was initiated even at low temperature with high external force for current simulation conditions. The Figure 3.5 gives the snapshots at the beginning and the near end of the simulation at low temperatures under the applied force of 0.006eV/Å. It can be seen that the GBS behaviour is extremely similar to that for applied force of 0.004eV/Å at corresponding temperatures. Besides, the GBS continued only by local atoms accommodation at low temperatures.

3.2.2 Grain boundary sliding of the Σ5 (210) GB driven by constant shear rate

In the constant rate model, the shear stress caused by the constant shear rate for the whole bicrystal system was tracked as a function of time. Figure 3.6 shows GBS behaviour at 500K and 750K with different shear rates. As a whole, the curves of shear stress versus time show the similar features at low (500K) and high (750K) temperatures: during the GBS the shear stress was gradually increased up to a peak stress and then decreased gradually to 0 when the two grains slid away from each other. However, the difference is that there was a second stress peak at the low temperature and it was especially obvious with low shear rate. This indicates that different GBS mechanisms were operated at low and high temperatures. Moreover, the GBS started with the saw-tooth stress characteristic or the so-called stick-slip GBS behaviour and it was also relatively obvious with low shear rate.

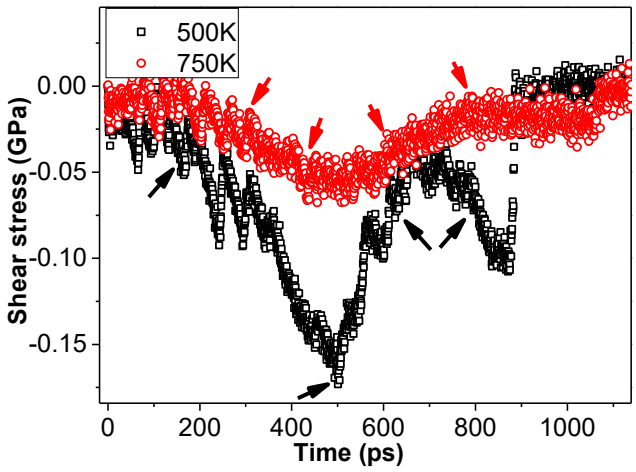

a)

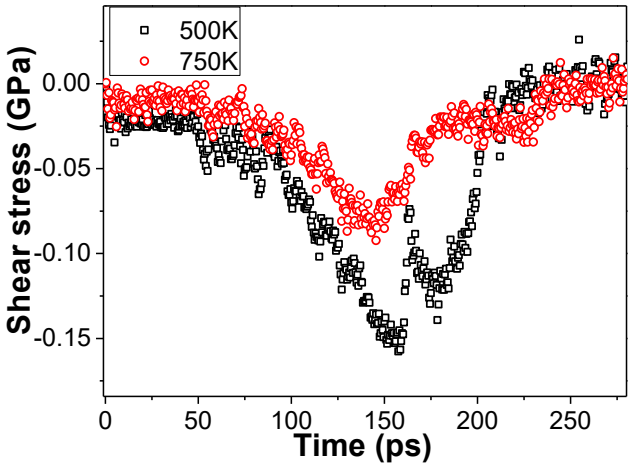

b)

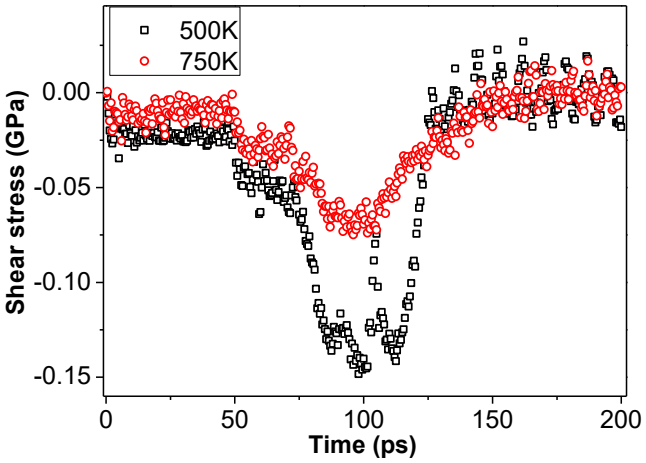

c)

Figure 3.6 The shear stress caused by constant shear rate in the whole bicrystal system versus the time for the symmetrical Σ5 (210) tilt grain boundary: a) 5.4273m/s, b) 27.1365m/s and c) 54.273m/s.

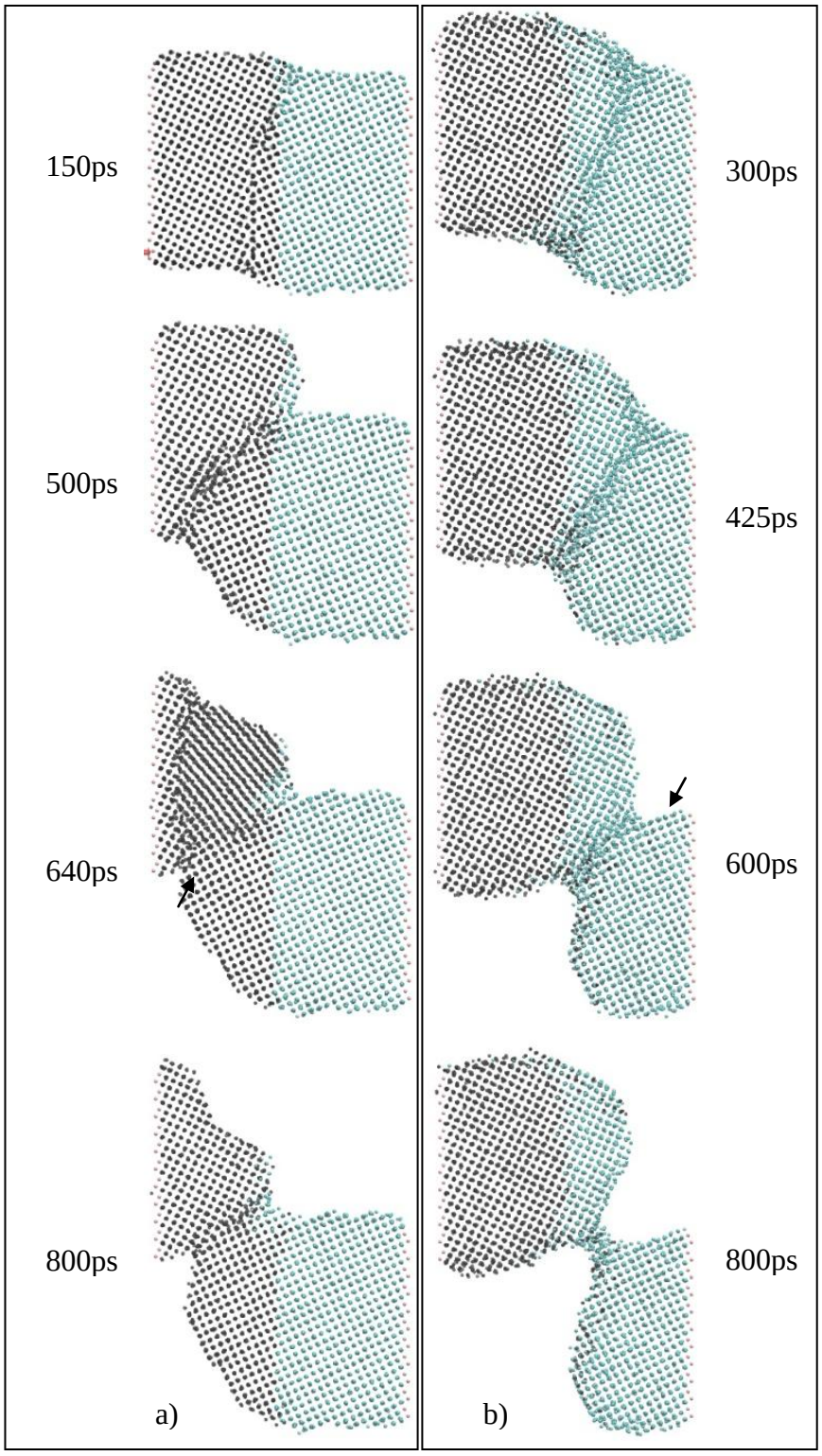

Figure 3.7 Snapshots at concerned stages during GBS as pointed by black arrows (500K) and red arrows (750K) in Figure 3.6a): a) 500K and b) 750K.

To investigate what mechanisms were operated at respective temperatures, snapshots at concerned stages during GBS as pointed by black arrows (500K) and red arrows (750K) in Figure 3.6a) are displayed in Figure 3.7. At 500K (Figure 3.7a), it can be

clearly seen that the GB rotation from the initial (210) plane to the (100) plane (in the reference of left grain) and coupled motion simultaneously occurred at the early stage (150ps). The GB coupled motion confirmed the saw-tooth behaviour at the early stage. The stick-slip GBS behaviour also indicates that the contribution of the GB coupled motion or rigid translation to a GBS process is increased with the decreasing temperature and shear rate. Thereafter, the GB rotation gradually took up the whole (100) plane (in the reference of left grain) and the shear stress correspondingly increased to overcome the normal stress on the rotated GB and keep up the same shear rate. The GBS mechanism operated at this stage is similar to that

of constant force model. At the next stage (500ps), the shear stress went up to the peak which even resulted in certain bending of the GB toward to left grain and the local atoms were obviously disordered. Consequently, the bicrystal system mediated the high shear stress by releasing dislocations. As the dislocations went through the grains, they even led to some grain rotation and the GB atoms rearranged (640ps). It can also be seen that the GB already rotated to (010) plane of the right grain equivalent to 63.43^{o} rotation from the initial GB plane at the later stage. Due to left border constraints and GB atoms rearrangement, the left grain rotated back to its original orientation at the last stage (800ps). Moreover, due to the large angle between GB and the driving force, GBS was relatively difficult in this stage and the shear stress increased to divide the GB by initiating cracks corresponding to the shear stress drop in Figure 3.6a).

At 750K (Figure 3.7b), the GBS mechanism is relatively uncomplicated and similar to that of the constant force model and that at early stage of 500K. The shear stress increased due to the GB rotation which led to an angle between the driving force and GB plane, and decreased due to the reduced GB area. Moreover, the viscous sliding behaviour was relatively obvious at this temperature, which accounts for the relatively smooth shear stress curves. The GBS also transferred partly on the (010) plane of the right grain (arrow in 600ps of Figure 3.7b).

It can be seen from the two bicrystal models that the bicrystal system always tended to resist the applied force by GB rotation regardless of the type of driving force. The GB rotation resulted from the combination of surface strain, GB migration or GB

coupled motion, and it led to an angle between the applied force and the new GBS plane.

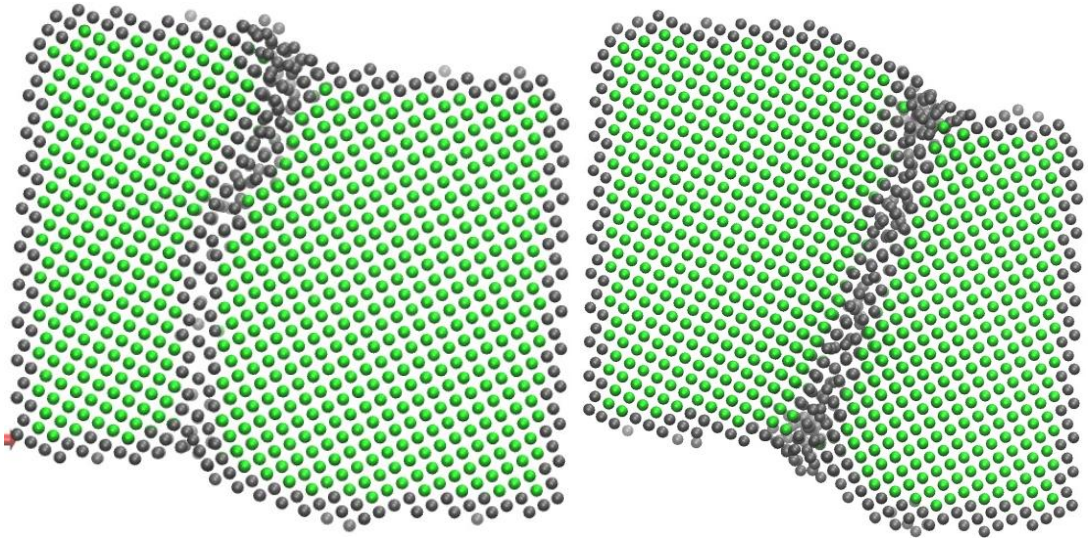

a) b)

Figure 3.8 Snapshots at concerned stages after energy minimization to show the favourable crystallographic planes for constant rate model with the symmetrical Σ5 (210) tilt grain boundary: a) 65ps at 500K and b) 75ps at 750K.

Moreover, the rotated angle had certain regularity, as the {100} crystallographic planes were energetically favourable for either of the grains. To clearly illustrate the favourable {100} crystallographic planes, the snapshots after energy minimization at concerned states of constant rate model are shown in Figure 3.8. It clearly shows the {100} oriented surface plane and grain boundaries. It also shows the grain interior was defects free, as the atomic thermal fluctuation was removed. Therefore, GB generally rotated to the (100) plane of the left grain by 26.57^{o} and sometimes to the (010) plane of the right grain by 63.43^{o}. Correspondingly, the external force was resolved along and normal to the GB plane respectively. The resolved stress along the GB plane was effective for the subsequent GBS, while the normal one was to separate the two grains. In light of this, there was some difference of the specific response of GBS behaviour to the different driving forces. For constant force, the GBS velocity decreased, as the resolved stress along the GB plane became smaller due to the GB rotation. The external force needed to overcome a critical value for further GBS and this critical value decreased with the increasing temperature. No

other defects such as dislocation or cracks initiated from the grain boundary under present conditions. However, it is proposed that higher external force would lead to less time for atomic accommodation and then cause crack initiation on GB. For constant rate, the resolved stresses increased due to GB rotation to keep the constant shear rate. On the other hand, at low temperature and high shear rate, the GB dividing could be neutralized not only by atomic accommodation, but also by initiating defects or even cracks.

3.3 Effect of Normal External Force on the Shear response of STGB

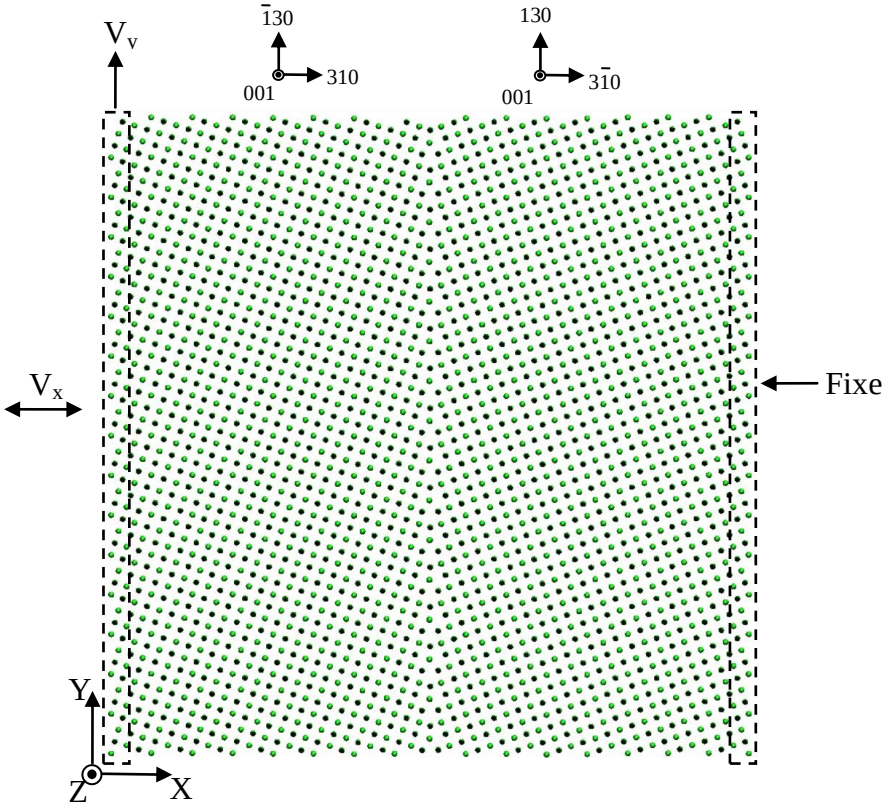

Figure 3.9 Geometry of the bicrystal grain boundary sliding model driven by constant shear rate with the Σ5 (310) tilting grain boundary used in the present study. The crystallographic orientations of the bicrystal are also indicated. The green and green with black shadow balls represent rows of atoms with positions in alternating (002) planes.

In this part, the three dimensional bicrystal GBS model driven by constant shear rate was constructed with the Al [001] symmetrical tilting Σ5 (310) GB and the geometry

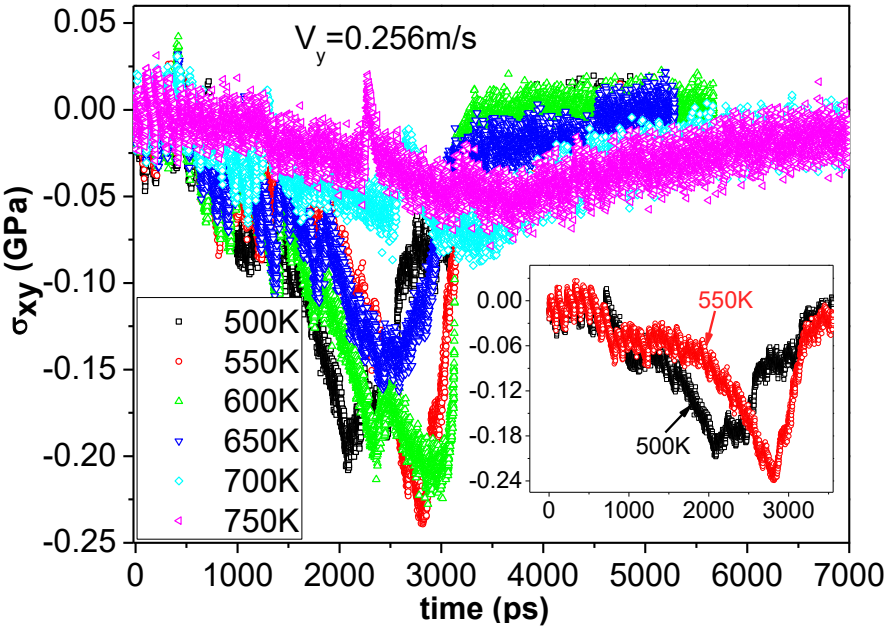

a)

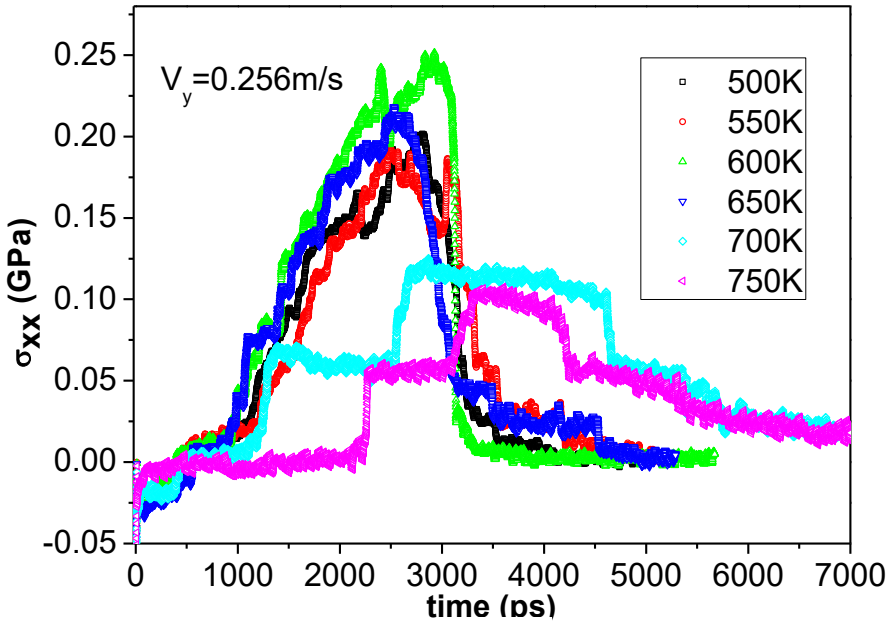

b)

Figure 3.10 a) The shear stress and b) normal stress caused by the constant shear rate in the whole bicrystal system versus the time of the Σ5 (310) GB at the V_y of 0.256m/s. Insert in a) shows the curves at 500K and 550K separately.

is illustrated in Figure 3.9. The model construction was similar to that for the Σ5 (210) GB shown in Figure 3.1b), while the model size was enlarged, especially in Y direction that is the GBS direction. The simulation system has a dimension of

102.3382×102.3382×51.1691 $Å^3$ in X×Y×Z and contains 25690 atoms. Periodic boundary condition was applied in the Z-direction which is parallel to the tilt axis and the GB plane. However, in the Y-direction the free boundary condition was applied. In the X-direction, the border atoms composed of three-layer atoms at each side were completely fixed in all directions. During the MD simulation, the GBS process was realized by moving the fixed atoms of the left grain with the same constant velocity V_y or (V_y+V_x). The fixed atoms in the right grain remained fixed. The V_x was used to impose the normal force on the GB.

The GBS behaviour was investigated in detail at the V_y of 0.256 m/s with the V_x of 0, ±0.051, ±0.077 and ±0.102 m/s. The minus V_x means an increased normal tensile force on the GB during GBS, while the plus V_x means an increased normal compressive force. The simulation temperatures of 500K, 550K, 600K, 650K, 700K and 750K were the same as the previous cases to cover the range of interest and were controlled by the isothermal-isobaric (NPT) ensemble (Nose–Hoover thermostat) with 0 pressures in each direction. The MD integration time step was 1fs. Before the driving force was applied, the bicrystal system was thermally relaxed at the corresponding simulation temperature for 20ps.

3.3.1 Shear response of the Σ5 (310) GB without normal external force

Figure 3.10a) shows the evolution of the shear stress in the bicrystal system during the shear deformation of the Σ5 (310) GB driven by the constant shear rate V_y of 0.2558455m/s at 500~750K. It can be seen that it is similar to the results obtained from the Σ5 (210) GB: during the shear deformation the shear stress was gradually increased up to a peak stress and then decreased gradually at higher temperatures (700~750K) or sharply at lower temperatures (500~650K) to 0 when the two grains slid away from each other. However, several remarkable features should be noted. Firstly, there is an obvious drop of the peak shear stress between the temperatures of 650K and 700K. Also, the peak shear stress is inversely proportional to the temperature. Below 650K, the peak shear stresses in the bicrystal systems are comparable in the range of 0.18~0.24GPa and the largest peak shear stress came up near the temperature of 550~600K. However, the peak shear stress reduced to 0.06GPa when the temperature went up to 700K. Secondly, the saw-tooth stress

characteristic is clearly shown only at the beginning at higher temperatures (700~750K). However, at lower temperatures (500~650K) it is detectable nearly through the whole process of the shear deformation. Thirdly, the double-peak shear stress characteristic which was found during GBS of the Σ5 (210) GB at the low temperature especially with low shear rate was not found in the present case. This is true even though the shear rate was much lower (nearly 20 times) than that for the Σ5 (210) GB. The normal stress σ_{xx} in the X direction was also monitored during the shear deformation. Interestingly, the shear deformation resulted in a tension of the normal stress σ_{xx} at all temperatures. Below 650K, the normal stress σ_{xx} increased with the shear deformation to a peak in tension and then decreased sharply. This is corresponding to the evolution of shear stress in the bicrystal system. Above 700K, however, there are several nearly flat stages for the normal stress σ_{xx} during the shear deformation and the normal stress σ_{xx} jumps up or drops down very quickly between adjacent stages.

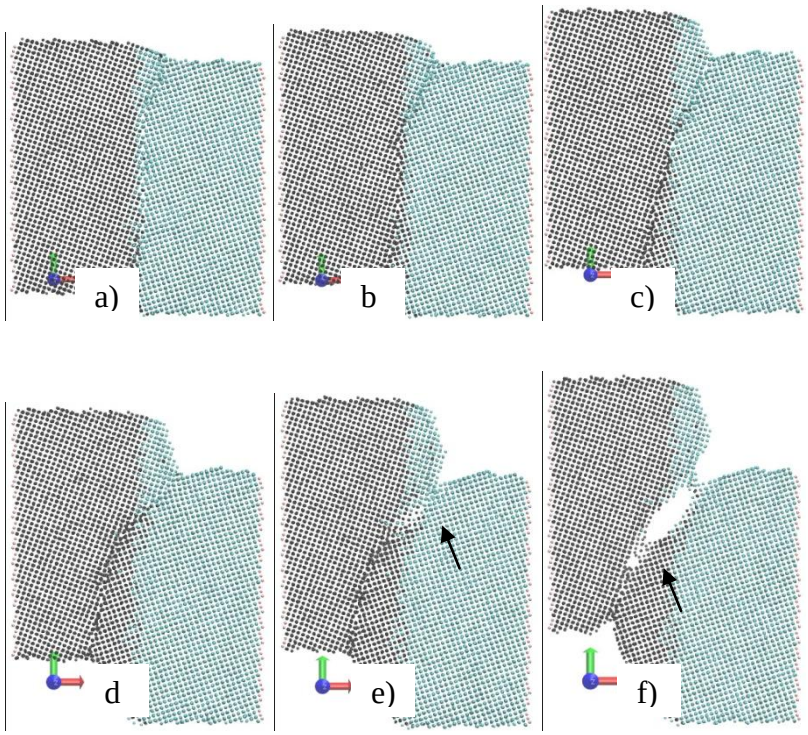

Figure 3.11 Snapshots at concerned stages during GBS of the Σ5 (310) at 500K: a) 710ps, b) 1020ps, c) 1350ps, d) 2020ps, e) 2400ps and f) 2842ps. The black arrows indicate the crack initiation.

Snapshots of the atomic configuration (projection along the tilt [001] axis) at the concerned stages during GBS are shown in Figure 3.11~ 3.14 to investigate the specific grain boundary deformation behaviour at respective temperature. At the early stage of 500K (Figure 3.11a~c), the inhomogeneous coupled GB motion and migration gradually led to the GB rotation from the initial (310) plane to the (100) plane of left grain and certain pure grain boundary sliding was also accompanied during this process. This can be identified by the discontinuous lattice steps at the top and bottom of the bicrystal. Now, it is readily understood that the normal stress σ_{xx} was caused by the GB rotation. Correspondingly, the shear stress increased to overcome the normal stress on the rotated GB and to keep up the same shear rate. This GB reaction during shear deformation is very similar to the results obtained from the Σ5 (210) GB, while the rotation angle of the present case is 18.435^{o}. It should also be noted that the saw-tooth characteristic of the shear stress versus time curves (shown in the Figure 3.10) after the complete GB rotation to the (100) plane of left grain (1350ps in Figure 3.11c) is obviously weakened compared to that before the complete rotation of the GB. This implies that the GBS proceeds relatively more smoothly after the GB rotation than before. With further shear deformation to the bicrystal, the shear stress was obviously increased and the resolved normal stress on the GB gradually led to an inhomogeneous GB migration. Correspondingly, the GB was gradually curved, which could also influence the resolved normal stress. Then the proceeding of grain boundary motion or sliding became difficult and the shear stress in the bicrystal reached the peak as expected (2020ps in Figure 3.11d). So far, the response of GB to the external shear deformation is similar to that of the Σ5 (210) GB. However, in the present case, the crack was initiated from the GB with further shear deformation (2400ps in Figure 3.11e) rather than mediating the high shear stress by releasing dislocations or even lattice rotation, followed by a sharp drop of the shear stress. On the one hand, as the bicrystal system size was increased and the shear stress was relatively small due to the low shear rate, it is relatively difficult to cause the lattice rotation in the present case. On the other hand, the occurrence of dislocation release or crack initiation at the grain boundary is dependent on the specific orientation relationship (Schmid factor), local stress condition and temperature etc and it can be very complicated to tell which one would occur first. Therefore, it is most likely that the critical stress for crack initiation is relatively

lower than the critical stresses for other shear deformation mediation manners with respect to the Σ5 (310) GB at 500K. Moreover, it can be seen in the Figure 3.11f) that with further shear deformation another crack initiated from the grain boundary. The first one, however, was propagating instead of only one crack propagation along the grain boundary. To some extent, this accounts for certain ductility of Al in this condition.

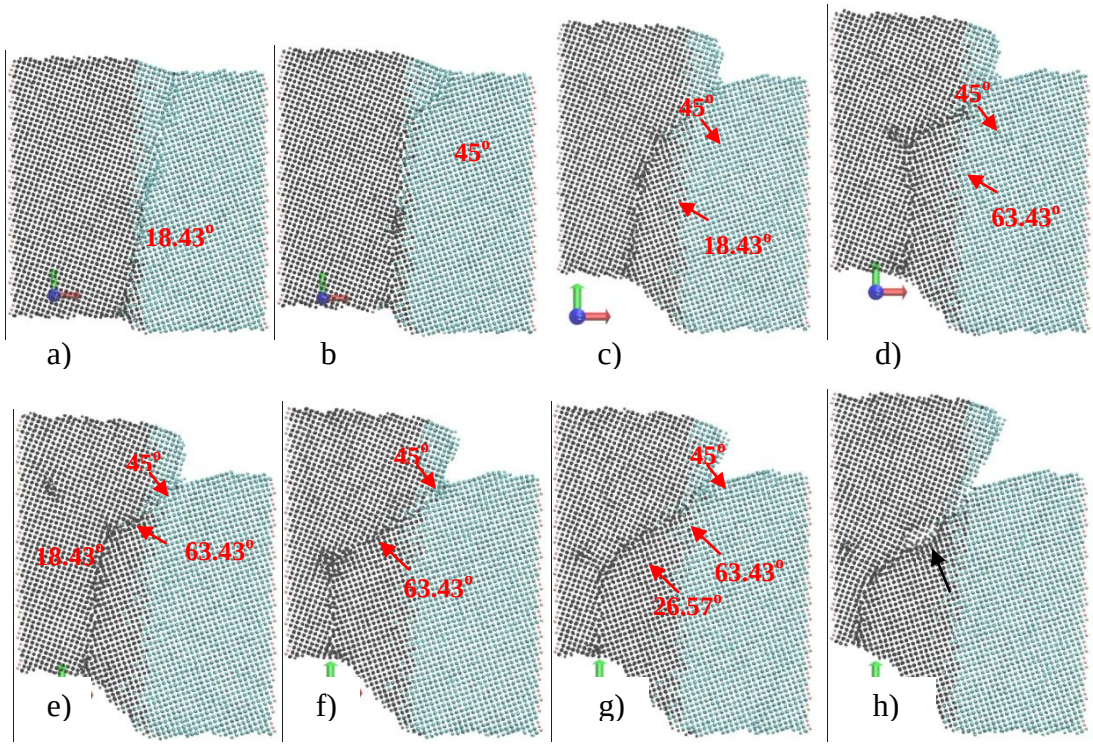

Figure 3.12 Snapshots at concerned stages during GBS of the Σ5 (310) at 550K: a) 450ps, b) 850ps, c) 1850ps, d) 1970ps, e) 1983ps, f) 2410ps, g) 2421ps and h) 2850ps.

At 550K (Figure 3.12), the response of grain boundary to external shear deformation was the most complicated case. First, the GB rotation to the (100) plane of left grain completed very soon under the shear deformation (450ps in Figure 3.12a). At this stage, the top surface of the bicrystal shows no obvious lattice steps. This indicates that the upper part experienced nearly pure couple/shear GB motion, while the bottom surface of certain lattice steps indicate that a small fraction of GBS occurred in the lower part. Then the GB moved to and fro in a small range with the shear deformation proceeding, which resulted from the dual behaviour of the coupled motion [234, 235]. (The dual behaviour of the coupled GB motion will be discussed in detail in Chapter 5.) As shown in Figure 3.12b), a large part of the GB from the

bottom to the upside nearly rotated back to vertical. At this stage, the shear deformation led to relatively stable GB coupled motion with a little GBS. It can also

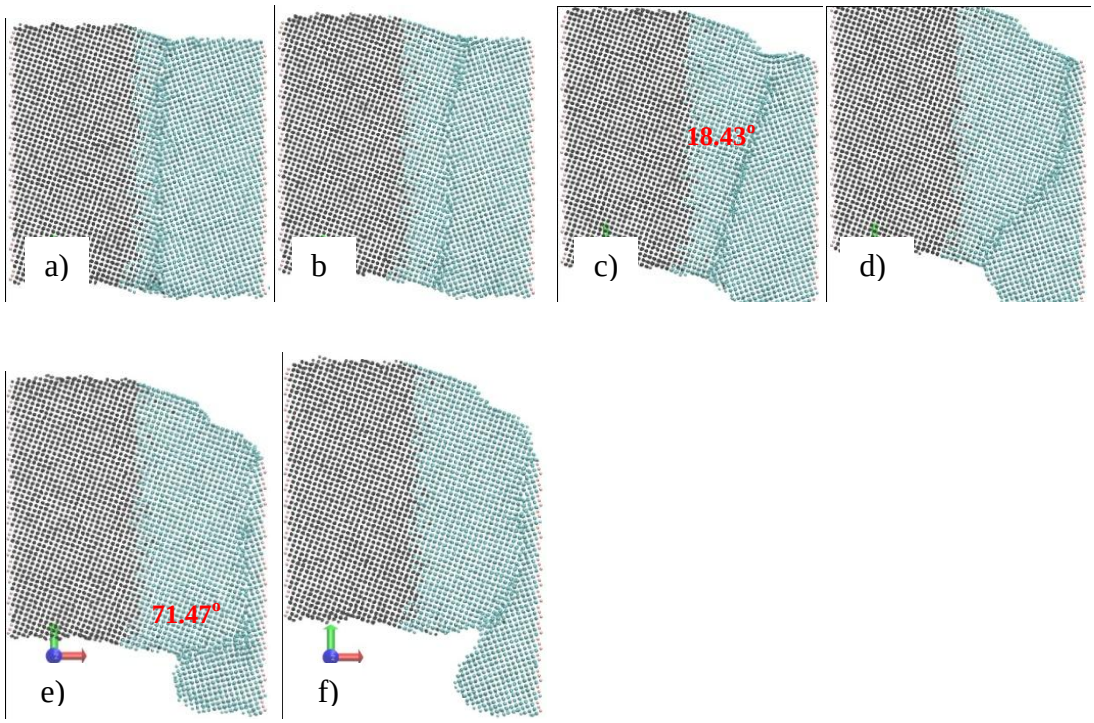

Figure 3.13 Snapshots at concerned stages during GBS of the Σ5 (310) at 600K: a) 460ps, b) 780ps, c) 1460ps, d) 1950ps, e) 2440ps and f) 3020ps.

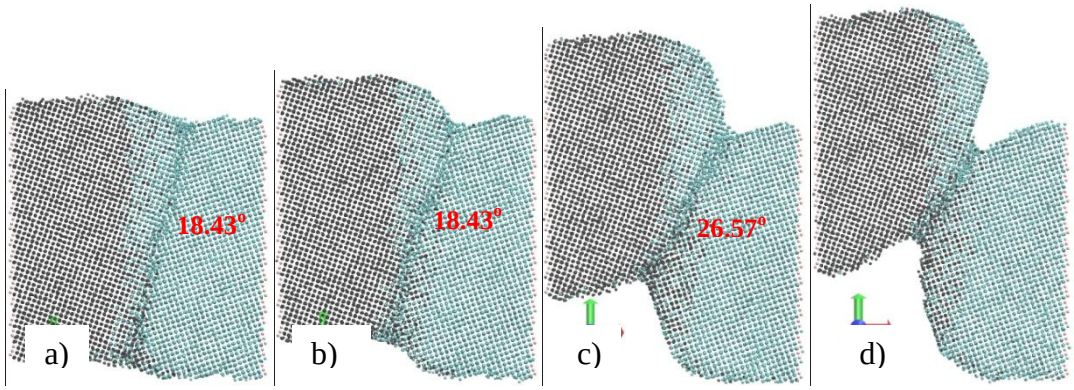

Figure 3.14 Snapshots at concerned stages during GBS of the Σ5 (310) at 750K: a) 620ps, b) 1220ps, c) 2700ps and d) 3400ps.

be confirmed from the corresponding shear stress versus time curve between 700~1500ps in Figure 3.10, that which part is relatively smooth saw-tooth like and nearly horizontal. With further shear deformation (1850ps in Figure 3.12c), the GB was gradually curved as what occurred at 500K and the shear stress in the system

was also increased. Moreover, considerable GBS had taken place at this stage. As the shear stress increased with the shear deformation, the uneven GB motion became more obvious due to the more inhomogeneous stress distribution and led to a cusp on the GB (1970ps in Figure 3.12d). Interestingly, instead of the crack initiation, a dislocation was nucleated at the cusp to mediate the stress concentration and the cusp area of GB became relatively smoother after the dislocation being released from the cusp than before (1983ps in Figure 3.12e). After another process of dislocation nucleation and release (Figure 3.12f and g), a crack finally initiated at the severely rotated GB with a sudden drop of the shear stress (Figure 3.12h). As mentioned previously, the occurrence of dislocation release or crack initiation at the grain boundary under shear deformation can be very complicated and is dependent on many factors such as the specific orientation relationship, local stress condition and temperature etc. In the present case, it is believed that the dislocation release at the GB rather than crack initiation was mainly due to the 50K higher temperature than 500K. Although this difference is not very large, it may increase the atomic activity and help the local atomic accommodation and GB motion or sliding. This might meet the requirements (dislocation nucleation and Schmid factor) for dislocation release. Consequently, as the Schmid factor permitted during GB mediation for the shear deformation, the dislocation may release at the GB. Besides, the required shear stress for dislocation release was much lower than that for crack initiation (insert in Figure 3.10). With further shear deformation, a large part of the GB rotated nearly perpendicular to the external shear stress after two dislocations release, which resulted in large resolved normal stress on this part of GB. Additionally, the second dislocation was blocked by the fixed boundary in the vicinity of GB, which would lead to a counterforce on the GB. Therefore, the shear stress kept increasing until the crack initiated at the mostly rotated GB. It should be noted that in the practical materials any hard impurities or particular grain boundaries may act as the fixed boundaries. The GB rotation and dislocation formation will be discussed in detail later.

The response of grain boundary to external shear deformation at 600K was similar to that of 650K and the GB evolution during shear deformation at 600K is shown in Figure 3.13. The most representative feature at this temperature range is the perfect

coupling motion of GB at the early stage during the shear deformation (Figure 3.13a and b). It can be seen that as the GB moved forward, a sheared lattice was left behind and the initial two grains transited very smoothly across the deformed area without any lattice steps at the top or bottom surface. Moreover, most part of the GB had

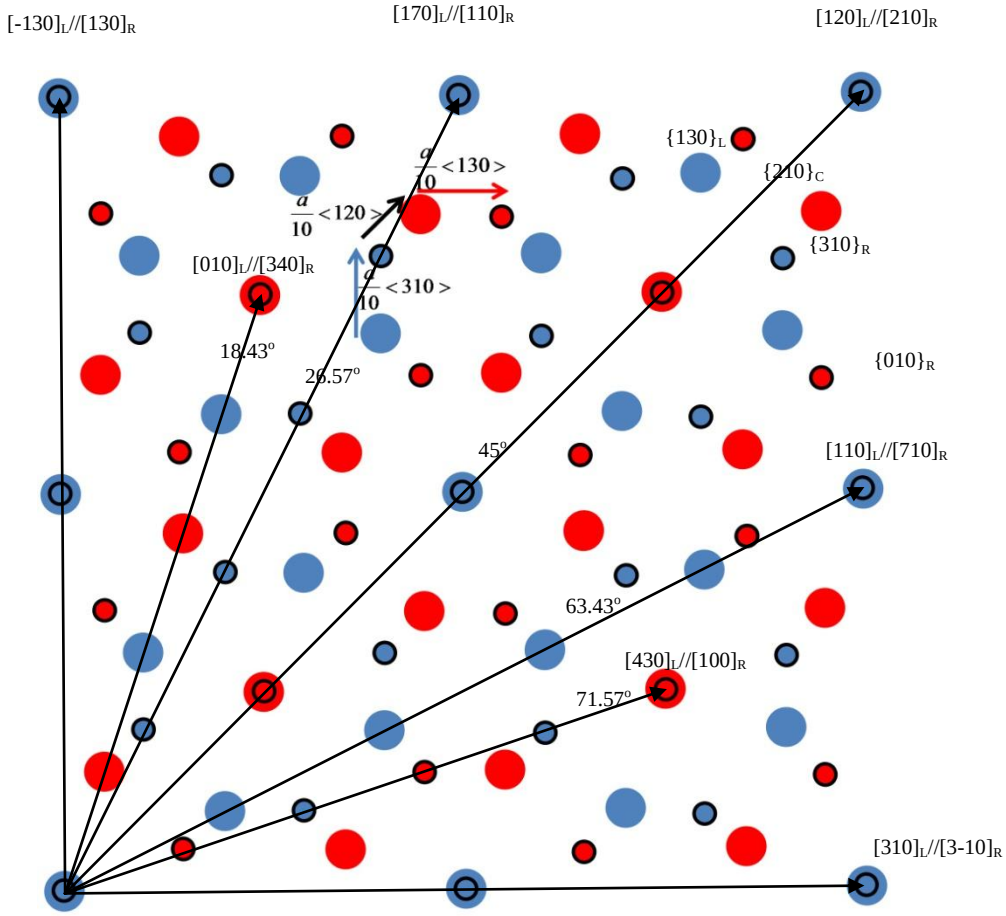

Figure 3. 15 The dichromatic pattern of the bicrystal for GBs with the misorientation relation given by Σ5 tilt grain boundaries in FCC crystals. The two interpenetrating crystals are represented by larger solid cycles for the left grain and smaller outlined cycles for the right grain. The different colours (blue and red) represent rows of atoms with positions in alternating (002) planes. Larger cycles with smaller rings inside are the coincident sites. The grain boundaries are vertical to the paper and the possible positions are along the black arrows. The indicated angles are referred to the vertical {310} grain boundary.

little rotation at the early stage of the shear deformation. With the increasing shear deformation, the GB gradually rotated to the (100) plane of the left grain as expected and a little GB sliding occurred in this stage (Figure 3.13c). With further shear deformation, the downside GB obviously rotated as the upside GB reached the fix

boundary due to the asymmetrical GB motion (Figure 3.13d and e). The shear stress in the bicrystal system kept building up in this process until the downside GB rotated nearly perpendicular to the external shear force (Figure 3.13e). Finally, as the most of the GB reached the fixed boundary, the simulation ended. It should be noted that no dislocation or crack was found through all the process and the deformation mechanisms were only related to the GB coupled motion or sliding.

Above 700K, the response of grain boundary to external shear deformation was basically in the way of viscous grain boundary sliding. This is consistent with that of the Σ5 (210) GB at corresponding temperatures. As shown in Figure 3.14, after a short while of perfect coupling at the early stage at 750K the GB quickly rotated about 18.43^{o} (Figure 3.14a) and the two grains smoothly slid away from each other on the new GB for a while under the shear deformation (Figure 3.14b). Then the GB further rotated to 26.57^{o} (Figure 3.14c) and the grain boundary sliding remained nearly on this new GB until the end of simulation. The relatively stable GB sliding on each GB is completely consistent with the flat stages of the normal stress in Figure 3.10b). This further confirms that the normal stress σ_{xx} was caused by the GB rotation and increased with the rotation. Since the GB rotation above 750K is relatively quick and complete at each stage, the normal stress σ_{xx} curves show flat stages. Subsequently, the shear stress and normal stress were further increased to slide the two grains from each other (Figure 3.14d). At the final stage, they were gradually decreased as the grain boundary area shrank.

It can clearly be seen that the response of the GB to the shear deformation is closely related to the temperature. The temperature directly determines the atom mobility, thereby correspondingly affecting the GB deformation mechanisms including atomic accommodation, shuffling and defects nucleation in the vicinity of the GB. The atom colour in the figures represents the atoms belonging to respective grains. As a result, the effect of temperature on the atom mobility can be clearly observed by the distance of the atoms diffusing away from the initial GB. In the reference of the left grain, this distance increased obviously with the temperature as shown in the Figure 3.11~4.14. Below 550K, the black atoms basically stayed at their initial positions except for a few atoms having moved certain distance through the surfaces. However, above 700K, considerable black atoms had diffused deeply into the right grain after

only 620ps during the shear deformation (Figure 3.14a). Therefore, at lower temperature the shear deformation is incompletely mediated by local atomic accommodation near the GB. Besides, it is readily for lattice defects or cracks to take place to further mediate the shear deformation. However, at higher temperature the shear deformation can be largely mediated by the atomic accommodation or shuffling in several atom layers near the GB. Moreover, at high enough temperature the GB may even present quasi-liquid (viscous) characteristic, causing more mobility of the GB and the corresponding macroscopic plasticity of the materials.

Now, it is worth noting the angles corresponding to respective GBs indicated by the red arrows. Taking a closer look at the curved grain boundaries in Figure 3.12, it can be seen that the rotated grain boundaries are composed of short flat boundaries rather than being smoothly curved. The angles between these flat boundaries and the original grain boundary are the rotation angles and are indicated on the Figure 3.12~3.14. It is worth noting that all the angles are specific and relevant to the tilt angle θ. This means there are relatively favourable positions for the GB rotation. To explain these favourable GB positions, the coincident site lattice (CSL) of FCC Σ5 grain boundaries is illustrated in Figure 3.15. The two grains interpenetrate each other and are represented by larger solid cycles for the left grain and smaller outlined cycles for the right grain. The different colours (blue and red) represent rows of atoms with positions in alternating (002) planes. Thus, the larger cycles with smaller rings inside are the coincident sites. For all CSL symmetrical tilt grain boundaries, a rotation of the grain boundary plane about the tilt axis by 45^o locates the other CSL symmetrical tilt grain boundary in the <100> system [240]. As shown in Figure 3.15, an inclination of the boundary plane by 45^o from the Σ5 (310) symmetrical tilt grain boundary (vertical or horizontal CSL lines) is the Σ5 (210) symmetrical tilt grain boundary (diagonal lines). However, other grain boundaries in between 0^o and 45^o are Σ5 asymmetric tilt grain boundaries for the <100> system. The black arrows along the CSL indicate some of the Σ5 asymmetrical or symmetrical tilt GB boundaries. It can be seen that the corresponding angles are also consistent with the present simulation. Therefore, the short flat boundaries found in the present study are other Σ5 asymmetrical or symmetrical tilt GB boundaries. As there is litter difference of the grain boundary energies among the Al Σ5 tilt grain boundaries, it is readily for

the GB to rotate from one to another one of the Σ5 tilt grain boundaries under external deformation.

To further analyse the dislocation reaction at 550K, minimization procedure was applied to remove the influence of thermal fluctuation on the atomic positions. Figure 3.16 shows the detail of dislocation emission from the grain boundary. The atoms are coloured by the common neighbour analysis (CNA) technique [314]: atoms with FCC structural order are blue, atoms with hcp structural order are light blue and atoms with other structural order are red. In the present case, the grain boundary and dislocations are mainly composed of red atoms with very few light blue atoms. Thus, the two examined dislocations are readily identified as pure edge dislocations with Burgers vectors of [-110]/2 (Figure 3.16a) and [-1-10]/2 (Figure 3.16b) by Burgers circuit method and the black arrows show the move directions. Combined with the observation in Figure 3.16c) where the FCC atoms are removed from the view, it clearly shows that the dislocation line direction is along the [001] tilt axis and the gliding planes are {110} planes. It is known that it is unusual for FCC lattice dislocations to glide on the {110} planes. Therefore, their formation must be ascribed to the reaction of grain boundary dislocations. Grain boundary dislocations are very complicated, as they have very specific Burgers vectors that can only occur in grain boundaries. In the present case, the tilt grain boundaries can be simplified as tilt walls of edge dislocations. They can be represented with dislocations with alternating perfect lattice Burgers vectors b^A and b^B [326]. Even so, the case is still complicated, as the grain boundary rotated to different Σ5 tilt grain boundaries during shear deformation and then the Burger vectors of the gliding grain boundary dislocations were always changed. However, it can be assumed that all the Burger vectors of the gliding grain boundary dislocations are a common variable [x y 0], since all the Burger vectors of the grain boundary dislocations are perpendicular to the tilt axis [001]. Thus, during the shear deformation only the x and y terms of the Burger vectors are affected by the reaction of grain boundary dislocations. When the grain boundary dislocations are converged by the shear deformation to a point in the particular case such as at 550K, it is readily understood that release of the <110>/2 lattice dislocations at the grain boundary to mediate the stress concentration is easiest because of their smallest Burgers vectors. For the consistency, the <110>/2 lattice

dislocations have the [001] line direction and glide on the {110} planes. *Secondly*, the Burgers vector character of the dislocations may be influenced differently depending on the sign of the resolved shear stress. In some cases, the dislocations can be activated only when the resolved shear stress (or Schmid factor) is positive due to the compressive or tensile normal loading was applied, and vice versa. *In addition*, the resolved stress normal to the slip plane, i.e. the non Schmid factor can also play an important role on the nucleation event [3-6]. For instance, the resolved normal stress is tensile in uniaxial tension and compressive in uniaxial compression. Tschopp et al.[6] reported an uncommon full dislocation slipped on {001} plane during the compressive loading was applied perpendicular to the GB plane. By calculating the resolved stress parameters for the {111} and {001} plane, they found that the {001} slip plane has both a higher resolved shear stress in the <110> slip direction and a higher resolved normal stress for some misorientation angles within a certain range. In this study, it is worth noting that an obvious tensile normal stress σ_{xx} was generated during the shear rate was applied, as shown in Figure 3.1, which can have an inevitable influence on this uncommon dislocation generations. Besides, due to the limited calculation ability the bycrystal model was built with a relatively small size, which might make this uncommon <110>/2 lattice dislocations able to steadily slide on {110} planes for some distance after the release from the tilt grain boundaries. It is believed that this uncommon slip system should not be a general fundamental process.

In summary, the full dislocation emission on the {110} plane is most likely due to the combination of the characteristic of grain boundary dislocation, the large resolved shear stress on the {110}<110> slip system and the tensile normal stress on the grain boundary plane. Moreover, a relative slow shear rate was applied in this study, considering the capacity of the current computer, only a simulation model with limited size was adopted, which may also caused this uncommon nucleation event. Some of the potential slip systems (common slip systems with dislocations slip on the {111} planes) may restricted due to the image force caused by the limited model size. A further study with a large size simulation model is necessary to comprehensively investigate the nucleation factors.

Shear response of the Al [001] symmetrical tilting Σ5 (310) grain boundary was simulated by molecular dynamics method with a three dimensional bicrystal at 500~750K. Following conclusions can be drawn:

The response of the grain boundary to the shear deformation is closely related to the temperature. At lower temperature (500~650K), the grain boundary responded to the shear deformation by the combination of grain boundary rotation, grain boundary sliding, grain boundary coupled motion, crack initiation or dislocation release. At higher temperatures (above 700K), after a short while of perfect coupling at the early stage the grain boundary quickly rotated and the two grains smoothly slid away from each other in the way of viscous grain boundary sliding under the shear deformation.

The grain boundary rotated among some of the Σ5 asymmetrical and symmetrical tilt GB boundaries under shear deformation, leading to the normal stress σ_{xx} in the bicrystal system.

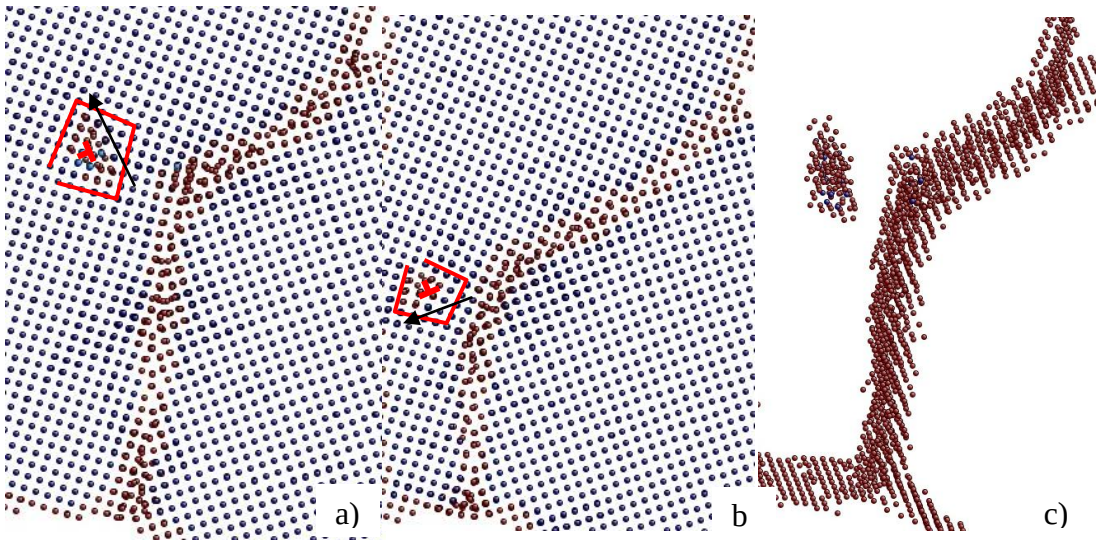

Figure 3.16 Lattice dislocations emitted from the grain boundary with Burgers vectors of a) [-110]/2 at 2014ps, b) [-1-10]/2 at 2451ps and c) dislocation structure of a). The red T indicates the edge characteristics of the lattice dislocations and the black arrows show the move direction of dislocations.

During shear deformation, reaction of the grain boundary dislocations under particular circumstances could release uncommon edge lattice dislocations from the grain boundary. The uncommon edge lattice dislocations with <110>/2 Burgers vectors have the [001] line direction and glide on the {110} planes.

3.3.2 Shear response of the Σ5 (310) GB with normal external force

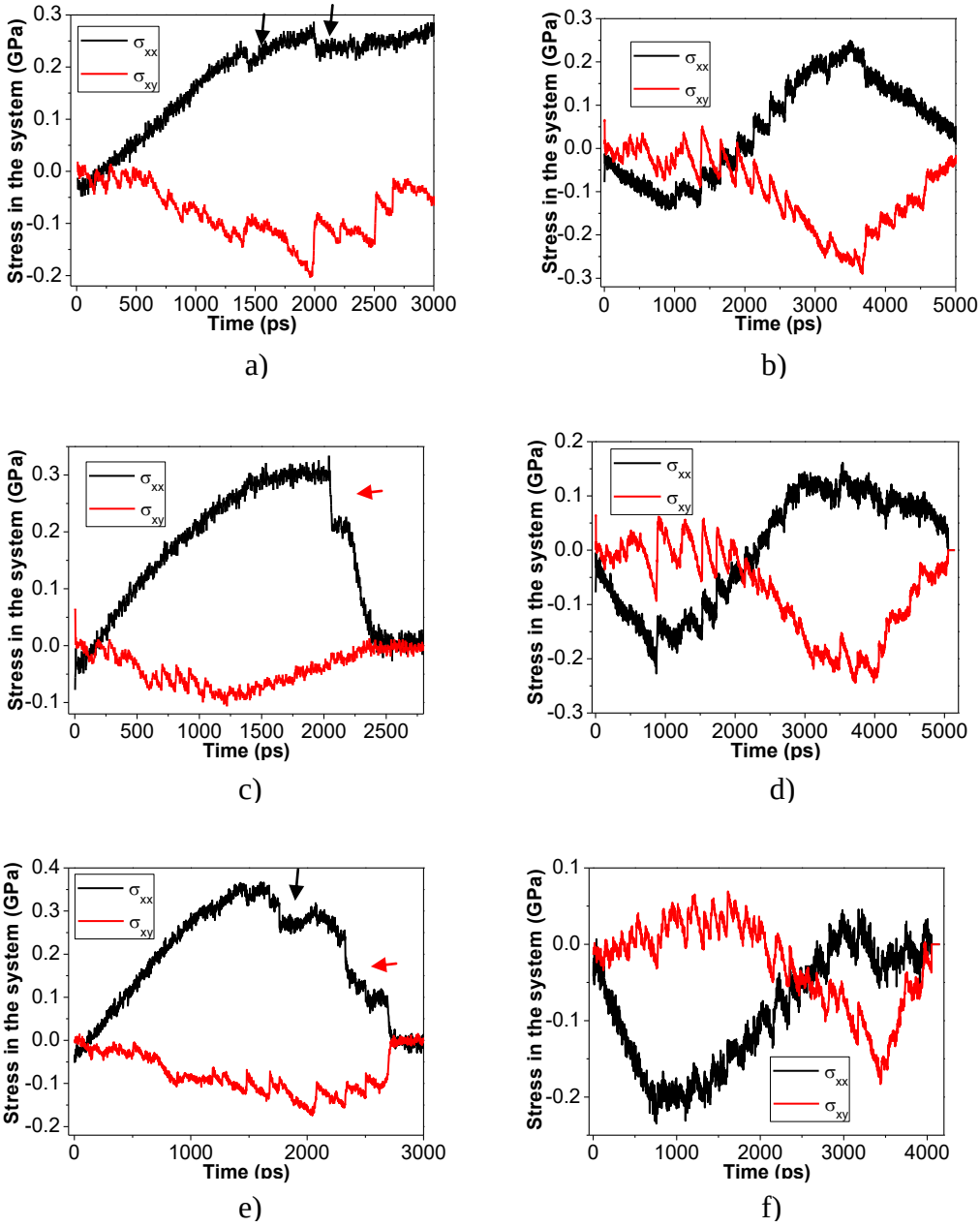

Figure 3.17 Stress evolution versus the time in the bicrystal system with the Σ5 (310) GB at 500K and the same V_y of 0.256m/s: a) V_x=0.051m/s in tension and b) in compression; c) V_x=0.077m/s in tension and d) in compression; e) V_x=0.102m/s in tension and f) in compression. The black arrows indicate the dislocation release, while the red arrows indicated the crack initiation.

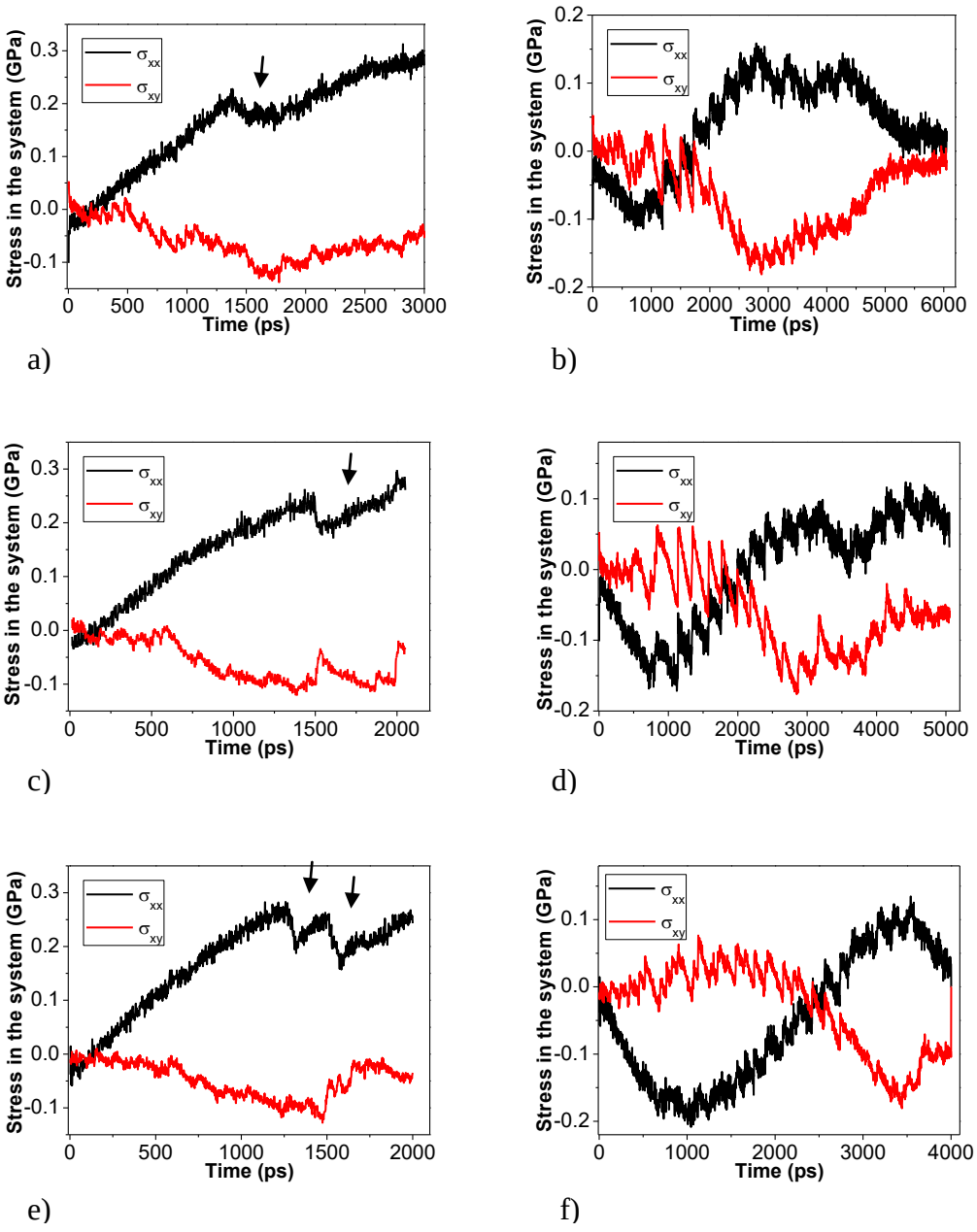

Figure 3.18 Stress evolution versus the time in the bicrystal system with the Σ5 (310) GB at 600K and the same V_y of 0.256m/s: a) V_x=0.051m/s in tension and b) in compression; c) V_x=0.077m/s in tension and d) in compression; e) V_x=0.102m/s in tension and f) in compression. The black arrows indicate the dislocation release, while the red arrows indicated the crack initiation.

To further compare the effect of external force on the GBS behaviour, the bicrystal system was also compressed or stretched perpendicular to the shear direction. As the compression and tension are implemented by the velocity V_x as shown in Figure 3.9, it is equivalent to an angled external force exerting on the initial GB. Figure

3.17~3.19 present the stress evolution in the bicrystal system with different external forces at representative temperatures. Several characteristics can be drawn:

i) The shear stress in the system overall evolved in a similar way with previous observations during shear deformation except that sign of the shear stress inversed at the early stage when V_x was large in compression;

ii) in the case of $V_x < 0$ (in tension), the normal stress along X direction kept increasing in tension until the end of simulations. Alternatively, the stress increased first and then decreased gradually to zero at the end of simulations. The former occurred for all the cases at 600K and for the lowest V_x at 500K, while the latter were found for all the cases at 750K and for the higher V_x at 500K. It should be mentioned that the end of each simulation was determined when the two grains slid away from each other or the grain boundary reached the fixed boundary;

iii) in the case of $V_x > 0$ (in compression), the stress evolution was basically similar at respective conditions. Firstly, the normal stress along X direction increased gradually in compression lineally and smoothly until a peak stress and then it started to decrease. Interestingly, as it decreased to zero in compression, it gradually increased in tension until another peak stress. It should be noted that, between these two stress peaks (compression and tension), the normal stress curves are saw-tooth like and nearly linear. Moreover, at 750K the stress peaks are relatively linear with sharper stress peaks compared to 500K and 600K;

iv) with respect to the temperatures, the magnitude of V_x had certain influence on the stress evolution manners at lower temperatures (500K and 600K), whereas at higher temperature (750K) it showed little influence. However, the shear stress curves at 750K showed obvious saw-tooth feature due to the presence of normal external force, especially in compression. This all indicated the variation of GB shear response to the magnitude of V_x.

The shear response of the Σ5 (310) GB with normal external force was also involved with the GB migration and rotation, dislocation release and crack initiation based on the observation of the atomic configuration evolution. However, GBS process varied with different V_x. Figure 3.20 shows the snapshots at concerned stages during GBS

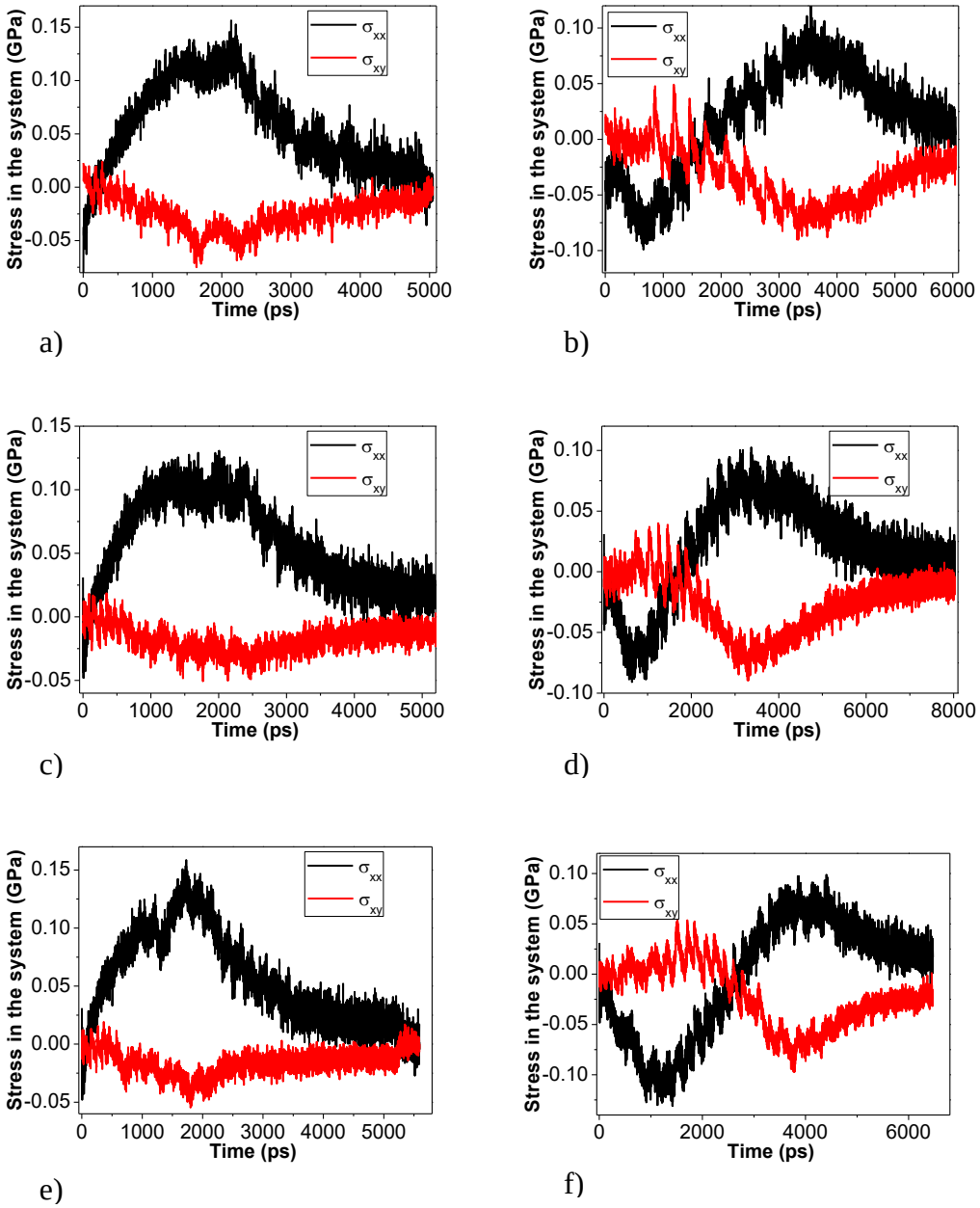

Figure 3.19 Stress evolution versus the time in the bicrystal system with the Σ5 (310) GB at 750K and the same V_y of 0.256m/s: a) V_x=0.051m/s in tension and b) in compression; c) V_x=0.077m/s in tension and d) in compression; e) V_x=0.102m/s in tension and f) in compression.

of the Σ5 (310) at 500K with V_x=0.051m/s in tension. Besides, the GB migration and rotation and dislocation release were found consistent with previous observations. Moreover, the dislocation release was found responsible for the moderate drops of the normal stress along X direction as shown in Figure 3.17 and 3.18 and indicated by black arrows. Compared to the case without normal external force at 500K

(Figure 3.11), however, the GB migration was influenced by the normal external force. This made the GB migrate relatively soon to the fixed boundary before the separation of two grains. Therefore, the normal stress along X direction kept increasing in tension until the end of simulations as shown in Figure 3.17 and 3.18.

On the other hand, when increasing the V_x at 500K, the normal stress along X direction finally decreased to zero at the end of simulations as shown in Figure 3.17. Figure 3.21 shows the snapshots at concerned stages during GBS of the Σ5 (310) at 500K with V_x=0.102m/s in tension. It can be seen that after several dislocations release from the GB a crack initiated from the GB and with further shear deformation the crack propagated along the GB. Therefore, the normal stress along X direction finally decreased to zero at the end of simulation. It should also be noted that while the dislocation release corresponds to the moderate drop of the normal stress along X direction, the crack initiation is associated with the relatively large drop of the normal stress (indicated by red arrows in Figure 3.17). In the cases of $V_x > 0$ (in compression), the GBS behaviour was insignificantly affected by the magnitude of V_x. Figure 3.22 shows the snapshots at concerned stages during GBS of the Σ5 (310) at 500K with V_x=0.051m/s in compression. At the first stage (before ~1000ps), the GB migration and rotation took place slightly (Figure 3.22a). Therefore, the corresponding normal stress curve in Figure 3.17b) is basically linear. Next, the GB gradually rotated 26.57^o clockwise as shown in Figure 3.22b) and then most GB sliding and certain migration proceeded on this new GB. In this process, dislocations were nucleated on the GB and released into the crystal. Importantly, the dislocations only nucleated on the GB when the normal stress along X direction became in tension. At the last stage, a crack was initiated at the GB and the normal stress along X direction decreased until the separation of the two grains. Figure 3.22b) shows the crack propagating along the grain boundary.

At 600K, the effect of the normal external force exerted by the V_x on the GBS behaviour of the Σ5 (310) is basically consistent with that at 500K. However, except GB migration, rotation and dislocation release etc, it was found at 600K that the large tensile normal external force led to different direction of the GB migration. Figure 3.23 shows the snapshots at concerned stages during GBS of the Σ5 (310) at 600K with different V_x in tension. It clearly shows the different direction of the GB

migration. This is due to the duality of the coupling behaviour as mentioned previously [234, 235].

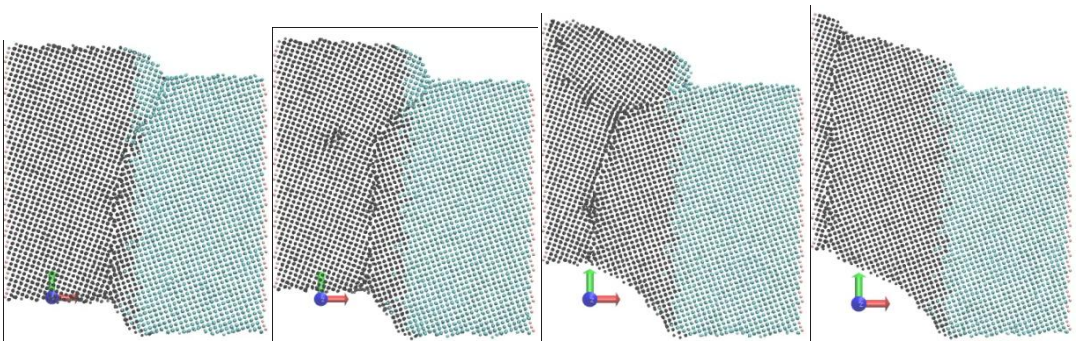

Figure 3.20 Snapshots at concerned stages during GBS of the Σ5 (310) at 500K with V_x=0.051m/s in tension: a) 1050ps, b) 1430ps, c) 1350ps, d) 2020ps.

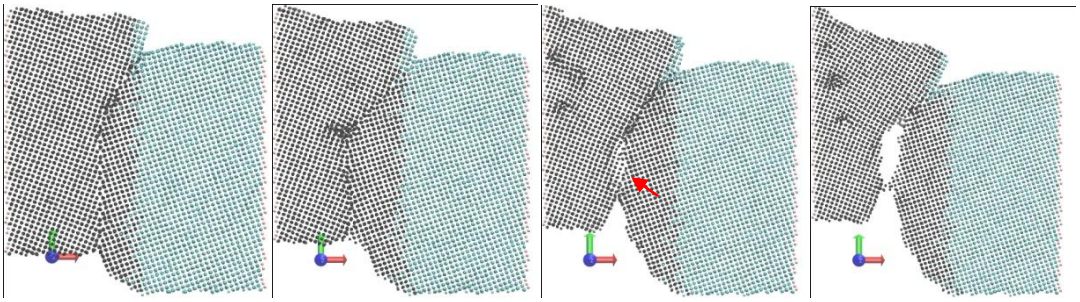

Figure 3.21 Snapshots at concerned stages during GBS of the Σ5 (310) at 500K with V_x=0.102m/s in tension: a) 1190ps, b) 1670ps, c) 2260ps and d) 2650ps. The black arrows indicate the crack initiation. The red arrow indicates the crack initiation.

At 750K, the effect of normal external force exerted by the negative V_x (in tension) on the GBS behaviour of the Σ5 (310) is relatively unobvious. The evolution of atomic configuration during shear deformation is similar to that without the normal external force as shown in Figure 3.14. However, the effect of normal external force exerted by the positive V_x (in compression) on the GBS behaviour is outstanding and the stress evolution is consistent with those at 500K and 600K. Figure 3.24 shows the representative atomic configurations during GBS of the Σ5 (310) at 750K with plus-minus V_x of 0.051m/s. It can be seen that due to the high temperature no dislocation or crack formed during the shear deformation. Besides, the two grains gradually slid from each other with certain GB rotation and migration. It is also worth noting that

the compressive normal external force obviously increased the GB migration at 750K, which might result from the coupling effect. Thus, the saw-tooth characteristic of the stress curve at such high temperature (Figure 3.19) can be readily understood.

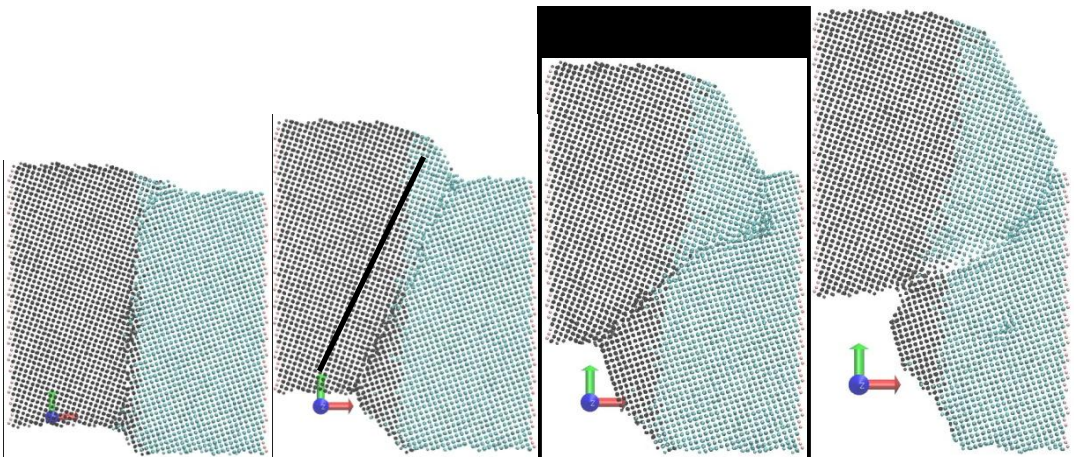

Figure 3.22 Snapshots at concerned stages during GBS of the Σ5 (310) at 500K with V_x=0.051m/s in compression: a) 892ps, b) 1750ps, c) 3160ps and d) 4330ps.

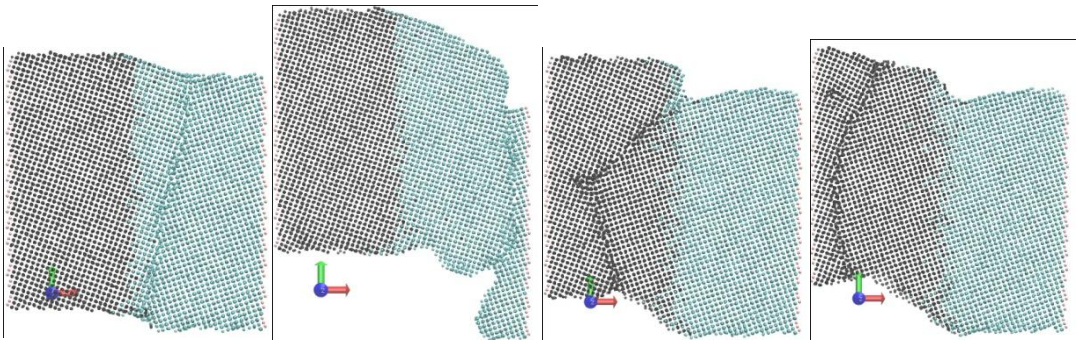

Figure 3.23 Snapshots at concerned stages during GBS of the Σ5 (310) at 600K with different V_x in tension: a) 740ps and b) 3050ps for V_x=0.0511691m/s; c) 1308ps and d) 1630ps for V_x=0.102m/s.

In summary, both the magnitude and direction of the normal force play a significant role in the general GB sliding behaviour of the symmetrical grain boundaries. Importantly, two points should be emphasized: one is that the normal force can affect the coupling behaviour which may provide potential flexibility of the grain boundary mediated plastic deformation, and the other one is that the dislocations only nucleate on the GB when the normal stress state on the grain boundary is in tension. A possible explanation for this effect is related to the normal stress component's dependence on the ideal shear strength by Ogata and Tschopp [327, 328], who have

shown that compressive stress components acting normal to the slip plane (non-Schmid stresses) can affect the critical resolved shear stress. It is well know that general dislocation nucleation is closely related to Schmid factors and the critical resolve shear stress. It is also shown in some circumstance that the stress required for dislocation nucleation does not directly correspond to the Schmid factors [329]. For the uncommon slip system <110>{110} in this study, the Schmid factors would be more complicated than the usual. Besides, the generalized stacking fault energy (GSF) curve which is closely related the energy barrier of dislocation nucleation[7], was introduced here to highlight the effect of stress state on the nucleation event. The GSF curve includes both stable stacking fault energy (γ_{sf}) and unstable stacking fault energy (γ_{usf}). Previous studies have shown that the preloading strain or stress on crystal structures can significantly influence the GSF curve. For instance, Zimmerman et al.[8] observed that the unrelaxed γ_{usf} value of 175 mJ/m^2 was reduced to 99 mJ/m^2 after biaxially stretch the lattice by 4% when calculating the GSF curve of Cu. Tschopp et al.[5] used MD simulations to investigate the influence of normal stress on the GSF curve in Cu, they found that the compressive (tensile) normal stress increases (decreases) the unstable stacking fault energy γ_{usf}, while the stable stacking fault energy γ_{sf} changes in an opposite manner. In addition, the stress influence on GSF curve is not only limited in the normal direction of the slip plane, lateral stress can also influence the value of generalized stacking fault energy. Ogata et al.[3] used DFT calculation of stacking fault energy for Al and Cu to study their ideal shear strength. The results indicated that the hydrostatic pressure has a significant effect on the critical resolved shear stress at the atomic scale. Our earlier simulation[9] showed that the calculated stacking fault energy (γ_{sf}) of Al decreased gradually with the increased preloading tensile stress applied perpendicular to the slip plane, which indicates that the nucleation barrier has decreased and the dislocation nucleation becomes easier. The preloaded compressive stress has seen an opposite effect.

Therefore, it is believed that the tensile normal stress component should increase the critical resolved shear stress for the unusual dislocation nucleation in this study. However, because the actual stress state is a complicated triaxial condition and given that the slip system is uncommon for <110>{110} in this study, one cannot ascertain

its real effect without an accurate stress analysis. Therefore, further study like ab initio calculations for the triaxial condition of the stress state near nucleation site will be carried on following the current PhD work to explain this phenomenon.

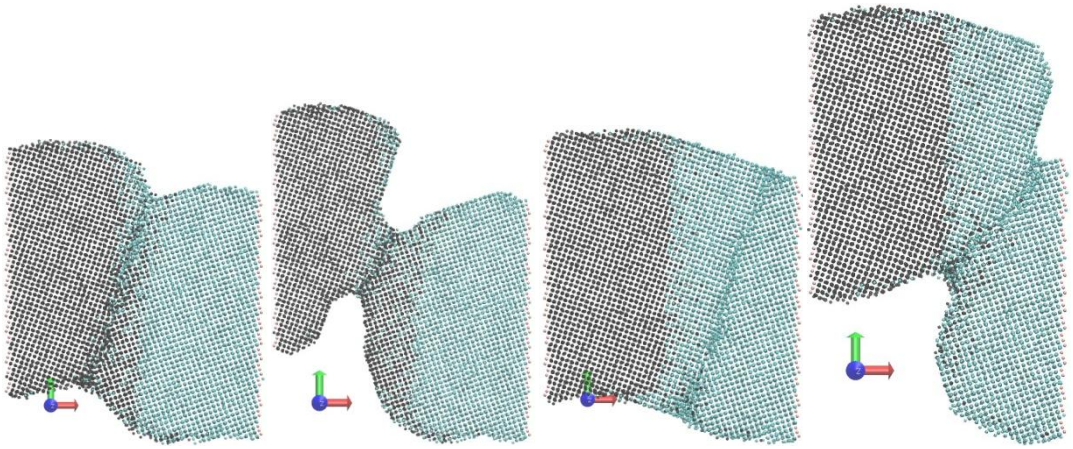

Figure 3.24 Snapshots at concerned stages during GBS of the Σ5 (310) at 750K with V_x=0.051m/s: a) 1450ps and b) 3050ps in tension; c) 1320ps and d) 4050ps in compression.

3.4 Grain Boundary Sliding for Asymmetrical Tilting Grain Boundaries

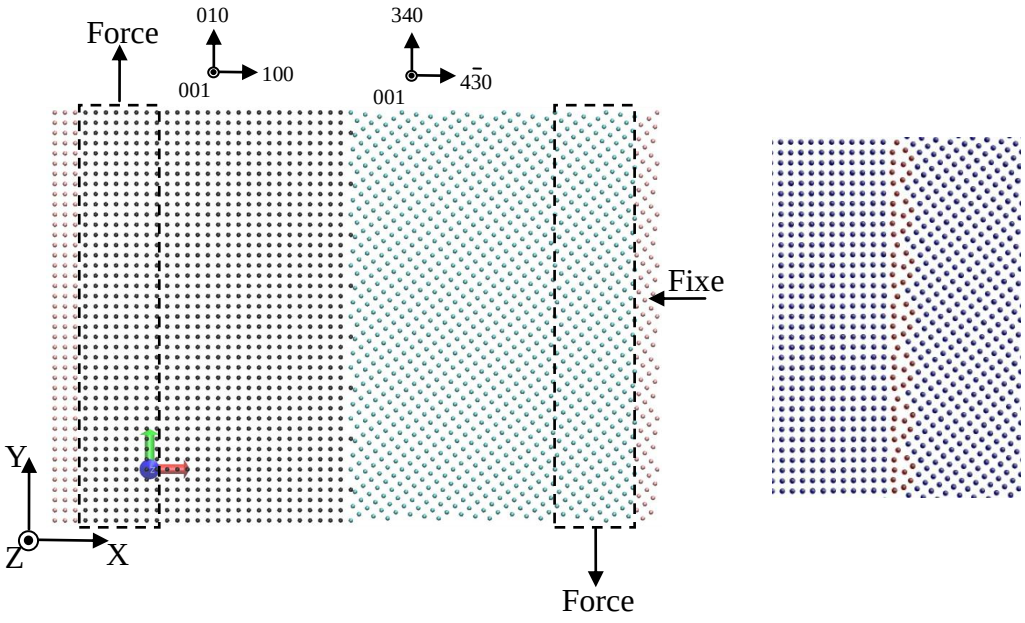

Figure 3.25 Geometry of the bicrystal grain boundary sliding model with the asymetrical Σ5 (100)//(430) tilt grain boundary constructed in the present work. The crystallographic orientations of the bicrystal are indicated respectively. The right insert shows the grain

boundary structure coloured by the common neighbour analysis (CNA) technique after energy minimization, where blue indicates FCC structure and red for irregular structure. The grain boundary sliding was driven by constant forces. (3280 atoms in left move group, 3240 atoms in the right)

It is known that most grain boundaries are asymmetrical in real polycrystalline materials. Asymmetrical boundaries have also been studied but not as extensively as symmetrical ones [212]. It can be seen in the previous sections that during the shear deformation the Σ5 symmetrical grain boundaries always rotated to their corresponding asymmetrical ones due to asymmetrical grain boundary migration and the unconstrained free surface in Y direction. After the grain boundary rotation, moreover, the grain boundary migration, sliding or coupling behaviours were obviously changed in each condition. Therefore, in this section, one of the asymmetrical Σ5 grain boundaries, Σ5 (100)/(430), was used in the grain boundary sliding model to see the possible differences that may occur. The asymmetrical Σ5 (100)/(430) was selected because of the following two reasons. First, it guarantees the misorientation angle (36.87^{o}) between the two grains same as those for the two corresponding symmetrical tilt grain boundaries Σ5 (210) and Σ5 (310) (due to the four fold crystal symmetry around the [001] tilt axis the maxim misorientation angle in [001] tilt grain boundaries is 45^{o}, so the actual misorientation angle for the symmetrical Σ5 (210) grain boundary is also 36.87^{o}). Especially, it was found most frequently in the previous sections.

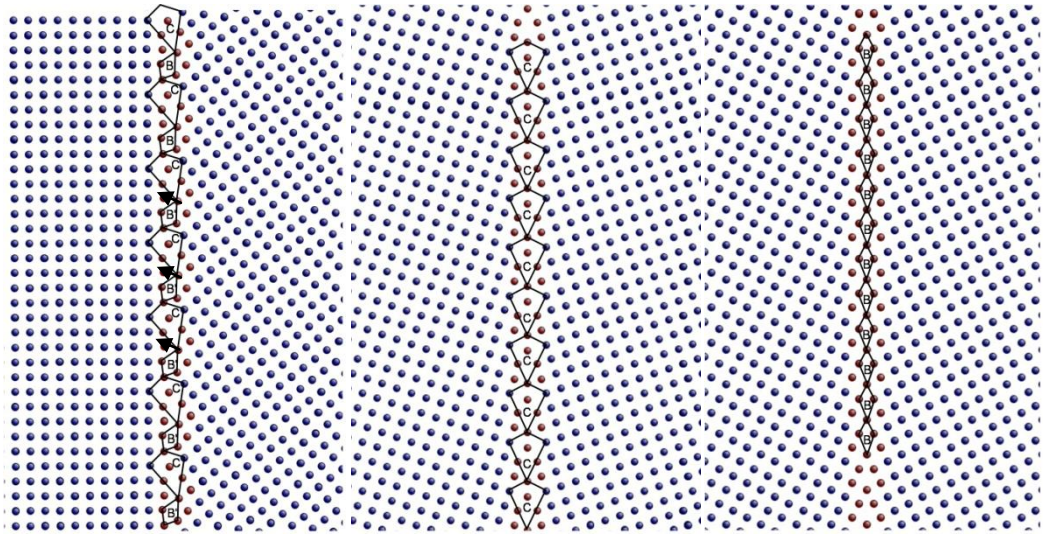

Figure 3.26 a) The asymmetrical Σ5 (100)//(430) tilt grain boundary structure with inclination angle of 18.43^{o} and the two corresponding Σ5 [001] symmetrical tilt grain boundary structures b) Σ5(310) and c) Σ5(210) in Al. The structures are viewed along the [100] tilt axis. The black arrows in a) indicate the facets formed by the structure units (C and B') of one period of the two corresponding symmetrical grain boundaries.

Figure 3.25 shows the geometry of the bicrystal model which has a dimension of $119.66 \times 80.91 \times 40.45 Å^3$ in $X \times Y \times Z$ and contains 24070 atoms. The boundary conditions are completely the same as the previous one shown in Figure 3.1a): periodic boundary condition was applied in the Z-direction which is parallel to the tilt axis and the GB plane, while in the Y-direction the free boundary condition was applied. Three layers of atoms at each side of the border in the x direction were conditionally fixed to be only able to move in the Y-Z plane. In the present case, however, it was very hard to keep the same quantity of atoms in the force zones adjacent to each side of the border atoms in such a small system. This is due to the asymmetrical orientations of the two grains. After the optimum grouping, there are 3280 atoms in the left force zone and 3240 atoms in the right counterpart, making the difference only about 1 percent. The applied force is in the same range of 0.002~0.006eV/Å on each atom. Therefore, the corresponding shear stresses imposed on the initial grain boundary were 1.32×10^{-2} GPa, 2.64×10^{-2} GPa and 3.95×10^{-2} GPa respectively.

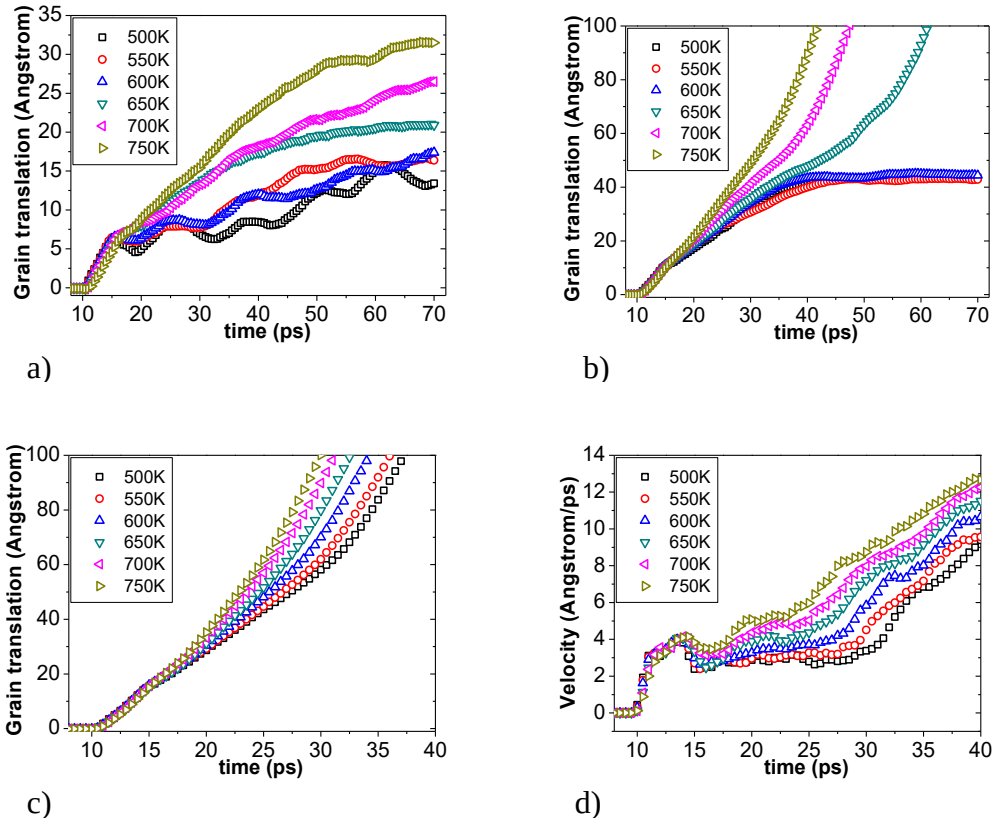

Figure 3.27 Grain translations as a function of time under different applied forces and temperatures with the asymetrical Σ5 (100)//(430) tilt grain boundary: a) 0.002eV/Å, b) 0.004eV/Å, c) 0.006eV/Å and d) grain boundary sliding velocity as a function of time under the applied force of 0.006eV/Å at different temperatures.

It should be noted that Figure 3.25 does not show the actual asymmetrical Σ5 (100)/(430) grain boundary structure but the initial atomic configuration. The actual asymmetrical Σ5 (100)/(430) grain boundary structure was obtained by energy minimization as shown in Figure 3.26a) which is consistent with previous studies [240]. Before explaining the asymmetrical Σ5 (100)/(430) grain boundary structure, it is necessary to simply introduce the concept of structure units. There is a definitive relationship to connect various tilt grain boundaries (both symmetrical and asymmetrical ones) with specific grain boundary structure units. First, each of the symmetrical tilt grain boundaries has a different grain boundary structure, which can be characterized by structural units [241]. Then, grain boundaries with certain disorientations angles correspond to “favoured” structural units, while all other grain boundaries consist of a combination of the structural units from the two surrounding favoured boundaries [240, 241, 247]. Many favoured boundaries correspond to low-

order coincidence site lattice (CSL) systems. In the present work, the favoured boundaries of Σ5 family for <100> tilt system are the symmetrical tilt grain boundary Σ5 (310) with the structural unit of C (Figure 3.26b) and the symmetrical tilt grain boundary Σ5 (210) with the structural unit of B'(Figure 3.26c) [240]. Tschopp et al.'s model has shown that if the ATGB ideally facets in its symmetric counterparts, the ATGB grain boundary period can be decomposed into the boundary periods of the two symmetric boundaries. The aim is to find the relative occurrence of the structural units of each STGB, similar to how STGBs can be decomposed into the structural units of favoured boundaries [238]. It can be seen in Figure 3.26 that the Σ5 (100)/(430) asymmetrical grain boundary are composed of facets with the structural units of the corresponding symmetrical ones and each facet also consists of the structure units of one period of the symmetrical grain boundaries .

Figure 3.27 shows the effect of applied force and temperature on the grain boundary sliding behaviour of the Σ5 (100)/(430) asymmetrical grain boundary. It can be seen that the shear response of the Σ5 (100)/(430) asymmetrical grain boundary under the constant shear force was similar to that of the Σ5 (210) symmetrical grain boundary: the two grains slid away from each other at certain distance which was increased with the increasing temperature, and then stopped sliding by oscillating around the balanced position at the force of 0.002eV/Å; for 0.004eV/Å, the GBS behaviour below 600K was similar to that for 0.002eV/Å, whereas the final sliding distances were larger than those at the same temperatures for 0.002eV/Å. Above 650K, two grains slid away completely from each other and the sooner the higher temperature;

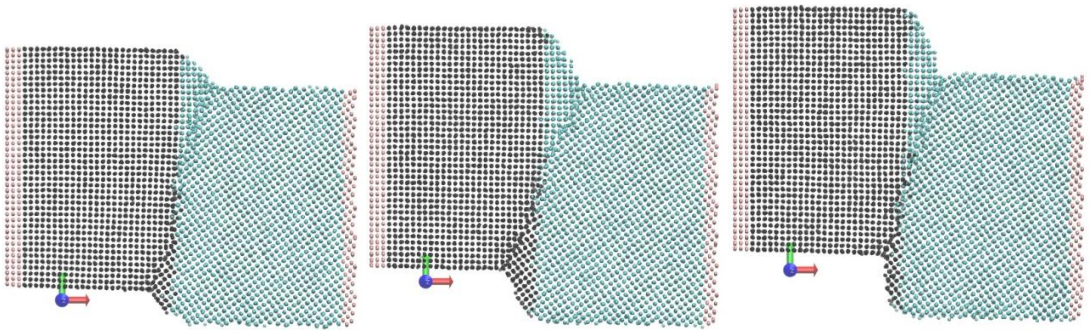

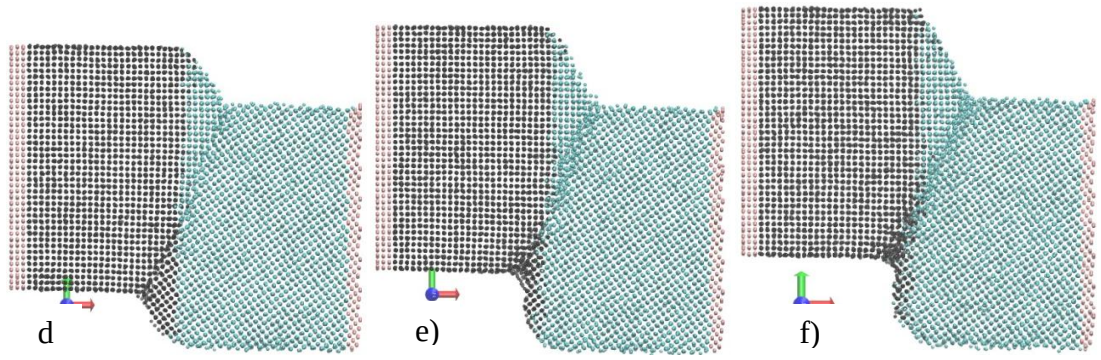

Figure 3.28 Snapshots at the near end of simulation at different temperatures under the applied force of 0.002eV/Å for the Σ5 (100)/(430) asymmetrical grain boundary: a) 500K, b) 550K, c) 600K, d) 650K, e) 700K and e) 750K.

as the force went up to 0.006eV/Å, two grains slid away completely from each other at all temperatures. Moreover, the pattern of sliding velocity versus simulation time was also consistent with previous results for the Σ5 (210) symmetrical grain boundary. In the present case, however, it is worth noting that the actual shear stresses imposed on the initial grain boundary are almost half the magnitudes of those imposed on the Σ5 (210) symmetrical grain boundary. For the Σ5 (210) symmetrical grain boundary the actual shear stress of 5.36×10^{-5} GPa led the two grains to complete separation only above 600K, while for the Σ5 (100)/(430) asymmetrical grain boundary the actual shear stress of mere 3.95×10^{-5} GPa already resulted in complete separation of the two grains at current entire temperature range. It demonstrates that the grain boundary sliding resistance to applied shear force of the asymmetrical grain boundaries is obviously smaller than that of the symmetrical ones. This means the grain boundary sliding resistance is increased with the coherency of grain boundaries, and extra shear stress is required to break this grain boundary symmetry. It is also worth noting that at low temperature and with small applied force the grain boundary sliding distance was increased in a fluctuant way (Figure 3.27 a). This indicates the grain boundary sliding process was not continuous in this condition.

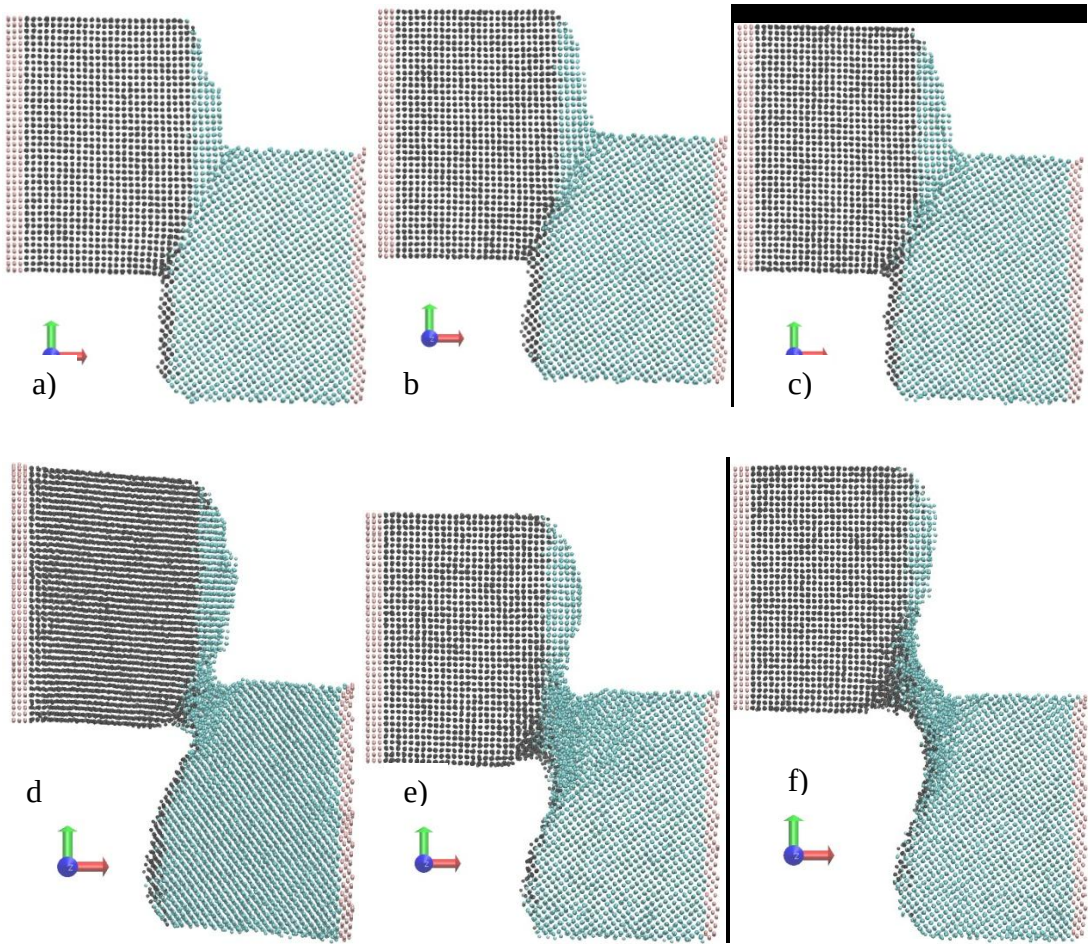

Figure 3.29 Snapshots at the near end of simulation at different temperatures under the applied force of 0.004eV/Å for the Σ5 (100)/(430) asymmetrical grain boundary: a) 500K, b) 550K, c) 600K, d) 650K, e) 700K and e) 750K.

To reveal the details, snapshots at the near end of simulation at different temperatures and applied forces are shown in Figure 3.28~3.30. It can be seen that the grain boundary rotation also took place more or less during shear deformation and was increased with both the simulation time and temperature. Therefore, relatively larger grain boundary rotation resulted from the longer simulation time in the cases of low applied force and high temperature or high applied force and low temperature. Besides, the largest rotation angle was found to be about 27^{o} in the present case. This indicates that the grain boundary rotated to the position around the Σ5 (210) symmetrical grain boundary according to the Figure 3.15 and kept basically steady. It is consistent with previous results that the grain boundary rotation responded to the shear deformation and also resulted in gliding resistance. Moreover, due to the relatively large shear force required for the Σ5 (210) symmetrical grain

boundary to slide, the grain boundary finally rotated and stopped around this position. However, it should be noted that in this condition the actual grain boundary has much lower coherency that the ideal Σ5 (210) symmetrical grain boundary especially at high temperature. As shown in Figure 3.28, the grain boundary rotation was not completed at low temperatures due to the slowly atomic accommodation. Then, the wavy pattern of the translation distance-time curves at low temperatures in Figure 3.27 a) can be understood by the locally slow grain boundary rotation. The rest of the results are consistent with previous simulation in the present study.

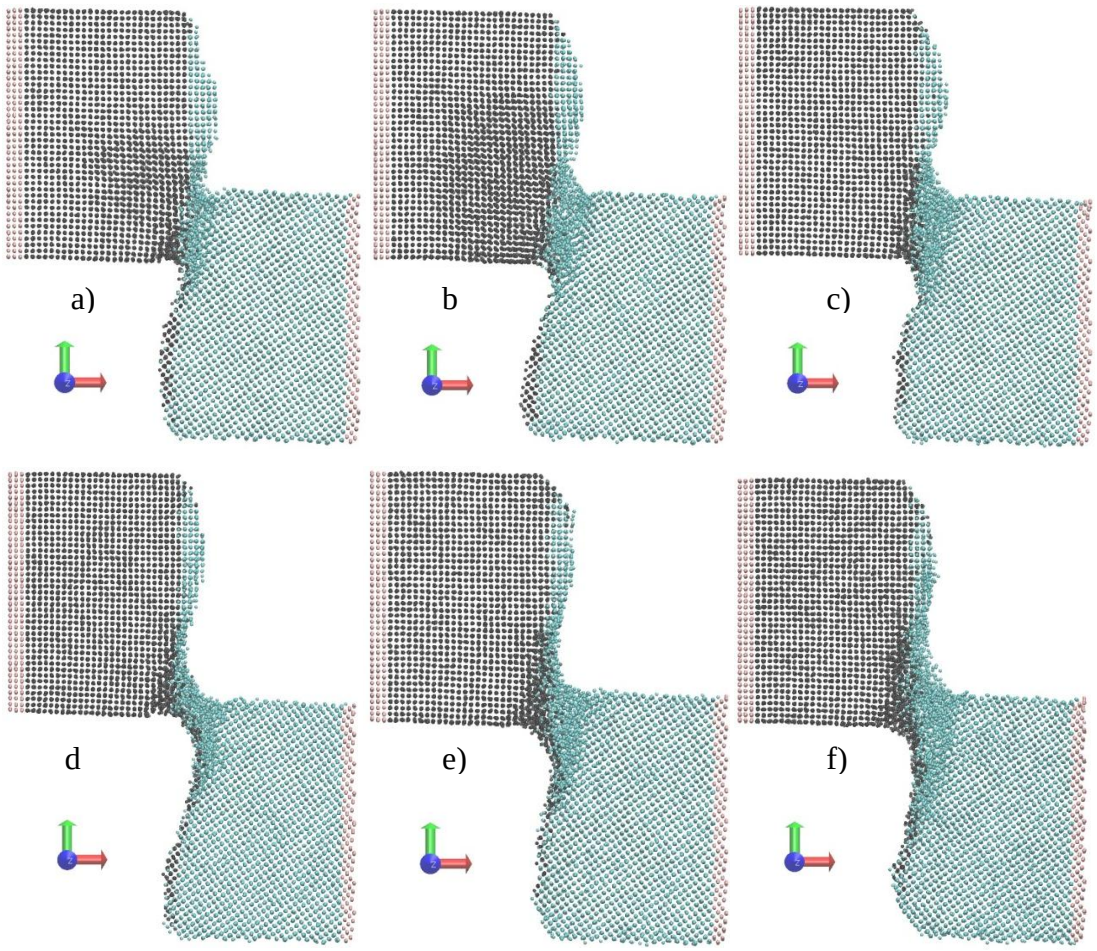

Figure 3.30 Snapshots at the near end of simulation at different temperatures under the applied force of 0.006eV/Å for the Σ5 (100)/(430) asymmetrical grain boundary: a) 500K, b) 550K, c) 600K, d) 650K, e) 700K and e) 750K.

3.5 Grain boundary sliding along tilt axis

It can be seen from previous results that the grain boundary always rotated around the [001] tilt axis during shear deformation. As discussed above, the tilt grain

boundaries can be simplified as tilt walls of edge dislocations which are along the [001] tilt axis and can be represented by dislocations with alternating perfect lattice Burgers vectors b^A and b^B [326]. It should be noted that the Burgers vectors of these edge grain boundary dislocations are all perpendicular to the [001] tilt axis. Therefore, the applied shear force that is also perpendicular to the [001] tilt axis will make the grain boundary dislocations glide on the planes with the same zone axis [001]. This results in the grain boundary motion (migration, coupled shear motion or rotation). To further investigate the grain boundary response to the shear deformation, in this section the shear force was implemented on the same symmetrical Σ5 (210) and asymmetrical Σ5 (100)/(430) tilt grain boundaries but along the [001] tilt axis.

Figure 3.31 shows the geometry of the bicrystal model with shear force along the [001] tilt axis. For the symmetrical Σ5 (210) tilt grain boundary the model has a dimension of $97.6914 \times 56.63378 \times 54.273 Å^3$ in $X \times Y \times Z$ and contains 18764 atoms (Figure 3.31 a). Meanwhile, for the asymmetrical Σ5 (100)/(430) tilt grain boundary the model has a dimension of $119.656415 \times 80.9054 \times 40.4527 Å^3$ in $X \times Y \times Z$ and contains 24354 atoms. The boundary conditions are also completely the same as the previous ones. For the symmetrical Σ5 (210) tilt grain boundary, the atoms in the two moving groups adjacent to each side of the border atoms are the same as 3814 atoms. The applied force is also in the range of 0.002~0.006eV/Å on each atom. Correspondingly, the shear stresses imposed on the initial grain boundary were 1.32×10^{-2} GPa, 2.645×10^{-2} GPa and 3.97×10^{-2} GPa respectively. For the asymmetrical Σ5 (100)/(430) tilt grain boundary, there are 3280 atoms in the left force zone and 3320 atoms in the right counterpart. With the same applied force of 0.002~0.006eV/Å on each atom, the corresponding shear stresses imposed on the initial grain boundary were 1.32×10^{-2} GPa, 2.64×10^{-2} GPa and 3.95×10^{-2} GPa respectively.

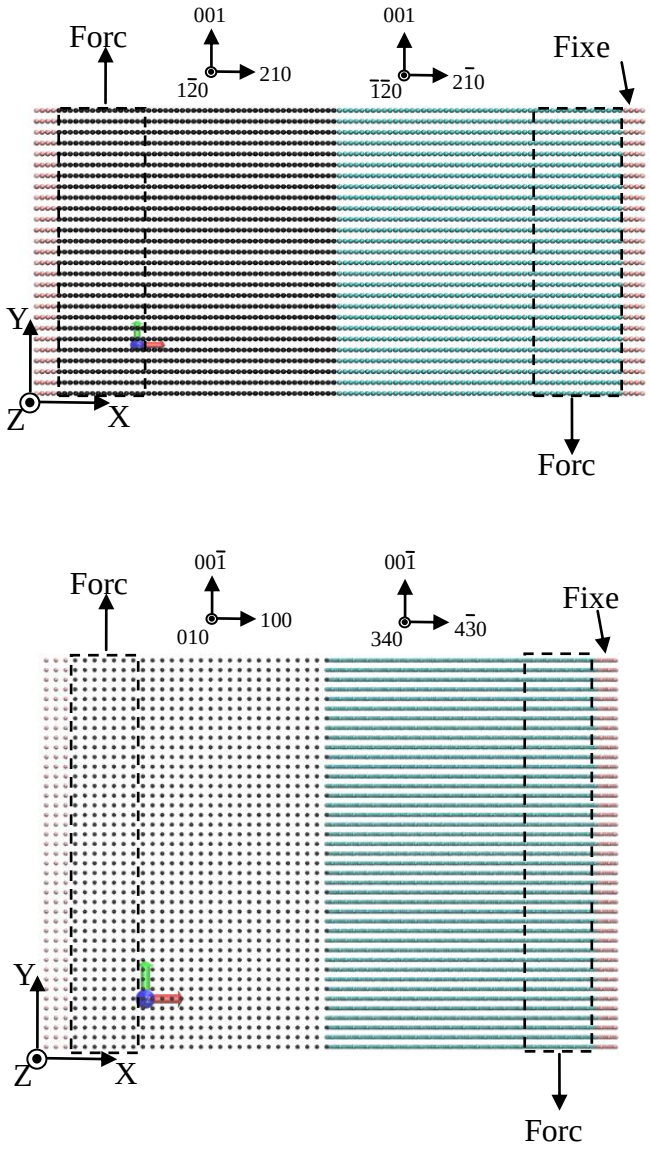

Figure 3.31 Geometry of the bicrystal grain boundary sliding model with shear force along the [001] tilt axis: a) the symmetrical Σ5 (210) tilt grain boundary and b) the asymmetrical Σ5 (100)/(430) tilt grain boundary. The crystallographic orientations of the bicrystal are indicated respectively. The grain boundary sliding was driven by constant forces.

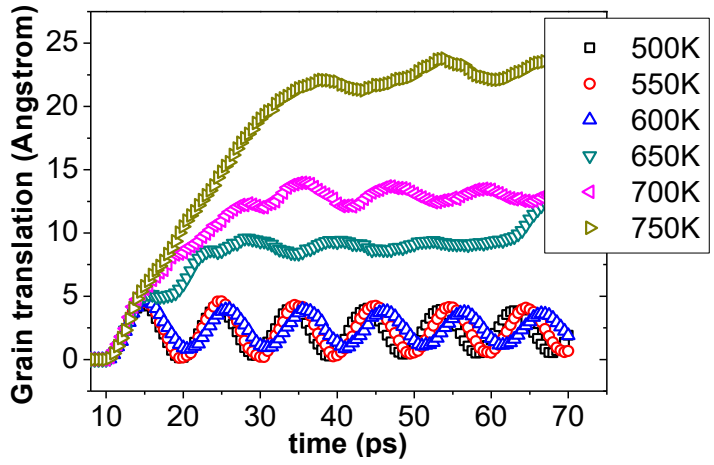

a)

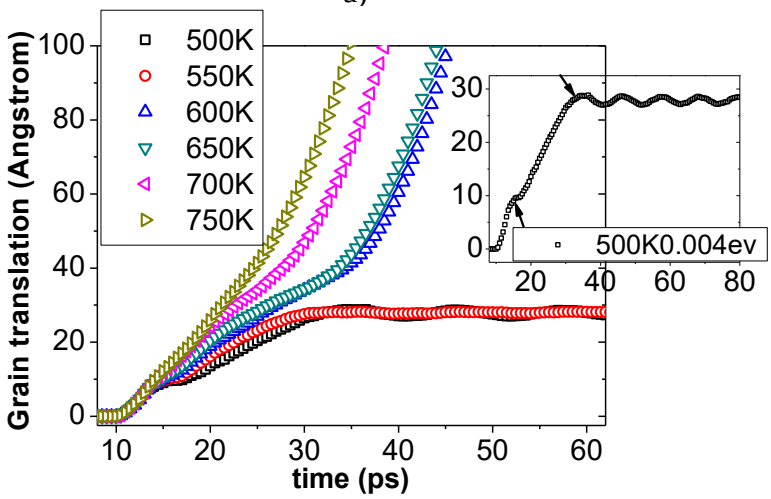

b)

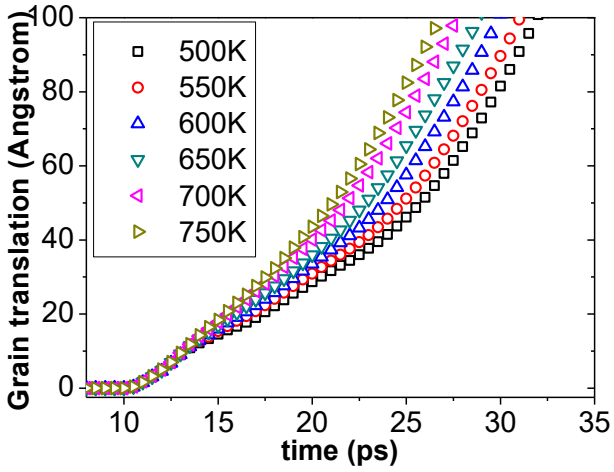

c)

Figure 3.32 Grain translations as a function of time under different applied forces and temperatures for the symmetrical Σ5 (210) tilt grain boundary with shear force along the [001] tilt axis: a) 0.002eV/Å, b) 0.004eV/Å and c) 0.006eV/Å.

Figure 3.32 shows the dependence of grain boundary translation on different applied forces and temperatures for the Σ5 (210) symmetrical grain boundary with shear force along the [001] tilt axis. Generally, the grain boundary sliding behaviour in the present case is consistent with previous results: the grain boundary translation displacement and speed were increased with the temperature and applied shear force. However, it is worth noting the typical sine characteristic of the grain translation versus simulation time curves for low applied force and low temperatures, which has not been found in the previous results. It indicates that when the applied shear force is smaller enough than a critical value, the relative displacement of the two grains and the simulation time are subjected to the characteristic of simple harmonic oscillation. It is also believed that this critical value should be decreased with the increasing temperature. Figure 3.33a) shows the atomic configuration simulated 15ps at 500K with the applied force 0.002eV/Å, which is corresponding to the peak amplitude of the grain boundary translation versus simulation time curve. It can be seen that the bicrystal system has been deformed to some extent by the shear force, but the shear force is still not large enough (larger than a critical value) to activate any grain boundary motion and other lattice defects. This means the shear deformation is still in the elastic domain. In this case, it is similar with that a torque is imposed by the applied shear force on the bicrystal system which acts as an elastic entity. Therefore, the relative movement of the two grains (Y) can be described with the simple harmonic oscillation formula as:

$$Y = A\cos(\omega t - \varphi) \qquad (3\text{-}1)$$

where A stands for the peak amplitude, ω is the angular frequency and the phase φ is related to the initial position. The ω can be described as $(k/m)^{1/2}$, where m is the inertial mass of the system and k is the spring constant which should be the shear elastic constant here and should be decreased with increasing the temperature. Therefore, the ω is inversely proportional to the temperature, which can be confirmed by Figure 3.32 a) where the period ($2\pi/\omega$) of the curves is obviously increased with the increasing temperature. On the other hand, other than the general elastic entity, the atomic friction in the present case can result in certain damping effect which gradually reduced the amplitude as shown in Figure 3.32 a).

With the increasing temperature, as the critical stress was decreased to smaller than the applied shear force, the grain boundary motion took place. It can be seen in Figure 3.32b) that part of the grain boundary has been rotated to some extent after 70ps at 650K with the applied force 0.002eV/Å due to the asymmetrical grain boundary migration. As discussed previously, this grain boundary rotation can cause certain shear resistance to counteract the applied shear force, thereby slowing down or even stopping the grain boundary sliding process. Due to the relatively low temperature and shear force, the grain boundary rotation proceeded slowly and was partially completed within the simulation time. With longer simulation time, the grain boundary rotation still proceeded, but with extremely low speed. The wavy pattern of the translation distance-time curves in the present case (Figure 3.32a) was also caused by the local slowly grain boundary accommodation and rotation. In contrast, at 750K, the grain boundary was basically rotated to another crystallographic plane within the simulation time (Figure 3.32c) and kept relatively stable. This new metastable grain boundary plane will be discussed later. It can also be seen in (Figure 3.32a) that the corresponding translation distance-time curve is relatively smoother than those at lower temperatures. Likewise, the applied shear force is still not large enough to activate further shear deformation.

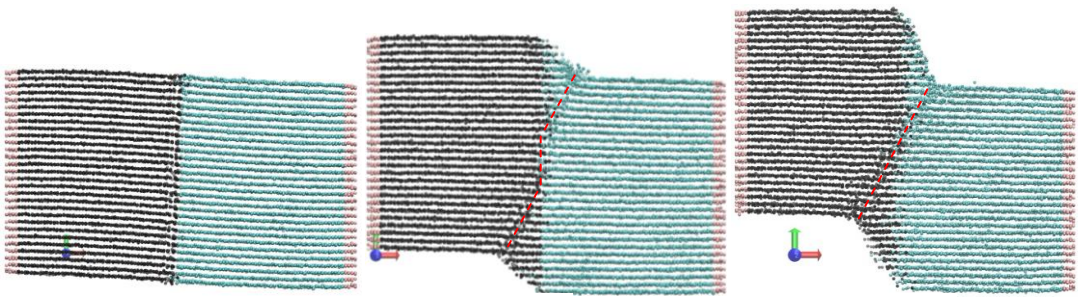

a) b) c)

Figure 3.33 Selected snapshots at different temperatures under the applied force of 0.002eV/Å along the [001] tilt axis of the Σ5 (210) symmetrical tilt grain boundary: a) 15ps at 500K, b) 70ps at 650K and c) 70ps at 750K. The red dash lines indicate the grain boundaries after incomplete or complete rotations.

In the case of 0.004eV/Å (Figure 3.32b), the shear force was large enough to activate the grain boundary motion, but still not enough to make the two grains slide away from each other below 550K. The insert shows the detail of the translation distance-time curve at 500K. It can be seen that after two slow-downs the relative

displacement between two grains is also subjected to the characteristic of simple harmonic oscillation. At first, the grain boundary sliding process was obviously slowed down near 15ps by some resistance. This was overcome shortly and the relative displacement between two grains increased sharply. Finally, the grain boundary sliding process was stopped at 32ps and the bicrystal system kept the simple harmonic oscillation with smaller amplitudes. Figure 3.34 a) and b) shows the corresponding atomic structures of 14ps and 32ps respectively at 500K under the applied force of 0.004eV/Å. Before 14ps, the applied force had not broken the grain boundary bonding and there was no grain boundary sliding actually. The bicrystal system was still deformed in the elastic domain. It is consistent with previous results that there is some minimal force to overcome the grain boundary sliding and this resistance can be interpreted as a static frictional force at the grain boundary [253]. In the present case, the applied force was larger than this critical force and could initiate the sliding. Therefore, after 14ps the grain boundary bonding was broken and grain boundary sliding took place, leading to the loss of atomic symmetry at grain boundary. Correspondingly, the grain boundary sliding resistance was decreased, while the sliding speed was increased. With further shear deformation, the grain boundary rotation also took place due to the unconstrained free surface in Y direction and asymmetrical grain boundary migration. As discussed previously, the grain boundary rotation could result in additional resistance and in the present case it totally counteracted the

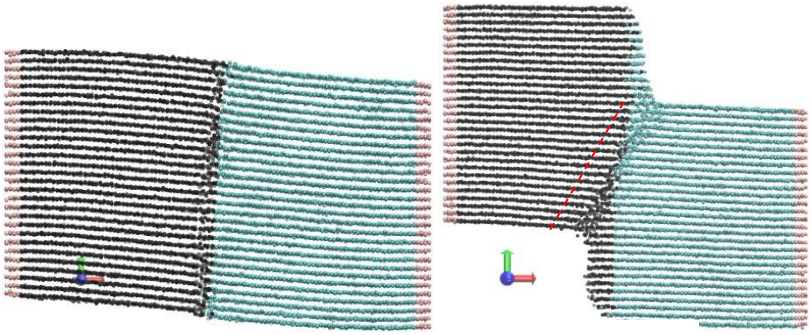

a) b)

Figure 3.34 Selected snapshots at different temperatures at 500K under the applied force of 0.004eV/Å along the [001] tilt axis of the Σ5 (210) symmetrical tilt grain boundary: a) 14ps and b) 32ps. The red dash lines indicate the grain boundaries after incomplete or complete rotations.

applied shear force. Therefore, the grains stopped sliding from each other and oscillated around the balance position. Above 600K with the force of 0.004eV/Å and for all the simulated temperatures with the force of 0.006eV/Å (Figure 3.32b), two grains slid away from each other finally and the sliding speed was increased with the temperature and the applied force. Figure 3.35 shows the atomic structures from different stages at 600K under the applied force of 0.004eV/Å, which are typical for the cases that two grains slid away from each other. It matches the previous results with three processes: activation of the grain boundary sliding, grain boundary rotation and the separation.

It shows in the previous cases where the shear force perpendicular to the tilt axis that the grain boundary rotated to the other symmetrical or asymmetrical grain boundaries of the same Σ group during the shear deformation. Moreover, apart from atomic accommodation and diffusion at the grain boundary, the applied shear force that is perpendicular to the [001] tilt axis can make the grain boundary dislocations glide on the planes with the same zone axis [001]. This can also result in the grain boundary motion. The grain boundary dislocations moved in steps related to the times of possible Burgers vector and the collective movements can be unlikely consistent. It can thus be seen that the grain boundary rotated gradually and the multiplicity of the rotated grain boundary morphology can also be shown. When the atomic activity and the effect of diffusion at grain boundary were increased at high temperatures or with long simulation time, the rotated grain boundaries tended to become flat. In the present case, however, the grain boundary would never rotate to any grain boundaries of the same Σ group, as the shear force along the tilt axis and the grain boundary rotation axis was not the tilt axis. Figure 3.35 shows the schematic grain boundary rotation during shear deformation for the Σ5 (210) symmetrical grain boundary with shear force along the [001] tilt axis. The crystallographic orientations of the bicrystal are the same as indicated in. It can be seen from the figure that the atoms are colored by the common neighbour analysis (CNA) technique, where blue indicates FCC structure and red for irregular structure (grain boundary here). Based on the crystallographic orientations, the grain boundary plane (red dash line) is (210) for the left grain and (-210) for the right grain at the initial position. During shear deformation, the grain boundary plane rotated clockwise around [21-1] zone axis of

the left grain or [2-1-1] zone axis of the right grain. Correspondingly, the plane normal of the grain boundary rotated from [210] to [00-1] for the left grain and from [-210] to [001] for the right grain. It can be seen that at any arbitrary rotation the grain boundary plane normal belongs to the same zone axis of both grains (for example in Figure 3.35 it is <211>), but the orientations in the grain boundary plane

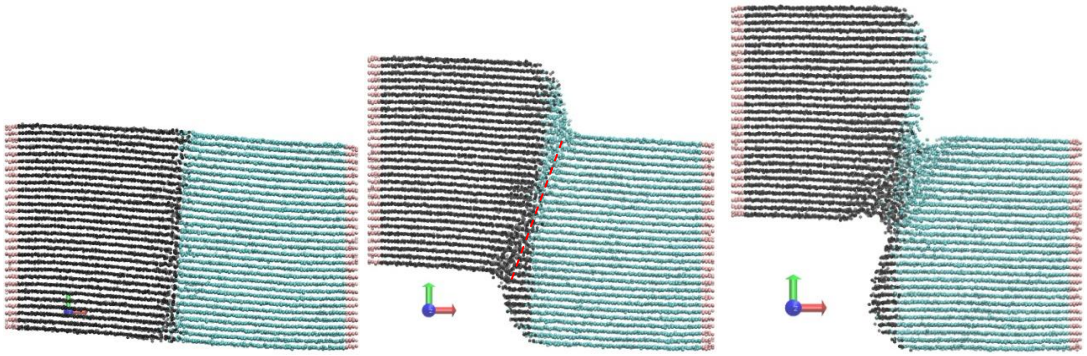

a) b c)

Figure 3.35 Selected snapshots at different temperatures at 650K under the applied force of 0.004eV/Å along the [001] tilt axis of the Σ5 (210) symmetrical tilt grain boundary: a) 13ps, b) 22ps and c) 32ps. The red dash lines indicate the grain boundaries after incomplete or complete rotations.

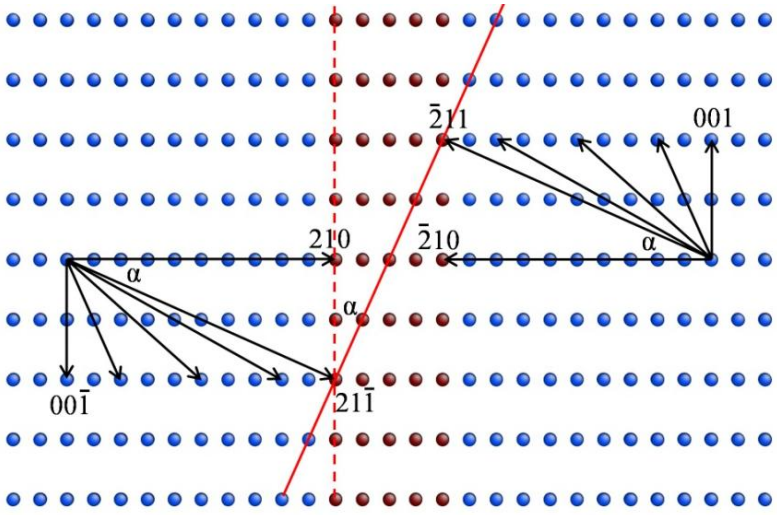

Figure 3.36 Schematic grain boundary rotation during shear deformation for the Σ5 (210) symmetrical grain boundary with shear force along the [001] tilt axis. The crystallographic orientations of the bicrystal are the same as indicated in Figure 3.30. The atoms are coloured by the common neighbour analysis (CNA) technique at the initial position, where blue indicates FCC structure and red for irregular structure (grain boundary here). The red dash line indicates the initial grain boundary, while the red line indicates one arbitrarily rotated grain boundary.

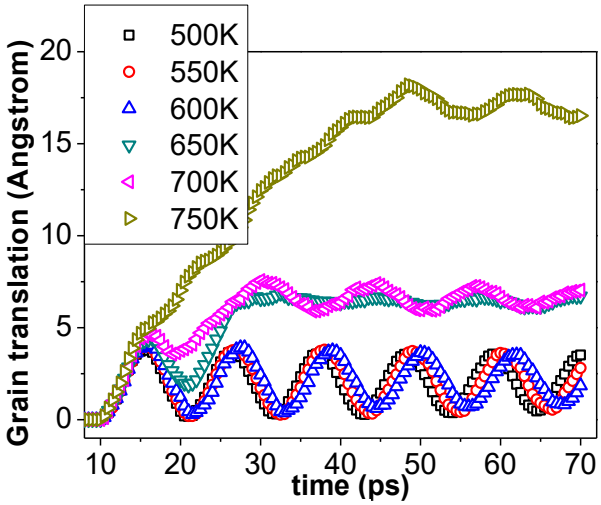

a)

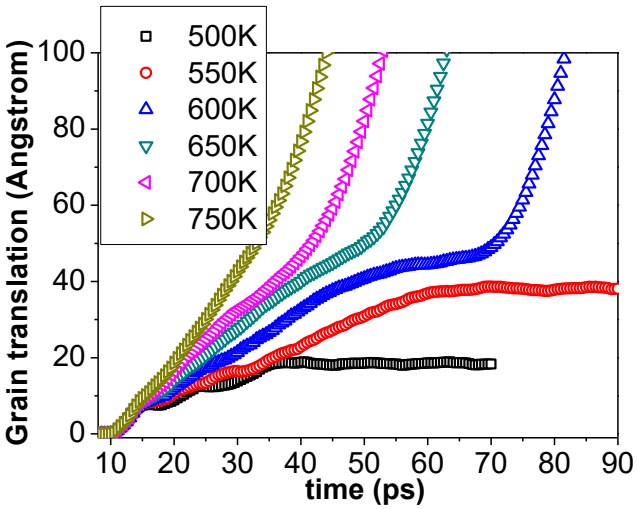

b)

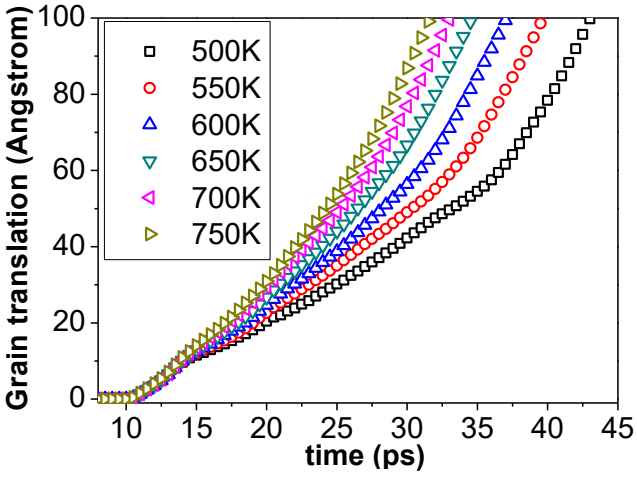

c)

Figure 3.37 Grain translations as a function of time under different applied forces and temperatures for the asymmetrical Σ5 (100)//(430) with shear force along the [001] tilt axis: a) 0.002eV/Å, b) 0.004eV/Å and c) 0.006eV/Å.

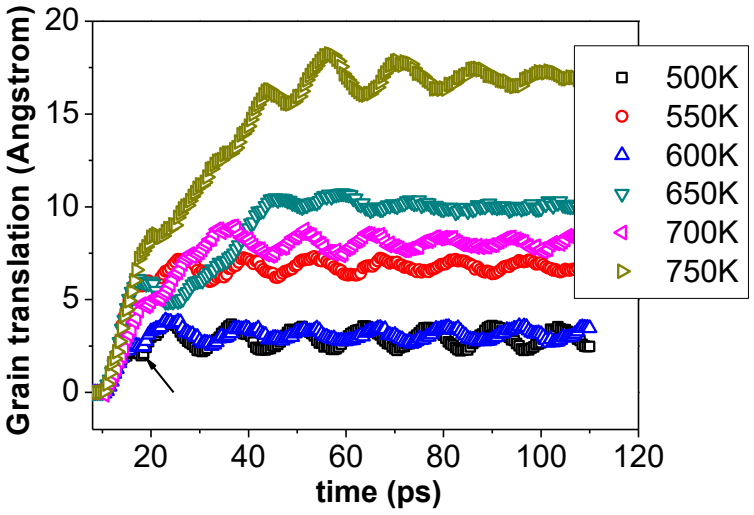

a)

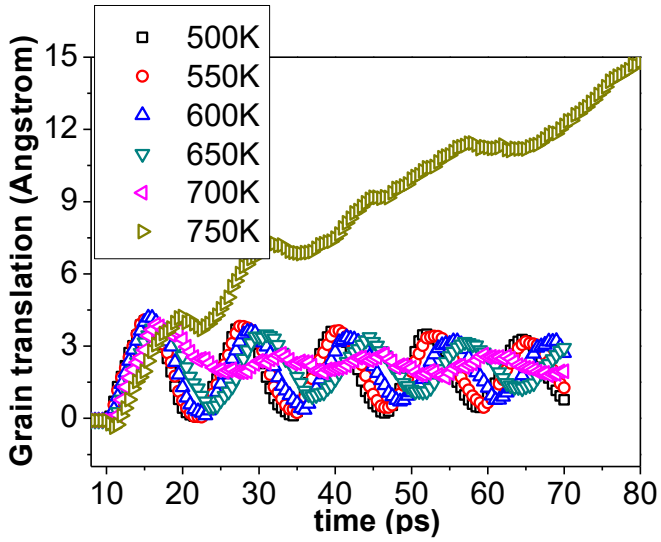

b)

Figure 3.38 Grain translation as a function of time with the applied force of 0.001eV/Å perpendicular to the [001] tilt axis: a) symmetrical Σ5 (210) tilt grain boundary and b) asymmetrical Σ5 (100)//(430) tilt grain boundary.

are different in the two grains. Therefore, the new rotated grain boundaries are twist grain boundaries. However, as these twist grain boundaries formed through atomic accommodation during shear deformation, they must differ from the corresponding ideal twist ones and there should be many misfits on the grain boundaries. On the other hand, it is also worth noting the grain boundary rotations which are basically confined in between 24~29^{o} (red dash lines in Figure 3.33~3.36). Based on Figure 3.35, the favourable rotated grain boundaries were nearly between {211} (24.1^{o}) and {845} (29.2^{o}) planes. First, the grain boundary rotation angle in this range was

proper to balance the applied shear force. Secondly, as the {211} planes index is lowest and the {845} planes index is also relatively low in the present case, the grain boundaries in this range would be favourable to keep the low-energy configuration.

Figure 3.37 shows the dependence of grain boundary translation on different applied forces and temperatures for the asymmetrical Σ5 (100)/(430) tilt grain boundary with shear force along the [001] tilt axis. It can be seen that the grain boundary sliding behaviour is consistent with that for the symmetrical one. After examining the atomic configurations at each condition, the grain boundary evolution during shear deformation is also consistent with previous results. However, the rotated grain boundaries have no regularity. Besides, the critical driving force to activate grain boundary motion (sliding or coupled motion) is different from that to separate the two grains, which will be discussed in the next section.

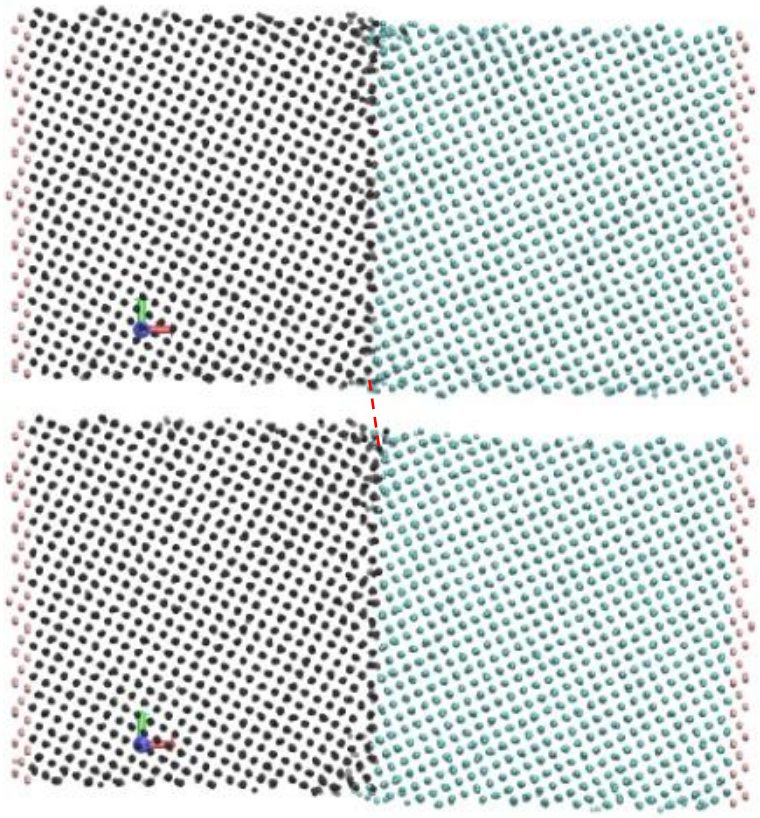

Figure 3.39 Selected snapshots at 500K under the applied force of 0.001eV/Å perpendicular to the [001] tilt axis of the Σ5 (210) symmetrical tilt grain boundary: a) 19ps and b) 25ps.

3.6 Discussion

So far, we have compared the shear response of several tilt grain boundaries with the same misorientation angle. Particularly in the case of constant applied force, where the driving force was applied on two tilt grain boundaries (symmetry and asymmetry) with two directions (normal or parallel to the tilt axis) for each grain boundary, the critical driving force to activate grain boundary motion (sliding or coupled motion) is different from case to case and it indicates the grain boundary sliding ability. Therefore, it means the grain boundary sliding behaviour is not only dependent on the misorientation angle, but also closely related to the boundary type and the sliding direction. To compare this critical driving force for the four cases, the conditions with applied force of 0.001eV/Å were supplemented for the cases with driving force perpendicular to the tilt axis. Figure 3.38 shows the dependence of grain boundary translation on temperatures with the applied force of 0.001eV/Å perpendicular to the [001] tilt axis for the symmetrical Σ5 (210) tilt grain boundary (Figure 3.38 a) and asymmetrical Σ5 (100)//(430) tilt grain boundary (Figure 3.38 b). It can be seen that when the applied shear force is small enough, the relative displacement of the two grains and the simulation time are also subjected to the characteristic of simple harmonic oscillation for the cases where the shear force is perpendicular to the tilt axis. It is worth noting the cusp (marked by black arrow) at the beginning of the low temperature curve in Figure 3.38 a). By examining the corresponding atomic configurations (Figure 3.39), it was found that one step of shear coupling occurred instead of the grain boundary sliding and then the bicrystal system experienced the simple harmonic oscillation until the end of simulation. Finally, compared with the Figure 3.32, Figure 3.37 and Figure 3.38, the mobility of the grain boundaries during shear deformation can be concluded and the sequence from easier to harder is Σ5 (100)/(430) with shear force perpendicular to the tilt axis < Σ5 (210) with shear force perpendicular to the tilt axis < Σ5 (210) with shear force along the tilt axis < Σ5 (100)/(430) with shear force along the tilt axis. First, it is much easier for the tilt grain boundaries to slide perpendicular to the tilt axis than to slide along the tilt axis. This is because in this direction it should be easier for the shear force to move the grain boundary dislocations around the [001] tilt axis than to cause the rigid atomic sliding. Second, in the case of shear force perpendicular to the tilt axis, the

asymmetrical tilt grain boundary Σ5 (100)/(430) is more mobile than the symmetrical tilt grain boundary Σ5 (210). The reason is possibly that the grain boundary sliding resistance is increased with the coherency of grain boundaries and extra shear stress is required to break this grain boundary symmetry. However, in the case of shear force along the tilt axis, the asymmetrical tilt grain boundary Σ5 (100)/(430) is slightly less mobile than the symmetrical tilt grain boundary Σ5 (210). In this direction, the grain boundary symmetry plays an insignificant role during the shear deformation, while the atomic bonding and specific grain boundary structure might play the crucial role and result in the little difference.

3.7 Summary

GBS behaviour was strongly sensitive to the temperature and regardless of the type of driving force and misorientation, the bicrystal system tended to resist the applied force by GB rotation.

At low temperatures, the GBS is very sensitive to the imposed ways of external applied forces which may lead to general crystal deformation such as GBS, grain or grain boundary rotation, coupled motion of grain boundary and dislocation release. Sometimes it may even lead to destruction of the materials by initiating cracks or de-bonding the grain boundaries. However, at high temperatures, the two grains smoothly slid away from each other in the way of viscous grain boundary sliding under the shear deformation.

The GB rotation resulted from surface strain, GB migration or GB coupled motion. Moreover, the grain boundary rotated among some of the Σ5 asymmetrical and symmetrical tilt GB boundaries under shear deformation and led to the normal stress σ_{xx} in the bicrystal system.

Under particular circumstances reaction of the grain boundary dislocations during shear deformation could release uncommon edge lattice dislocations from the grain boundary. The uncommon edge lattice dislocations with <110>/2 Burgers vectors have the [001] line direction and glide on the {110} planes.

4 COUPLED GRAIN BOUNDARY MOTION

4.1 Introduction

Grain boundary (GB) migration is defined as the movement of a grain boundary in the perpendicular direction to the boundary plane. Besides, GB plays an important role in recrystallisation, grain growth, and the plasticity of nanocrystalline (NC) materials. Grain boundary migration can be induced by a gradient of stored plastic deformation energy, boundary curvature, anisotropy of physical properties and applied shear stress [330, 331]. During the last decade, shear stress induced GB migration has attracted significant research interest because it has been found to be a generic deformation mechanism of NC materials that is related to their exceptional strength and ductility [332-335]. Stress-induced GB migration is usually accompanied by grain boundary sliding, which is defined as the relative movement of the two adjacent grains in the direction parallel to the boundary plane. This phenomenon is often called coupled GB motion characterised by a factor β, namely the ratio of the GB sliding speed to the GB migration speed [234].

The shear stress-induced coupled motion of small-angle grain boundary was first observed experimentally in Zinc by Washburn and Parker [336] and then in the same material by Li et al. [260]. Winning and his co-workers [266, 267, 330] investigated the motion of planar symmetrical and asymmetrical tilt GBs in high-purity aluminium under the influence of external shear stress and found that the migrations of low-angle and high-angle GBs can be induced by the imposed external stress. This phenomenon has recently been investigated in experiments using bicrystals [337-339], NC materials [332, 335], and coarse grained polycrystalline materials [269, 340].

Gleiter [341] proposed a step model to explain the migration mechanism of grain boundary. In the study, it was assumed that a grain boundary has step-like structure formed by the (111) planes of the adjacent grains in face-centred cubic (FCC) metals. Atoms are emitted from the steps of the shrinking grain into the grain boundary while the steps of the growing grain absorb the same number of atoms out of the grain boundary, leading to GB migration. Ashby [342] postulated using a bubble model. In this model, if sliding is accompanied by migration, the grain boundary

structure does not change during the GB motion. However, Cahn and Taylor [343] developed a unified approach to study the motion of grain boundaries. It was concluded that the coupled migration and sliding is a general motion phenomenon for most GBs and the coupling factor depends on grain misorientation.

With the advent of more powerful computers, the coupled GB motion has been studied extensively by atomistic simulations. It has been a unique tool to understand the dynamic response and evolution of the atomic structure during the coupled GB motion. Bishop Jr et al. [344] studied the dynamics of a high-angle tilt boundary by molecular dynamics and found that atomic motions in a grain boundary were highly cooperative and depended largely on the boundary structure. They explained the coupled GB migration and sliding by a grain boundary dislocation mechanism. Molteni et al. [345] conducted an ab initio simulation of the sliding process at a Σ5(001) twist grain boundary in germanium (Symmetrical coincidence site lattice (CSL) GB are designated as ΣN(h k l), where Σ is the reciprocal density of CSL sites, N is a Σ value and (h k l) is the indices of the GB plane). They found that sliding occurred through a stick-slip mechanism. Chandra and Dang [251] studied the sliding and migration of [110] symmetric tilt grain boundaries in aluminium under applied displacement and applied force conditions. It was found that pure grain boundary sliding without migration was caused by applying external displacement, while the coupled migration and sliding was induced by applied force. The former finding was inconsistent with other simulation studies. Ballo and his co-workers [325, 346] investigated the effects of temperature and vacancies on the GB sliding and migration. They observed that the annealing temperature played an important role in determining the grain boundary energetics and mobility, and the sliding and migration properties were partially dependent on the position of the vacancy in the GB core. Sansoz and Molinari [254] studied the mechanical response of symmetric tilt GBs and asymmetric tilt GBs in Cu and Al under simple shear. Here, the deformation of the boundaries was found to operate by three modes, depending on the GB equilibrium configuration: GB sliding by uncorrelated atomic shuffling, nucleation of partial dislocations from the interface to the grains, and GB migration. Zhang and his co-workers conducted molecular dynamics simulations to study the elastically driven GB migration [347], curvature driven GB migration [274], and

shear stress-driven GB migration [271]. Cahn et al. [235] and Suzuki and Mishin [348] conducted molecular dynamics simulations to investigate the stress-induced migration of [001] symmetrical tilt GBs in copper, and then provided a detailed description of the atomic motions during the coupled GB motion. They found that the GB coupling factor is a geometric constant whose value can be predicted from simple geometric considerations. They also identified two distinct modes of coupled GB motion. Indeed their predictions on the coupling factors of [001] symmetrical tilt GBs have been proven to be in excellent agreement with the subsequent bicrystal experiments [337]. Trautt et al. [349] applied a combination of molecular dynamics and phase field crystal simulations to investigate the stress-driven motion of asymmetrical GBs, and demonstrated that the coupling factor exhibited a non-trivial dependence on the misorientation and inclination angles.

It is widely accepted that the GB coupling factor is a geometric constant that only depends on GB crystallography [275]. However, experiments [350-353] and atomistic studies [354-358] have demonstrated that for a given set of misorientation and inclination of the boundary plane, the atomic structure of the grain boundary is not necessarily unique. Therefore, there is a strong scientific interest in investigating whether different GB structures with the same GB crystallography could cause different GB behaviours. A multiplicity of GB structures can be induced by segregation and absorption or the emission of point defects [354]. Merkle and Smith [350] observed the atomic structures of NiO bicrystals near $\Sigma=5(310)$ and $\Sigma=13(510)$ GBs in a high resolution transmission electron microscopy (HRTEM). By doing this, they found: (1) several different grain boundary structures existed for each GB; (2) asymmetric structural units were quite common, even in symmetric GB's; (3) the $\Sigma13(510)$ boundary deviated on an atomic scale from a planar configuration in analogy to surface roughening or surface reconstruction. Distinct grain boundary structures (structural multiplicity) were also detected experimentally in $\Sigma9(221)$ symmetric tilt boundaries in aluminium [351, 352] and in $\Sigma17(410)$ symmetrical tilt boundaries in gold [353]. As an effective alternative, atomistic simulation provides deeper insights into grain boundary structures. Structural multiplicity has been predicted in a number of atomistic simulations [354-358]. To the best of the author’s

knowledge, the effect of GB structural multiplicity on GB coupled motion has rarely been studied.

In the present study we investigated the structural multiplicity of the symmetric tilt Σ5(310) boundary in aluminium and its influence on GB behaviour by molecular dynamics simulations. It was thus found that the GB structural multiplicity did affect the GB behaviour. Three different GB structures were observed in the MD simulations and they were found to be responsible for three types of GB behaviours. A detailed analysis has also been conducted to gain a deeper understanding of the atomistic mechanism of GB coupled motion.

4.2 Simulation method

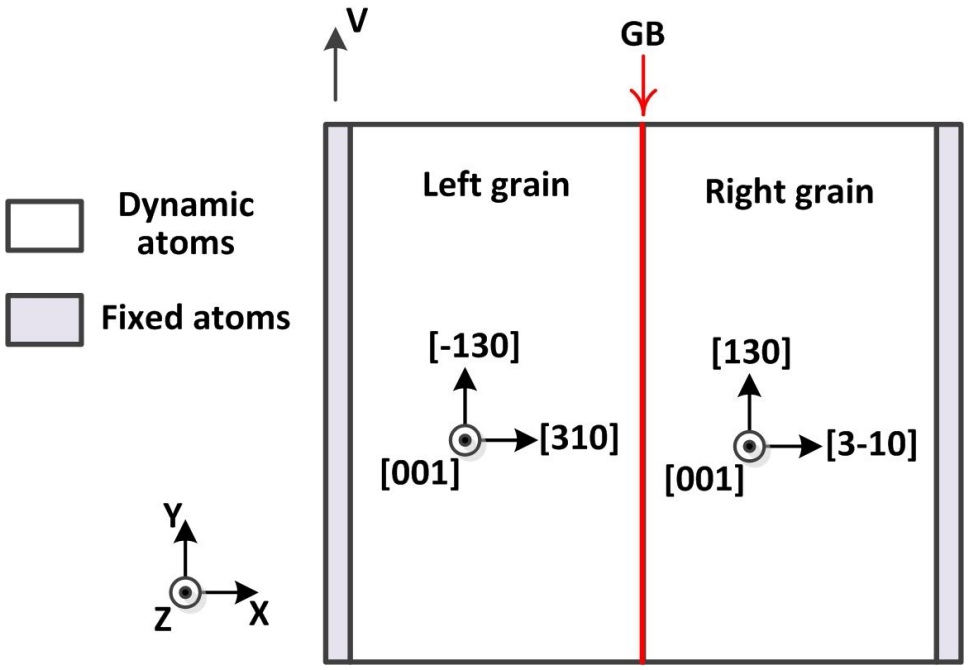

Figure 4.1 Schematic of the bicrystal simulation system with a symmetric tilt Σ5(310) boundary.

The grain boundary (GB) studied in this paper was the symmetric tilt Σ5(310) boundary in aluminium, where a bicrystal structure was used in the simulation. Figure 4.1 illustrates the simulation cell. Two identical aluminium crystals were initially aligned with the coordinate system with [100], [010] and [001] parallel to the X, Y, and Z axes, respectively. The lattice constant was a_0 = 4.05 Å. One crystal was then rotated around the Z axis (tilt axis) by θ/2 (θ=36.87^o) in a clockwise

direction, while the other crystal was rotated around the same axis by θ/2 in an anticlockwise direction. The GB plane was set parallel to the Y-Z plane so that the first crystal formed the left grain and the second crystal formed the right grain. The GB plane was the (310) crystallographic plane in the left grain and the $(3\bar{1}0)$ plane in the right grain, as shown in Figure 4.1. The dimensions of the simulation cell along the X, Y, and Z axes were 102.3 Å, 102.3 Å and 40.5 Å, respectively.

The previous study [355] indicated that distinct GB structures can be achieved by removing or adding different numbers of atomic layers parallel to the boundary in the starting configuration. In the present study two starting atomic configurations were used, as shown in Figure 4.2. In the first starting configuration (SC-1), the distance between the furthest right (310) plane of the left grain and the furthest left $(3\bar{1}0)$ plane of the right grain was 2.558 Å. The second starting configuration (SC-2) was generated by adding three $(3\bar{1}0)$ layers of atoms to the right grain of the first starting configuration, as shown in Figure 4.2b). Each added layer consisted of 160 atoms. 100 randomly selected atoms in the left added layer, as marked by the hollow circles in Figure 4.2b), were then deleted. The total numbers of dynamic atoms in SC-1 and SC-2 were 24320 and 24700, respectively.

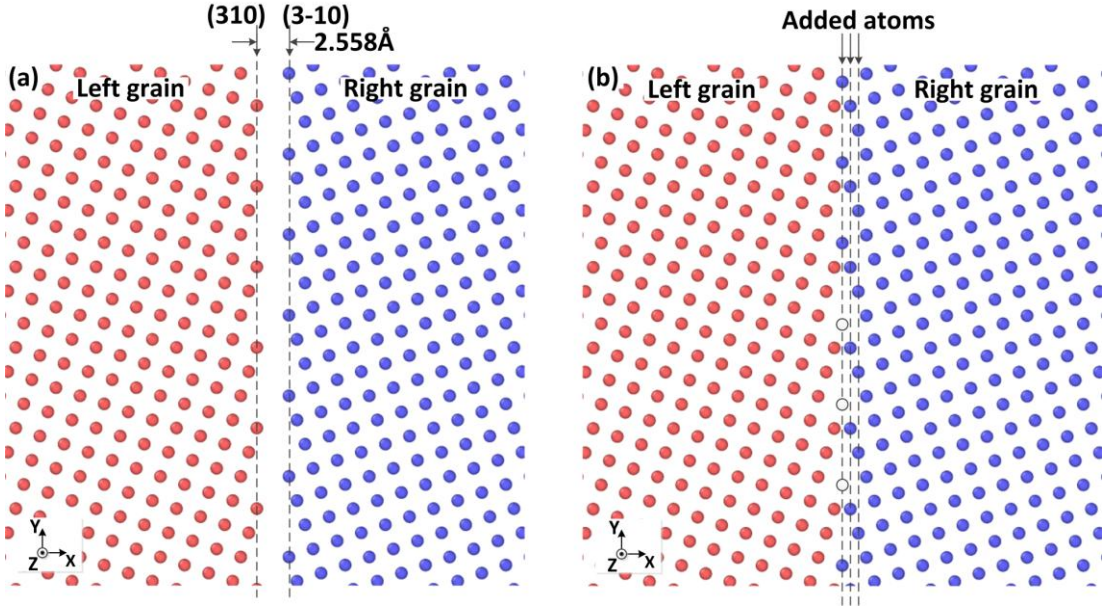

Figure 4.2 Starting atomic configuration around the GB: (a) first starting configuration (SC-1); (b) second starting configuration (SC-2).

There was a slab of fixed atoms on the left hand side and the right hand side of the simulation cell, and the slab was 1.279 Å thick along the X direction. During the simulation, the fixed atoms were frozen in their perfect lattice positions relative to one another, but they still imposed inter-atomic forces on their neighbouring dynamic atoms. During the MD simulations, the bicrystal system was thermally relaxed at the corresponding simulation temperature for 50 ps. Then a shear parallel to the GB was applied by moving all the fixed atoms from the left grain at a constant velocity of V = 0.51 m/s, while the fixed atoms from the right grain remained motionless. Simulation temperatures of 300K, 400K, 500K, and 600K were selected in this study to cover the range of interest. A molecular dynamics code LAMMPS was used in all the simulations. The interatomic potential adopted for Al was the embedded-atom method (EAM) potential of Mishin et al. [359] that was developed by fitting a large set of experimental and ab initio databases. This EAM potential could accurately reproduce the basic equilibrium properties of Al, the elastic constants, the phonon-dispersion curves, the vacancy formation and migration energies, the stacking fault energies, and the surface energies [359]. The MD simulations were performed in the isothermal-isobaric (NPT) ensemble (Nose–Hoover thermostat) with zero pressure in all directions. The equations of atomic motion were integrated using the velocity Verlet algorithm with an integration time step of 1 fs. The simulation results were stored at 3000 time step intervals.

The common neighbour analysis (CNA) pattern was calculated for all atoms at each storing interval. The CNA pattern is a useful measure to characterise the type of local lattice structure. There are five CNA patterns, numbered from 1 to 5, that correspond to FCC lattice, hexagonal close packed (HCP) lattice, body-centred cubic (BCC) lattice, icosahedral lattice, and unknown lattice. Most atoms around the GB and some atoms near the thermally activated vacancy at high temperature were categorised into unknown lattices, namely CNA=5. A histogram for the X coordinates of all CNA=5 atoms was plotted and then fitted by a single-peak Gaussian distribution function for each stored simulation time step. The peak of the fitted distribution function gave the average position of the GB. The stress components were calculated using the expression taken from the Virial theorem, and the average atom volume was used in the stress calculations [312].

4.3 Results

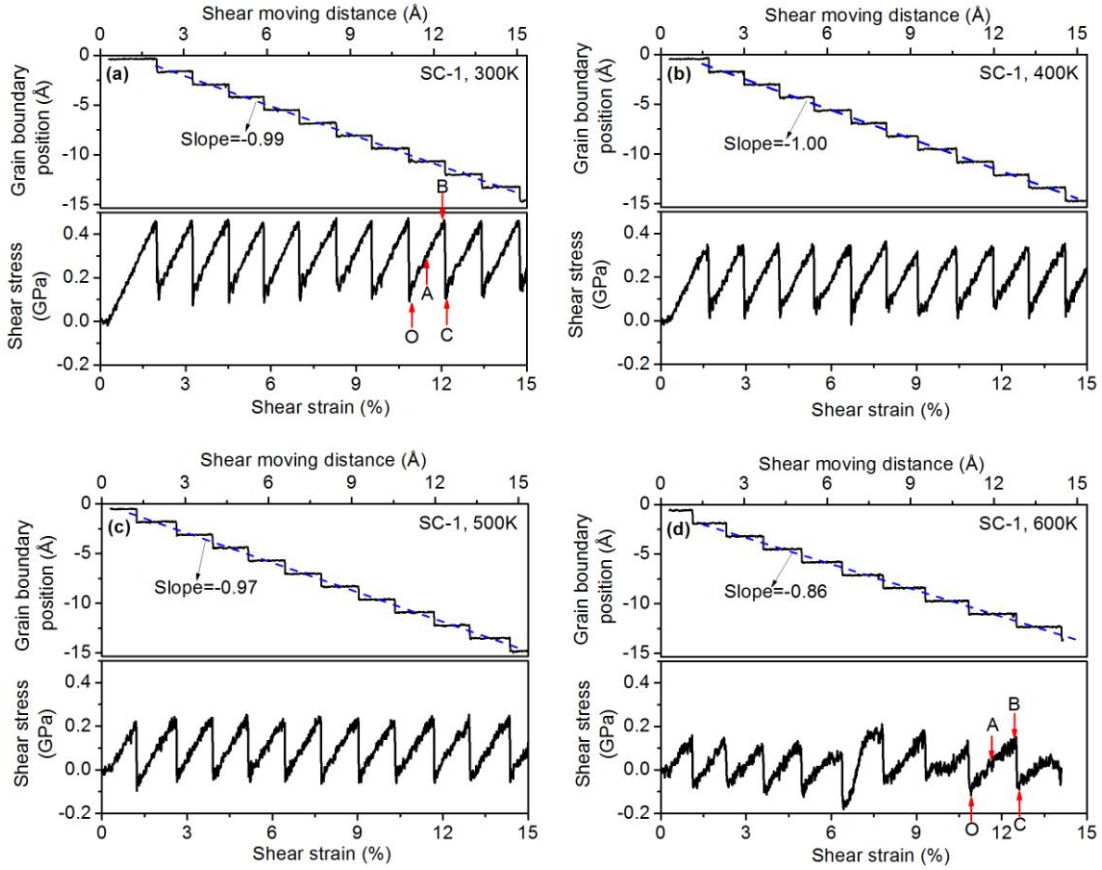

Figure 4.3 Calculated grain boundary position and shear stress at various temperatures for SC-1: (a) 300K; (b) 400K; (c) 500K; (d) 600K.

Figure 4.3 shows the grain boundary position in the upper panels and average shear stress in the lower panels as functions of the shear moving distance and the shear strain for the first starting configuration (SC-1). The shear moving distance was calculated by multiplying the applied velocity by the deformation time, while the shear strain was the shear moving distance divided by the width of the simulation cell along the X direction. Figure 4.3a)-d) correspond to the simulation temperatures of 300K, 400K, 500K, and 600K, respectively. The shear stress shown in the figures is the average of the shear stresses over all the atoms. A coupled GB motion is clearly observed in the upper panels of the figures. All the GBs move to the negative X direction, i.e. the left hand side of Figure 4.1, under the applied shear deformation. At all four temperatures the GBs exhibit in a stop-and-go mechanism. As the shear deformation proceeds the GB position remains unchanged for a period of time ('stop'

period), but when the increment of shear strain reaches a certain value, the GB suddenly moves ('go' period). This GB movement results in a plateau followed by a step in the GB position curve.

The blue dashed line in the upper panel of Figure 4.3 represents the linear regression line of the GB position curve. The coupling factor (β) of the GB motion can be determined as the slope of the blue dashed line, where β is 0.99, 1.00, 0.97 and 0.86 for T=300K, 400K, 500K and 600K, respectively. The calculated coupling factors at 300K and 400K are very close to unity, which agrees with the results of the experiments conducted at room temperature [337]. As the temperature increases to 500K, however, the coupling factor decreases slightly and then drops suddenly to 0.86 at a temperature of 600K.

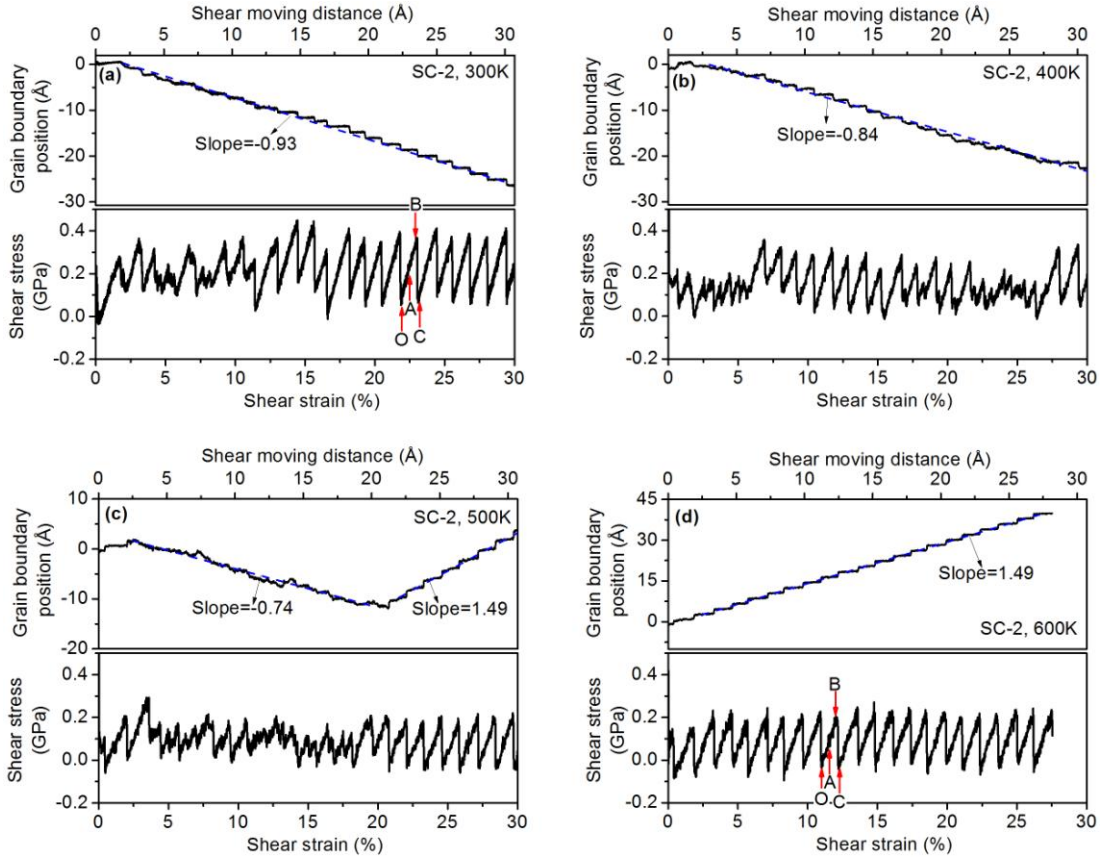

Figure 4.4 Calculated GB position and shear stress at various temperatures for SC-2: (a) 300K; (b) 400K; (c) 500K; (d) 600K.

Like the stop-and-go mechanism of GB movement, the shear stress is of the stick-slip behaviour, as shown in the lower panels of Figure 4.3. During the 'stop' period

of GB motion, the shear stress increases with the shear strain. An almost linear relationship between the shear stress and shear strain is observed for temperatures from 300K to 500K, although a non-linear relationship exists in some stick-slip cycles at 600K. When the GB moves (‘go’ period), the shear stress suddenly drops from the maximum value to the minimum value.

Figure 4.4 shows the calculated GB position and shear stress at four temperatures for the second starting configuration (SC-2). Figure 4.4a) shows that the GB moves to the negative X direction, consistent with the observation in Figure 4.3a). However, the stop-and-go mechanism of the GB movement for SC-2 is not very obvious and the shear stress does not exhibit clear stick-slip behaviour prior to a shear strain of about 11.4%. When the shear strain exceeds 11.4% the stop-and-go GB movement appears in Figure 4.4a). Besides, the shear stress exhibits stick-slip behaviour even though the maximum and minimum shear stresses vary in different stick-slip cycles. The coupling factor is 0.93 at T=300K for SC-2, which is lower than SC-1 at the same temperature. The curves of T=400K in Figure 4.4b) are generally similar to those in Figure 4.4a). Compared to T=300K the coupling factor of T=400K decreases to 0.84.

When the temperature reaches 500K a dual GB behaviour can be seen in Figure 4.4c): the GB initially moves to the negative X direction under the imposed shear deformation and then changes to the positive X direction when the shear strain exceeds 20.8%. The first GB behaviour is similar to that observed in Figure 4.4a) and Figure 4.4b). However, compared with these figures, the curves of the GB position and shear stress in Figure 4.4c) are more stochastic and the coupling factor has dropped to 0.74. The second GB behaviour observed in Figure 4.4c) exhibits periodicity, which looks similar to that observed in the SC-1 cases (Figure 4.3), but a careful inspection indicates that they are not identical. Unlike the SC-1 cases, the GB after a shear strain of 20.8% in Figure 4.4c) does not maintain a fixed position when the shear stress increases with the shear strain. In other words the GB does not have a fully ‘stop’ period; it continues to move slowly during this period. A GB coupled motion cycle can be divided into a ‘slowly move’ period and a ‘quickly go’ period. The ratio of the GB migration distance during the ‘quickly go’ period to the ‘slowly-move’ period is approximately 2. The GB behaviour at T=600K, as shown in Figure

4.4d), is the same as the second GB behaviour of Figure 4.4c), and they both have the same GB coupling factor (1.49).

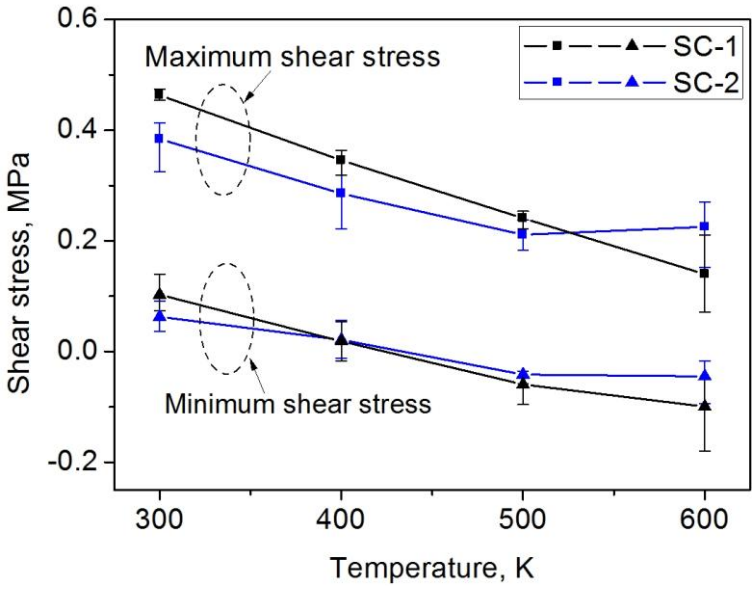

Figure 4.5 The maximum and minimum shear stress as functions of the simulation temperature.

According to the results of Figure 4.3 and Figure 4.4, three types of the GB behaviour have been observed. In the first, the GB motion exhibits a periodic stop-and-go mechanism and the shear stress is of regular stick-slip behaviour. The coupling factor is close to unity at lower temperatures and it decreases with the temperature. The SC-1 cases at a temperature range of 300K - 600K (Figure 4.3a)-d)) exhibit this type of GB behaviour. The second type of GB behaviour occurs in the SC-2 cases at T=300K and 400K and the first part of the simulation with SC-2 at T=500K. In this type of behaviour the GB motion and shear stress are more stochastic. Besides, its coupling factor is smaller than the first type of GB behaviour at the same temperature. In the first two types of GB behaviour the GB migrates to the negative X direction, but in the third type the GB motion exhibits the slowly-move and quickly-go mechanism, and the GB migrates in a direction opposite to the previous two types. The coupling factor of the third type of the GB behaviour is much higher than the other two types. The T=600K case with SC-2 and the second part of the SC-2 case at T=500K exhibit the third type of GB behaviour.

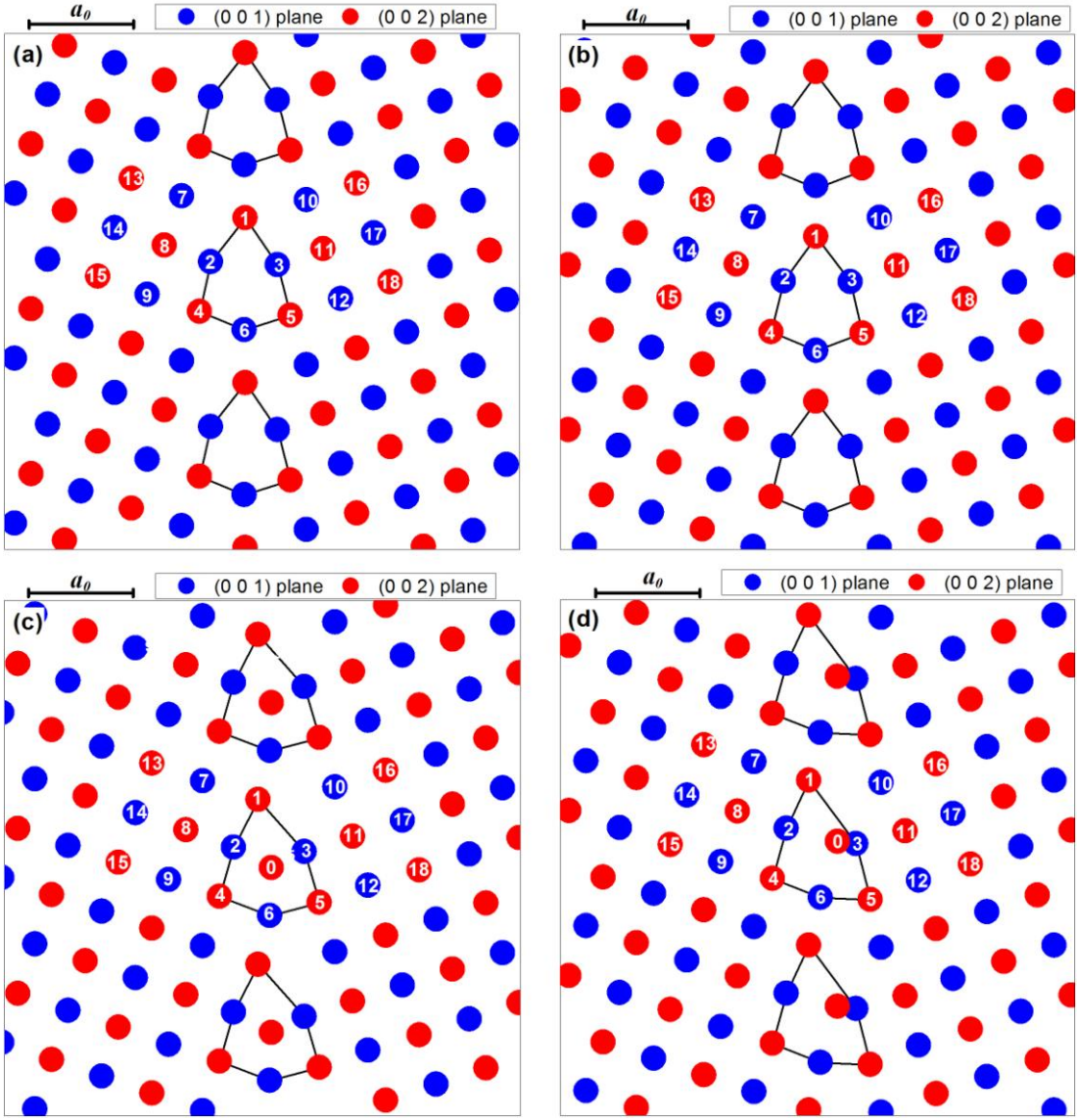

Figure 4.6 Re-constructed atomic configuration around the GB: (a) SC-1 and T=300K; (b) SC-1 and T=600K; (c) SC-2 and T=300K; (d) SC-2 and T=600K.

Figure 4.3 and Figure 4.4 show how the shear stress varies between the maximum and minimum values in each GB motion cycle. The average values the variations of the maximum and minimum shear stress for all the GB motion cycles were calculated and and plotted against temperature in Figure 4.5. The solid square symbols and solid triangular symbols represent the average values of the maximum and minimum shear stress, respectively. It is clear that the maximum and minimum shear stress are dependent of the temperature, and in fact decrease with the temperature. All the maximum shear stresses are positive, but the minimum shear stress could be negative at higher temperatures (500K and 600K). The SC-1 cases

have higher maximum shear stresses than the corresponding SC-2 cases at temperatures up to 500K. When T=600K, the SC-2 case needs a higher shear stress to migrate the GB. The SC-1 case and the SC-2 case have similar minimum shear stresses at T=400K and T=500K. The SC-1 case has a higher minimum shear stress than the SC-2 case at T=300k, and they are opposite at T=600K. The variations in the maximum and minimum shear stress are represented by the error bars in Figure 4.5. Both cases generally have larger variations of shear stresses at T=600K, but from T=300K to T=500K the maximum stress shows larger variation for the SC-2 cases than the SC-1 cases.

This study aimed to investigate the effect that GB structural multiplicity has on GB behaviour under shear deformation. Two distinct starting GB configurations were intentionally used in the simulations and three types of GB behaviours are shown in Figure 4.3 and Figure 4.4. The first question to be answered is: have the two starting GB configurations resulted in different GB structures after thermal relaxation? It is always difficult to display the motion pattern of an atom in the MD simulations of higher temperatures because the higher frequency motion of the atom has been disturbed. The common approach used to solve this problem is to calculate the time averages of each atomic coordinate over a number of simulation time steps [331, 344], but it may smooth out any sudden atomic movement. In this study we traced the atomic movements in a different way. Here the GB used in our MD simulations consisted of about 160 GB structural units. Since all the structural units were distributed periodically, all the structural units and their neighbouring atoms were first moved to a pre-defined position according to the known period relationship. Then the average of the coordinates of the atoms located at the same local position was calculated to obtain the equivalent local coordinates, and an equivalent structural unit was formed. To help facilitate the analysis, the simulation cell was re-constructed by the equivalent structural units through the known periodic relationship.

Figure 4.6 shows the re-constructed atomic structures around the GBs for four selected simulation cases (SC-1 and SC-2 at T=300K and 600K) after thermal relaxation (at Points O given in Figure 4.3 and Figure 4.4. The atoms are observed along the Z direction. Figure 4.6 only shows the atoms at two successive (001)

planes; they are then called the (001) plane and the (002) plane, respectively. The (001) plane and the (002) plane shown in Figure 4.6 are in blue and red, respectively. Note that all the GBs consist of periodically distributed structural units which are marked as solid lines. With the SC-1 cases (Figure 4.6a) and Figure 4.6b)), the structural unit has a kite shape and each structural unit is made up by six atoms. Such a structural unit was widely observed in the experiments [360] and predicted by MD simulations [234, 354, 355]. Besides, it has long been recognised as the most stable GB structural unit with the lowest energy for the symmetric tilt Σ5(310) boundary of FCC metals [355, 360]. This structural unit is called C1 in the following sections. The constitutive atoms of C1 are labelled 1~6 in Figure 4.6a) and Figure 4.6b), and the neighbouring atoms of the GB structural unit, namely Atoms 7-18, are also marked in the figures.

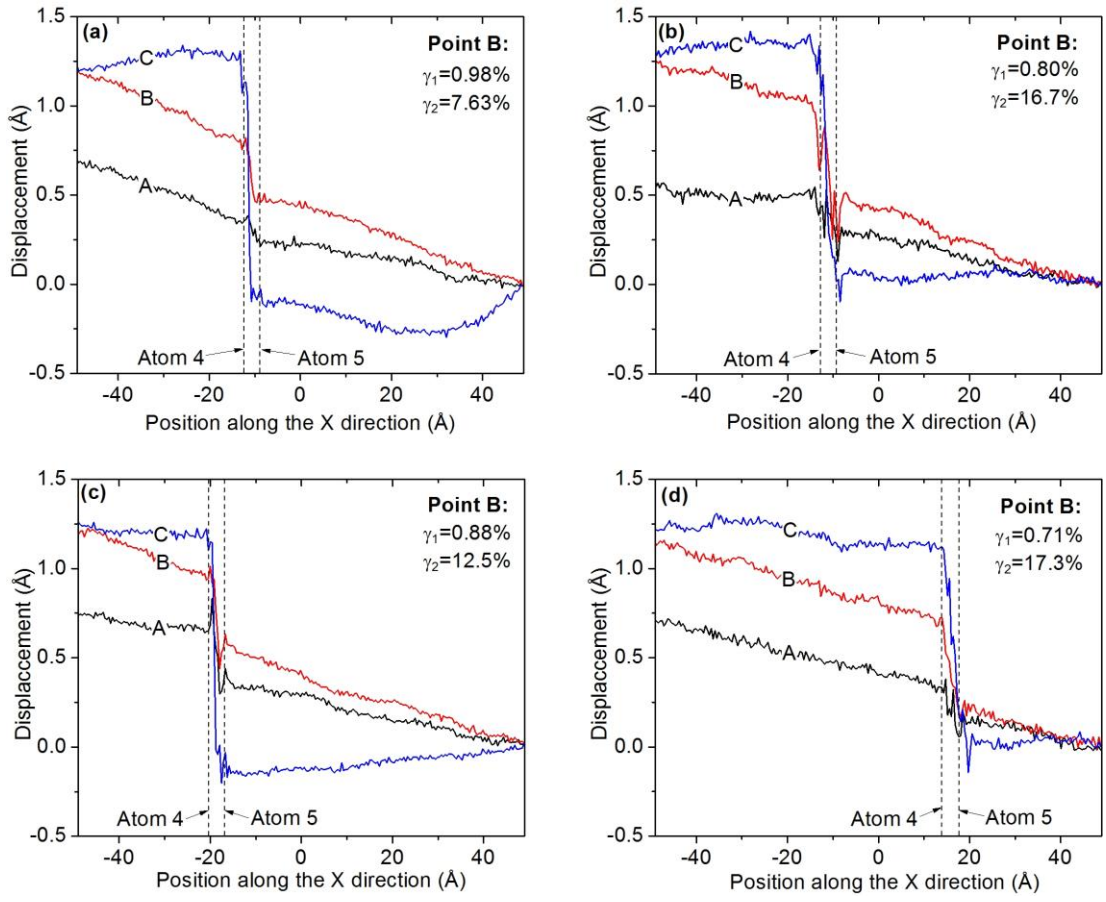

Figure 4.7 Distribution of the average displacement along the Y direction: (a) SC-1 and T=300K; (b) SC-1 and T=600K; (c) SC-2 and T=300K; (d) SC-2 and T=600K.

Figure 4.6c) and Figure 4.6d) show that the GB structural units of the SC-2 cases consist of seven atoms. Six of them are connected by solid lines, which are analogous to the GB structural units of the SC-1 cases. An extra atom is seen in the midst of these six atoms. The extra atom is located at the core of the structural unit at T=300K (Figure 4.6c)), but it is close to the right hand side of the structural unit at T=600K (Figure 4.6d)). It should be noted that an extra atom does not exist in all GB structural units. It should also be noted that while there were 160 GB structural units, there were only 60 extra atoms in each simulation cell. The extra atoms were used intentionally to represent the diffused interstitial atoms in the GB. Since their number was smaller than that of GB structural units, they can easily be diffused along the Z direction. The GB structural unit in Figure 4.6c) is called C2 in this study. Vitek et al. [354] investigated the multiplicity of GB structures by atomistic simulations and then predicted two GB structures for the tilt Σ5(310) boundary in Cu. They were the same as the C1 and C2 GB structures that have been obtained.

The shape of the GB structural unit for the SC-2 case at T=600K differs from C1 and C2. The GB structural unit in Figure 4.6d) is defined as C3. C3 has a triangular shape, whereas C1 and C2 are kite shaped. In the C3 GB structure, Atom 0 is close to Atom 3, but Atom 0 and Atom 3 are on different (001) planes. Merkle and Smith [350] observed the bicrystal specimens of NiO with the FCC structure in a high-resolution transmission electron microscopy (HRTEM), and found two different GB core structures (Structure A and Structure B) in the Σ5(310) tilt grain boundary of NiO. The C3 GB structure predicted in the present study was similar to Structure B observed experimentally by Merkle and Smith, but Atom 0 was not shown in the HRTEM image. This is because only fully relaxed structures can be observed in HRTEM. Since Atom 0 has higher energy and is highly unstable, it can travel easily through the core of the GB structure in the Z direction and escape from the GBs near the surface of the HRTEM specimen.

Our MD simulations clearly showed that the GB structure is not necessarily unique for a given misorientation. Indeed due to the diffusion of vacancies, interstitials, or segregation GBs with local minimum energy configurations could exist in real materials. The C2 and C3 structural units can be regarded as the C1 structural unit with a diffused interstitial atom (Atom 0) occupying two different locations.

In the MD simulations a shear displacement was applied at the left boundary of the simulation cell. It would be interesting to know how the shear deformation is transferred to the GB and whether the distribution of shear deformation is uniform in the simulation cell. In order to answer the second question, the simulation cell was divided evenly into 250 slabs along the X direction. The average displacement along the Y direction and the average X coordinate were calculated for the dynamic atoms in each slab at Points A, B, and C, which have been marked in Figure 4.3 and Figure 4.4. For the displacement calculation, the atomic positions at Point O (marked in Figure 4.3 and Figure 4.4) were selected as references. Figure 4.7 plots the average Y displacement against the average X coordinate for four cases, and the slope of the displacement curve is the shear strain. The dashed lines give the average X coordinates of Atoms 4 and 5, and also indicate the location of the GB structural unit. Figure 4.7 shows that the curves of four cases have similar trends. At Point A the displacement curve is almost linear inside two grains and has made an abrupt change around the GB (between two dashed lines). This means that the shear strain in the grains is almost constant but it has a larger value around the GB. At Point B the shear strain inside the grains and around the GB has increased more than that at Point A, but the increasing shear strain around the GB is more profound. Once the GB migration is completed, namely at Point C, the displacement curve inside two grains tends to become flat and a very large slope of the displacement curve can be seen around the GB. This occurs because there was a relative slip between two grains inside the GB structural unit and the shear stress in two grains had been released. The average values of the shear strain in grains ($\gamma 1$) and in the GB structural unit ($\gamma 2$) at Point B, corresponding to the maximum shear stress before the GB migration, are given in the figures. It is shown that $\gamma 2$ is much larger than $\gamma 1$ for all the cases, indicating that the GB has less resistance to shear deformation than the bulk grains, but as the temperature increases, $\gamma 1$ decreases and $\gamma 2$ increases. A comparison between the SC-1 cases and the SC-2 cases shows that $\gamma 1$ of the SC-1 case is less than that of the SC-2 case for the same temperature, whereas $\gamma 2$ has an opposite relationship.

4.4 Discussion

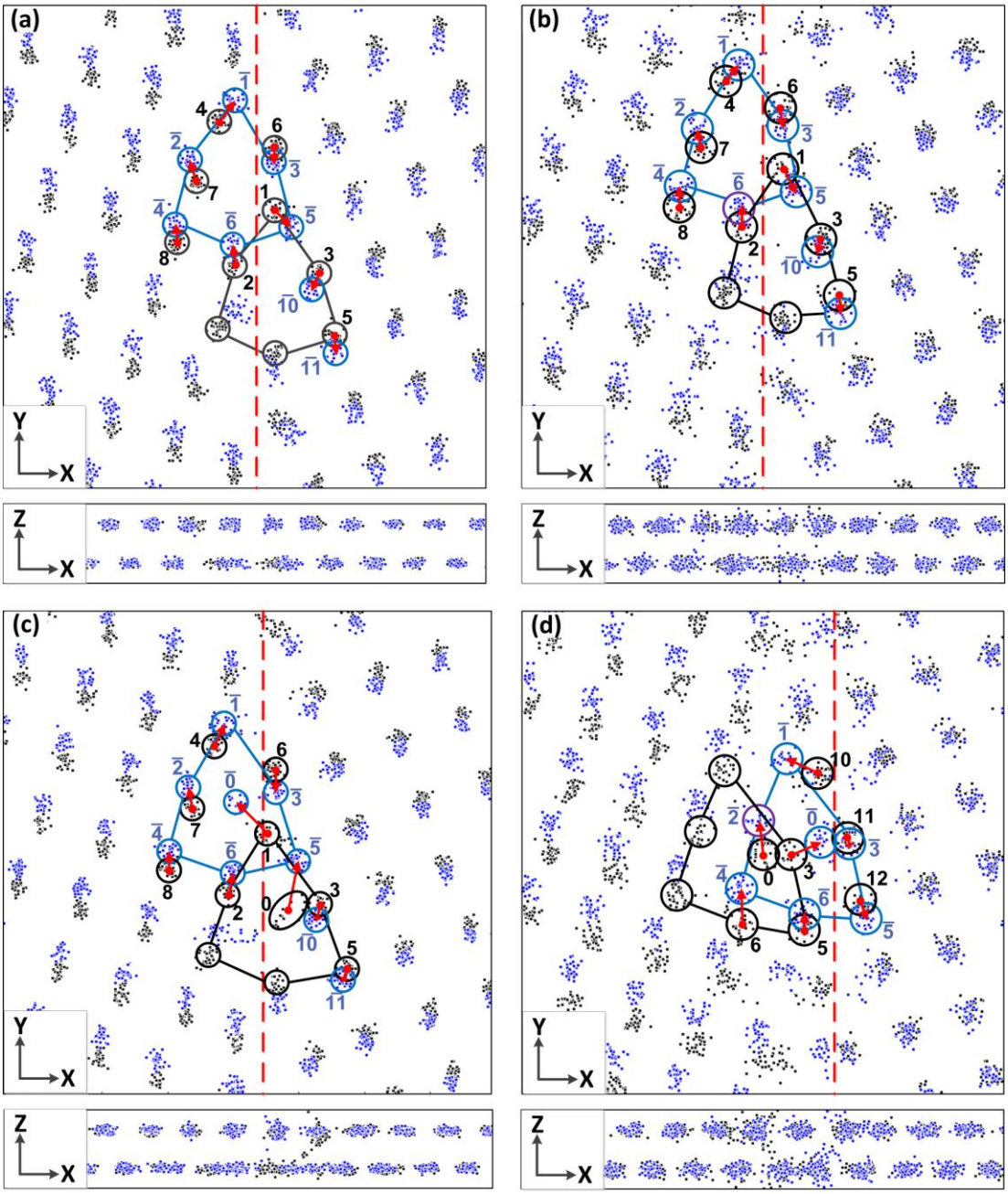

Figure 4.8 Atomic trajectories during the GB migration: (a) SC-1 and T=300K; (b) SC-1 and T=600K; (c) SC-2 and T=300K; (d) SC-2 and T=600K.

Three GB structures (C1, C2 and C3) were observed in Figure 4.6 and three types of GB behaviours were also shown in Figure 4.3 and Figure 4.4. It is clear that three GB structures are responsible for three types of GB behaviours, so in this section we will discuss: 1) how the atoms move during GB migration; 2) how the shear deformation

is transferred to the GB, and 3) why different GB structures induce different GB behaviours.

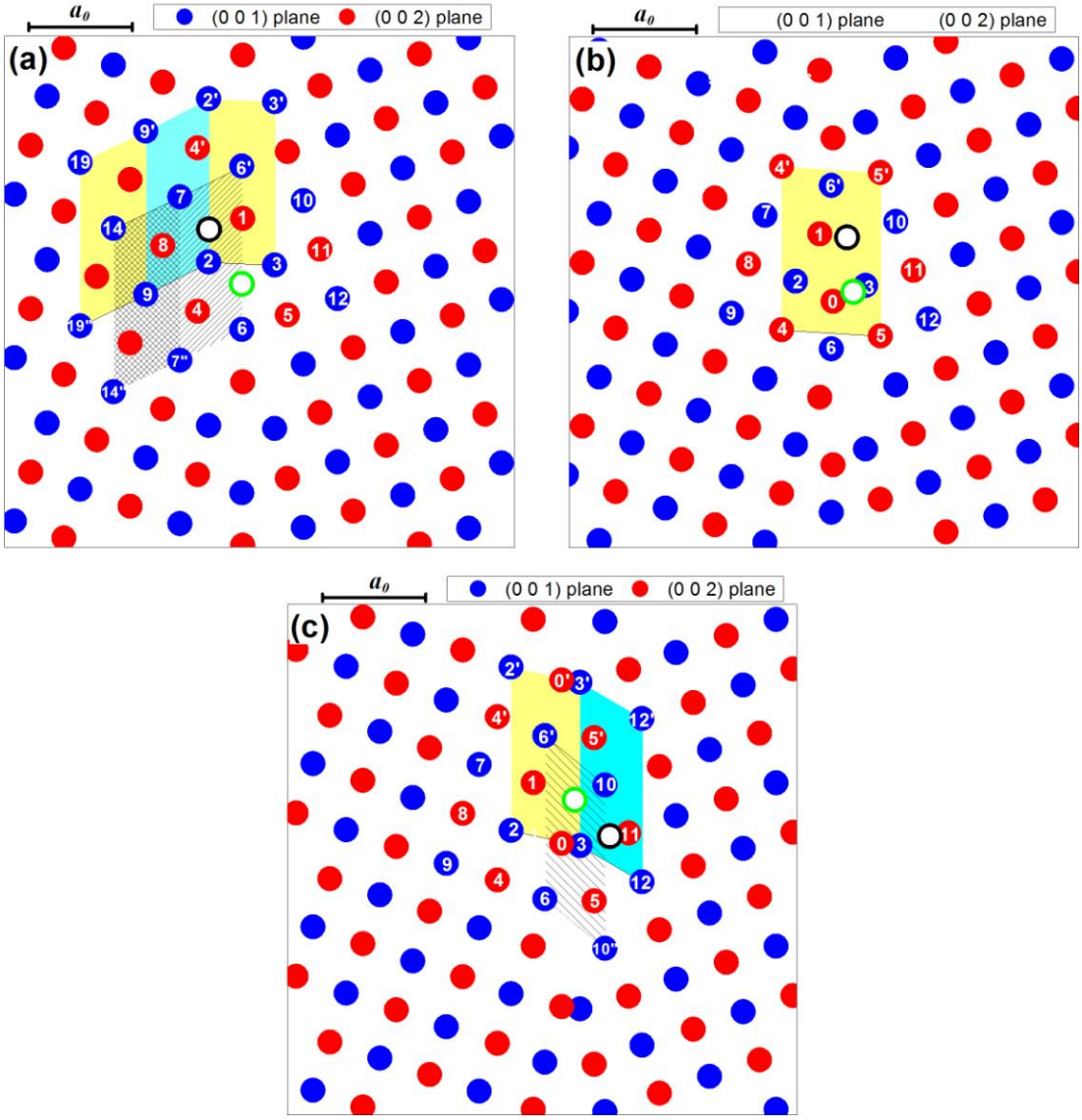

Figure 4.9 Atomic positions with marked shear units around the GB: (a) C1 GB structure; (b) C2 GB structure; (c) C3 GB structure.

Figure 4.8 shows the atomic positions at the multiple simulation times with an interval of 3 ps for a period of 180 ps. The X-Y plane view is shown in the upper panel and the X-Z plane view in the lower panel. The black and blue dots represent the atomic positions before and after the GB migration, respectively. The black and blue circles cover most of the positions of the atoms (concentrations of the atomic positions) before and after the GB migration, respectively. The red arrows link the

centres of the black and blue circles, and also indicate the atomic displacement vector. Figure 4.8 shows the movements of the atoms from their positions in one grain, before GB migration, to their new positions in another grain after GB migration. For the sake of brevity, the GB structures before and after their migration are called the old GB structure and the new GB structure, respectively.

Figure 4.8 a)-b) show the results of the SC-1 cases where T=300K and T=600K, respectively. These results indicate how the atomic trajectories are similar to each another. The only difference between these two simulations is that the area where the atoms concentrate at T=600K is larger due to the stronger thermal fluctuation at higher temperature. In these two cases, when the GB migrates the atoms in the left grain jump up and the atoms in the right grain move down. The atoms in and near the old GB structure are labelled by black numbers. Besides, those in and near the new GB structure are marked by blue numbers with a bar on the top of each number. The old and new GB both consist of C1 structural units. Like the internal atoms of the left grain, Atoms 2 and 8 move straight up by an average distance of about 1.36 Å during the GB migration period to become Atoms $\bar{6}$ and $\bar{4}$, respectively, in the new GB structure. Atom 7 has a similar upward movement with a slight bias to the left, where it forms Atom $\bar{2}$. Atoms 3, 5, and 6 tend to coincide with the internal atoms of the right grain and they still evolve to Atoms $\overline{10}$, $\overline{11}$ and $\bar{3}$ in the new GB structure, respectively. Atoms 1 and 4 have special movements; Atom 1 moves to the lower right to form Atom $\bar{5}$ while Atom 4 proceeds to the upper right to become Atom $\bar{1}$. A dashed red line is drawn to separate the atoms moving up from those moving down during the abrupt GB migration, and to indicate an interface where two grains have a relative sliding. The lower panels of Figure 4.8 a)-b) show that all the atoms vibrate at their own (001) planes, but at T=600K (Figure 4.8b)) the atoms have larger amplitude of vibration. Indeed, some atoms could jump to their neighbouring (001) planes due to thermal activation.

For the SC-2 case at T=300K (Figure 4.8c)), most atoms move like their counterparts in the SC-1 cases, apart from Atom 0 and Atom 1. In the SC-1 cases Atom 1 moves to the lower left to form Atom $\bar{5}$ but in the SC-2 case at T=300K, Atom 1 jumps into the core of the new GB structural unit and becomes Atom $\bar{0}$, while Atom 0 evolves into Atom $\bar{5}$ subjected to a upward movement. The dashed red line indicates the

sliding interface between two grains. A comparison between the old GB structural unit and the new GB structural unit indicates that they have different local structures; the new GB structural unit in Figure 4.8c) is the same as the C2 structural unit identified in Figure 4.6, while the old GB structural unit was similar to the C3 structural unit. This means that after GB migration the extra atom (Atom 0) was located in the core of the GB structure, but as shear deformation proceeds Atom 0 tends to occupy the site near Atom 3 (Atom 0 site in C3). Both positions are metastable and have higher potential energies. During the shear deformation, Atom 0 could frequently move between two positions, but this switch of position also affects the positions of the other surrounding atoms. It should be noted that the GB position was calculated as the average X coordinates of all the disordered atoms around the GB. Therefore, this frequent switch of position by Atom 0 induces stochastic GB positions, which is why we did not see an obvious stop-and-go behaviour for the SC-2 case at T=300K in Figure 4.4a). When Atom 0 is located close to Atom 3 (in the old GB structure), it can jump to another (001) plane and swap positions with Atoms 3. While Atom 0 can push one of two neighbouring Atoms 3 away and occupy this position, another Atom 3 may fill up the gap left by Atom 0. This behaviour is indicated by the black dots between two (001) planes in the lower panel of Figure 4.8c).

Figure 4.8d) is indicative of the SC-2 case at T=600K where the internal atoms of the left grain move up and those of the right grain move down slightly. The magnitudes at which these atoms move in the two grains differ in that the former is larger than the latter. Atoms 1, 2, and 4 in the old GB structure have similar movement to the internal atoms of the left grain, where Atoms 0, 5, and 6 jump upwards over different distance. Atoms 11 and 12 have a similar movement to the atoms inside the right grain but Atoms 10 and 3 had special movements, so that Atom 10 moves to the upper left and Atom 3 moves to the upper right. Atoms 3, 10, 0, 11, 6, 12 and 5 in the old GB structure evolve into Atoms $\bar{0}$-$\bar{6}$ in the new GB structure via a GB migration. The dashed red line in Figure 4.8d) indicates the sliding interface between two grains and also shows that both the old GB and the new GB consist of C3 structural units. The lower panel of Figure 4.8d) shows that Atoms 0 and Atoms 3 switch positions frequently in the old GB structure, whereas Atoms $\bar{0}$ and Atoms $\bar{3}$ had similar

behaviour in the new GB structure. This is shown by the black and blue dots between the two (001) planes in Figure 4.8d).

Table 4.1 lists the potential energies of key atoms in the old GB structure and the new GB structure for the four simulation cases. The potential energies given in the table were calculated at Point B for the old GB structure and at Point C for the new GB structure, respectively. Here the potential energies of some atoms decrease after GB migration, while those of other atoms increase. The atoms with the highest potential energy are Atom 2 for SC-1 at both T=300K and T=600K, Atom 0 for SC-2 at T=300K, and Atom 3 for SC-2 at T=600K, respectively. These atoms play a key role in the coupled GB motion.

An analysis of all the simulation cases showed the atoms around the GB tend to occupy three metastable sites: 1) the parent lattice site of the left grain; 2) the parent lattice site of the right grain, and 3) the symmetric position of two grains. In the C1 structural unit, as seen in the SC-1 cases at T=300K and 600K, Atoms 2 and 4 are close to the parent lattice sites of the left grain, Atoms 3 and 5 are near the parent lattice sites of the right grains, and Atoms 1 and 6 are at the symmetric positions of two grains. In the C2 structural unit Atoms 1-6 have the same local positions as those in the C1 structural unit, but the extra atom, Atom 0, is mostly at the symmetric positions of two grains. In the C3 structural unit, Atom 0 and Atoms 1 are at sites close to the parent lattice sites of the left grain.

In order to analyse the transmission of the shear deformation in the simulation cell, several structural units on the (001) plane in the left grain and around the C1 GB are considered; they are shown as shaded in Figure 4.9a) and will be called the shear units. The first shear unit consists of Atoms 9, 9′, 19 and 19″ and the second unit consists of Atoms 7″, 7, 14 and 14″. Both of them are shaped like a parallelogram. Atom 14 is at the centre of the first shear unit and at the corner of the second shear unit. If the thermal activity is ignored, Atom 14 will be always located at the symmetric centre of parallelogram 9-9′-19-19″ during deformation, which will give Atom 14 a stable condition with the lowest energy. When the shear deformation is transferred to the shear unit 9-9′-19-19″, Atoms 19 and 19″ will move up relative to Atoms 9′ and 9 and induce a shear strain in this unit. Since Atom 14 is firmly

constrained by Atoms 9, 9′, 19 and 19″, the movement of Atoms 19 and 19″ will drag Atom 14 up. This will indicate that the shear deformation has been transferred from the first shear unit to the second shear unit. In the same manner the shear deformation in the second shear unit will move its central atom (Atom 9) upwards, and in turn transfer the shear deformation to the next shear unit (2-2′-9′-9). The shear units inside the grains possess a perfect lattice structure without any defect, and thus they are tightly interlocked with their neighbouring units. The atom at the centre of each shear unit acts like an interlock pin. Interlocking the shear units means that the shear strain can be distributed uniformly inside the grains under the applied shear deformation, as observed in Figure 4.7.

The shear unit 3-3′-2′-2 is the unit on the C1 GB and the shear unit 6-6′-7-7″ is the unit linking the interior shear unit 2-2′-9′-9 and the GB shear unit 3-3′-2′-2. Unlike the shear units in the grains, there is no stable central position for these two units because the atoms around the GB are disturbed. This means the interlock pin atoms of these two shear units (Atom 2 and Atom 6′) can only occupy metastable positions. In fact they may move from one metastable position to another under the influence of shear deformation. The interlocking of shear units 3-3′-2′-2 and 6-6′-7-7″ is not as strong as the shear units inside the grains, so the GB exhibits less resistance to shear deformation and has larger shear strain than the bulk grains, as observed in Figure 4.7.

Atom 2 inside shear unit 6-6′-7-7″ tends to occupy a site close to the parent lattice site of the left grain. Table 4.1 shows that Atom 2 has the highest potential energy in the entire system. It also shows that when the shear deformation is transmitted to the shear unit 6-6′-7-7″, Atoms 7 and 7’ move up and Atom 2 could not fully keep step with Atoms 7 and 7′. As the deformation proceeds the potential energy of Atom 2 increases, but when it exceeds the energy barrier Atom 2 will move to other metastable positions. Atom 2 has already occupied a site close to the parent lattice site of the left grain. Under shear deformation, it will move to other types of metastable positions, that is, either a parent lattice site of the right grain or a symmetric position between grains. The core of the GB structure unit, schematically marked by a green circle in Figure 4.9a), is a symmetric position of two grains, but

this position is situated at the lower right side of Atom 2. Since Atom 2 is dragged upwards by Atoms 7 and 7′, it is impossible for Atom 2 to occupy this core position. A parent lattice site of the right grain, marked by a black circle in Figure 4.9a), is the only possible metastable position that can be occupied by Atom 2. When it overcomes the energy barrier, Atom 2 can jump from the old metastable position to the new metastable position to become Atom $\bar{6}$ in the new GB structure. During this period it will release its potential energy which will help other atoms overcome their energy barriers. Atom 1 is initially located at the symmetric position, but when Atom 2 moves it pushes Atom 1 to occupy a parent lattice site of the right grain so that Atom 1 becomes Atom $\bar{5}$ in the new GB structure. As Atom 2 moves from its old metastable position to its new metastable position, the connection between Atom 2 and the atoms to its left are weakened considerably. This results in an instantaneous disconnection between two grains. Therefore, a relative slip between two grains at the interface were observed and marked in Figure 4.8. This instantaneous disconnection also releases the elastic energy stored in both grains, leading to a sudden drop in the shear stress and a release of the shear stress at Point C, as shown in Figure 4.3a) and Figure 4.7a), respectively. As the atoms around the GB proceed to their new positions, they will build new connections with surrounding atoms and form a new GB structure.

Figure 4.9b) shows the atomic positions with a marked shear unit on the (002) plane around the C2 GB for the SC-2 case at T=300K. The shear unit 5-5′-4′-4 coloured yellow in Figure 4.9b) is a unit around the GB in which Atoms 0 and 1 are located. Table 4.1 shows that Atom 0 has the highest potential energy, and as the shear deformation proceeds it tends to move to two other possible metastable positions; one is schematically marked by a green circle, which is the parent lattice site of the left grain, and the other position, marked by a black circle, is the parent site of the right grain. If Atom 0 occupies the first position (green circle), it will easily swap its position with Atom 3, as can be seen in Figure 4.8c). This does not result in any GB migration. When the potential energy of Atom 0 exceeds its energy barrier, it could move to the second metastable position (black circle) and become Atom $\bar{5}$ in the new GB structure. However, Atom 0 also pushes Atom 1 to occupy the core of the new GB structure and Atom 1 then becomes Atom $\bar{0}$. As the consequence of the above

collective atomic movements, the GB migrates to a negative X position, as shown in Figure 4.4a).

Table 4.1 Potential energies of the key atoms before and after GB migration.

Simulation cases	Before GB migration (Point B)		After GB migration (Point C)		Change in potential energy (eV)
	Atom id	Potential energy (eV)	Atom id	Potential energy (eV)	
SC-1 T=300K	1	-3.298	$\bar{5}$	-3.313	0.015
	2	-3.184	$\bar{6}$	-3.211	0.027
	3	-3.206	$\overline{10}$	-3.336	0.130
	4	-3.308	$\bar{1}$	-3.298	-0.010
	5	-3.316	$\overline{11}$	-3.344	0.028
	6	-3.204	$\bar{3}$	-3.195	-0.009
	7	-3.306	$\bar{2}$	-3.189	-0.117
	8	-3.338	$\bar{4}$	-3.312	-0.026
SC-1 T=600K	1	-3.245	$\bar{5}$	-3.260	0.015
	2	-3.151	$\bar{6}$	-3.166	0.015
	3	-3.172	$\overline{10}$	-3.263	0.091
	4	-3.254	$\bar{1}$	-3.241	-0.013
	5	-3.260	$\overline{11}$	-3.283	0.022
	6	-3.155	$\bar{3}$	-3.152	-0.003
	7	-3.247	$\bar{2}$	-3.163	-0.083
	8	-3.279	$\bar{4}$	-3.261	-0.019
CS-2 T=300K	0	-3.160	$\bar{5}$	-3.180	0.020
	1	-3.232	$\bar{0}$	-3.228	-0.004
	2	-3.242	$\bar{6}$	-3.261	0.019
	3	-3.236	$\overline{10}$	-3.312	0.076
	4	-3.290	$\bar{1}$	-3.231	-0.059
	5	-3.294	$\overline{11}$	-3.329	0.036
	6	-3.252	$\bar{3}$	-3.228	-0.024
	7	-3.313	$\bar{2}$	-3.237	-0.076
	8	-3.337	$\bar{4}$	-3.299	-0.038
CS-2 T=600K	0	-3.167	$\bar{2}$	-3.222	0.055
	1	-3.240	$\bar{7}$	-3.285	0.044
	2	-3.250	$\bar{8}$	-3.305	0.055
	3	-3.147	$\bar{0}$	-3.158	0.011
	4	-3.309	$\bar{9}$	-3.314	0.005
	5	-3.218	$\bar{6}$	-3.211	-0.007
	6	-3.223	$\bar{4}$	-3.297	0.074
	10	-3.235	$\bar{1}$	-3.214	-0.020
	11	-3.212	$\bar{3}$	-3.168	-0.044
	12	-3.288	$\bar{5}$	-3.223	-0.065

When Atom 0 occupies the green circled position in Figure 4.9b), the GB structural unit looks similar to the C3 GB structural unit, but they have different shapes. The former is shaped like a kite while the latter looks like a triangle. When the simulation temperature of the SC-2 case increases to 500K the initial GB structure unit is the same as that of 300K. However, when the shear deformation reaches a certain level, the thermal energy may trigger a transformation from the C2 structure to the C3 structure which is responsible for the dual behaviour observed at T=500K.

Figure 4.9c) shows the atomic positions with marked shear units on the (001) plane around the C3 GB for the SC-2 case at T=600K. In this case Atom 3 has the highest potential energy. Besides, it is located inside the shear unit 5-5′-6′-6 and occupies the site close to the parent site of the right grain. Under shear deformation Atom 3 tends to move to two possible metastable positions; the first position is schematically marked by the green circle and the second one is marked by the black circle, as shown in Figure 4.9c), respectively. Both of them are the parent sites of the left grain. If Atom 3 moves to the first position, it will be very close to Atom 10, which is not energy preferred. Therefore, Atom 3 tends to occupy the second position and push Atom 10 to occupy the first position. This results in a GB migration to the positive direction, as can be seen in Figure 4.4d).

4.5 Summary

The structural multiplicity of the symmetric tilt Σ5(310) boundary in aluminium and its influence on the behaviour of the GB at a temperature range of 300K - 600K by molecular dynamics simulations were investigated in this chapter. Two starting atomic configurations were adopted in the simulations. The major findings can be summarised as follows:

Two starting atomic configurations led to three different GB structures (C1, C2 and C3) after thermal relaxation, all of which consisted of structural units. The C1 GB existed for the first starting atomic configuration (SC-1) at temperatures from 300K to 600K. The C1 structural unit had a kite shape made up of six atoms, while the C2 structural unit had a similar kite shape but with an extra atom located at the core of the unit. The C2 GB appeared in those cases with a second starting configuration (SC-2) at a temperature range of 300K - 400K. The C3 structural unit was almost

triangular in shape, with an extra atom situated near the right hand side of the unit. The SC-2 case at a temperature of 600K had C3 GB. In the SC-2 case at a temperature of 500K, the GB structure changed from C2 to C3 when the shear deformation reached a certain level.

Three GB structures induced three types of GB behaviours, all of which clearly demonstrated that the structural multiplicity of GB did affect its behaviour. With the first type of behaviour the GB motion displayed a periodic stop-and-go mechanism and the shear stress was of regular stick-slip behaviour. The coupling factor was close to unity at lower temperatures and it decreased with the temperature. With the second type of behaviour the GB motion and shear stress were more stochastic and its coupling factor was smaller than that in the first type of behaviour at the same temperature. In the first two types of GB behaviour the GB migrated to the negative X direction, but for the third type, the GB motion displayed a slowly-move and quickly-go mechanism, while the GB migrated in an opposite direction to the previous two types. The coupling factor for the third type of GB behaviour was much higher than the other two types. Because the GB changed its structure during deformation, the SC-2 case at a temperature of 500K displayed a dual behaviour. That is, the GB first moved to the negative X direction under the imposed shear deformation and then changed to the positive X direction when the shear strain exceeded a certain value.

The atomic mechanism responsible for the behaviour of each GB has been analysed in detail. The results have revealed that the atoms around the GB tended to occupy three metastable sites: 1) the parent lattice site of the left grain; 2) the parent lattice site of the right grain; 3) the symmetric position of two grains. Under the applied shear deformation the atoms around the GB moved from one metastable site to another, but its direction of migration mainly depended on the new metastable position occupied by the atom with the highest energy. While the GB atoms moved from the old metastable position to the new metastable position, an instantaneous disconnection between two grains occurred. This resulted in the fact that the shear stress suddenly dropped and was then released in the grains. As the atoms around the GB proceeded to their new positions they would build new connections with surrounding atoms and form a new GB structure.

5 INTERACTION OF DISLOCATIONS AND GRAIN BOUNDARY

5.1 Introduction

In the previous chapter, the shear response of grain boundaries and the coupling behaviour were investigated. In some particular cases, dislocations were found to be released from the grain boundaries. In this chapter, the interaction between incoming dislocations and grain boundaries are simulated and discussed.

The prediction of slip transferring across grain boundaries is of special significance, as they play a significant role in mechanical properties of materials. For example, the strength and plasticity of polycrystalline metal films depend on the interaction between lattice dislocations and grain boundaries, which act as obstacles to dislocation motion [285]. However, many aspects with respect to the interaction between interfaces and dislocations are still not well understood. In the recent twenty years, the atomic-level simulation of materials has provided many fundamental insights into this area [93, 212, 233, 243, 248, 285, 290-306].

By investigating the interaction between screw dislocations and coherent twin boundaries for Al, Cu and Ni, Jin et al. found that a screw dislocation approaching the coherent twin boundary from one side may either propagate into the adjacent twin grain by cutting through the boundary. Alternatively, it may dissociate within the boundary plane, depending on both the applied strain and the material dependent energy barrier for the nucleation of Shockley partial dislocations [292]. Later, purely stress-driven interactions between 60^o non-screw lattice dislocation and coherent twin boundaries are simulated by the same authors [291]. Additionally, the 60^o non-screw lattice dislocation can dissociate into different partial dislocations gliding into the twin as well as along the twin boundary, it was also found that a sessile dislocation lock may be generated at the CTB if the transited slip is incomplete. The energy barriers for the formation of Shockley partial dislocations still played the dominant role. To determine the influence of material and interatomic potential on the interaction between an a/2<110>{111} screw dislocation and a Σ3{111}<110> coherent twin boundary, a range of FCC metals were modelled with a total of 10

embedded-atom method (EAM) potentials by Chassagne et al. [304]. The studies showed that the absorption of the dislocation into the coherent twin boundary or transmission into the twinned region and reaction stress depend strongly on the potential used. Besides, the transmission process is controlled by the material parameter $\gamma_S/\mu b_P$, rather than the sign of the ratio $(\gamma_{US}-\gamma_S)/(\gamma_{UT}-\gamma_S)$ [292] (where γ_S is the stacking fault energy, μ the shear modulus, b_P the Shockley partial Burgers vector, γ_{US} the unstable stacking fault and γ_{UT} the unstable twinning energies). Moreover, there exists a critical reaction stress independent of the potential, below which the dislocation is absorbed in the CTB and above which the dislocation is transmitted into the twinned region. Dewald et al. investigated the interaction of screw-dislocations with a series of symmetric <110> tilt coincident grain boundaries (Σ3, Σ9 and Σ11) in Al and found that it is very difficult for the lattice dislocations to cut through the low energy high-symmetry Σ3 and Σ11 boundaries. This was true even if the head dislocation was fully absorbed and a pile-up formed in one grain [290]. However, for the Σ9 boundary with a relatively complex atomic structure, the incoming screw dislocations were absorbed on one side, nucleated newly on the other side and then cut through the boundary. Moreover, this process depends very sensitively on the orientation of the applied stress and on the precise location where the dislocations enters the boundary. By simulating the interactions of lattice dislocations with symmetrical and asymmetrical tilt grain boundaries in Ni, Bachurin et al. also found the important parameters determining the ability of the dislocation to penetrate the boundary [285]. Such parameters include the exact site where the dislocation meets the grain boundary, the misorientation angle of the grain boundary and the sign of the Burgers vector of the incoming dislocation. Interestingly, the inclination angle does not make an important difference on the transmission scenario of full dislocations. Besides, only limited partial dislocation nucleation was found at the investigated high-angle grain boundary. Atomistic simulations of the interactions between dislocations and grain boundaries were also studied for Bcc metals. Similar results were then obtained for the interactions between the 1/2<111> edge dislocation and three symmetric tilt grain boundaries in tungsten [294]. For example, the dislocation may be both absorbed and transmitted, and the outcome depends sensitively on the grain boundary structure and the exact site of the interaction. Furthermore, the interaction is often related to the nucleation of grain boundary

dislocations, and the motion of grain boundary dislocations associated with grain boundary migration is always found to accompany the transmission process.

It can be seen that the interaction between dislocations and grain boundaries is a very complicated process which is dependent on a series of factors summarised as below [93, 212, 233, 243, 248, 285, 290-306]:

1. EAM potentials (Materials);

2. the angle between the lines of intersection between the slip planes of the incoming and emitted dislocations in the grain boundary plane;

3. the characteristics of incoming dislocations (the magnitude of the Burgers vector, edge, screw or mixed);

4. the applied stresses and the resolved shear stress acting on the dislocation;

5. the exact site of the interaction and local atomic grain boundary structure.

Therefore, it is difficult to take into account of all these factors in a particular simulation. Moreover, most MD simulations were performed with symmetrical grain boundaries, while the interaction between dislocations and asymmetrical grain boundaries has not been adequately studied [285].

In this chapter, to simplify the problem and obtain more accurate results, the interaction between a straight 1/2[110] screw dislocation with several [110] asymmetrical tilt grain boundaries in Al has been investigated by MD method with different applied shear stresses. Correspondingly, the EAM potential, the exact site of the interaction, the incoming dislocation characteristic and the intersection angle are all in the same conditions for the MD simulations.

5.2 Methods

The 3D bi-crystal simulation model is illustrated in Figure 5.1 and Table 5.1 gives the orientations of the bi-crystals and the corresponding asymmetrical tilt angles. The simulation system has a dimension of $150 \times 114 \times 57.8 Å^3$ in $X \times Y \times Z$ and contains

58203, 58805, 58829 and 58554 atoms respectively depending on the orientation. Periodic boundary condition was applied in the Z-direction which is parallel to the tilt axis and the GB plane, while in the X- and Y- directions the free boundary condition was applied. First, the right grain position was fixed and used to introduce the incident screw dislocation and the left grain is equivalent to rotate the right grain clockwise or counterclockwise around the Z-axis ([-110]) as detailed in the Table 5.1. Consequently, the asymmetrical tilt grain boundaries were created.

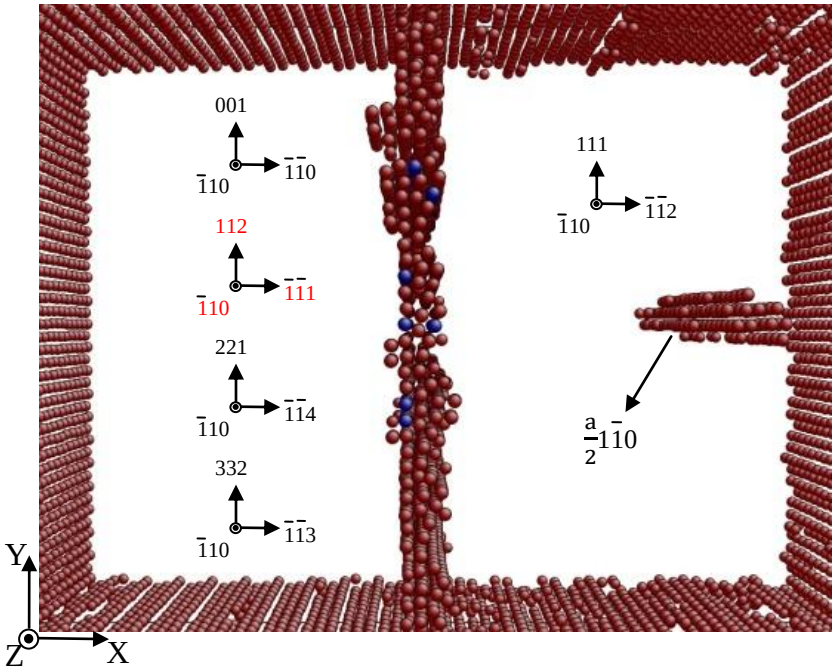

Figure 5.1 Geometry of the bicrystal grain boundary model with the $a\sqrt{2}/2$ full screw dislocation. The crystallographic orientations of the bicrystal are indicated respectively.

Table 5.1 Orientations of the bi-crystals and the corresponding asymmetrical tilt angles (Figure 5.1 uses the blue bold orientation as an example).

Left grain orientation			Right grain orientation			Angle
X	Y	Z	X	Y	Z	
[-1-10]	[001]	[-110]	[-1-12]	[111]	[-110]	54.74°
[-1-11]	**[112]**	**[-110]**				19.47°
[-1-13]	[332]	[-110]				-10.02 °
[-1-14]	[221]	[-110]				-15.79°

Second, the a[1-10]/2 screw dislocation was introduced in the right grain using the same method from Jin's study [292]. After introducing the incident dislocation, the

outer layer of the system was fixed and the whole system was relaxed at 10K for 2ps. In the present study, the leading and trailing Shockley partials were attracted with each other together during relaxation as shown in Figure 5.1. After the relaxation, a constant shear strain (ε_{yz}) was applied homogeneously to the entire MD cell at the (111)[1-10] (or the Y-Z) shear plane in 1ps. MD runs were independent to each other at any specified ε_{yz}. During the shear deformation, the outer layer atoms were set free in the Z-direction, but were still fixed in the X- and Y- directions. After the shear deformation, the outer layer atoms were fixed again in all the three directions. Therefore, this constant strain ε_{yz}, corresponding to a simple shear stress $\sigma_{yz} = \mu\varepsilon_{yz}$, was applied to provide a constant driving force for dislocation motion given by $f_{appl} = \mathbf{b}\sigma_{yz}$, where b = $a\sqrt{2}/2$ is the magnitude of the Burgers vector and $\mu = (C_{11} - C_{12} + C_{44})$, the shear modulus in the {11 1} <110> shear plane [292, 361].

5.3 Results and Discussion

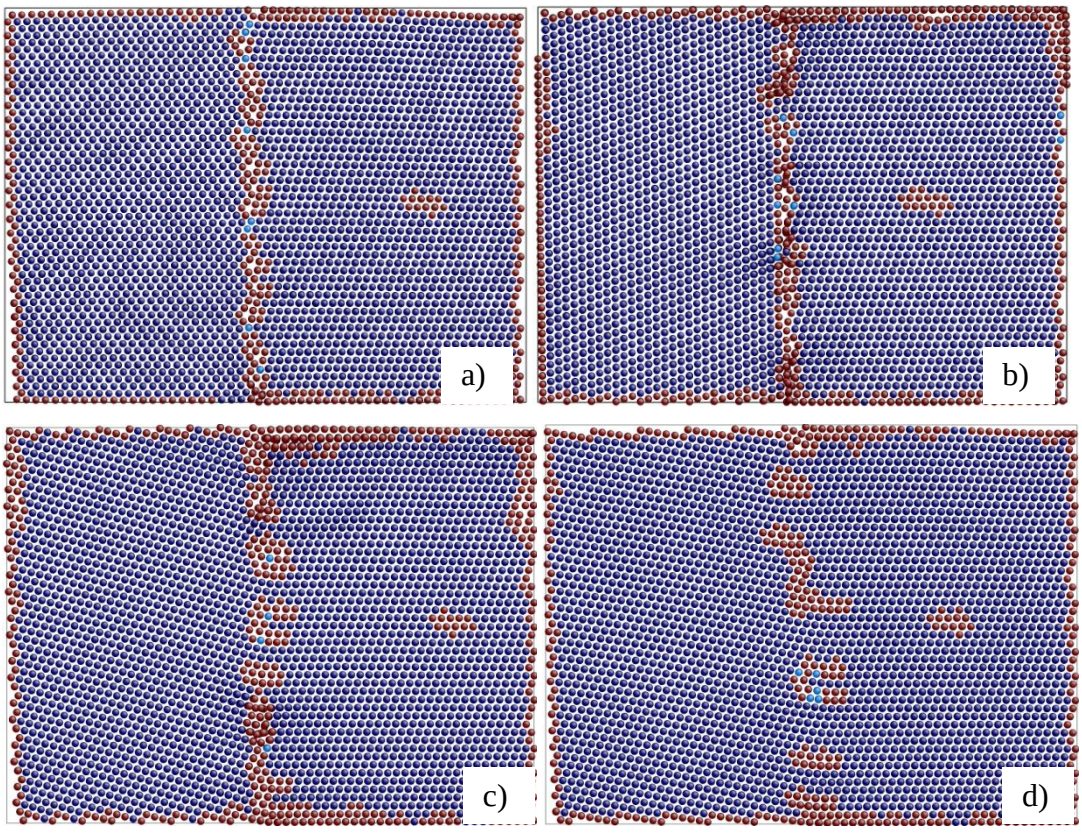

Figure 5.2 The relaxed asymmetrical grain boundary structures with the incident a$\sqrt{2}/2$ screw dislocations for a) 54.74^{o}, b) 19.47^{o}, c) -15.79^{o} and d) -10.02 ^{o}. The misorientation angles are referred to Table 5.1. The atoms are colored by the common neighbour analysis (CNA) technique.

5.3.1 Initial stage prior to the interaction between grain boundaries and dislocations

Figure 5.2 shows the relaxed asymmetrical grain boundary structures with the incident $a\sqrt{2}/2$ screw dislocations. It can be seen that for the relatively lager misorientations the grain boundaries were straight and stable. However, as the misorientation decreased, the grain boundary became unstable. Especially for the misorientation of 10.02^{o}, extended dislocations [243] already nucleated from the grain boundary, but the grain boundary was still unmovable under the shear deformation used in this study. It should be noted that when the misorientation was smaller than 10^{o}, the grain boundary was moved by the shear deformation.

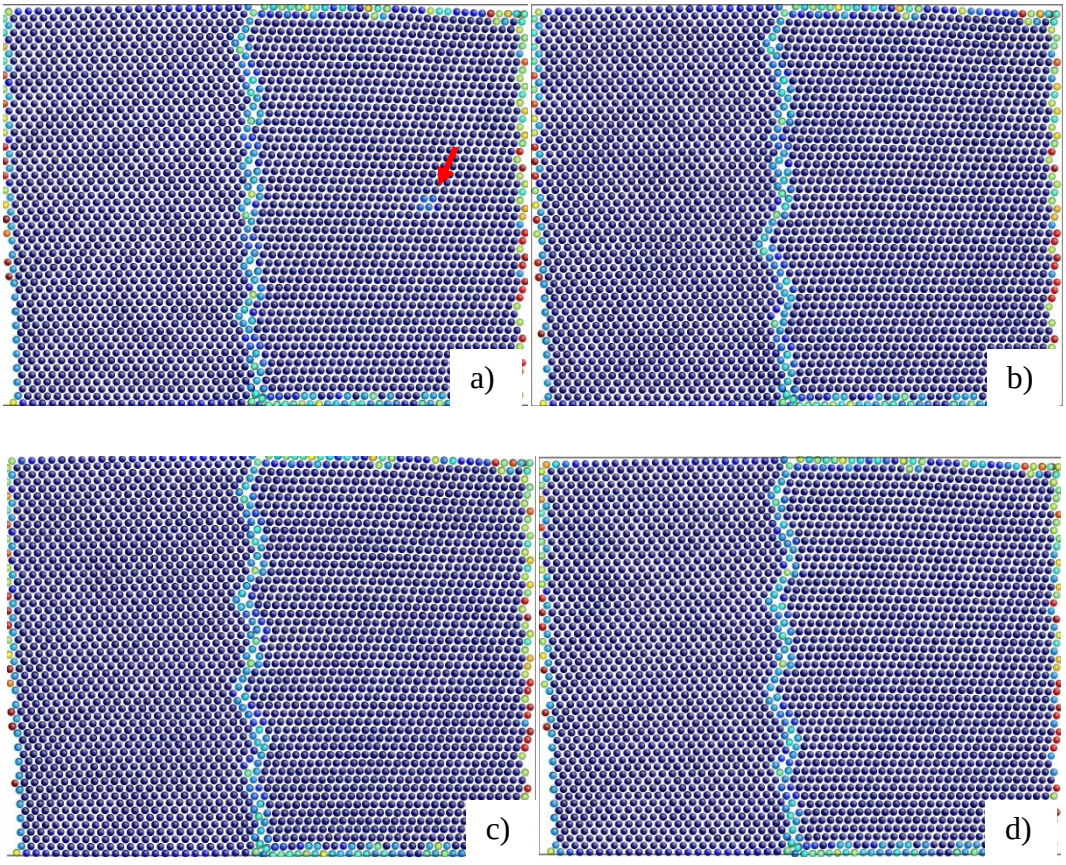

Figure 5.3 The grain boundary structure change before a) and after the interaction between grain boundaries and the incoming dislocations with different shear strain ε_{yz} for the misorientation of 54.74^{o}: b) 0.01, c) 0.02 and d) 0.1. The misorientation angles are referred to Table 5.1. The incident dislocation is marked by the red arrow in a) and the atoms are colored by the centro-symmetry parameter.

5.3.2 The interaction between grain boundaries and dislocations for large misorientation

Figure 5.3 shows the interaction between grain boundaries and the incoming dislocations with different shear strain ε_{yz} for the misorientation of 54.74°. Before the interaction, the grain boundary was straight and continuous. Moreover, all the imposed shear strains could not affect the grain boundary structure. In this study, the incident $a\sqrt{2}/2$ screw dislocation always glided in the full dislocation type on the {111} plane and was never separated into leading and trailing partial dislocations before the interaction. It can be seen that the incident dislocation was absorbed by the grain boundary and could not cut through the grain boundary regardless of the imposed shear strain. After the absorption of the dislocation the grain boundary structure was modified locally and the whole grain boundary obviously became wavy in a stable stage. Moreover, the grain boundary structure and morphology were not related to the imposed shear strain.

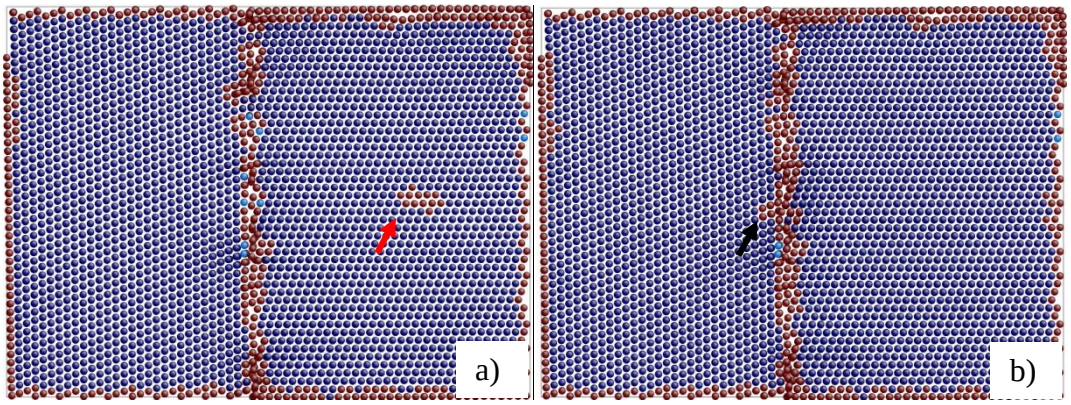

Figure 5.4 The grain boundary structure change before a) and after b) the interaction between grain boundaries and the incoming dislocations at the shear strain ε_{yz} of 0.01 for the misorientation of 19.47°. The misorientation angles are referred to Table 5.1. The incident dislocation is marked by the red arrow and the black arrow indicates the dislocation extension after the interaction. The atoms are colored by the common neighbour analysis (CNA) technique.

For the misorientation of 19.47°, the incident dislocation was also absorbed by the grain boundary and still could not cut across the grain boundary regardless of the imposed shear strain (Figure 5.4). However, in this case, the incident dislocation led to the dislocation extension [243], which may form new dislocation under proper

circumstances, on the other side of the grain boundary. Moreover, formation of this dislocation extension took out most local atoms adjustment caused by the incident dislocation. Correspondingly, the whole grain boundary was hardly affected and was still straight.

5.3.3 The interaction between GB and dislocations for small misorientation

When the misorientation was decreased to 15.79^{o}, the incident dislocation could transmit from one grain across the asymmetrical grain boundary into the neighboring grain for certain shear strain.

Figure 5.5 shows the interaction between grain boundaries and the incident dislocation for the shear strain of 0.01 with the misorientation of 15.79^{o}. Although the incident dislocation could not cut across the grain boundary for the shear strain of 0.01, the dislocation extension already formed on the other side of the GB. In the present study, the dislocation extension was characterized as the nucleation of the 30^{o} Shockley partial dislocation. It is worth noting that the incoming slip plane and outgoing slip plane were different with a plane shift. This is consistent with Dewald's founding that [290] the dislocation transmission across a grain boundary is not as simple as often envisioned, and that sometimes relaxation of the grain boundary is required to accommodate the shift in slip planes.

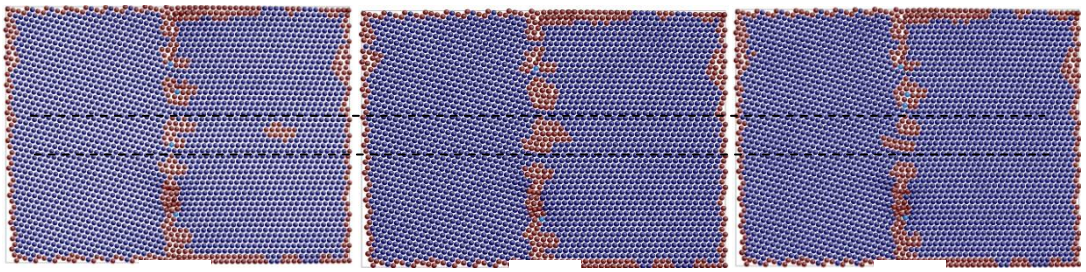

a) b) c)

Figure 5.5 The interaction between grain boundaries and the incident dislocation for the shear strain of 0.01 with the misorientation of 15.79^{o}: a) before interaction, b) absorption by the grain boundary and c) dislocation extension formation with a shift of the slip planes. The black dot lines indicate the shift of the slip planes. The atoms are colored by the common neighbour analysis (CNA) technique.

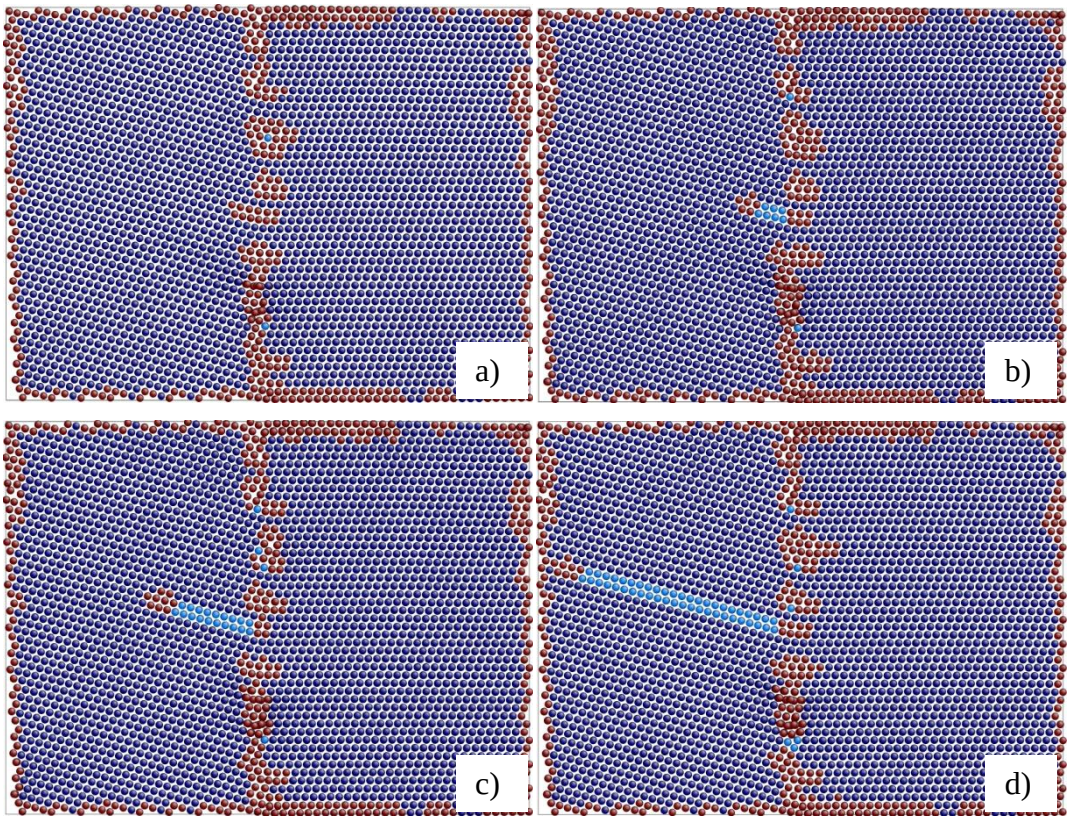

Figure 5.6 The dependence of the partial dislocations traveling distance on the imposed shear strain with the misorientation of 15.79^{o}: a) 0.02, b) 0.03, c) 0.04 and d) 0.05. The atoms are colored by the common neighbour analysis (CNA) technique.

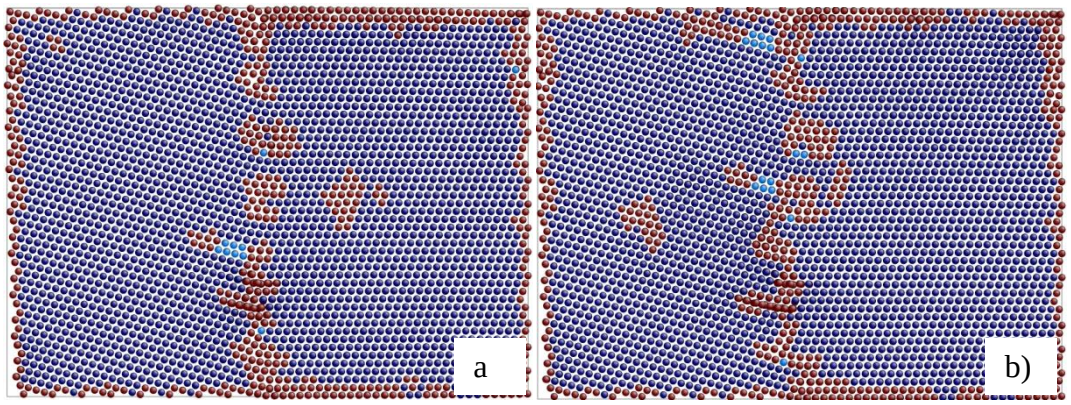

Figure 5.7 The interaction between grain boundaries and the incident dislocation for the shear strain of 0.1 with the misorientation of 15.79^{o}: a) before interaction and b) absorption by the grain boundary.

For the shear strain of 0.02, the results were basically the same as that for the shear strain of 0.01. With the further increasing shear strain, however, the partial dislocation gradually cut in the other side grain with a stacking fault behind as shown

in the Figure 5.6. It is readily understood that the partial dislocations traveling distance is proportional to the imposed shear strain. Besides, even for the shear strain of 0.05 when the leading partial dislocation already reached the system boundary, the trailing partial dislocation was always kept at the grain boundary. In order to see if the shear strain could lead to the depinning of the trailing partial dislocation, the shear strain was increased directly to 0.1. As shown in Figure 5.7, before the incident dislocation approached the grain boundary, the large imposed shear strain already led to the formation of dislocation extension from the grain boundary. When the incident dislocation approached the grain boundary, the grain boundary dislocation extension cut in the left grain and the depinning of the trailing partial dislocation occurred very soon. This led to a full strew dislocation formation. Besides, it can be seen that this small angle grain boundary was severely deformed by the large shear strain and emission of the partial dislocations from several parts of the grain boundary. It is worth noting that the partial dislocation nucleation sites were not necessarily the positions where the incident dislocation cut in. Therefore, in the process of the reaction between incident dislocations and grain boundaries, the motion of dislocations can be seen as the deformation transmission, while a relatively large part (not just the reaction site) of the grain boundary underwent the transmitted deformation as a whole. Correspondingly, the outgoing dislocation nucleation sites should be those energetically or structurally favorable sites for dislocation nucleation like dislocation extensions or defects on the relevant part of the grain boundary. Since the asymmetrical grain boundaries used in this study are relatively more realistic to the practical grain boundaries than those symmetrical grain boundaries, the results are relatively more consistent with the experimental results.

It can be seen in Figure 5.8 that the asymmetrical grain boundary became irregular for the very small misorientation of 10.02^{o}. Because of the small misorientation, the grain boundary can be considered as the combination of grain boundary dislocations which are relatively unsteady. Therefore, the grain boundary was twisted with some demonstrated dislocation extensions.

The results for the misorientation of 10.02^{o} are consistent with those for the misorientation of 15.79^{o}. First, the incoming slip plane and outgoing slip plane were different due to a much larger shift as shown in Figure 5.8., which also demonstrates

that the grain boundaries harmonize the deformation as a whole. Second, the incident dislocation could transmit from one grain across the asymmetrical grain boundary into the neighboring grain for certain shear strain and the partial dislocations traveling distance is proportional to the imposed shear strain (Figure 5.9). Furthermore, the depinning of the trailing partial dislocation occurred as the large shear strain was imposed (Figure 5.9 b).

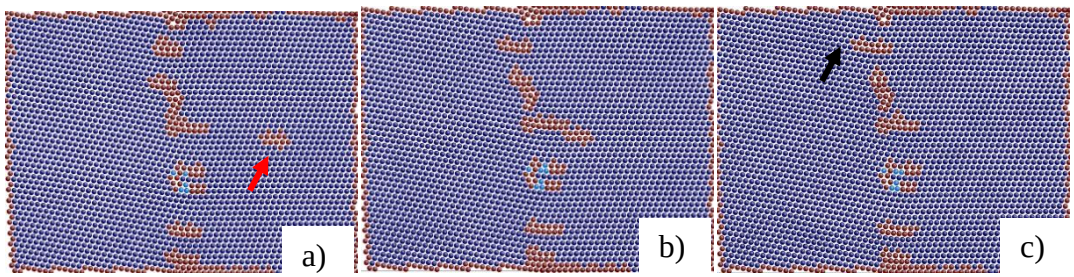

Figure 5.8 The interaction between grain boundaries and the incident dislocation for the shear strain of 0.01 with the misorientation of 10.02^{o}: a) before interaction, b) absorption by the grain boundary and c) dislocation extension formation with a shift of the slip planes. The incident dislocation is marked by the red arrow and the black arrow indicates the dislocation extension after the interaction. The atoms are colored by the common neighbour analysis (CNA) technique.

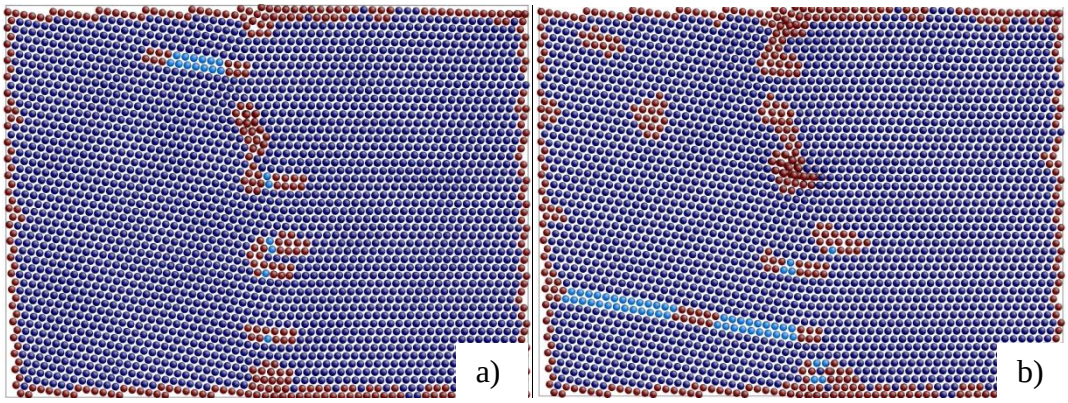

Figure 5.9 The dependence of the partial dislocations traveling distance on the imposed shear strain with the misorientation of 10.02^{o}: a) 0.04 and b) 0.1. The atoms are colored by the common neighbour analysis (CNA) technique.

In order to make the result more clear, I have recalculated the simulation models of low-angle GBs (θ=10.02 ° and θ=15.79 °) by removing the incoming dislocations. By

comparing the configurations of the outgoing dislocations with and without the incoming dislocations, the following two conclusions can be made.

(1) For the investigated low-angle dislocation, the incoming dislocation played a little role on the emission of the outgoing dislocation. The nucleation sites of the outgoing dislocation were almost the same with and without the incoming dislocation. The outgoing dislocation was mainly due to the extension of the initial GB dislocations under the applied shear strain.

(2) The incoming dislocation may cause the increase of local stress concentration at boundary plane, resulting in the emission of outgoing dislocations in advance. For example in Fig.(a), Fig.(b) and Fig.(d), when the same shear strain was applied, the outgoing dislocation has just nucleated without the incoming dislocation while the outgoing dislocation has already travelled some distances with incoming dislocations. Fig.(c) and Fig.(e) show that when the full screw dislocation has already emitted to the left grain (circled in the Figs) in the cases of with incoming dislocation, the trailing partial are still not observed in the cases without incoming dislocation.

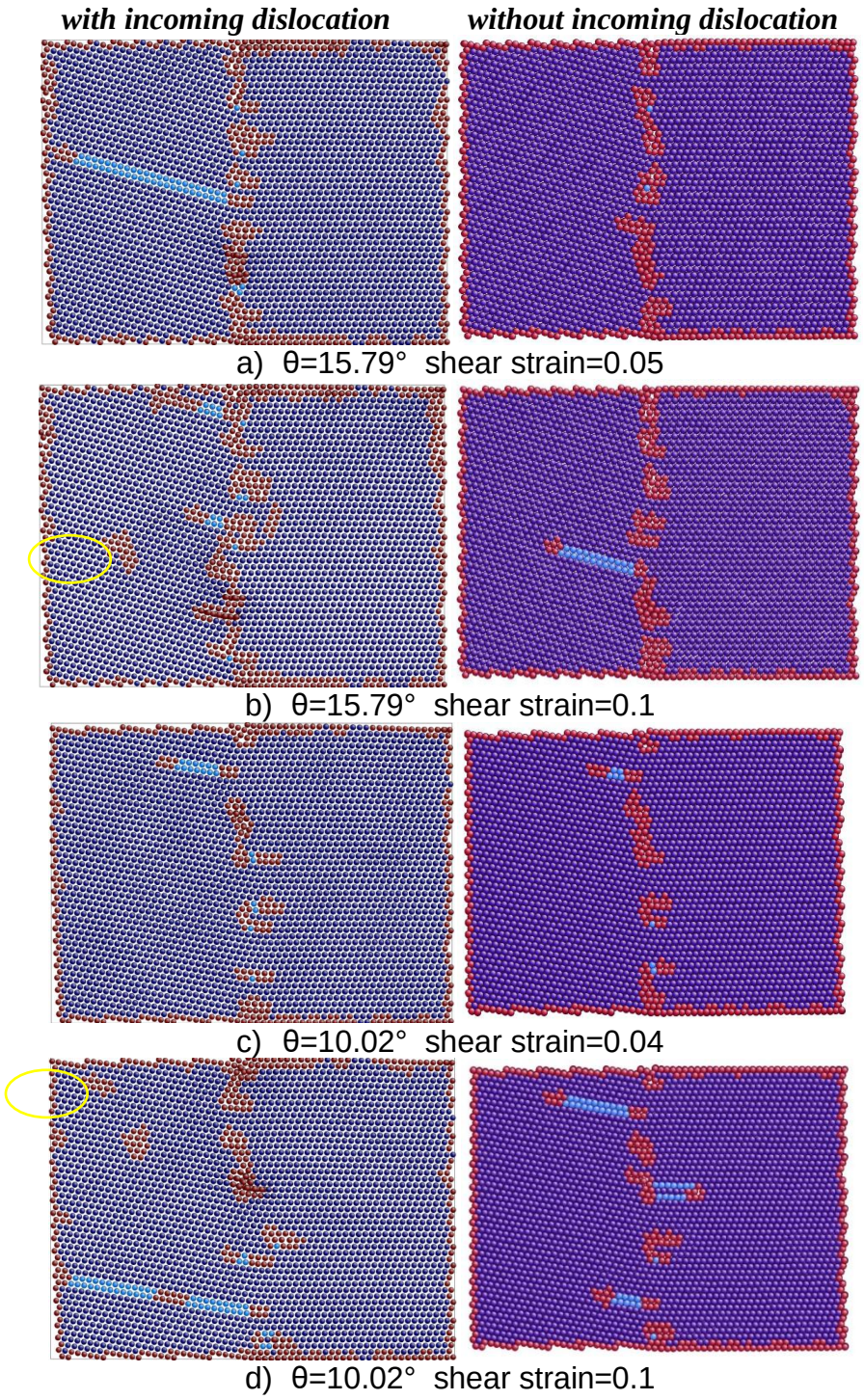

Figure 5.10 The dependence of the dislocations nucleation on the imposed shear strain with the misorientation of 10.02°: a) θ=15.79 ° shear strain=0.05, b) θ=15.79 ° shear strain=0.1, c) θ=10.02 ° shear strain=0.04 and d) θ=10.02 ° shear strain=0.1. The atoms are colored by the common neighbour analysis (CNA) technique.

5.4 Summary

In this chapter, a simple bicrystal model was applied to simulate the interaction between a straight 1/2[110] screw dislocation with several [110] asymmetrical tilt grain boundaries in Al. Correspondingly, as the EAM potential, the exact site of the interaction, the incoming dislocation characteristic and the intersection angle are fixed in all the MD simulations, the effects of grain boundary misorientation and the imposed shear stress were relatively simple to reveal. It is found that:

It is easier for the $a\sqrt{2}/2$ full screw dislocation to cut through the lower misorientation grain boundaries than the higher misorientation grain boundaries.

As the incident dislocation could transmit from one grain across the asymmetrical grain boundary into the neighboring grain for low misorientation tilt asymmetrical grain boundaries, the partial dislocations traveling distance is proportional to the imposed shear strain.

The depinning of the trailing partial dislocation required relatively large shear strain.

The incoming slip plane and outgoing slip plane were not necessarily the same and the grain boundaries harmonized the deformation as a whole.

6 SIZE EFFECT AND TENSION-COMPRESSION ASYMMETRY

6.1 Introduction

In the previous chapter, the shear response of grain boundaries was investigated. In this chapter, the applied force will be imposed normal to the grain boundary with different grain sizes, which would not only disclose the deformation mechanisms operated in atomistic scale but also macroscopically reflect the mechanical properties of materials.

Because of the outstanding mechanical properties of nanocrystalline metal material, understanding the mechanical properties becomes vital and many experimental or calculation results have been performed [329, 362, 363]. It is believed that material microstructure progresses towards nanometer scale dimensions to achieve enhanced functional properties.

It is difficult to experimentally study in detail the effect of specific interior boundaries on the mechanical behaviour and investigate the local response of twin boundaries to stress at the nanoscales. In this regard, atomistic simulation is a useful tool to investigate material structures and corresponding mechanical properties at the nanoscale, while dislocations have very limited free space or free paths to move at this scale.

Yue et al.'s simulation results suggest that the twin boundary blocks dislocation movement is more effective and the degree of emitting dislocations under stress is considerably lower than that of grain boundary, leading to superior mechanical behaviour [362]. Besides, the inverse Hall-Petch relation is not applicable to the nanotwinned system. It is also demonstrated that the inverse Hall-Petch relation occurring in nanograined materials does not necessarily result from grain boundary sliding [362]. Tschopp et al. found that dislocations are nucleated at a strain very close to the maximum stress for all single crystal models. In some cases, dislocations appeared to nucleate slightly before the maximum stress is reached (1.0% below the maximum stress) [329]. Moreover, the asymmetry in dislocation nucleation stress between tension and compression is of particular interest. Atomistic simulations also provide an effective tool for analyzing this tension-compression asymmetry. [329]

In this chapter, the Σ13 (320) symmetrical tilt grain boundary was used to simulate the size effect and tension-compression asymmetry in Al.

6.2 Methods

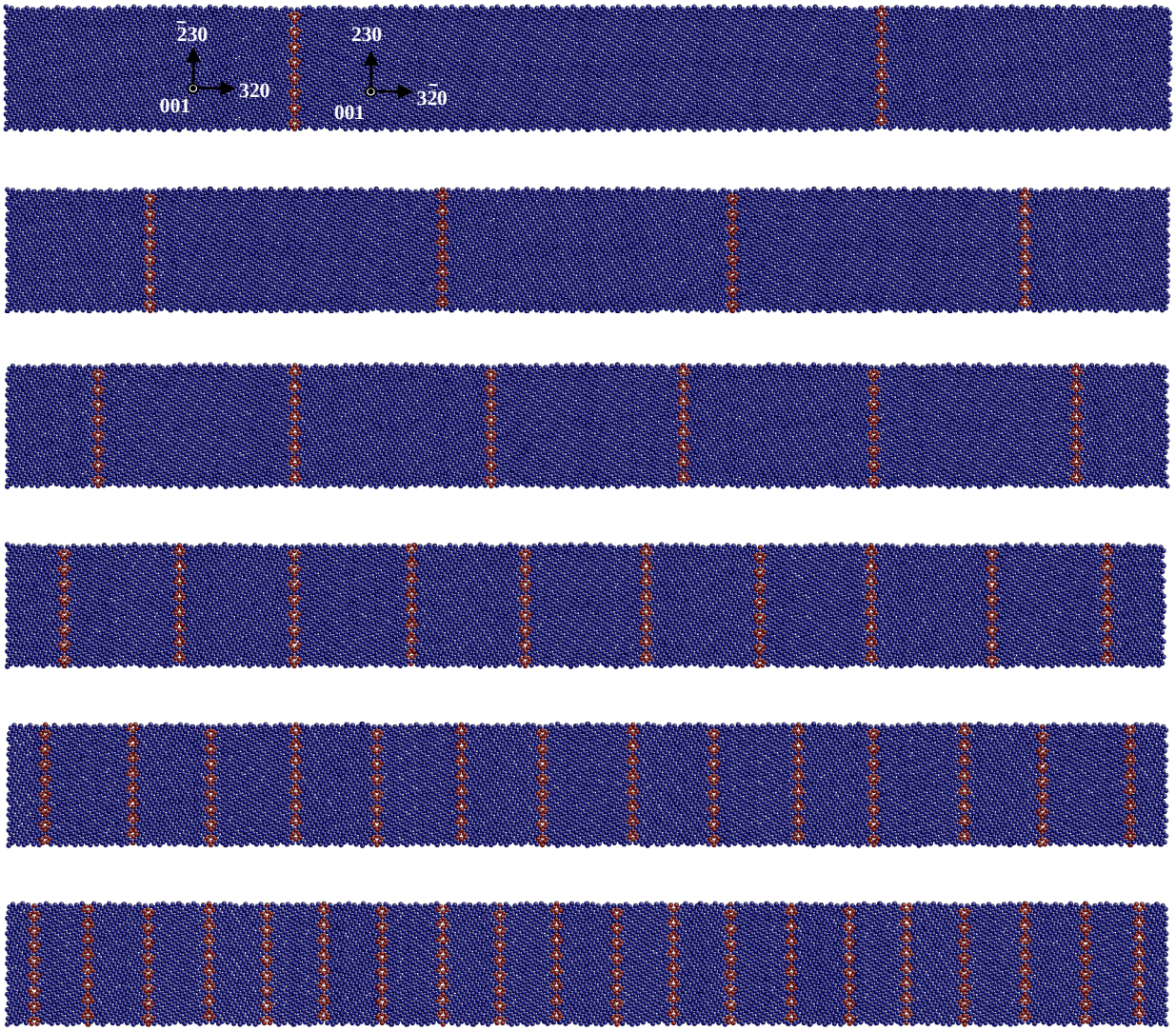

Figure 6.1 The simulation model is illustrated using the Σ13 (320) grain boundary as an example.

The simulation model is illustrated in Figure 6.1 with the Σ13 (320) symmetrical tilt grain boundary. First, a fixed simulation box was constructed with 100 period cells in the X-direction, 10~11 period cells dependent on orientations in Y-direction to guarantee the period continuity, and 10 period cell periods in Z-direction. Then, the tilt grain boundaries were constructed perpendicular to X-direction with equal spacing. To investigate the size effect, 2, 4, 6, 10, 14 and 20 grain boundaries were

constructed for each case of the tilt grain boundaries, where the orientation is the same for every other grain. Thus, the total atoms in each system varied with the orientations and the number of grain boundaries. Figure 6.2 shows the dependence of total atoms on the orientations and the number of grain boundaries. It can be seen that the maximum difference of the total atoms caused by grain boundaries is less than 2% and the total atoms in the system decreased linearly with the increasing grain boundaries.

Besides, the grain boundary structures for Σ13 (320) are all regular regardless of the number of grain boundaries as shown in Figure 6.1. Throughout this work, periodic boundary conditions were used in all directions. After the setup of the grain boundaries, the system was equilibrated using MD in the NPT ensemble at a pressure of 0 bar and the corresponding tested temperatures (10K and 300K in this work) for 50000 timesteps. The timestep is 1 fs. Next, the system was uniaxially strained in tension or compression with a constant strain rate of 1×10^{8} s^{-1} applied perpendicular to the boundary (in X-direction) while controlling the lateral boundary motion using a zero stress condition governed by the NPT equations of motion. During the tension or compression the system stress was calculated by the virial definition.

6.3 Macroscopically elastic and mechanical behaviours (Modulus and yielding)

Figure 6.3 shows the stress-strain curves obtained during tensile and compressive deformation at the strain of 1×10^{8} s^{-1} at 10K. As a whole, it can be seen that the slopes of stress-strain curves evolve differently before obvious yielding with respect to the load directions, which indicates the tension-compression asymmetric ability of the Σ13 (320) symmetrical tilt grain boundary.

First, the slopes are linear and basically with the same as the values around 76 GPa at the very beginning of deformation (0.2%) regardless of in tension or in compression. This stage is strictly elastic and reflects the intrinsic property of Al. In the second stage, with the increasing grain boundaries the reduction in the Young's modulus can be readily observed from the slightly decreasing slopes for both tension and compression. It can be clearly seen in the right inset of Figure 6.3 that the Young's modulus, which was obtained between the strains of -1% and 1% for each grain size,

decreased with the decreasing grain size. It is well known that the elastic modulus of a solid is determined by its atomic bond strength and crystal structure and that it should be affected by interfaces such as grain boundaries [362]. Since the system size was fixed in the present study, the volume fraction of grain boundaries would increase linearly with the grain boundaries. Besides, it will be shown in the next section that the thickness of grain boundaries obviously increased during deformation in this stage, which also contributed to the volume fraction of grain boundaries. Therefore, the influence of the boundaries on the elastic modulus was clearly observed in the present study. It is also worth noting the square part that is enlarged in the inset at the up left corner of Figure 6.3. With the increasing grain boundaries, the stress-strain curves show obvious steps like small yielding before the serious yielding. This is another evidence of the effect of grain boundary volume fraction and will be further explained in the next section.

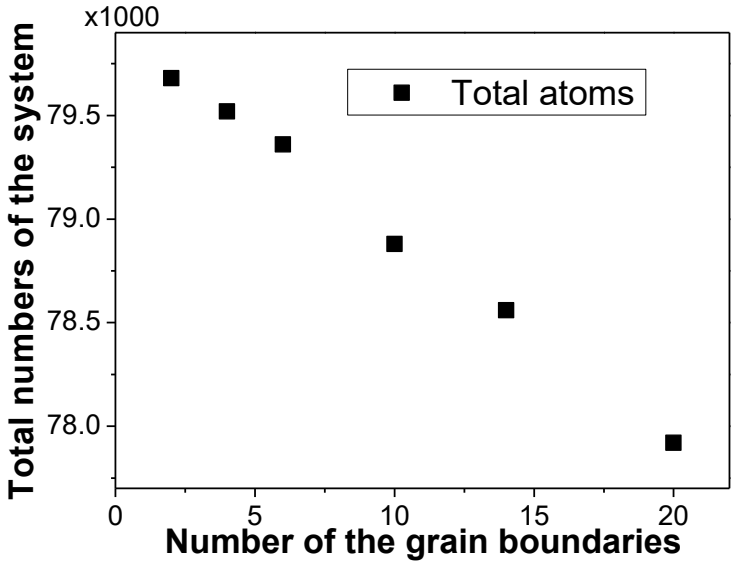

Figure 6.2 The dependence of total atoms on the orientations and the number of grain boundaries for the Σ13 (320) symmetrical tilt grain boundary.

On the other hand, the slopes gradually decreased with deformation in tension but increased with deformation in compression. This shows the tension-compression asymmetric ability of the Σ13 (320) grain boundary. As the maximum tensile or compressive stresses are achieved, the stress-strain curves show sharp drops. It shows later that this stage was either associated with the partial dislocation

nucleation event or the grain boundary fracture. Therefore, the yield strength was regarded as the maximum tensile or compressive stress achieved during deformation throughout this work. Figure 6.4 shows the yield strength and the corresponding yield strain with respect to the grain size at 10K. It can be seen that both the tensile and compressive yield strength are decreased with the decreasing grain size, which obeys the inverse Hall-Petch relationship in the current range of grain size. Moreover, the compressive yield strength is obviously higher than the tensile yield strength. It also shows that the corresponding yield strain is increased with the decreasing grain size for compression. Although the relationship between the corresponding yield strain and the grain size seems relatively irregular in tension, it is in the trend for most cases that the corresponding yield strain is increased with the increasing grain size. This load-direction dependent relationship between the corresponding yield strain and the grain size is clearly evident at 300K as shown in Figure 6.5.

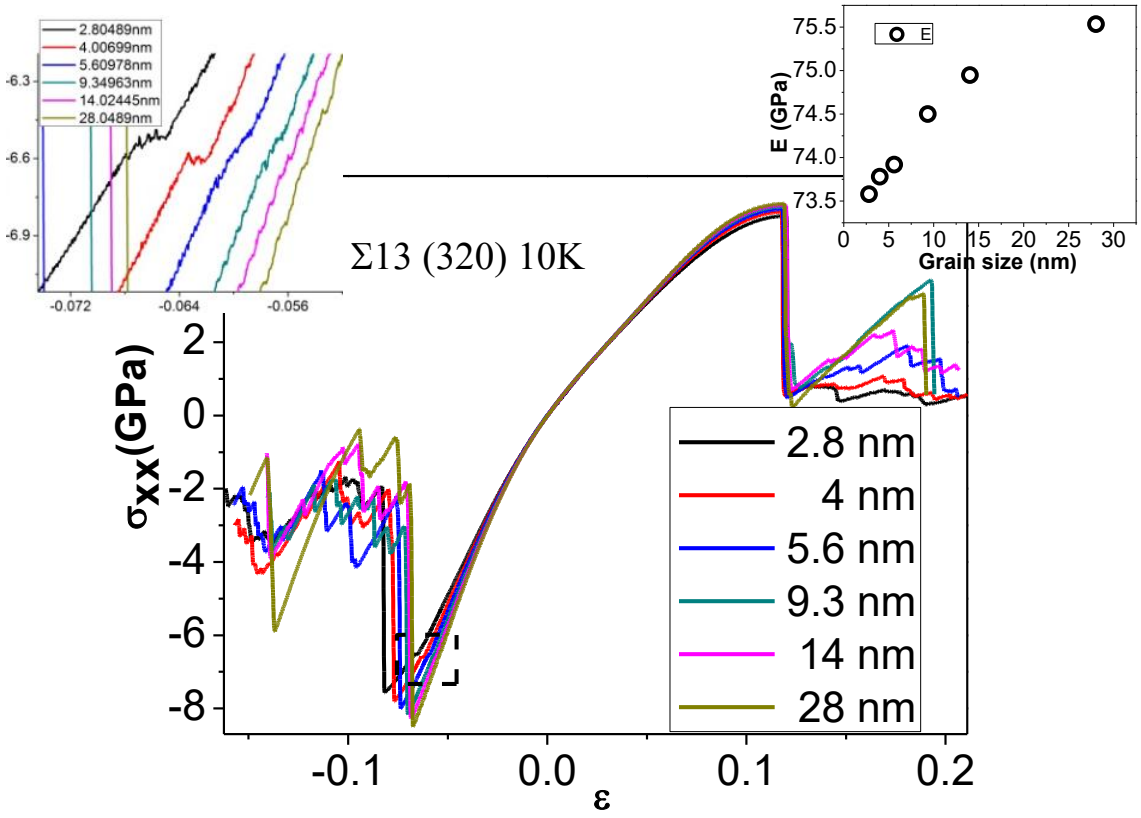

Figure 6.3 The stress-strain curves obtained during tensile and compressive deformation at the strain of 1×10^{8} s^{-1} at 10K. The black dash square part is enlarged in the inset at the up left corner and the right inset shows the Young's modulus obtained between the strains of -1% and 1% for each grain size.

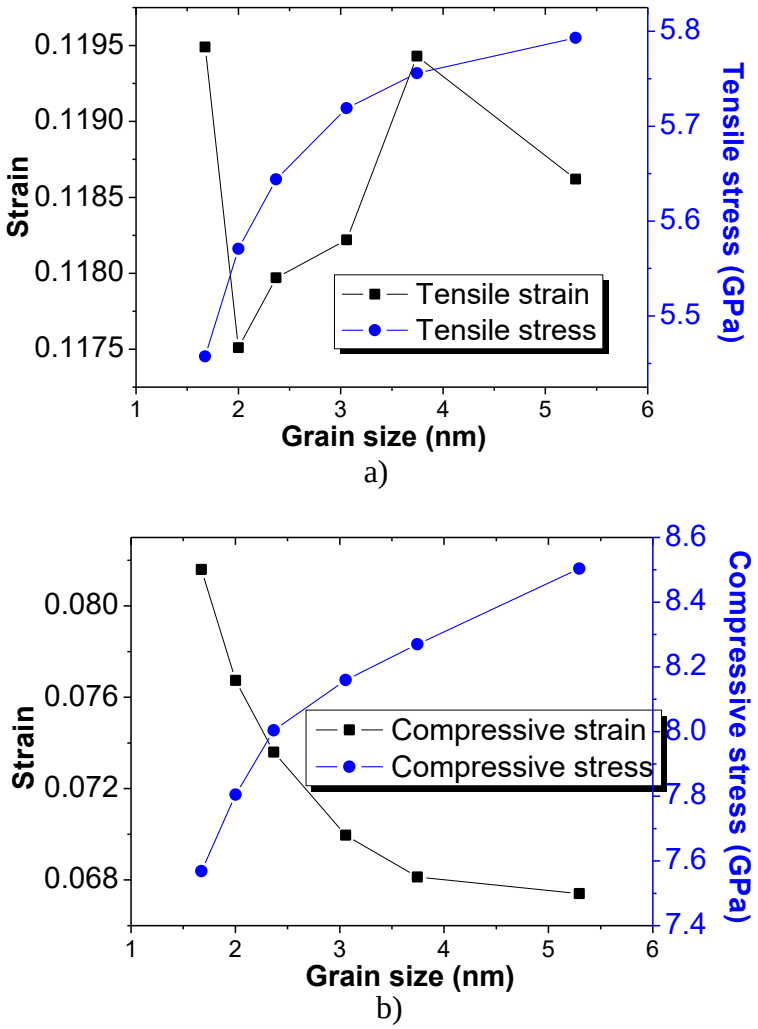

Figure 6.4 Yield strength and the corresponding yield strain with respect to the root of grain size ($d^{1/2}$) at 10K: a) in tension and b) in compression.

Figure 6.5 shows the corresponding elastic and mechanical behaviours at 300K. It can be seen that most of the same phenomena observed at 10K are also evident at 300K. First, the slopes are linear only at the very beginning of deformation and with further deformation they are decreased with the increasing grain boundaries regardless of in tension or in compression. Second, as the grain boundaries increase, the stress-strain curves show obvious steps like small yielding before the serious yielding. Third, the slopes gradually decreased with deformation in tension but increased with deformation in compression. Most importantly, both the tensile and compressive yield strength obey the inverse Hall-Petch relationship in the current

range of grain size and the compressive yield strength is obviously higher than the tensile yield strength.

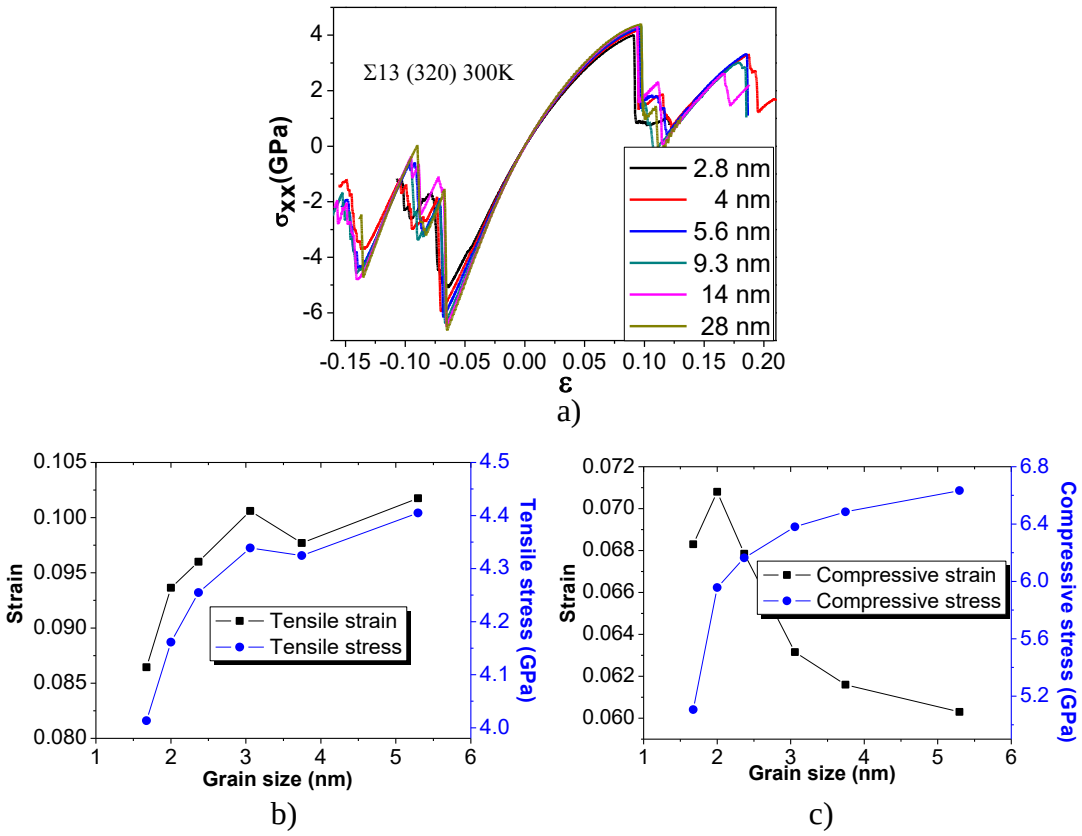

Figure 6.5 The corresponding elastic and mechanical behaviours at 300K: a) the stress-strain curves obtained during tensile and compressive deformation at the strain of 1×10^{8} s^{-1}, b) yield strength and the corresponding yield strain with respect to the root of grain size ($d^{1/2}$) in tension and c) in compression.

Besides, the corresponding yield values are obviously lower than those at 10K due to the temperature dependence of the yield stress [364]. Finally, the reverse trends of the corresponding yield strain varying with the grain size due to the opposite load directions can be clearly observed at 300K. This is another evidence of the tension-compression asymmetric ability of the Σ13 (320) grain boundary.

6.4 Microstructural observation

In order to obtain more detailed and specific information for better understanding of the yielding behaviour, size effect and the tension-compression asymmetric ability of

the Σ13 (320) grain boundary etc, the atomic structures and the corresponding stress distributions at different stages were carefully investigated and analyzed.

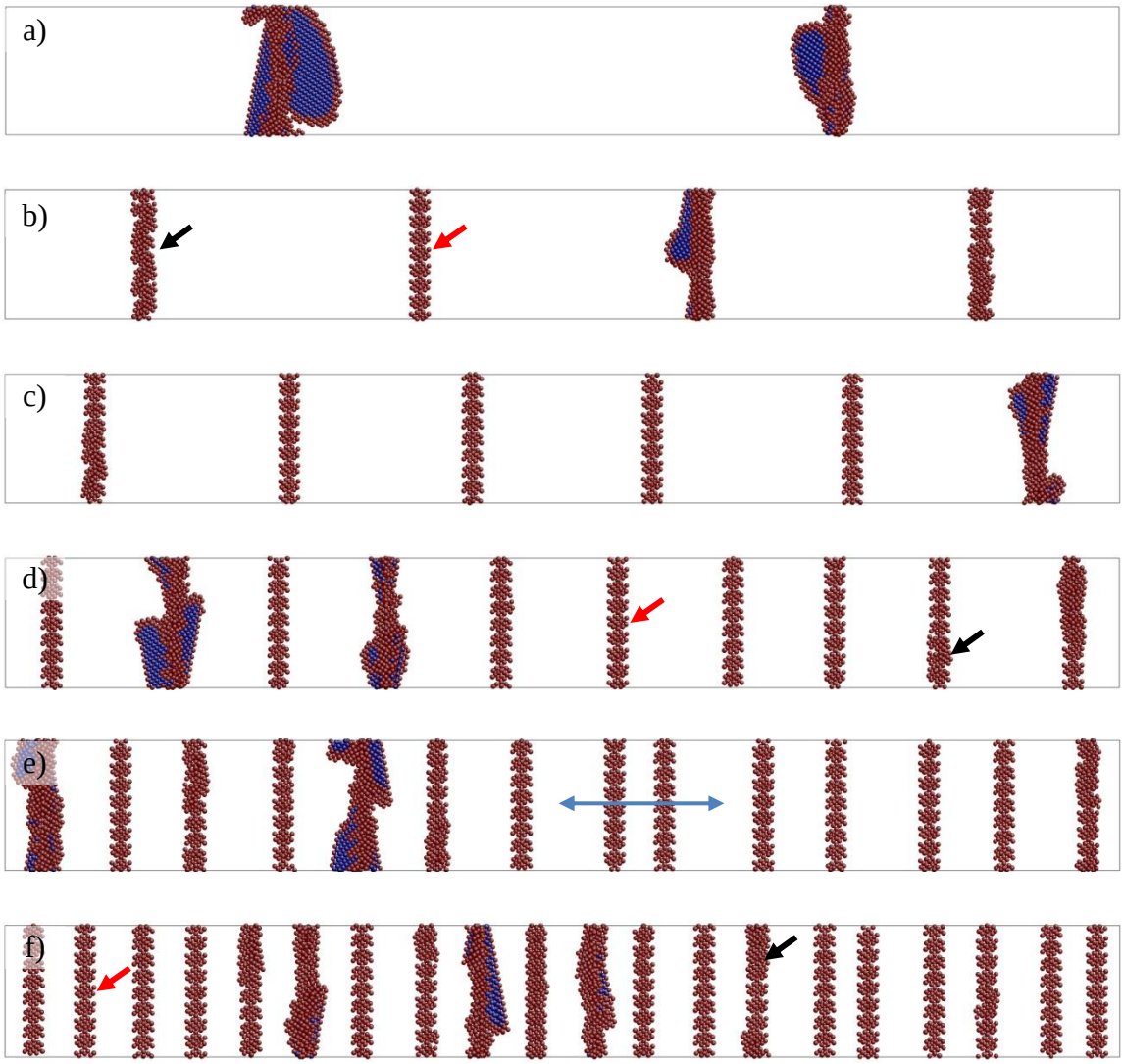

Figure 6.6 Nucleation of dislocations from the grain boundaries at the beginning of the yielding stage with different grain sizes in compression at 10K: a) 28 nm, b) 14 nm, c) 9.3 nm, d) 5.6 nm, e) 4 nm and f) 2.8 nm. The atoms are colored according to the CNA number. The atoms with a CNA parameter of 1 were removed to facilitate viewing of the defect structures. The red arrows point out the thickened grain boundaries caused by the compression and the black arrows for the distorted grain boundaries just prior to the dislocation nucleation. The blue arrow indicates the occurrence of grain boundary migration.

a. Yielding causes

Since the causes of yielding are usually mostly concerned, the yielding behaviour is firstly investigated.

Figure 6.6 shows the atomic configurations at the beginning of the yielding stage with different grain sizes in compression at 10K. It can be seen that regardless of the grain size the severe yielding was always caused by the nucleation of partial dislocations at the grain boundaries for compression. This is confirmed by many previous studies where the grain boundaries act as the dislocation resources [243, 303].

Yue et al. argued that the general grain boundaries usually have disordered structure with vacancies and some free space which result in higher strain energy of the grain boundaries, making them as the preferential region for the dislocation emission. However, it is difficult for the twin boundary to generate or emit dislocations due to its ordered structure [362]. Therefore, the ordered symmetry of grain boundaries plays a significant role in dislocation emission. The symmetrical tilt grain boundaries, such as the Σ13 (320) grain boundary for the present simulation, have higher symmetry than general grain boundaries but lower than the twin boundaries. It is worth noting that the grain boundaries have been severely thickened by the compressive deformation. The coarsened grain boundaries still kept certain symmetry at first and then were distorted just prior to the yielding. They thereby became disordered and acted as the preferential region for the dislocation emission. The coarsened and distorted grain boundaries indicate the concentration of both deformation and stress at the grain boundaries in compression. Figure 6.7 shows the atomic configurations just before the grain boundaries were distorted by the compressive deformation with the grain size of 9.34963nm at 10K, where the atoms are colored according to the CNA parameter, coordination number and the stress σ_{xx} respectively. It can be seen that the coarsened grain boundaries show the good symmetry in this stage (Figure 6.7 a) and b)) and it is consistent with Spearot et al.'s results that the coarsening at the interface distorts the interface structural units in such a way as to increase the local coordination of atoms in the vicinity of the interface as shown in Figure 6.7 b) [363]. The stress concentration was also confirmed at the grain boundaries. Therefore, the dislocation always nucleated at the grain boundaries in compression.

On the other hand, the coarsened grain boundaries also indicate that the grain boundaries were compressed or deformed more than the bulk. As shown previously, with the increasing grain boundaries the Young's Modulus decreases. This also means that the grain boundary part is relatively softer than the bulk. Therefore, the system can take more compressive deformation prior to yielding with the increasing grain boundaries (or the decreasing grain size). This well explains that the corresponding yield strain is increased with the decreasing grain size as shown in Figure 6.4b) and 6.5 c). Besides, unlike Yue et al.'s method no atom was fixed

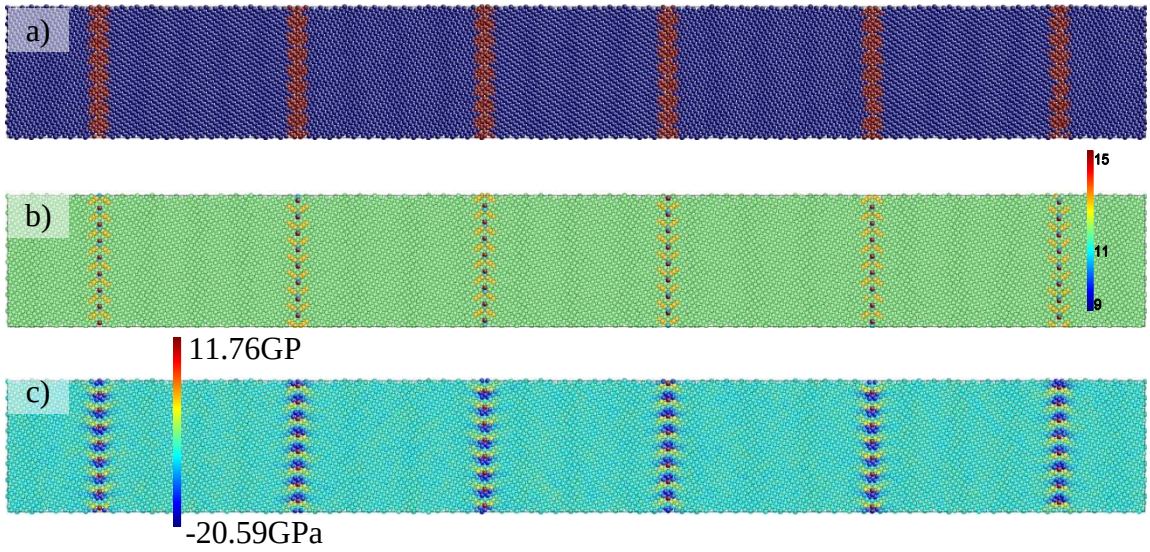

Figure 6.7 The atomic configurations just before the grain boundaries were distorted by the compressive deformation with the grain size of 9.3 nm at 10K, where the atoms are colored according to a) the CNA parameter, b) coordination number and c) the stress σ_{xx}.

during the simulation in the present study. Therefore, although the applied stress is uniaxial and normal to the grain boundaries, the high applied stress can cause the relative movement of the adjacent grains in the Y and Z directions (coupling or grain boundary sliding). As shown in Figure 6.6 e), the grain boundary coupling obviously occurred during the compressive deformation. The grain boundary sliding may also take place, though little. It is found that the contribution of these kinds of grain boundary motion to the yielding is insignificant and indirect. However, the occurrence of them would result in unavoidable perturbations to the grain boundary symmetry and then make it easy for dislocation emission. As the grain size is smaller, the relative movement between adjacent grains becomes easier to take place and correspondingly it is easier for dislocations to nucleate at the grain boundaries. In the

present study, the simulation systems are free of dislocations, so the yield strength is directly related to the dislocation nucleation. Therefore, the yield strength and the grain size obey the so-called inverse Hall-Petch relation. Our results from the simulation also suggest that the softening of nanocrystalline metals might be related to any kinds of the grain boundary motion but not necessarily. This is consistent with Yue et al.'s results [362].

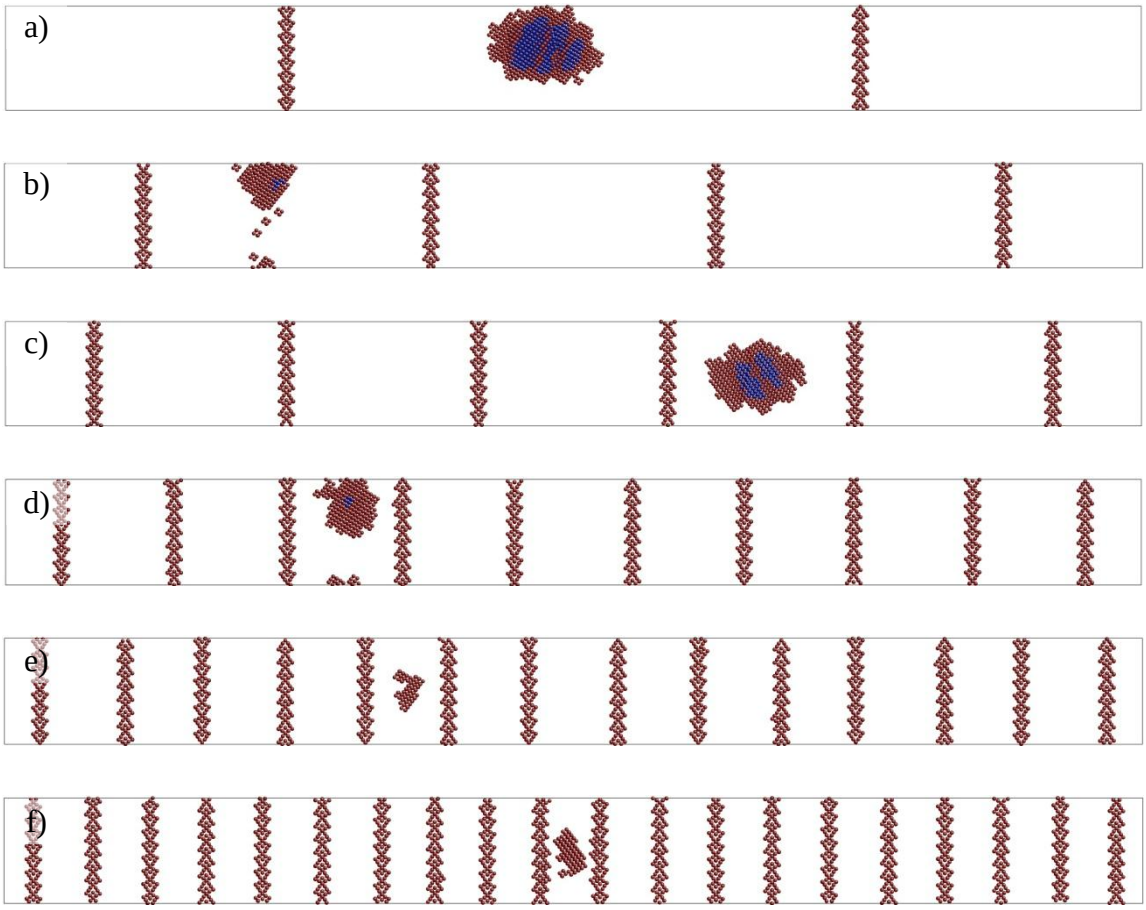

Figure 6.8 Nucleation of dislocations inside the grains at the beginning of the yielding stage with different grain sizes in tension at 10K: a) 28 nm, b) 14 nm, c) 9.3 nm, d) 5.6 nm, e) 4 nm and f) 2.8 nm. The atoms are colored according to the CNA number. The atoms with a CNA parameter of 1 were removed to facilitate viewing of the defect structures.

Figure 6.8 shows the atomic configurations at the beginning of the yielding stage with different grain sizes in tension at 10K. Very interestingly, for tension the severe yielding was always caused by the nucleation of partial dislocations inside the grains rather than at the grain boundaries regardless of the grain size. The grain boundaries were also coarsened by the tensile deformation. However, the coarsened grain

boundaries were relatively thinner than those under compression and still maintained the symmetry after the nucleation of dislocation. Figure 6.9 shows the atomic configurations just prior to the nucleation of dislocations inside grains under tension with the grain size of 28 nm at 10K, where the atoms are colored according to the CNA parameter, coordination number and the stress σ_{xx} respectively. Apart from

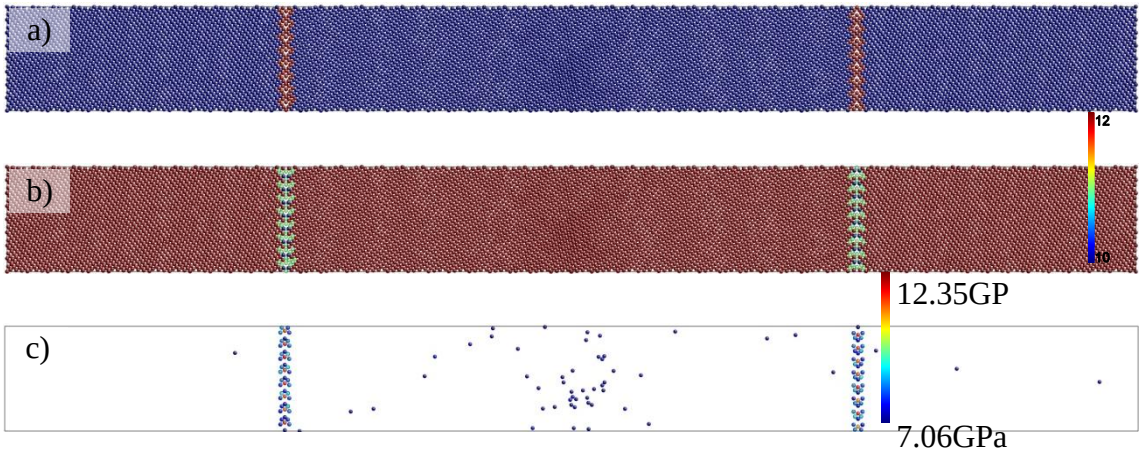

Figure 6.9 The atomic configurations just before the nucleation of dislocation inside grains under tension with the grain size of 28 nm at 10K, where the atoms are colored according to a) the CNA parameter, b) coordination number and c) the stress σ_{xx}, where the atoms with stress value below 7.06GPa were removed to clearly show the stress concentration.

the well maintained symmetry of the grain boundaries, it is contrary that the coordination number of the grain boundary atoms was decreased in the trend during tensile deformation compared to the compressive deformation. This trend can be readily understood due to the increase of the atom volume caused by tensile deformation. Importantly, the obvious change of the coordination number of the grain boundary atoms compared to the bulk ones also indicates that the grain boundaries were deformed more than the bulk during tension. This explains the relatively softer nature of the grain boundaries and the decrease of Young's modulus with the increasing grain boundaries. However, since the dislocation nucleated inside grains, the yielding was not mainly related to the grain boundaries but to the structure fluctuation inside grains. The yield strain then seemed irregular with the number of grain boundaries at 10K due to the uncertainty at extremely low temperature. In Figure 6.9 c), the atoms with stress value below 7.06GPa were removed to clearly show the stress concentration. It can be seen that the stress was still concentrated at

the grain boundaries primarily and then at the middle of the grain in the next place. The dislocation was not nucleated at the grain boundaries but inside the grains during tension. This fact might be because it is harder to break the tilt grain boundary symmetry than to start a new dislocation inside the grains. This is consistent with Yue et al.'s results for the twin boundary under tension [362].

To carefully investigate the dislocation nucleation behaviour under tension, the atomic configurations were carefully examined every femtosecond near the yielding point.

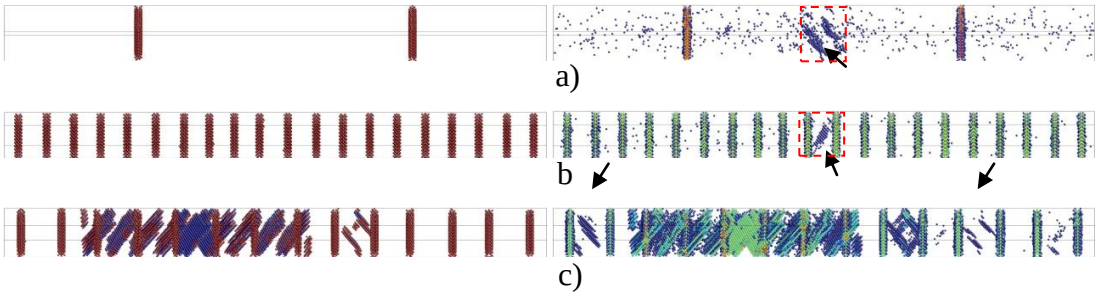

Figure 6.10 Comparison of the atomic configurations coloured by CNA (left) and centro-symmetry parameters (right) respectively at different stages for different grain sizes at 10K: a) prior to yielding with the grain size of 28 nm, b) prior to yielding with the grain size of 2.8 nm and c) after yielding with the grain size of 2.8 nm. The atoms are colored according to the CNA number. For the CNA method the atoms with a CNA parameter of 1 were removed, while for the centro-symmetry parameters only the atoms with the value between 0.15 and 10 were remained. The potential planes of partial dislocation nucleation are indicated by black arrows. The red dash square parts are analyzed in Figure 6.11.

The animation film 'Nucleation in tension' in the attachment shows that: at first the vacancies appeared and disappeared arbitrarily inside the grains prior to the yielding, then the vacancies started to gather at the middle of the grain on a particular crystallographic plane which belongs to {111} group, and finally the partial dislocation which results in the yielding nucleated at the same position and on the same crystallographic plane. The centro-symmetry parameter was used to further investigate the yielding behaviour, as it is a continuous rational number >= 0 and consequently render each atom more specific information. For FCC materials, the centro-symmetry parameters of the atoms from the bulk, dislocation cores, stacking faults and free surface are 0, ~1.0, ~5.0 and ~23.0 respectively. Therefore, the

regularity of atoms near the yielding point may be found by properly selecting the range value to keep or screen out particular atoms. Figure 6.10 shows the atomic configurations coloured by CNA (left) and centro-symmetry parameters (right) respectively at different stages for different grain sizes at 10K. For the CNA method the atoms with a CNA parameter of 1 (FCC structure) were removed, while for the centro-symmetry parameters only the atoms with the value between 0.15 and 10 were remained. Apart from the atoms at grain boundaries, the centro-symmetry parameters for the atoms are roughly between 0.15 and 1. It can be seen that prior to the yielding the potential planes for partial dislocation nucleation can be clearly observed inside the grains (Figure 6.10 a and b). These potential planes are the particular {111} planes mentioned above. Besides, these potential planes can be also found during the dislocation propagation in the system (Figure 6.10 c). This further demonstrates that the dislocations nucleate inside the grains during tension for the Σ13 (320) symmetrical tilt grain boundary.

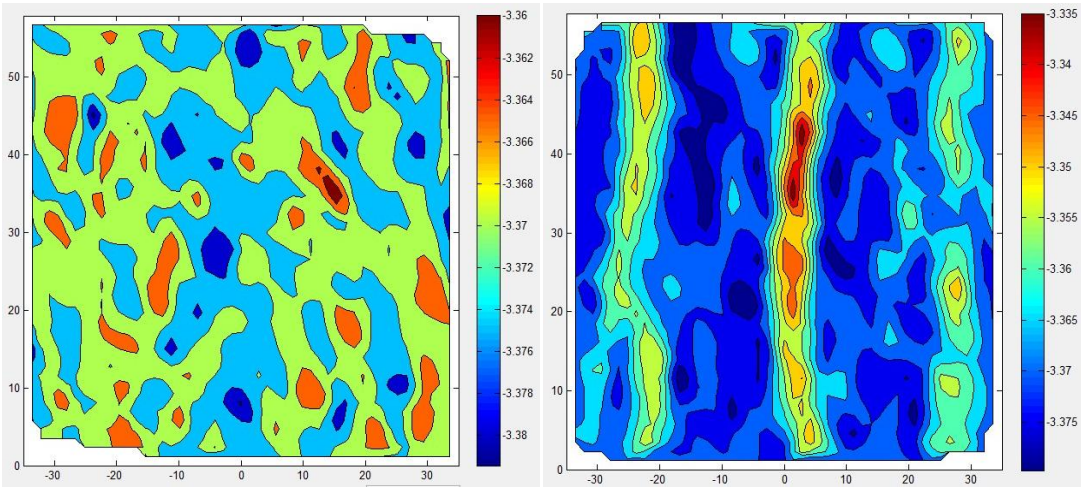

a) b)

Figure 6.11 The change of atomic potentials before yielding for the grain size of 28 nm at 10K for the interest area marked by the red dash square in Figure 6.10 a): a) 5ps prior to yielding and b) the same stage with Figure 6.10 a).The atomic potentials were averaged through the selected two typical alternative (001) planes which are indicated by two solid cycles with different colors.

These findings indicate that when approaching the yielding point with the tensile load the atoms on the potential planes inside grains for dislocation nucleation gradually deviated from the ideal FCC structure first due to particular stress

conditions or potentials. Then with further tensile deformation any of the fluctuations from the energy, stress or structure on these potential planes might lead to the nucleation of the partial dislocation. As shown in the animation film ‘Nucleation in tension’, the arbitrary vacancies are most likely the structure fluctuation for the nucleation of the partial dislocation in the present study, since the grain boundaries have relatively good symmetry and the inside grains are ideal crystals. It is also shown in the Figure 6.9 c) that the stress is concentrated inside the grains apart from the grain boundaries, which accounts for the stress fluctuation. The change of potentials during tension near the yield point was also carefully investigated. Figure 6.11 shows the change of atomic potentials before yielding for the grain size of 28 nm at 10K for the interest area marked by the red dash square in Figure 6.10 a). For the convenience of calculation, two typical alternative (001) planes across the potential plane for dislocation nucleation were selected to calculate the potential distribution. It can be seen that far from the yielding the distribution of the atomic potentials was basically uniform and the atoms hardly moved in Z direction. Just prior to yielding, however, the atomic potentials at the potential planes for dislocation nucleation were obviously higher than those nearby and the atoms in Z direction moved regularly like the saw-tooth. Figure 6.12 shows the distribution of atomic potentials just before yielding for the grain size of 2.8 nm at 10K for the interest area marked by the red dash square in Figure 6.10 b). This time four typical alternative (001) planes were analyzed and the analyzed area was large enough to enclose two grain boundaries. It can be seen that the atomic potentials were highest at grain boundary cores, secondly highest in the middle of the grain and lowest at the edges of the grain or the grain boundary. In other words, the atomic potentials descended gradually from the grain boundary to the middle of the grain except for the grain boundary cores. Although the atomic potentials were highest at grain boundary cores near the yielding point during tension, the dislocation did not nucleate from the grain boundary due to the high symmetry and structure stability here. On the other hand, the dislocation nucleated from the middle of the grain where the atomic potentials were relatively higher.

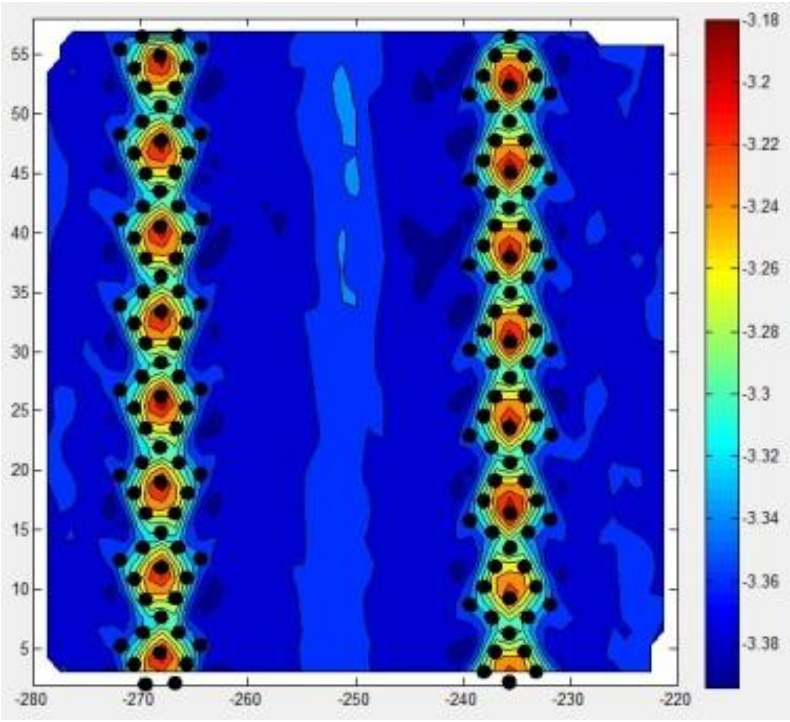

Figure 6.12 The change of atomic potentials before yielding for the grain size of 2.8 nm at 10K for the interest area marked by the red dash square in Figure 6.10 b).The atomic potentials were averaged through the selected four typical alternative (001) planes which are indicated by two solid cycles with different colours.

b. Microstrucural evolution

In the present study, the calculation and research were not only focused on the deformation mechanisms at the yielding point but also on those before and after the yielding point. For each case, several hardening and softening processes after the yielding were investigated in detail as well as the initial deformation process before yielding. The full tension-compression stress-strain curve and the corresponding microstructural evolution at each representative stage at 10K for the grain size of 28 nm are shown in Figure 6.13 to typically explain the common deformation mechanisms during tension and compression.

In tension, the microstructural evolution is relatively brief and clear, and can be described as follow.

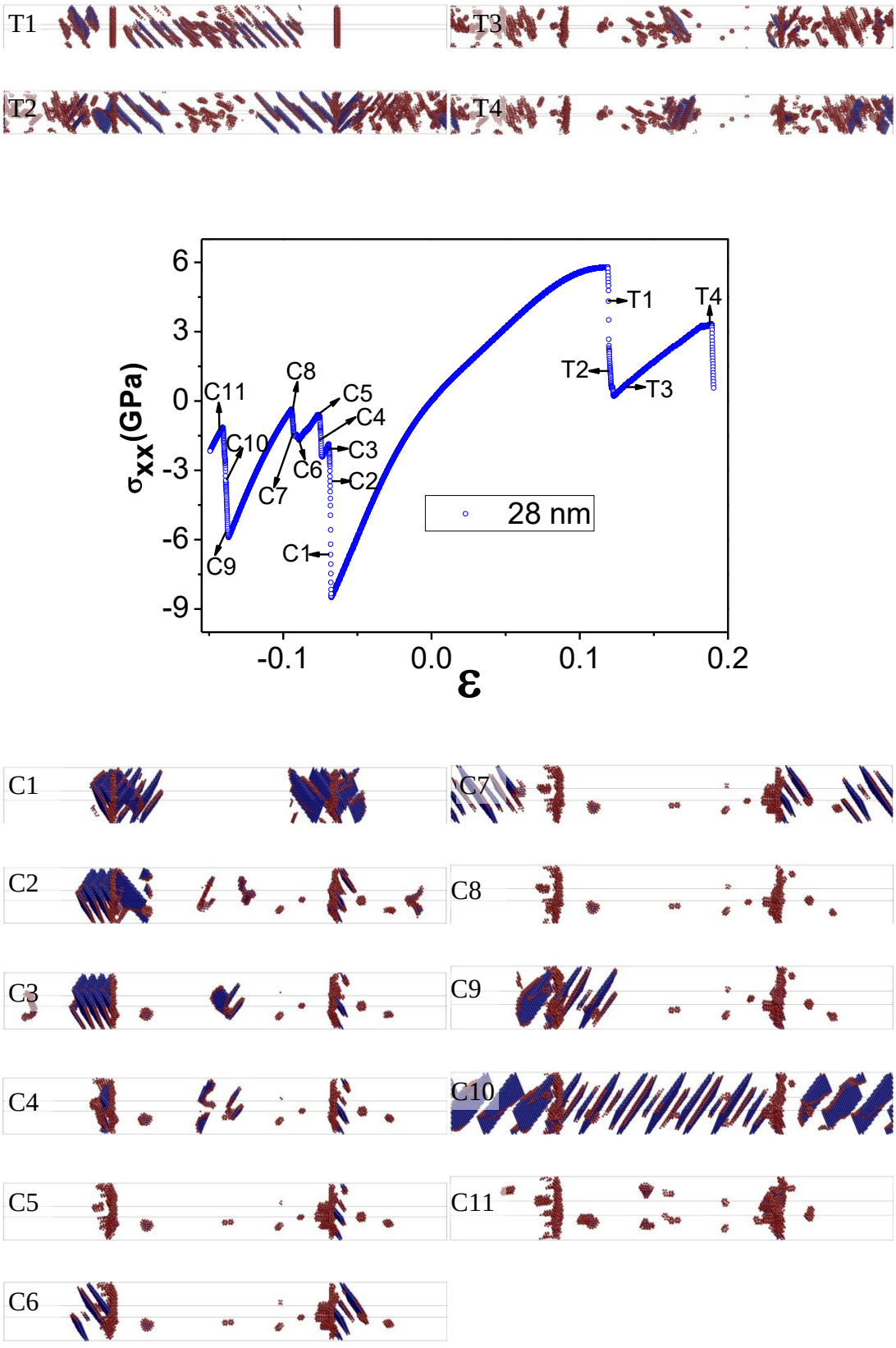

Figure 6.13 The full tension-compression stress-strain curve and the corresponding microstructural evolution at each representative stage at 10K for the grain size of 28 nm.

1) At first, the partial dislocation was nucleated on one (111) plane and the trailing dislocation turned up in a short while. Therefore, the dislocations propagated in the form of full dislocations with short stacking faults in between the leading and trailing dislocations (Figure 6.13 T1). The tensile stress severely dropped during this process.

2) Secondly, the dislocations propagated through the system; some cut through and some stopped at the grain boundaries; a few dislocations interacted and left some disordered structures inside the grains (Figure 6.13 T2). In this process the tensile stress kept reduced due to the continuous movement of dislocations.

3) Then, with the further dislocation interactions and grain boundary blocks, the dislocations were interlocked at the interacted area or stopped at the grain boundaries (Figure 6.13 T3). Thus, the microstructure became relatively stable and the tensile stress increased, which shows the hardening behaviour of the system.

4) With the continuous increase of tensile deformation and stress the partial dislocations expanded out from the interacted area of the previous dislocations (Figure 6.13 T4). Finally, one of the distorted grain boundaries could no longer undertake the relatively high tensile stress, leading to fracture at the grain boundary and sharp drop of the tensile stress.

In compression, the microstructural evolution is complicated and can be different case by case. Here, the general deformation process for each case can be described as follows based on the Figure 6.13 and the specific deformation details for particular cases will be presented in the next part.

1) Firstly, the partial dislocations generally nucleated on two (111) plains at the grain boundaries and propagated for a relatively long distance in the form of leading dislocations and wide stacking faults (Figure 6.13 C1).The compressive stress severely dropped during this process.

2) Secondly, it was found that there are two ways of dislocation propagation based on the particular propagation direction: when along the intersection line of two (111) planes, the dislocations propagated steadily with two stacking faults on (111) planes respectively; when perpendicular to the intersection line of two (111) planes, one of the two (111) partial dislocations gradually became predominant in propagation and

the trailing dislocation turned up after a while, which finally led to the full dislocation propagation (Figure 6.13 C2). In this process the compressive stress kept reduced due to the continuous movement of dislocations.

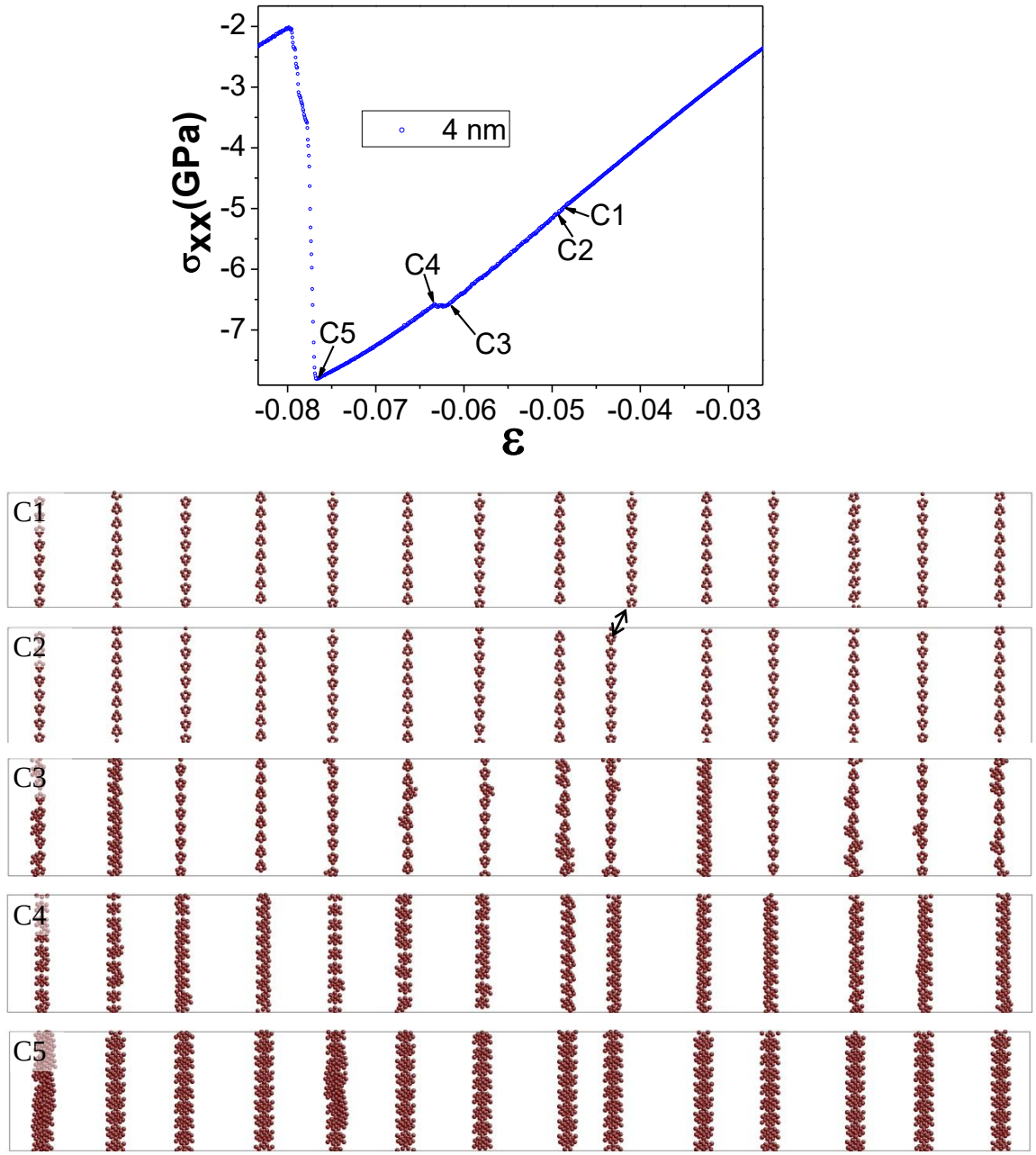

Figure 6.14 Microstructure evolutions before yielding and the corresponding stress-strain curve in compression with the grain size of 4 nm at 10K. The black arrow indicates the grain boundary coupling behaviour.

3) Next, two of the full dislocations met in the middle of the grain and formed the Lomer-Cottrell dislocations which play a significant role in work hardening, while

another full dislocation kept propagating (Figure 6.13 C3). The effect of work hardening caused by the Lomer-Cottrell dislocations can be clearly reflected in the stress-strain curve, where there is a small increase of the compressive stress.

4) With further deformation, the Lomer-Cottrell lock was separated back into two full dislocations which just had the inverse trailing and leading with previous ones and moved back toward the grain boundaries at each side; another full dislocation met and interacted with the previous steady stacking faults (Figure 6.13 C4). The softening was caused by the breakup of the Lomer-Cottrell lock and the compressive stress decreased.

5) Next, all the dislocations were sunk and blocked at the grain boundaries with some disordered structures which left on the traveled paths of the dislocations (Figure 6.13 C5). The microstructure kept stable and the compressive stress increased. This time, the work hardening was obvious and caused by the grain boundary blocking.

6) As the compressive deformation continually increased, the leading dislocations with stacking faults bowed out from the grain boundaries for some distance and stopped with small vibration (Figure 6.13 C6). The compressive stress reached to a peak and then slowly reduced.

7) Next, the trailing dislocation released from the grain boundaries and the dislocations propagated in the grains with large stacking faults in between the leading and trailing dislocations (Figure 6.13 C7). The compressive stress dropped.

8) Later the dislocations were sunk and blocked again at the grain boundaries (Figure 6.13 C8). Again, the microstructure kept stable and the compressive stress increased. This time, the work hardening effect caused by the grain boundary blocking was much larger than before.

9) The compressive stress severely increased until the leading dislocations emitted from the grain boundaries (Figure 6.13 C9).

10) Interestingly, the dislocations propagated with leading dislocations and stacking faults. Besides, the trailing dislocations were either held by the grain boundaries or

fixed by the disordered structures inside the grains. The compressive stress obviously dropped (Figure 6.13 C10).

11) Finally, the dislocations were sunk and blocked again at the grain boundaries. The material was hardened and the compressive stress increased again (Figure 6.13 C11).

It is believed that the above processes would always repeat with further deformation.

Therefore, the MD calculation demonstrates that in general the material was softened by nucleation and movement of dislocations and was hardened by dislocation interactions and grain boundary blocking. The softening and hardening effects were related to specific deformation mechanisms. The stress dropped sharply when dislocations generated from grain boundaries or inside grains, while the stress gradually decreased when the dislocations glided in the grains. On the other hand, the hardening effect was relatively smaller when the dislocations confronted and interacted with the other grain boundaries than when the dislocations were blocked by the grain boundaries. Therefore, for general polycrystalline materials, the yield strength is directly related to the dislocation nucleation and the barrier to its movement as well.

With the increasing grain boundaries (decreasing grain size), the effect of the grain boundary on the deformation mechanisms became obvious, especially in compression. As it was shown previously in Figure 6.3, with the increasing grain boundaries, the stress-strain curves show obvious steps like small yielding before the serious yielding. Figure 6.14 shows microstructure evolutions before yielding and the corresponding stress-strain curve in compression with the grain size of 4.00699nm at 10K. It can be seen that the grain boundary coupling was clearly observed during compression by comparing Figure 6.14 C1 with Figure 6.14 C2. Interestingly, the strain-stress curve is smooth during the grain boundary coupling, indicating that the grain boundary coupling process hardly affected the normal compressive stress in the present case. With further deformation, the compressive stress increased and the grain boundaries started to thicken gradually (Figure 6.14 C3). During the thickening process of the grain boundaries, the compressive stress slightly decreased (Figure 6.14 C4). Therefore, the small decrease of the compressive stress before yielding was

caused by the grain boundary thickening, which seems like some kind of grain boundary yielding. It is readily understood that this grain boundary thickening effect would become more obvious with smaller grain size. Near the yield point, some grain boundaries, where the dislocations nucleated, were obviously distorted (Figure 6.14 C5).

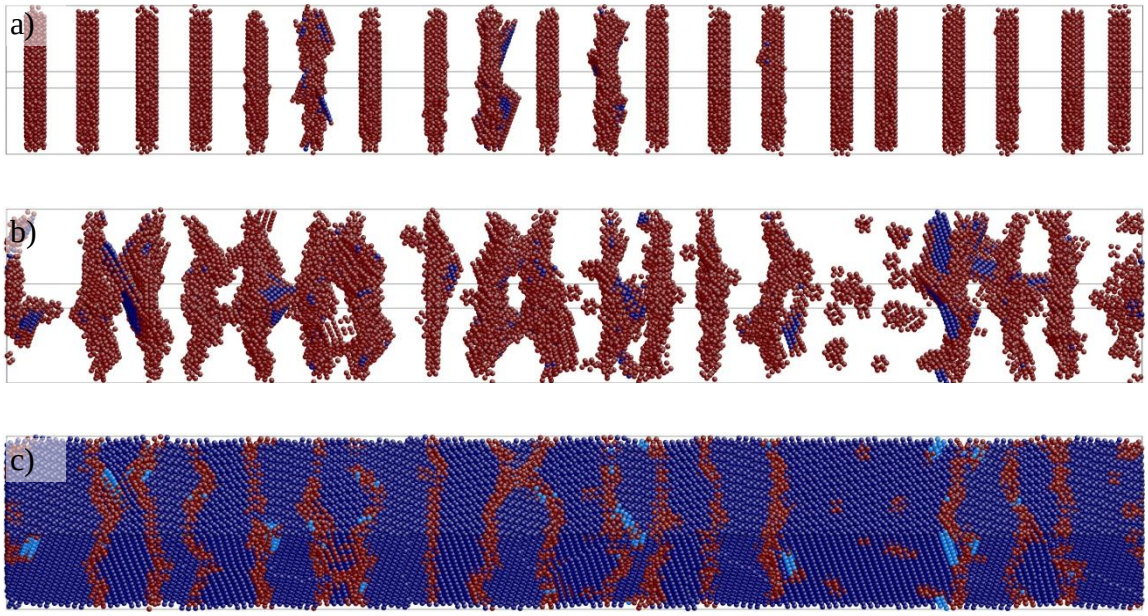

Figure 6.15 Microstructure evolutions during compression with the grain size of 2.8 nm at 10K: a) 960ps, b) 1620ps and c) 1827ps.

Figure 6.15 shows microstructure evolutions during compression with the grain size of 2.8 nm at 10K. This covers the grain boundary coupling and dislocation nucleation at grain boundaries (Figure 6.15 a), grain boundary migration, amalgamation and distortion during compressive deformation (Figure 6.15 b and c).

The thermal fluctuation became relatively severe at 300K, which led to abundant vacancies in the simulated systems. However, the yielding causes and mechanical response are basically consistent with those at 10K.

6.5 Summary

The Σ13 (320) symmetrical tilt grain boundary presented strong tension-compression asymmetric ability: the asymmetry of stress-strain curves with respect to the load directions; the yield strain was increased with the decreasing grain size for

compression , while for tension the corresponding yield strain was increased with the increasing grain size.

The Young's modulus decreased with the decreasing grain size (or increasing the grain boundary volume fraction). Both tensile and compressive yield strength were decreased with the decreasing grain size, which obeys the inverse Hall-Petch relationship in the current range of grain size.

For compression: the severe yielding was caused by the nucleation of partial dislocations at the grain boundaries regardless of the grain size; before yielding the grain boundaries have been severely thickened by the compressive deformation but still kept certain symmetry, and then became disordered and acted as the preferential region for the dislocation emission; the concentration of stress and deformation were confirmed at the grain boundaries; although the contribution of grain boundary yielding (coupling, sliding and thickening) to the yielding was insignificant and indirect, the occurrence of them would result in unavoidable perturbations to the grain boundary symmetry and then make it easy for dislocation nucleation; as the grain size was smaller, the relative movement between adjacent grains became easier to take place and correspondingly it was easier for dislocations to nucleate at the grain boundaries, which explains the inverse Hall-Petch relation.

For tension: the severe yielding was caused by the nucleation of partial dislocations inside the grains rather than that at the grain boundaries regardless of the grain size; the dislocation nucleation was dependent on the comprehensive combination of the stress concentration and the fluctuations of energy and local structure; when approaching the yielding point the atoms on the potential planes inside grains for dislocation nucleation gradually deviated from the ideal FCC structure and some arbitrary vacancies formed, which provided the structure fluctuation in the middle of the grain; the dislocation nucleated from the middle of the grain where the atomic potentials and the stress concentration were secondly highest in the system. The most important finding in the present study is that the inverse Hall-Petch relation is not necessarily related to the grain boundary deformation.

Regarding the deformation mechanisms, the softening was caused by the grain boundary yielding and the nucleation and propagation of dislocations, while the hardening was caused by dislocation interactions and grain boundary blocking.

CONCLUSIONS AND RECOMMENDATIONS

In the present thesis, atomic simulation method was used to investigate the grain boundary sliding behaviour, grain boundary coupling behaviour, the interaction between grain boundaries and dislocations, and the grain boundary tension-compression asymmetry.

In Chapter 3, the grain boundary sliding behaviour was investigated for a serial of Σ5 symmetrical and asymmetrical tilting grain boundaries under different conditions. The following was concluded:

1) Grain boundary sliding (GBS) behaviour was strongly sensitive to the temperature and regardless of the type of driving force and misorientation, the bicrystal system tended to resist the applied force by GB rotation;
2) At low temperatures, the GBS was very sensitive to the imposed ways of external applied forces. They maight lead to general crystal deformation such as GBS, grain or grain boundary rotation, coupled motion of grain boundary and dislocation release, and sometimes even led to destruction of the materials by initiating cracks or de-bonding the grain boundaries. However, at high temperatures, the two grains smoothly slid away from each other in the way of viscous grain boundary sliding under the shear deformation;
3) The GB rotation resulted from surface strain, GB migration or GB coupled motion. Moreover, the grain boundary rotated among some of the Σ5 asymmetrical and symmetrical tilt GB boundaries under shear deformation and led to the normal stress σ_{xx} in the bicrystal system;
4) Under particular circumstances reaction of the grain boundary dislocations during shear deformation could release uncommon edge lattice dislocations from the grain boundary. The uncommon edge lattice dislocations with <110>/2 Burgers vectors have the [001] line direction and glide on the {110} planes.

In the Chapter 4, the structural multiplicity of the symmetric tilt Σ5(310) boundary and its influence on grain boundary behaviour were investigated. It has been found that:

1) Two starting atomic configurations led to three different GB structures (C1, C2 and C3) after thermal relaxation, all of which consisted of structural units. The C1 GB existed for the first starting atomic configuration (SC-1) at temperatures from 300K to 600K. The C1 structural unit had a kite shape and was made up of six atoms. The C2 structural unit, on the other hand, had a similar kite shape but with an extra atom located at the core of the unit. The C2 GB appeared in those cases with a second starting configuration (SC-2) at a temperature range of 300K - 400K. The C3 structural unit was almost triangular in shape, with an extra atom situated near the right hand side of the unit. The SC-2 case at a temperature of 600K had C3 GB. In the SC-2 case at a temperature of 500K, the GB structure changed from C2 to C3 when the shear deformation reached a certain level;
2) Three GB structures induced three types of GB behaviours, all of which clearly demonstrated that the structural multiplicity of GB did affect its behaviour. With the first type of behaviour the GB motion displayed a periodic stop-and-go mechanism and the shear stress was of regular stick-slip behaviour. The coupling factor was close to unity at lower temperatures and it decreased with the temperature. With the second type of behaviour the GB motion and shear stress were more stochastic. Besides, its coupling factor was smaller than the first type of behaviour at the same temperature. In the first two types of GB behaviour the GB migrated to the negative X direction, but for the third type, the GB motion displayed a slowly-move and quickly-go mechanism, while the GB migrated in an opposite direction to the previous two types. The coupling factor for the third type of GB behaviour was much higher than that for the other two types. Because the GB changed its structure during deformation, the SC-2 case at a temperature of 500K displayed a dual behaviour. That is, the GB first moved to the negative X direction under the imposed shear deformation and then changed to the positive X direction when the shear strain exceeded a certain value;

3) The atomic mechanism responsible for the behaviour of each GB has been analysed in detail. The results have revealed that the atoms around the GB tended to occupy three metastable sites: i) the parent lattice site of the left grain; ii) the parent lattice site of the right grain; iii) the symmetric position of two grains. Under the applied shear deformation the atoms around the GB moved from one metastable site to another, but its direction of migration depended mainly on the new metastable position occupied by the atom with the highest energy. While the GB atoms moved from the old metastable position to the new metastable position, an instantaneous disconnection between two grains occurred. This resulted in the fact that the shear stress suddenly dropped and was then released in the grains. As the atoms around the GB proceeded to their new positions they would build new connections with surrounding atoms and form a new GB structure.

In the Chapter 5, the interaction between a straight 1/2[110] screw dislocation with several [110] asymmetrical tilt grain boundaries were simulated with different applied shear stress. It can be concluded that:

1) It was easier for the $a\sqrt{2}/2$ full screw dislocation to cut through the lower misorientation grain boundaries than the higher misorientation grain boundaries;
2) As the incident dislocation could transmit from one grain across the asymmetrical grain boundary into the neighboring grain for low misorientation tilt asymmetrical grain boundaries, the partial dislocations traveling distance was proportional to the imposed shear strain;
3) The depinning of the trailing partial dislocation required relatively large shear strain.
4) The incoming slip plane and outgoing slip plane were not necessarily the same and the grain boundaries harmonized the deformation as a whole.

In the Chapter 6, the Σ13 (320) symmetrical tilt grain boundary was used to simulate the size effect and tension-compression asymmetry. The following conclusions were drawn:

1) The Σ13 (320) symmetrical tilt grain boundary presented strong tension-compression asymmetric ability: the asymmetry of stress-strain curves with respect to the load directions; the yield strain was increased with the decreasing grain size for compression, while for tension the corresponding yield strain was increased with the increasing grain size;
2) The Young's modulus decreased with the decreasing grain size (or increasing the grain boundary volume fraction). Both tensile and compressive yield strength were decreased with the decreasing grain size, which obeyed the inverse Hall-Petch relationship in the current range of grain size;
3) For compression: the severe yielding was caused by the nucleation of partial dislocations at the grain boundaries regardless of the grain size; before yielding the grain boundaries have been severely thickened by the compressive deformation but still kept certain symmetry, and then became disordered and acted as the preferential region for the dislocation emission; the concentration of stress and deformation were confirmed at the grain boundaries; although the contribution of grain boundary yielding (coupling, sliding and thickening) to the yielding was insignificant and indirect, the occurrence of them would result in unavoidable perturbations to the grain boundary symmetry and then make it easy for dislocation nucleation; as the grain size was smaller, the relative movement between adjacent grains became easier to take place and correspondingly it was easier for dislocations to nucleate at the grain boundaries, which explains the inverse Hall-Petch relation;
4) For tension: the severe yielding was caused by the nucleation of partial dislocations inside the grains rather than at the grain boundaries regardless of the grain size; the dislocation nucleation was dependent on the comprehensive combination of the stress concentration and the fluctuations of energy and local structure; when approaching the yielding point the atoms on the potential planes inside grains for dislocation nucleation gradually deviated from the ideal FCC structure and some arbitrary vacancies formed, which provided the structure fluctuation in the middle of the grain; the dislocation nucleated from the middle of the grain where the atomic potentials and the stress concentration were secondly highest in the system. The most important

finding in this study is that the inverse Hall-Petch relation is not necessarily related to the grain boundary deformation;

5) Regarding the deformation mechanisms, the softening was caused by the grain boundary yielding and the nucleation and propagation of dislocations, while the hardening was caused by dislocation interactions and grain boundary blocking.

Recommendation and future work

The molecular dynamics method and models in the current study have proved to be very effective to simulate the grain boundary deformation behaviour. Some profound results have been concluded. However, this is still far less than expected and more simulation work should be done and supplemented in the future studies.

The model for interactions between dislocations and grain boundaries should be strongly improved and the corresponding post-processing methods will be also developed in the future studies.

Regarding the size effect and tension-compression asymmetry, a serial of symmetrical tilt grain boundaries other than the Σ13 (320) are already being simulated and analyzed using the same method. The results show some consistency. The asymmetric models are still in the stage of testing.

REFERENCES

[1] Langdon TG. An evaluation of the strain contributed by grain boundary sliding in superplasticity. Materials Science and Engineering A. 1994;174:225-30.
[2] Kulas MA, Green WP, Taleff EM, Krajewski PE, McNelley TR. Deformation mechanisms in superplastic AA5083 materials. Metallurgical and Materials Transactions A: Physical Metallurgy and Materials Science. 2005;36:1249-61.
[3] Barnes AJ. The industrial application of aluminum superplastic forming. Materials Research Society Symposium - Proceedings. 2000;601:207-21.
[4] Barnes AJ. Superplastic forming 40 years and still growing. Journal of Materials Engineering and Performance. 2007;16:440-54.
[5] Kulas MA, Green WP, Taleff EM, Krajewski PE, McNelley TR. Failure mechanisms in superplastic AA083 materials. Metallurgical and Materials Transactions A: Physical Metallurgy and Materials Science. 2006;37:645-55.
[6] Schroers J. The superplastic forming of bulk metallic glasses. JOM. 2005;57:35-9.
[7] Gleiter H. Nanocrystalline materials. Progress in Materials Science. 1989;33:223-315.
[8] Gryaznov VG, Trusov LI. Size effects in micromechanics of nanocrystals. Progress in Materials Science. 1993;37:289-401.
[9] Hono K. Nanoscale microstructural analysis of metallic materials by atom probe field ion microscopy. Progress in Materials Science. 2002;47:621-729.
[10] Meyers MA, Mishra A, Benson DJ. Mechanical properties of nanocrystalline materials. Progress in Materials Science. 2006;51:427-556.
[11] Pande CS, Cooper KP. Nanomechanics of Hall-Petch relationship in nanocrystalline materials. Progress in Materials Science. 2009;54:689-706.
[12] Valiev RZ, Langdon TG. Principles of equal-channel angular pressing as a processing tool for grain refinement. Progress in Materials Science. 2006;51:881-981.
[13] Všianská M, Šob M. The effect of segregated sp-impurities on grain-boundary and surface structure, magnetism and embrittlement in nickel. Progress in Materials Science. 2011;56:817-40.
[14] Zhang ZF, Wang ZG. Grain boundary effects on cyclic deformation and fatigue damage. Progress in Materials Science. 2008;53:1025-99.
[15] Zhu T, Li J. Ultra-strength materials. Progress in Materials Science. 2010;55:710-57.
[16] Zhu YT, Liao XZ, Wu XL. Deformation twinning in nanocrystalline materials. Progress in Materials Science. 2012;57:1-62.

[17] Gleiter H. Nanostructured materials: basic concepts and microstructure. Acta Materialia. 2000;48:1-29.
[18] Palumbo G, Thorpe SJ, Aust KT. On the contribution of triple junctions to the structure and properties of nanocrystalline materials. Scripta Metallurgica et Materiala. 1990;24:1347-50.
[19] Bringa EM, Caro A, Wang Y, Victoria M, McNaney JM, Remington BA, et al. Materials science: Ultrahigh strength in nanocrystalline materials under shock loading. Science. 2005;309:1838-41.
[20] Hemker KJ. Understanding How Nanocrystalline Metals Deform. Science. 2004;304:221-3.
[21] Schiøtz J, Jacobsen KW. A maximum in the strength of nanocrystalline copper. Science. 2003;301:1357-9.
[22] Chen J, Lu L, Lu K. Hardness and strain rate sensitivity of nanocrystalline Cu. Scripta Materialia. 2006;54:1913-8.
[23] Shankar MR, Chandrasekar S, King AH, Compton WD. Microstructure and stability of nanocrystalline aluminum 6061 created by large strain machining. Acta Materialia. 2005;53:4781-93.
[24] Sort J, Zhilyaev A, Zielinska M, Nogués J, Surińach S, Thibault J, et al. Microstructural effects and large microhardness in cobalt processed by high pressure torsion consolidation of ball milled powders. Acta Materialia. 2003;51:6385-93.
[25] Tian YZ, Li JJ, Zhang P, Wu SD, Zhang ZF, Kawasaki M, et al. Microstructures, strengthening mechanisms and fracture behavior of Cu-Ag alloys processed by high-pressure torsion. Acta Materialia. 2012;60:269-81.
[26] Tian YZ, Wu SD, Zhang ZF, Figueiredo RB, Gao N, Langdon TG. Microstructural evolution and mechanical properties of a two-phase Cu-Ag alloy processed by high-pressure torsion to ultrahigh strains. Acta Materialia. 2011;59:2783-96.
[27] Valiev RZ, Ivanisenko YV, Rauch EF, Baudelet B. Structure and deformaton behaviour of Armco iron subjected to severe plastic deformation. Acta Materialia. 1996;44:4705-12.
[28] Vidal V, Thilly L, Lecouturier F, Renault PO. Effects of size and geometry on the plasticity of high-strength copper/tantalum nanofilamentary conductors obtained by severe plastic deformation. Acta Materialia. 2006;54:1063-75.
[29] Ward DK, Curtin WA, Qi Y. Mechanical behavior of aluminum-silicon nanocomposites: A molecular dynamics study. Acta Materialia. 2006;54:4441-51.
[30] Wei W, Wei KX, Fan GJ. A new constitutive equation for strain hardening and softening of fcc metals during severe plastic deformation. Acta Materialia. 2008;56:4771-9.

[31] Widjaja A, Van der Giessen E, Needleman A. Discrete dislocation analysis of the wedge indentation of polycrystals. Acta Materialia. 2007;55:6408-15.
[32] Xu C, Horita Z, Langdon TG. The evolution of homogeneity in processing by high-pressure torsion. Acta Materialia. 2007;55:203-12.
[33] Xu C, Horita Z, Langdon TG. The evolution of homogeneity in an aluminum alloy processed using high-pressure torsion. Acta Materialia. 2008;56:5168-76.
[34] Xu C, Schroeder S, Berbon PB, Langdon TG. Principles of ECAP-Conform as a continuous process for achieving grain refinement: Application to an aluminum alloy. Acta Materialia. 2010;58:1379-86.
[35] Xu C, Xia K, Langdon TG. The role of back pressure in the processing of pure aluminum by equal-channel angular pressing. Acta Materialia. 2007;55:2351-60.
[36] Yang B, Vehoff H. Dependence of nanohardness upon indentation size and grain size - A local examination of the interaction between dislocations and grain boundaries. Acta Materialia. 2007;55:849-56.
[37] Zhang S, Hu W, Berghammer R, Gottstein G. Microstructure evolution and deformation behavior of ultrafine-grained Al-Zn-Mg alloys with fine η' precipitates. Acta Materialia. 2010;58:6695-705.
[38] Zhang X, Misra A, Wang H, Shen TD, Nastasi M, Mitchell TE, et al. Enhanced hardening in Cu/330 stainless steel multilayers by nanoscale twinning. Acta Materialia. 2004;52:995-1002.
[39] Zhao YH, Liao XZ, Jin Z, Valiev RZ, Zhu YT. Microstructures and mechanical properties of ultrafine grained 7075 Al alloy processed by ECAP and their evolutions during annealing. Acta Materialia. 2004;52:4589-99.
[40] Korznikov AV, Dimitrov O, Korznikova GF, Dallas JP, Quivy A, Valiev RZ, et al. Nanocrystalline structure and phase transformation of the intermetallic compound TiAl processed by severe plastic deformation. Nanostructured Materials. 1999;11:17-23.
[41] Provenzano V, Valiev R, Rickerby DG, Valdre G. Mechanical properties of nanostructured chromium. Nanostructured Materials. 1999;12:1103-8.
[42] Stolyarov VV, Zhu YT, Lowe TC, Islamgaliev RK, Valiev RZ. Two step SPD processing of ultrafine-grained titanium. Nanostructured Materials. 1999;11:947-54.
[43] Ngo DT, Duong HG, Nguyen HH, Nguyen C, Basith M, Hoang DQ. The microstructure, high performance magnetic hardness and magnetic after-effect of an α- FeCo/Pr2Fe14B nanocomposite magnet with low Pr concentration. Nanotechnology. 2009;20.
[44] Guo H, Yan PF, Wang YB, Tan J, Zhang ZF, Sui ML, et al. Tensile ductility and necking of metallic glass. Nature Materials. 2007;6:735-9.

[45] Valiev R. Nanostructuring of metals by severe plastic deformation for advanced properties. Nature Materials. 2004;3:511-6.
[46] Zhu YT, Liao X. Nanostructured metals: Retaining ductility. Nature Materials. 2004;3:351-2.
[47] Szlufarska I, Nakano A, Vashishta P. Materials science: A crossover in the mechanical response of nanocrystalline ceramics. Science. 2005;309:911-4.
[48] Pu Z, Yang S, Song GL, Dillon Jr OW, Puleo DA, Jawahir IS. Ultrafine-grained surface layer on Mg-Al-Zn alloy produced by cryogenic burnishing for enhanced corrosion resistance. Scripta Materialia. 2011;65:520-3.
[49] Valiev RZ, Mishral RS, Grozal J, Mukherjee AK. Processing of nanostructured nickel by severe plastic deformation consolidation of ball-milled powder. Scripta Materialia. 1996;34:1443-8.
[50] Dobatkin SV, Odessky PD, Shagalina SV. Ultrafine grained low carbon steels processed by severe plastic deformation. Goslar2008. p. 623-30.
[51] Glaessgen EH, Phillips DR, Yamakov V, Saether E. Multiscale modeling for the analysis of grain-scale fracture within aluminum microstructures. Austin, TX2005. p. 598-606.
[52] Glaessgen EH, Saether E, Phillips DR, Yamakov V. Multiscale modeling of grain-boundary fracture: Cohesive zone models parameterized from atomistic simulations. Newport, RI2006. p. 959-70.
[53] Greer AL. Nanostructured materials - From fundamentals to applications. 1998. p. 3-10.
[54] Salvatori I. Ultra grain refinement of low C steels by accumulative roll bonding. Fukuoka2006. p. 311-6.
[55] Bravo-Leon A, Morikawa Y, Kawahara M, Mayo MJ. Fracture toughness of nanocrystalline tetragonal zirconia with low yttria content. Acta Materialia. 2002;50:4555-62.
[56] Cui GR, Ma ZY, Li SX. The origin of non-uniform microstructure and its effects on the mechanical properties of a friction stir processed Al-Mg alloy. Acta Materialia. 2009;57:5718-29.
[57] Dai K, Villegas J, Stone Z, Shaw L. Finite element modeling of the surface roughness of 5052 Al alloy subjected to a surface severe plastic deformation process. Acta Materialia. 2004;52:5771-82.
[58] Qin EW, Lu L, Tao NR, Tan J, Lu K. Enhanced fracture toughness and strength in bulk nanocrystalline Cu with nanoscale twin bundles. Acta Materialia. 2009;57:6215-25.
[59] Roters F, Eisenlohr P, Hantcherli L, Tjahjanto DD, Bieler TR, Raabe D. Overview of constitutive laws, kinematics, homogenization and multiscale methods

in crystal plasticity finite-element modeling: Theory, experiments, applications. Acta Materialia. 2010;58:1152-211.
[60] Singh A, Tang L, Dao M, Lu L, Suresh S. Fracture toughness and fatigue crack growth characteristics of nanotwinned copper. Acta Materialia. 2011;59:2437-46.
[61] Guisbiers G, Herth E, Buchaillot L, Pardoen T. Fracture toughness, hardness, and Young's modulus of tantalum nanocrystalline films. Applied Physics Letters. 2010;97.
[62] Stolyarov VV, Valiev RZ, Zhu YT. Enhanced low-temperature impact toughness of nanostructured Ti. Applied Physics Letters. 2006;88:1-3.
[63] Wang YM, Ma E, Chen MW. Enhanced tensile ductility and toughness in nanostructured Cu. Applied Physics Letters. 2002;80:2395-7.
[64] Zaera R, Rodríguez-Martínez JA, Casado A, Fernández-Sáez J, Rusinek A, Pesci R. A constitutive model for analyzing martensite formation in austenitic steels deforming at high strain rates. International Journal of Plasticity. 2012;29:77-101.
[65] Gosh G. Elastic properties, hardness, and indentation fracture toughness of intermetallics relevant to electronic packaging. Journal of Materials Research. 2004;19:1439-54.
[66] Liu Y, Zhou J, Shen T, Hui D. Effects of ultrafine nanograins on the fracture toughness of nanocrystalline materials. Journal of Materials Research. 2011;26:1734-41.
[67] Berger S, Porat R, Rosen R. Nanocrystalline materials: A study of WC-based hard metals. Progress in Materials Science. 1997;42:311-20.
[68] Fullwood DT, Niezgoda SR, Adams BL, Kalidindi SR. Microstructure sensitive design for performance optimization. Progress in Materials Science. 2010;55:477-562.
[69] Kenny P, Campbell JD. Fracture toughness an examination of the concept in predicting the failure of materials. Progress in Materials Science. 1968;13:135-81.
[70] Malakondaiah G, Srinivas M, Rama Rao P. Ultrahigh-strength low-alloy steels with enhanced fracture toughness. Progress in Materials Science. 1997;42:209-42.
[71] Hassan HA, Lewandowski JJ. Laminated nanostructure composites with improved bend ductility and toughness. Scripta Materialia. 2009;61:1072-4.
[72] Samuel E, Jonas JJ, Samuel FH, MacEwen SR. Superplasticity in coarse-grained Al-Mg alloys. Vancouver2006. p. 1285-90.
[73] Semenova IP, Saitova LR, Raab GI, Korshunov AI, Zhu YT, Lowe TC, et al. Microstructural features and mechanical properties of the Ti-6Al-4V ELI alloy processed by severe plastic deformation. Fukuoka2006. p. 757-62.

[74] Dao M, Lu L, Asaro RJ, De Hosson JTM, Ma E. Toward a quantitative understanding of mechanical behavior of nanocrystalline metals. Acta Materialia. 2007;55:4041-65.
[75] Dao M, Lu L, Shen YF, Suresh S. Strength, strain-rate sensitivity and ductility of copper with nanoscale twins. Acta Materialia. 2006;54:5421-32.
[76] Delincé M, Bréchet Y, Embury JD, Geers MGD, Jacques PJ, Pardoen T. Structure-property optimization of ultrafine-grained dual-phase steels using a microstructure-based strain hardening model. Acta Materialia. 2007;55:2337-50.
[77] Frederiksen SL, Jacobsen KW, Schiøtz J. Simulations of intergranular fracture in nanocrystalline molybdenum. Acta Materialia. 2004;52:5019-29.
[78] Hebesberger T, Stüwe HP, Vorhauer A, Wetscher F, Pippan R. Structure of Cu deformed by high pressure torsion. Acta Materialia. 2005;53:393-402.
[79] Jérusalem A, Dao M, Suresh S, Radovitzky R. Three-dimensional model of strength and ductility of polycrystalline copper containing nanoscale twins. Acta Materialia. 2008;56:4647-57.
[80] Kulkarni Y, Asaro RJ. Are some nanotwinned fcc metals optimal for strength, ductility and grain stability? Acta Materialia. 2009;57:4835-44.
[81] Ovid'ko IA, Sheinerman AG. Enhanced ductility of nanomaterials through optimization of grain boundary sliding and diffusion processes. Acta Materialia. 2009;57:2217-28.
[82] Saraev D, Miller RE. Atomic-scale simulations of nanoindentation-induced plasticity in copper crystals with nanometer-sized nickel coatings. Acta Materialia. 2006;54:33-45.
[83] Tang F, Gianola DS, Moody MP, Hemker KJ, Cairney JM. Observations of grain boundary impurities in nanocrystalline Al and their influence on microstructural stability and mechanical behaviour. Acta Materialia. 2012;60:1038-47.
[84] Wang YB, Qu DD, Wang XH, Cao Y, Liao XZ, Kawasaki M, et al. Introducing a strain-hardening capability to improve the ductility of bulk metallic glasses via severe plastic deformation. Acta Materialia. 2012;60:253-60.
[85] Zhao Y, Topping T, Bingert JF, Thornton JJ, Dangelewicz AM, Li Y, et al. High tensile ductility and strength in bulk nanostructured nickel. Advanced Materials. 2008;20:3028-33.
[86] Fan C, Inoue A. Ductility of bulk nanocrystalline composites and metallic glasses at room temperature. Applied Physics Letters. 2000;77:46-8.
[87] Li H, Liaw PK, Choo H, Misra A. Effect of grain orientation on ductility in a nanocrystalline Ni-Fe alloy. Applied Physics Letters. 2008;93.

[88] Mo Y, Szlufarska I. Simultaneous enhancement of toughness, ductility, and strength of nanocrystalline ceramics at high strain-rates. Applied Physics Letters. 2007;90.
[89] Wang L, Zhang Z, Ma E, Han XD. Transmission electron microscopy observations of dislocation annihilation and storage in nanograins. Applied Physics Letters. 2011;98.
[90] Youssef KM, Scattergood RO, Murty KL, Horton JA, Koch CC. Ultrahigh strength and high ductility of bulk nanocrystalline copper. Applied Physics Letters. 2005;87:1-3.
[91] Qin L, Lian J, Jiang Z, Wang G, Jiang Q. Dual-phase nanocrystalline Ni-Co alloy with high strength and enhanced ductility. Journal of Materials Research. 2010;25:401-5.
[92] Wang G, Jiang Z, Zhang H, Lian J. Enhanced tensile ductility in an electrodeposited nanocrystalline copper. Journal of Materials Research. 2008;23:2238-44.
[93] Li X, Wei Y, Lu L, Lu K, Gao H. Dislocation nucleation governed softening and maximum strength in nano-twinned metals. Nature. 2010;464:877-80.
[94] Lu L, Chen X, Huang X, Lu K. Revealing the maximum strength in nanotwinned copper. Science. 2009;323:607-10.
[95] Gu C, Lian J, Jiang Z, Jiang Q. Enhanced tensile ductility in an electrodeposited nanocrystalline Ni. Scripta Materialia. 2006;54:579-84.
[96] Karimpoor AA, Erb U, Aust KT, Palumbo G. High strength nanocrystalline cobalt with high tensile ductility. Scripta Materialia. 2003;49:651-6.
[97] Divinski SV. Diffusion in nanostructured materials. Lanzarote2009. p. 623-32.
[98] Kolobov YR, Grabovetskaya GP, Ivanov KV, Ivanov MB. Diffusion and properties of bulk nanostructured metals and alloys processed by severe plastic deformation. 2003. p. 253-62.
[99] Watanabe H, Mukai T, Kohzu M, Tanabe S, Higashi K. Effect of temperature and grain size on the dominant diffusion process for superplastic flow in an AZ61 magnesium alloy. Acta Materialia. 1999;47:3753-8.
[100] Wagendristel A, Tschegg E, Semerad E, Bangert H. Computer simulation of interdiffusion in polycrystalline thin film couples. Applied Physics. 1976;10:237-43.
[101] Quang P, Krishnaiah A, Sun IH, Hyoung SK. Coupled analysis of heat transfer and deformation in equal channel angular pressing of Al and steel. Materials Transactions. 2009;50:40-3.
[102] Hirth JP. Effects of coherency on diffusivity in multilayers. Scripta Materialia. 2004;50:793-5.

[103] Tereshina IS, Burkhanov GS, Dobatkin SV, Chistyakov OD, Tereshina EA, Drulis H. Magnetic parameters of R2Fe14B compounds with nanograin structure. Goslar2008. p. 950-4.
[104] Wei DH, Yao YD. Enhanced magnetic properties in FePt (001) epitaxial thin films by Cu capping layer. Hongkong2010. p. 704-5.
[105] Cui BZ, Han K, Garmestani H, Su JH, Schneider-Muntau HJ, Liu JP. Enhancement of exchange coupling and hard magnetic properties in nanocomposites by magnetic annealing. Acta Materialia. 2005;53:4155-61.
[106] Chbihi A, Sauvage X, Genevois C, Blavette D, Gunderov D, Popov AG. Optimization of the magnetic properties of FePd alloys by severe plastic deformation. Advanced Engineering Materials. 2010;12:708-13.
[107] González J. Magnetic properties arising from two additive contributions in soft magnetic nanocrystalline alloys. Applied Physics Letters. 2004;85:5944-6.
[108] Kemény T, Kaptás D, Kiss LF, Balogh J, Bujdosó L, Gubicza J, et al. Structure and magnetic properties of nanocrystalline (Fe 1-xCo x) 90Zr 7B 2Cu 1 ($0 \leqslant x \leqslant 0.6$). Applied Physics Letters. 2000;76:2110-2.
[109] Marín P, Hernando A. Enhanced magnetic properties of FeCo ribbons nanocrystallized in magnetic field. Applied Physics Letters. 2009;94.
[110] Yue M, Wang KJ, Liu WQ, Zhang DT, Zhang JX. Structure and magnetic properties of bulk nanocrystalline Dy metal prepared by spark plasma sintering. Applied Physics Letters. 2008;93.
[111] Yue M, Zhang JX, Zhang DT, Pan LJ, Liu XB, Altounian Z. Structure and magnetic properties of bulk nanocrystalline Sm Co6.6 Nb0.4 permanent magnets. Applied Physics Letters. 2007;90.
[112] Daróczi L, Beke DL, Posgay G, Kis-Vargal M. Magnetic properties of ball milled nanocrystalilne Ni and Fe. Nanostructured Materials. 1995;6:981-4.
[113] Daróczi L, Beke DL, Posgay G, Zhou GF, Bakker H. Production and magnetic properties of nanocrystalline Fe and Ni. Nanostructured Materials. 1993;2:515-25.
[114] Frase HN, Shull RD, Hong LB, Stephens TA, Gao ZQ, Fultz B. Soft magnetic properties of nanocrystalline Ni3Fe and Fe75Al12.5Ge12.5. Nanostructured Materials. 1999;11:987-93.
[115] Jartych E, Zurawicz JK, Oleszak D, Pękała M. Magnetic properties and structure of nanocrystalline Fe-Al and Fe-Ni alloys. Nanostructured Materials. 1999;12:927-30.
[116] Krill CE, Merzoug F, Krauss W, Birringer R. Magnetic properties of nanocrystalline Gd and W/Gd. Nanostructured Materials. 1997;9:455-8.
[117] Ramin D, Riehemann W. Dependence of magnetic properties of finemet on nanocrystallisation conditions. Nanostructured Materials. 1999;12:867-9.

[118] Ha ND, Phan MH, Kim CO. Novel nanostructure and magnetic properties of Co-Fe-Hf-O films. Nanotechnology. 2007;18.
[119] Lu N, Song X, Zhang J. Crystal structure and magnetic properties of ultrafine nanocrystalline SmCo3 compound. Nanotechnology. 2010;21.
[120] Lei Y, Cai W, Wilde G. Highly ordered nanostructures with tunable size, shape and properties: A new way to surface nano-patterning using ultra-thin alumina masks. Progress in Materials Science. 2007;52:465-539.
[121] Krajewski PE, Montgomery Jr GP. Mechanical behavior and modeling of AA5083 at 450 ℃. In: Taleff EM, Friedman PA, Krajewski PE, Mishra RS, Schrith JG, editors. Charlotte, NC.2004. p. 341-50.
[122] Deng C, Sansoz F. Fundamental differences in the plasticity of periodically twinned nanowires in Au, Ag, Al, Cu, Pb and Ni. Acta Materialia. 2009;57:6090-101.
[123] Fu HC, Huang JC, Wang TD, Bampton CC. Evolution of microstructure and superplastic deformation mechanism in super α2Ti3Al base alloys. Acta Materialia. 1998;46:465-79.
[124] Wang J, Misra A. An overview of interface-dominated deformation mechanisms in metallic multilayers. Current Opinion in Solid State and Materials Science. 2011;15:20-8.
[125] Hokka M, Kokkonen J, Seidt J, Matrka T, Gilat A, Kuokkala VT. High Strain Rate Torsion Properties of Ultrafine-Grained Aluminum. Experimental Mechanics. 2012;52:195-203.
[126] Ni S, Wang YB, Liao XZ, Alhajeri SN, Li HQ, Zhao YH, et al. Strain hardening and softening in a nanocrystalline Ni-Fe alloy induced by severe plastic deformation. Materials Science and Engineering A. 2011;528:3398-403.
[127] Ni S, Wang YB, Liao XZ, Figueiredo RB, Li HQ, Zhao YH, et al. Strain softening in nanocrystalline Ni-Fe alloy induced by large HPT revolutions. Materials Science and Engineering A. 2011;528:4807-11.
[128] Su CW, Chua BW, Lu L, Lai MO. Properties of severe plastically deformed Mg alloys. Materials Science and Engineering A. 2005;402:163-9.
[129] Kaibyshev R, Goloborodko A, Musin F, Nikulin I, Sakai T. The role of grain boundary sliding in microstructural evolution during superplastic deformation of a 7055 aluminum alloy. Materials Transactions. 2002;43:2408-14.
[130] Figueiredo RB, Cetlin PR, Langdon TG. Stable and unstable flow in materials processed by equal-channel angular pressing with an emphasis on magnesium alloys. Metallurgical and Materials Transactions A: Physical Metallurgy and Materials Science. 2010;41:778-86.
[131] Carlton CE, Ferreira PJ. What is behind the inverse Hall-Petch effect in nanocrystalline materials? Acta Materialia. 2007;55:3749-56.

[132] Shen TD, Schwarz RB, Feng S, Swadener JG, Huang JY, Tang M, et al. Effect of solute segregation on the strength of nanocrystalline alloys: Inverse Hall-Petch relation. Acta Materialia. 2007;55:5007-13.
[133] Zhang B, Shim VPW. Effect of strain rate on microstructure of polycrystalline oxygen-free high conductivity copper severely deformed at liquid nitrogen temperature. Acta Materialia. 2010;58:6810-27.
[134] Buehler MJ, Hartmaier A, Duchaineau MA, Abraham FF, Gao H. Dynamical complexity of work-hardening: A large-scale molecular dynamics simulation. Acta Mechanica Sinica/Lixue Xuebao. 2005;21:103-11.
[135] Chang IL, Ding WC. The atomistic study of textured polycrystalline nanofilms. CMES - Computer Modeling in Engineering and Sciences. 2010;68:297-312.
[136] Buehler MJ, Hartmaier A, Gao H, Duchaineau M, Abraham FF. Atomic plasticity: Description and analysis of a one-billion atom simulation of ductile materials failure. Computer Methods in Applied Mechanics and Engineering. 2004;193:5257-82.
[137] Barai P, Weng GJ. Mechanics of very fine-grained nanocrystalline materials with contributions from grain interior, GB zone, and grain-boundary sliding. International Journal of Plasticity. 2009;25:2410-34.
[138] Cleri F. A two-phase model of large-strain plasticity in covalent nanostructures. International Journal of Plasticity. 2012;37:31-52.
[139] Zheng C, Zhang YW. A molecular dynamics study of the effect of voids on the deformation behavior of nanocrystalline copper. Journal of Nanomaterials. 2007;2007.
[140] Capolungo L, Spearot DE, Cherkaoui M, McDowell DL, Qu J, Jacob KI. Dislocation nucleation from bicrystal interfaces and grain boundary ledges: Relationship to nanocrystalline deformation. Journal of the Mechanics and Physics of Solids. 2007;55:2300-27.
[141] Tomar V, Zhou M. Analyses of tensile deformation of nanocrystalline α-Fe2O3+fcc-Al composites using molecular dynamics simulations. Journal of the Mechanics and Physics of Solids. 2007;55:1053-85.
[142] Desai TG, Millett P, Wolf D. Is diffusion creep the cause for the inverse Hall-Petch effect in nanocrystalline materials? Materials Science and Engineering A. 2008;493:41-7.
[143] Kadau K, Germann TC, Lomdahl PS, Holian BL, Kadau D, Entel P, et al. Molecular-dynamics study of mechanical deformation in nano-crystalline aluminum. Metallurgical and Materials Transactions A: Physical Metallurgy and Materials Science. 2004;35 A:2719-23.

[144] Marchenko A, Zhang H. Effects of Location of Twin Boundaries and Grain Size on Plastic Deformation of Nanocrystalline Copper. Metallurgical and Materials Transactions A: Physical Metallurgy and Materials Science. 2012:1-9.
[145] Buehler MJ, Hartmaier A, Gao H. Hierarchical multi-scale modelling of plasticity of submicron thin metal films. Modelling and Simulation in Materials Science and Engineering. 2004;12:S391-S413.
[146] Rajgarhia RK, Koh SW, Spearot D, Saxena A. Microstructure stability of nanocrystalline materials using dopants. Molecular Simulation. 2008;34:35-40.
[147] Zhao Y, Shen TD, Zhang J. High P-T nano-mechanics of polycrystalline nickel. Nanoscale Research Letters. 2007;2:476-91.
[148] Song HW, Guo SR, Hu ZQ. Coherent polycrystal model for the inverse Hall-Petch relation in nanocrystalline materials. Nanostructured Materials. 1999;11:203-10.
[149] Heino P, Ristolainen E. Strength of nanoscale polycrystalline copper under shear. Philosophical Magazine A: Physics of Condensed Matter, Structure, Defects and Mechanical Properties. 2001;81:957-70.
[150] Yamakov V, Wolf D, Phillpot SR, Mukherjee AK, Gleiter H. Deformation mechanism crossover and mechanical behaviour in nanocrystalline materials. Philosophical Magazine Letters. 2003;83:385-93.
[151] Vo NQ, Averback RS, Bellon P, Caro A. Limits of hardness at the nanoscale: Molecular dynamics simulations. Physical Review B - Condensed Matter and Materials Physics. 2008;78.
[152] Li M, Xu T. Topological and atomic scale characterization of grain boundary networks in polycrystalline and nanocrystalline materials. Progress in Materials Science. 2011;56:864-99.
[153] Sun CQ. Thermo-mechanical behavior of low-dimensional systems: The local bond average approach. Progress in Materials Science. 2009;54:179-307.
[154] Sun CQ. Size dependence of nanostructures: Impact of bond order deficiency. Progress in Solid State Chemistry. 2007;35:1-159.
[155] Giga A, Kimoto Y, Takigawa Y, Higashi K. Demonstration of an inverse Hall-Petch relationship in electrodeposited nanocrystalline Ni-W alloys through tensile testing. Scripta Materialia. 2006;55:143-6.
[156] Wolf D, Yamakov V, Phillpot SR, Mukherjee AK. Deformation mechanism and inverse Hall-Petch behavior in nanocrystalline materials. Zeitschrift fuer Metallkunde/Materials Research and Advanced Techniques. 2003;94:1091-7.
[157] Charit I, Mishra RS. Low temperature superplasticity in a friction-stir-processed ultrafine grained Al-Zn-Mg-Sc alloy. Acta Materialia. 2005;53:4211-23.

[158] Du N, Qi Y, Krajewski PE, Bower AF. Aluminum R3 grain boundary sliding enhanced by vacancy diffusion. Acta Materialia. 2010;58:4245-52.
[159] Gu P, Dao M, Asaro RJ, Suresh S. A unified mechanistic model for size-dependent deformation in nanocrystalline and nanotwinned metals. Acta Materialia. 2011;59:6861-8.
[160] Ma ZY, Liu FC, Mishra RS. Superplastic deformation mechanism of an ultrafine-grained aluminum alloy produced by friction stir processing. Acta Materialia. 2010;58:4693-704.
[161] Saada G, Kruml T. Deformation mechanisms of nanograined metallic polycrystals. Acta Materialia. 2011;59:2565-74.
[162] Frøseth AG, Derlet PM, Van Swygenhoven H. Grown-in twin boundaries affecting deformation mechanisms in nc-metals. Applied Physics Letters. 2004;85:5863-5.
[163] Gurao NP, Suwas S. Deformation mechanisms during large strain deformation of nanocrystalline nickel. Applied Physics Letters. 2009;94.
[164] Wang YM, Hodge AM, Biener J, Hamza AV, Barnes DE, Liu K, et al. Deformation twinning during nanoindentation of nanocrystalline Ta. Applied Physics Letters. 2005;86:1-3.
[165] Mitra R, Chiou WA, Weertman JR. In situ study of deformation mechanisms in sputtered free-standing nanocrystalline nickel films. Journal of Materials Research. 2004;19:1029-37.
[166] Tao NR, Wu XL, Sui ML, Lu J, Lu K. Grain refinement at the nanoscale via mechanical twinning and dislocation interaction in a nickel-based alloy. Journal of Materials Research. 2004;19:1623-9.
[167] Van Swygenhoven H, Spaczer M, Caro A. Role of low and high angle grain boundaries in the deformation mechanism of nanophase Ni: A molecular dynamics simulation study. Nanostructured Materials. 1998;10:819-28.
[168] Liao XZ, Huang JY, Zhu YT, Zhou F, Lavernia EJ. Nanostructures and deformation mechanisms in a cryogenically ball-milled Al-Mg alloy. Philosophical Magazine. 2003;83:3065-75.
[169] Luque A, Aldazabal J, Martínez-Esnaola JM, Gil Sevillano J. Plastic deformation by conservative shear-coupled migration of tilt boundaries with intergranular nano-cracks or precipitates. Philosophical Magazine. 2010;90:3743-56.
[170] Horita Z, Smith DJ, Nemoto M, Valiev RZ, Langdon TG. Observations of grain boundary structure in submicrometer-grained Cu and Ni using high-resolution electron microscopy. Journal of Materials Research. 1998;13:446-50.
[171] Merkle KL. Atomic structure of grain boundaries. Journal of Physics and Chemistry of Solids. 1994;55:991-1005.

[172] Schiøtz J, Di Tolla FD, Jacobsen KW. Softening of nanocrystalline metals at very small grain sizes. Nature. 1998;391:561-3.
[173] Van Swygenhoven H. Grain boundaries and dislocations. Science. 2002;296:66-7.
[174] Yip S. The strongest size. Nature. 1998;391:532-3.
[175] Ke M, Hackney SA, Milligan WW, Aifantis EC. Observation and measurement of grain rotation and plastic strain in nanostructured metal thin films. Nanostructured Materials. 1995;5:689-97.
[176] Youngdahl CJ, Weertman JR, Hugo RC, Kung HH. Deformation behavior in nanocrystalline copper. Scripta Materialia. 2001;44:1475-8.
[177] Kumar KS, Suresh S, Chisholm MF, Horton JA, Wang P. Deformation of electrodeposited nanocrystalline nickel. Acta Materialia. 2003;51:387-405.
[178] Hugo RC, Kung H, Weertman JR, Mitra R, Knapp JA, Follstaedt DM. In-situ TEM tensile testing of DC magnetron sputtered and pulsed laser deposited Ni thin films. Acta Materialia. 2003;51:1937-43.
[179] Van Swygenhoven H, Weertman JR. Preface to the viewpoint set on: Mechanical properties of fully dense nanocrystalline metals. Scripta Materialia. 2003;49:625-7.
[180] Shan Z, Stach EA, Wiezorek JMK, Knapp JA, Follstaedt DM, Mao SX. Grain boundary-mediated plasticity in nanocrystalline nickel. Science. 2004;305:654-7.
[181] Ivanisenko Y, Kurmanaeva L, Weissmueller J, Yang K, Markmann J, Rösner H, et al. Deformation mechanisms in nanocrystalline palladium at large strains. Acta Materialia. 2009;57:3391-401.
[182] Mao X, Shan Z. Nanomechanics on grain boundary mediated plasticity in nanocrystalline material. Huangshan2008. p. 78.
[183] Sergueeva AV, Mara NA, Krasilnikov NA, Valiev RZ, Mukherjee AK. Cooperative grain boundary sliding in nanocrystalline materials. Philosophical Magazine. 2006;86:5797-804.
[184] Sergueeva AV, Mara NA, Mukherjee AK. Plasticity at really diminished length scales. Materials Science and Engineering A. 2007;463:8-13.
[185] Wiezorek JMK, Kulovits AK, Yanar C, Soffa WA. Grain boundary mediated displacive-diffusional formation of τ-phase MnAl. Metallurgical and Materials Transactions A: Physical Metallurgy and Materials Science. 2011;42:594-604.
[186] Ovid'ko IA. Superplasticity and ductility of superstrong nanomaterials. Reviews on Advanced Materials Science. 2005;10:89-104.
[187] Bate PS, Ridley N, Zhang B. Mechanical behaviour and microstructural evolution in superplastic Al-Li-Mg-Cu-Zr AA8090. Acta Materialia. 2007;55:4995-5006.

[188] Naydenkin EV, Grabovetskaya GP. Deformation behavior and plastic strain localization of nanostructured materials produced by severe plastic deformation. In: Zhao Y, Liao X, editors.2010. p. 107-19.
[189] Ovid'Ko IA, Sheinerman AG, Aifantis EC. Effect of cooperative grain boundary sliding and migration on crack growth in nanocrystalline solids. Acta Materialia. 2011;59:5023-31.
[190] Zhang QK, Zhang ZF. In situ observations on creep fatigue fracture behavior of Sn-4Ag/Cu solder joints. Acta Materialia. 2011;59:6017-28.
[191] Pancholi V, Kashyap BP. Microstructural evolution during superplastic forming of Al-Li 8090 alloy. Mumbai2012. p. 374-7.
[192] Spigarelli S, El Mehtedi M, Regev M, Gariboldi E, Lecis N. High Temperature Creep and Superplasticity in a Mg-Zn-Zr Alloy. Journal of Materials Science and Technology. 2012;28:407-13.
[193] Tanimoto H. Mechanical spectroscopy of nanocrystalline metals and nanometer-thick films: Characteristic properties originated in nanostructures. Lausanne2012. p. 42-51.
[194] Walley JL, Wheeler R, Uchic MD, Mills MJ. In-Situ Mechanical Testing for Characterizing Strain Localization During Deformation at Elevated Temperatures. Experimental Mechanics. 2012;52:405-16.
[195] Syed B, Catoor D, Mishra R, Kumar KS. Coupled motion of [1010] tilt boundaries in magnesium bicrystals. Philosophical Magazine. 2012;92:1499-522.
[196] Watanabe T, Yamada M, Shima S, Karashima S. MISORIENTATION DEPENDENCE OF GRAIN BOUNDARY SLIDING IN 101-BAR-O-DIRECTION TILT ZINC BICRYSTALS. Philosophical Magazine A: Physics of Condensed Matter, Structure, Defects and Mechanical Properties. 1979;40:667-83.
[197] Sheikh-Ali AD. On the contribution of extrinsic grain boundary dislocations to grain boundary sliding in bicrystals. Acta Materialia. 1997;45:3109-14.
[198] Sheikh-Ali AD, Lavrentyev FF, Kazarov YG. Sliding behaviour of $\Sigma = 9\{1212\}$ symmetric tilt boundary in zinc bicrystals. Acta Materialia. 1997;45:4505-12.
[199] Sheikh-Ali AD, Valiev RZ. Dislocation analysis of the coupling of grain boundary sliding and migration during the deformation of Zn bicrystals. Physica Status Solidi (A) Applied Research. 1990;117:429-36.
[200] Maruyama K, Wananabe Y, Oikawa H. Grain boundary strengthening at elevated temperatures: Creep of aluminum doped zinc bicrystals and polycrystals. Acta Metallurgica. 1986;34:2343-51.
[201] Miura S, Okada T, Onaka S, Hashimoto S. Effects of a boundary node on grain-boundary sliding and intergranular fracture in Cu-9at.%Al tricrystals. Journal de physique Colloque. 1990;C1:587-92.

[202] Matsunaga K, Nishimura H, Hanyu S, Muto H, Yamamoto T, Ikuhara Y. HRTEM study on grain boundary atomic structures related to the sliding behavior in alumina bicrystals. Applied Surface Science. 2005;241:75-9.
[203] Matsunaga K, Nishimura H, Saito T, Yamamoto T, Ikuhara Y. High-resolution transmission electron microscopy and computational analyses of atomic structures of [0001] symmetric tilt grain boundaries of Al2O3 with equivalent grain-boundary planes. Philosophical Magazine. 2003;83:4071-82.
[204] Zhang S, Wang Y, Jiang H, Zhou J. Constitutive model for plastic deformation of nanocrystalline materials with shear band. Meccanica. 2012:1-11.
[205] Li S, Zeng X, Ren B, Qian J, Zhang J, Jha AK. An atomistic-based interphase zone model for crystalline solids. Computer Methods in Applied Mechanics and Engineering. 2012;229-232:87-109.
[206] Lee WM, Zikry MA. High strain-rate modeling of the interfacial effects of dispersed particles in high strength aluminum alloys. International Journal of Solids and Structures. 2012.
[207] Przybyla CP, McDowell DL. Microstructure-sensitive extreme-value probabilities of high-cycle fatigue for surface vs. subsurface crack formation in duplex Ti-6Al-4V. Acta Materialia. 2012;60:293-305.
[208] Zhu T, Gao H. Plastic deformation mechanism in nanotwinned metals: An insight from molecular dynamics and mechanistic modeling. Scripta Materialia. 2012;66:843-8.
[209] Zhang Y, Millett PC, Tonks M, Zhang L, Biner B. Molecular dynamics simulations of He bubble nucleation at grain boundaries. Journal of Physics Condensed Matter. 2012;24.
[210] Zhang J, Zhao J, Lu J. Intrinsic strength and failure behaviors of graphene grain boundaries. ACS Nano. 2012;6:2704-11.
[211] Trautt ZT, Mishin Y. Grain boundary migration and grain rotation studied by molecular dynamics. Acta Materialia. 2012;60:2407-24.
[212] Mishin Y, Asta M, Li J. Atomistic modeling of interfaces and their impact on microstructure and properties. Acta Materialia. 2010;58:1117-51.
[213] Yuasa M, Amemiya T, Mabuchi M. Enhanced grain boundary embrittlement of an Fe grain boundary segregated by hydrogen (H). Journal of Materials Research. 2012;27:1589-97.
[214] Wang Z, Zhou YG, Bang J, Prange MP, Zhang SB, Gao F. Modification of defect structures in graphene by electron irradiation: Ab initio molecular dynamics simulations. Journal of Physical Chemistry C. 2012;116:16070-9.

[215] Ivanovskii AL. Mechanical and electronic properties of diborides of transition 3d-5d metals from first principles: Toward search of novel ultra-incompressible and superhard materials. Progress in Materials Science. 2012;57:184-228.
[216] Barnard L, Odette GR, Szlufarska I, Morgan D. An ab initio study of Ti-Y-O nanocluster energetics in nanostructured ferritic alloys. Acta Materialia. 2012;60:935-47.
[217] Jensen F. Introduction to Computational Chemistry. Chichester, England: John Wiley and Sons; 2007.
[218] Fu HH, Benson DJ, Meyers MA. Analytical and computational description of effect of grain size on yield stress of metals. Acta Materialia. 2001;49:2567-82.
[219] Fu HH, Benson DJ, Meyers MA. Computational description of nanocrystalline deformation based on crystal plasticity. Acta Materialia. 2004;52:4413-25.
[220] Wei Y, Anand L. A constitutive model for powder-processed nanocrystalline metals. Acta Materialia. 2007;55:921-31.
[221] Benson DJ, Fu HH, Meyers MA. On the effect of grain size on yield stress: Extension into nanocrystalline domain. Materials Science and Engineering A. 2001;319-321:854-61.
[222] Meyers MA, Benson DJ, Vöhringer O, Kad BK, Xue Q, Fu HH. Constitutive description of dynamic deformation: Physically-based mechanisms. Materials Science and Engineering A. 2002;322:194-216.
[223] Yamakov V, Wolf D, Phillpot SR, Gleiter H. Dislocation-dislocation and dislocation-twin reactions in nanocrystalline Al by molecular dynamics simulation. Acta Materialia. 2003;51:4135-47.
[224] Yamakov V, Wolf D, Phillpot SR, Mukherjee AK, Gleiter H. Dislocation processes in the deformation of nanocrystalline aluminium by molecular-dynamics simulation. Nature Materials. 2002;1:45-8.
[225] Yamakov V, Wolf D, Salazar M, Phillpot SR, Gleiter H. Length-scale effects in the nucleation of extended dislocations in nanocrystalline Al by molecular-dynamics simulation. Acta Materialia. 2001;49:2713-22.
[226] Van Swygenhoven H, Caro A. Plastic behavior of nanophase Ni: A molecular dynamics computer simulation. Applied Physics Letters. 1997;71:1652-4.
[227] Yamakov V, Wolf D, Phillpot SR, Gleiter H. Dislocation processes and deformation twinning in nanocrystalline Al. In: Laudon M, Romanowicz B, editors. San Juan2002. p. 283-6.
[228] Bilde-Sørensen JB, Schiøtz J. Nanocrystals get twins. Science. 2003;300:1244-5.

[229] Hasnaoui A, Van Swygenhoven H, Derlet PM. Cooperative processes during plastic deformation in nanocrystalline fcc metals: A molecular dynamics simulation. Physical Review B - Condensed Matter and Materials Physics. 2002;66:1841121-8.
[230] Howe JM. Interfaces in Materials. New York: John Wiley & Sons, Inc; 1997.
[231] Wikipedia. http://enwikipediaorg/wiki/Grain_boundary.
[232] http://www.tf.uni-kiel.de/.
[233] Bachurin DV, Gumbsch P. Accommodation processes during deformation of nanocrystalline palladium. Acta Materialia. 2010;58:5491-501.
[234] Cahn JW, Mishin Y, Suzuki A. Coupling grain boundary motion to shear deformation. Acta Materialia. 2006;54:4953-75.
[235] Cahn JW, Mishin Y, Suzuki A. Duality of dislocation content of grain boundaries. Philosophical Magazine. 2006;86:3965-80.
[236] Mishin Y, Suzuki A, Uberuaga BP, Voter AF. Stick-slip behavior of grain boundaries studied by accelerated molecular dynamics. Physical Review B - Condensed Matter and Materials Physics. 2007;75.
[237] Rittner JD, Seidman DN. Limitations of the structural unit model. 1996. p. 333-6.
[238] Rittner JD, Seidman DN. <110> symmetric tilt grain-boundary structures in fee metals with low stacking-fault energies. Physical Review B - Condensed Matter and Materials Physics. 1996;54:6999-7015.
[239] Tschopp MA, Tucker GJ, McDowell DL. Structure and free volume of 〈1 1 0〉 symmetric tilt grain boundaries with the E structural unit. Acta Materialia. 2007;55:3959-69.
[240] Tschopp MA, McDowell DL. Asymmetric tilt grain boundary structure and energy in copper and aluminium. Philosophical Magazine. 2007;87:3871-92.
[241] Sutton AP, Vitek V. Phil Trans R Soc A. 1983;309:1.
[242] Brown JA, Mishin Y. Dissociation and faceting of asymmetrical tilt grain boundaries: Molecular dynamics simulations of copper. Physical Review B - Condensed Matter and Materials Physics. 2007;76:134118.
[243] Shimokawa T. Asymmetric ability of grain boundaries to generate dislocations under tensile or compressive loadings. Physical Review B - Condensed Matter and Materials Physics. 2010;82:174122.
[244] Read WT, Shockley W. Dislocation models of crystal grain boundaries. Physical Review. 1950;78:275-89.
[245] Zhang H. Atomistic simulation of sliding of [1010] tilt grain boundaries in Mg. Journal of Materials Research. 2009;24:3446-53.
[246] Tschopp MA, McDowell DL. Structural unit and faceting description of Σ3 asymmetric tilt grain boundaries. Journal of Materials Science. 2007;42:7806-11.

[247] Tschopp MA, McDowell DL. Structures and energies of Σ3 asymmetric tilt grain boundaries in copper and aluminium. Philosophical Magazine. 2007;87:3147-73.
[248] Tschopp MA, McDowell DL. Dislocation nucleation in Σ3 asymmetric tilt grain boundaries. International Journal of Plasticity. 2008;24:191-217.
[249] Hamilton JC, Siegel DJ, Daruka I, Léonard F. Why do grain boundaries exhibit finite facet lengths? Physical Review Letters. 2003;90:246102/1-/4.
[250] Wu ZX, Zhang YW, Srolovitz DJ. Grain boundary finite length faceting. Acta Materialia. 2009;57:4278-87.
[251] Chandra N, Dang P. Atomistic simulation of grain boundary sliding and migration. Journal of Materials Science. 1999;34:655-66.
[252] Namilae S, Chandra N, Nieh TG. Atomistic simulation of grain boundary sliding in pure and magnesium doped aluminum bicrystals. Scripta Materialia. 2002;46:49-54.
[253] Qi Y, Krajewski PE. Molecular dynamics simulations of grain boundary sliding: The effect of stress and boundary misorientation. Acta Materialia. 2007;55:1555-63.
[254] Sansoz F, Molinari JF. Mechanical behavior of Σ tilt grain boundaries in nanoscale Cu and Al: A quasicontinuum study. Acta Materialia. 2005;53:1931-44.
[255] Kurtz RJ, Hoagland RG, Hirth JP. Computer simulation of extrinsic grain-boundary defects in the Σ11, <101>{131} symmetric tilt boundary. Philosophical Magazine A: Physics of Condensed Matter, Structure, Defects and Mechanical Properties. 1999;79:683-703.
[256] Kurtz RJ, Hoagland RG, Hirth JP. Effect of extrinsic grain-boundary defects on grain-boundary sliding resistance. Philosophical Magazine A: Physics of Condensed Matter, Structure, Defects and Mechanical Properties. 1999;79:665-81.
[257] Hoagland RG, Kurtz RJ. The relation between grain-boundary structure and sliding resistance. Philosophical Magazine A: Physics of Condensed Matter, Structure, Defects and Mechanical Properties. 2002;82:1073-92.
[258] Du N, Qi Y, Krajewski PE, Bower AF. The effect of solute atoms on aluminum grain boundary sliding at elevated temperature. Metallurgical and Materials Transactions A: Physical Metallurgy and Materials Science. 2011;42:651-9.
[259] Washburn J, Parquer ER. Journal of Metals AIME Transaction. 1952;4:1076.
[260] Li CH, Edwards EH, Washburn J, Parker ER. Stress-induced movement of crystal boundaries. Acta Metallurgica. 1953;1:223-9.
[261] McLean D. Interaction between crystal slip and grain boundary movement [5]. Nature. 1953;172:300-1.

[262] Khayutin SG. DEFORMATION OF POLYCRYSTALS DUE TO THE MIGRATION OF GRAIN BOUNDARIES. Physics of Metals and Metallography. 1974;37:161-9.
[263] Jessell MW. Grain boundary migration and fabric development in experimentally deformed octachloropropane. Journal of Structural Geology. 1986;8:527-42.
[264] Guillope M, Poirier JP. A model for stress-induced migration of tilt grain boundaries in crystals of NaCl structure. Acta Metallurgica. 1980;28:163-7.
[265] Winning M, Rollett AD. Transition between low and high angle grain boundaries. Acta Materialia. 2005;53:2901-7.
[266] Winning M, Gottstein G, Shvindlerman LS. Stress induced grain boundary motion. Acta Materialia. 2001;49:211-9.
[267] Winning M, Gottstein G, Shvindlerman LS. On the mechanisms of grain boundary migration. Acta Materialia. 2002;50:353-63.
[268] Molodov DA, Shvindlerman LS. Interface migration in metals (IMM): "Vingt Ans Après" (Twenty Years Later). International Journal of Materials Research. 2009;100:461-82.
[269] Mompiou F, Caillard D, Legros M. Grain boundary shear-migration coupling-I. In situ TEM straining experiments in Al polycrystals. Acta Materialia. 2009;57:2198-209.
[270] Legros M, Gianola DS, Hemker KJ. In situ TEM observations of fast grain-boundary motion in stressed nanocrystalline aluminum films. Acta Materialia. 2008;56:3380-93.
[271] Zhang H, Du D, Srolovitz DJ. Effects of boundary inclination and boundary type on shear-driven grain boundary migration. Philosophical Magazine. 2008;88:243-56.
[272] Zhang H, Mendelev MI, Srolovitz DJ. Mobility of Σ5 tilt grain boundaries: Inclination dependence. Scripta Materialia. 2005;52:1193-8.
[273] Zhang H, Srolovitz DJ, Douglas JF, Warren JA. Characterization of atomic motion governing grain boundary migration. Physical Review B - Condensed Matter and Materials Physics. 2006;74.
[274] Zhang H, Upmanyu M, Srolovitz DJ. Curvature driven grain boundary migration in aluminum: Molecular dynamics simulations. Acta Materialia. 2005;53:79-86.
[275] Ivanov VA, Mishin Y. Dynamics of grain boundary motion coupled to shear deformation: An analytical model and its verification by molecular dynamics. Physical Review B - Condensed Matter and Materials Physics. 2008;78.

[276] Jin M, Minor AM, Stach EA, Morris Jr JW. Direct observation of deformation-induced grain growth during the nanoindentation of ultrafine-grained Al at room temperature. Acta Materialia. 2004;52:5381-7.
[277] Zhang K, Weertman JR, Eastman JA. The influence of time, temperature, and grain size on indentation creep in high-purity nanocrystalline and ultrafine grain copper. Applied Physics Letters. 2004;85:5197-9.
[278] Mughrabi H, Höppel HW, Kautz M. Fatigue and microstructure of ultrafine-grained metals produced by severe plastic deformation. Scripta Materialia. 2004;51:807-12.
[279] Zhang K, Weertman JR, Eastman JA. Rapid stress-driven grain coarsening in nanocrystalline Cu at ambient and cryogenic temperatures. Applied Physics Letters. 2005;87.
[280] Van Swygenhoven H, Weertman JR. Deformation in nanocrystalline metals. Materials Today. 2006;9:24-31.
[281] Fan GJ, Fu LF, Qiao DC, Choo H, Liaw PK, Browning ND. Grain growth in a bulk nanocrystalline Co alloy during tensile plastic deformation. Scripta Materialia. 2006;54:2137-41.
[282] Gianola DS, Warner DH, Molinari JF, Hemker KJ. Increased strain rate sensitivity due to stress-coupled grain growth in nanocrystalline Al. Scripta Materialia. 2006;55:649-52.
[283] Brandstetter S, Zhang K, Escuadro A, Weertman JR, Van Swygenhoven H. Grain coarsening during compression of bulk nanocrystalline nickel and copper. Scripta Materialia. 2008;58:61-4.
[284] Schäfer J, Albe K. Influence of solutes on the competition between mesoscopic grain boundary sliding and coupled grain boundary motion. Scripta Materialia. 2012;66:315-7.
[285] Bachurin DV, Weygand D, Gumbsch P. Dislocation-grain boundary interaction in 〈1 1 1〉 textured thin metal films. Acta Materialia. 2010;58:5232-41.
[286] Dellas NS, Harper JME. Effect of deposition angle on fiber axis tilt in sputtered aluminum nitride and pure metal films. Thin Solid Films. 2006;515:1647-50.
[287] Gao SF, Liu L, Zhao XB, Huang TW, Zhang J, Fu HZ. Effects of spiral geometries on grain selection during casting of single crystal superalloys. Materials Science and Technology. 2011;27:1783-7.
[288] Zhao XB, Liu L, Gao SF, Ge BM, Zhang J, Li YL, et al. Effect of orientation on the microstructure of nickel-based crystalline superalloys. Crystal Research and Technology. 2011;46:1291-5.

[289] Bernstein N. The influence of geometry on grain boundary motion and rotation. Acta Materialia. 2008;56:1106-13.
[290] Dewald MP, Curtin WA. Multiscale modelling of dislocation/grain boundary interactions. II. Screw dislocations impinging on tilt boundaries in Al. Philosophical Magazine. 2007;87:4615-41.
[291] Jin ZH, Gumbsch P, Albe K, Ma E, Lu K, Gleiter H, et al. Interactions between non-screw lattice dislocations and coherent twin boundaries in face-centered cubic metals. Acta Materialia. 2008;56:1126-35.
[292] Jin ZH, Gumbsch P, Ma E, Albe K, Lu K, Hahn H, et al. The interaction mechanism of screw dislocations with coherent twin boundaries in different face-centred cubic metals. Scripta Materialia. 2006;54:1163-8.
[293] Cheng Y, Mrovec M, Gumbsch P. Crack nucleation at the Σ 9 (2 over(2,¯) 1) symmetrical tilt grain boundary in tungsten. Materials Science and Engineering A. 2008;483-484:329-32.
[294] Cheng Y, Mrovec M, Gumbsch P. Atomistic simulations of interactions between the 1/2 〈111〉 edge dislocation and symmetric tilt grain boundaries in tungsten. Philosophical Magazine. 2008;88:547-60.
[295] Rao SI, Hazzledine PM. Atomistic simulations of dislocation-interface interactions in the Cu-Ni multilayer system. Philosophical Magazine A: Physics of Condensed Matter, Structure, Defects and Mechanical Properties. 2000;80:2011-40.
[296] Chen Z, Jin Z, Gao H. Repulsive force between screw dislocation and coherent twin boundary in aluminum and copper. Physical review B. 2007;75:212104.
[297] Hoagland RG, Mitchell TE, Hirth JP, Kung H. On the strengthening effects of interfaces in multilayer fcc metallic composites. Philosophical Magazine A: Physics of Condensed Matter, Structure, Defects and Mechanical Properties. 2002;82:643-64.
[298] Wang J, Hoagland RG, Hirth JP, Misra A. Atomistic modeling of the interaction of glide dislocations with "weak" interfaces. Acta Materialia. 2008;56:5685-93.
[299] Wang J, Hoagland RG, Hirth JP, Misra A. Atomistic simulations of the shear strength and sliding mechanisms of copper-niobium interfaces. Acta Materialia. 2008;56:3109-19.
[300] Wang J, Hoagland RG, Hirth JP, Capolungo L, Beyerlein IJ, Tomé CN. Nucleation of a (over(1,¯) 0 1 2) twin in hexagonal close-packed crystals. Scripta Materialia. 2009;61:903-6.
[301] Wang J, Hoagland RG, Liu XY, Misra A. The influence of interface shear strength on the glide dislocation- interface interactions. Acta Materialia. 2011;59:3164-73.

[302] Wang J, Misra A, Hoagland RG, Hirth JP. Slip transmission across fcc/bcc interfaces with varying interface shear strengths. Acta Materialia. 2012;60:1503-13.
[303] Tschopp MA, Tucker GJ, McDowell DL. Atomistic simulations of tension-compression asymmetry in dislocation nucleation for copper grain boundaries. Computational Materials Science. 2008;44:351-62.
[304] Chassagne M, Legros M, Rodney D. Atomic-scale simulation of screw dislocation/coherent twin boundary interaction in Al, Au, Cu and Ni. Acta Materialia. 2011;59:1456-63.
[305] Hoagland RG, Kurtz RJ, Henager Jr CH. Slip resistance of interfaces and the strength of metallic multilayer composites. Scripta Materialia. 2004;50:775-9.
[306] Henager Jr CH, Kurtz RJ, Hoagland RG. Interactions of dislocations with disconnections in fee metallic nanolayered materials. Philosophical Magazine. 2004;84:2277-303.
[307] http://en.wikipedia.org/wiki/Molecular_dynamics.
[308] Lennard-Jones JE. On the Determination of Molecular Fields. Proceedings of the Royal Society of London Series A. 1924;738:463-77.
[309] Daw MS, Baskes MI. Semiempirical, quantum mechanical calculation of hydrogen embrittlement in metals. Physical Review Letters. 1983;50:1285-8.
[310] Daw MS, Baskes MI. Embedded-atom method: Derivation and application to impurities, surfaces, and other defects in metals. Physical Review B. 1984;29:6443-53.
[311] D.C. R. The Art Of Molecular Dynamics Simulation. Second Edition ed. United States of America by Cambridge University Press, New York: Cambridge University Press; 2004.
[312] Plimpton S. Fast parallel algorithms for short-range molecular dynamics. Journal of Computational Physics. 1995;117:1-19.
[313] Mendelev MI, Kramer MJ, Becker CA, Asta M. Analysis of semi-empirical interatomic potentials appropriate for simulation of crystalline and liquid Al and Cu. Philosophical Magazine. 2008;88:1723-50.
[314] Faken D, Jónsson H. Systematic analysis of local atomic structure combined with 3D computer graphics. Computational Materials Science. 1994;2:279-86.
[315] Kelchner CL, Plimpton SJ, Hamilton JC. Dislocation nucleation and defect structure during surface indentation. Physical Review B - Condensed Matter and Materials Physics. 1998;58:11085-8.
[316] Humphrey W, Dalke A, Schulten K. VMD: Visual molecular dynamics. Journal of Molecular Graphics. 1996;14:33-8.
[317] Li J. AtomEye: An efficient atomistic configuration viewer. Modelling and Simulation in Materials Science and Engineering. 2003;11:173-7.

[318] Langdon TG. Grain boundary sliding as a deformation mechanism during creep. Phil Mag. 1970;22:689-700.
[319] Langdon TG. A unified approach to grain boundary sliding in creep and superplasticity. Acta Metallurgica Et Materialia. 1994;42:2437-43.
[320] Gifkins RC, Gittins A, Bell RL, Langdon TG. The dependence of grain-boundary sliding on shear stress. Journal of Materials Science. 1968;3:306-13.
[321] Gifkins RC, Langdon TG. Grain boundary displacements due to diffusional creep. Scripta Metallurgica. 1970;4:563-6.
[322] Sherby OD, Wadsworth J. Superplasticity-Recent advances and future directions. Progress in Materials Science. 1989;33:169-221.
[323] Kokawa H, Watanabe T, Karashima S. SLIDING BEHAVIOUR AND DISLOCATION STRUCTURES IN ALUMINIUM GRAIN BOUNDARIES. Philosophical Magazine A: Physics of Condensed Matter, Structure, Defects and Mechanical Properties. 1981;44:1239-54.
[324] Fukutomi H, Yamamoto T, Nonomura K, Takada K. Examination of dislocation mechanism on grain boundary sliding in high angle grain boundaries by stress change test. Interface Science. 1999;7:141-6.
[325] Ballo P, Kioussis N, Lu G. Grain boundary sliding and migration: Effect of temperature and vacancies. Physical Review B - Condensed Matter and Materials Physics. 2001;64:241041-7.
[326] Hirth JP, Pond RC, Lothe J. Disconnections in tilt walls. Acta Materialia. 2006;54:4237-45.
[327] Ogata S, Li J, Yip S. The Effect of Size-Dependent Nanoparticle Energetics on Catalyst Sintering. Science. 2002;298:5.
[328] Tschopp MA, Spearot DE, McDowell DL. Atomistic simulations of homogeneous dislocation nucleation in single crystal copper. Modelling and Simulation in Materials Science and Engineering. 2007;15:693-709.
[329] Tschopp MA, McDowell DL. Tension-compression asymmetry in homogeneous dislocation nucleation in single crystal copper. Applied Physics Letters. 2007;90.
[330] Winning M, Gottstein G, Shvindlerman LS. Migration of grain boundaries under the influence of an external shear stress. Materials Science and Engineering A. 2001;317:17-20.
[331] Bishop Jr GH, Harrison RJ, Kwok T, Yip S. Computer molecular-dynamics studies of grain-boundary structures. I. Observations of coupled sliding and migration in a three-dimensional simulation. Journal of Applied Physics. 1982;53:5596-608.

[332] Fang TH, Li WL, Tao NR, Lu K. Revealing extraordinary intrinsic tensile plasticity in gradient nano-grained copper. Science. 2011;331:1587-90.
[333] Gianola DS, Van Petegem S, Legros M, Brandstetter S, Van Swygenhoven H, Hemker KJ. Stress-assisted discontinuous grain growth and its effect on the deformation behavior of nanocrystalline aluminum thin films. Acta Materialia. 2006;54:2253-63.
[334] Li J, Soh AK. On shear-coupled migration of grain boundaries in nanocrystalline materials. Applied Physics Letters. 2012;101.
[335] Rupert TJ, Gianola DS, Gan Y, Hemker KJ. Experimental observations of stress-driven grain boundary migration. Science. 2009;326:1686-90.
[336] Washburn J, Parker ER. Kinking in Zinc single-crystal tension specimens. Journal of Metals. 1952;4:1075-8.
[337] Gorkaya T, Molodov DA, Gottstein G. Stress-driven migration of symmetrical 〈1 0 0〉 tilt grain boundaries in Al bicrystals. Acta Materialia. 2009;57:5396-405.
[338] Gorkaya T, Burlet T, Molodov DA, Gottstein G. Experimental method for true in situ measurements of shear-coupled grain boundary migration. Scripta Materialia. 2010;63:633-6.
[339] Molodov DA, Gorkaya T, Gottstein G. Migration of the Σ7 tilt grain boundary in Al under an applied external stress. Scripta Materialia. 2011;65:990-3.
[340] Mompiou F, Legros M, Caillard D. Direct observation and quantification of grain boundary shear-migration coupling in polycrystalline Al. Journal of Materials Science. 2011;46:4308-13.
[341] Gleiter H. The mechanism of grain boundary migration. Acta Metallurgica. 1969;17:565-73.
[342] Ashby MF. Boundary defects, and atomistic aspects of boundary sliding and diffusional creep. Surface Science. 1972;31:498-542.
[343] Cahn JW, Taylor JE. A unified approach to motion of grain boundaries, relative tangential translation along grain boundaries, and grain rotation. Acta Materialia. 2004;52:4887-98.
[344] Bishop Jr GH, Harrison RJ, Kwok T, Yip S. Computer molecular dynamics simulation studies of grain-boundary structures. II. Migration, sliding, and annihilation in a two-dimensional solid. Journal of Applied Physics. 1982;53:5609-16.
[345] Molteni C, Marzari N, Payne MC, Heine V. Sliding Mechanisms in Aluminum Grain Boundaries. Physical Review Letters. 1997;79:869-72.
[346] Ballo P, Degmová J, Slugeň V. Grain boundary sliding and migration in copper: Vacancy effect. Physical Review B - Condensed Matter and Materials Physics. 2005;72.

[347] Zhang H, Mendelev MI, Srolovitz DJ. Computer simulation of the elastically driven migration of a flat grain boundary. Acta Materialia. 2004;52:2569-76.
[348] Suzuki A, Mishin Y. Atomic mechanisms of grain boundary motion Materials Science Forum. 2005;502:157-62.
[349] Trautt ZT, Adland A, Karma A, Mishin Y. Coupled motion of asymmetrical tilt grain boundaries: Molecular dynamics and phase field crystal simulations. Acta Materialia. 2012;60:6528-46.
[350] Merkle KL, Smith DJ. Atomic structure of symmetric tilt grain boundaries in NiO. Physical Review Letters. 1987;59:2887-90.
[351] Mills MJ, Daw MS, Thomas GJ, Cosandey F. High-resolution transmission electron microscopy of grain boundaries in aluminum and correlation with atomistic calculations. Ultramicroscopy. 1992;40:247-57.
[352] Mills MJ. High resolution transmission electron microscopy and atomistic calculations of grain boundaries in metals and intermetallics. Materials Science and Engineering A. 1993;166:35-50.
[353] Krakow W. Multiplicity of atomic structure for Σ = 17/[001] symmetrical tilt boundaries in gold. Acta Metallurgica et Materialia. 1990;38:1031-6.
[354] Vitek V, Sutton AP, Wang GJ, Schwartz D. On the multiplicity of structures and grain boundaries. Scripta Metallurgica. 1983;17:183-9.
[355] Wang GJ, Sutton AP, Vitek V. A computer simulation study of 〈001〉 and 〈111〉 tilt boundaries: the multiplicity of structures. Acta Metallurgica. 1984;32:1093-104.
[356] Hyde B, Farkas D, Caturla MJ. Atomistic sliding mechanisms of the ∑=5 symmetric tilt grain boundary in bcc iron. Philosophical Magazine. 2005;85:3795-807.
[357] Monk J, Hyde B, Farkas D. The role of partial grain boundary dislocations in grain boundary sliding and coupled grain boundary motion. Journal of Materials Science. 2006;41:7741-6.
[358] Wan L, Wang S. Shear response of the Σ 9 〈110〉 {221} symmetric tilt grain boundary in fcc metals studied by atomistic simulation methods. Physical Review B - Condensed Matter and Materials Physics. 2010;82.
[359] Mishin Y, Farkas D, Mehl MJ, Papaconstantopoulos DA. Interatomic potentials for monoatomic metals from experimental data and ab initio calculations. Physical Review B - Condensed Matter and Materials Physics. 1999;59:3393-407.
[360] Cosandey F, Chan SW, Stadelmann P. Atomic structure of a ∑ = 5 (310) symmetric tilt boundary in Au. Scripta Metallurgica. 1988;22:1093-6.
[361] Hirth JP, Lothe J. Theory of Dislocations. Second Edition ed. Malabar, Florida: Krieger Publishing Company; 1982.

[362] Yue L, Zhang H, Li DY. A closer look at the local responses of twin and grain boundaries in Cu to stress at the nanoscale with possible transition from the P-H to the inverse P-H relation. Acta Materialia. 2010;58:2677-84.
[363] Spearot DE, Tschopp MA, Jacob KI, McDowell DL. Tensile strength of 〈1 0 0〉 and 〈1 1 0〉 tilt bicrystal copper interfaces. Acta Materialia. 2007;55:705-14.
[364] Spearot DE, Jacob KI, McDowell DL. Nucleation of dislocations from [0 0 1] bicrystal interfaces in aluminum. Acta Materialia. 2005;53:3579-89.